



# Advanced Manufacturing of Non-Isocyanate Polyurethanes by Chemical Design

A manuscript submitted to the

University of the Basque Country  
(UPV/EHU) & University of Liège (Uliege)

Donostia-San Sebastián · Spain · June 2025

PhD Thesis

Presented by

Marco Caliarì

Under the supervision of

Dr. Haritz Sardon (UPV/EHU)

Dr. Christophe Detrembleur (Uliege)





*"Curiosity is the most powerful driving force in the universe because it can overcome the two greatest braking forces in the universe: reason and fear"*

**Walter Moers**





## Abstract

Non-isocyanate polyurethanes belong to a class of materials that has seen rising interests thanks to their higher safety when compared to their isocyanate-based counterparts. Of all non-isocyanate polyurethanes, polyoxazolidones have shown promising applications as the result of their particular chemical reactivity.

While promising, polyoxazolidones are relatively unexplored, especially in their manufacturing. This work focuses on finding new chemistries involving oxazolidones and combining them with advanced manufacturing, offering a platform for the development of this class of non-isocyanate polyurethanes.

In **Chapter 1**, we describe state-of-the-art in 3D printing techniques and their role in rendering manufacturing more sustainable. We follow by giving a bird's eye view of non-isocyanate polyurethane chemistry and its recent developments. We complete the chapter by describing the characteristics of dynamic networks since they are going to be a central theme in the following chapters.

In **Chapter 2**, we implement extrusion-based 3D printing techniques together with dynamic materials with advanced properties. We develop phase separated materials with mechanical properties that are spatially tuned by selective thermal annealing.

**Chapter 3** is devoted to expanding the printability of these materials towards light-based 3D printing techniques. To do so, we develop a new photocuring procedure and systematically search for reactive diluents to have a desirable viscosity of the resin.

In **Chapter 4**, we move to monomer design in order to endow the oxazolidone-based materials with degradability. We develop a new type

## Abstract

of dynamic bond, study its formation and dynamics, and finally, introduce it in DLP printable materials with tuneable degradability.

**Chapter 5** describes further developments through monomer design where we heighten the hydrolytic stability of the network material at ambient conditions. This enables us to have materials that are stable in water and prepare them in high yields that were not possible with the chemistry developed in **Chapter 4**. We introduce a new dynamic bond in mechanically and chemically recyclable materials that are hydrolytically degradable.

The last experimental chapter, **Chapter 6**, describes the implementation of dynamic oxazolidone crosslinkers in a proof-of-concept slippery coating for biomedical use.

Finally, **Chapter 7**, holds the main conclusions from the experimental chapter together with a look at future developments of the materials here described.

## Resumen

Los poliuretanos sin isocianatos son una clase de materiales que ha despertado un creciente interés gracias a su mayor seguridad en comparación con sus homólogos basados en isocianatos. Dentro de los poliuretanos sin isocianatos, los polioxazolidononas han mostrado aplicaciones prometedoras debido a su particular reactividad química.

Si bien son prometedores, la investigación sobre esta clase de polímeros sigue siendo limitada, especialmente en lo que respecta a su fabricación. Este trabajo se centra en encontrar nuevas químicas que involucren oxazolidonas y combinarlas con manufactura avanzada, ofreciendo una plataforma para el desarrollo de esta clase de poliuretanos no isocianatos.

En el **Capítulo 1**, describimos el estado del arte en la química de poliuretanos sin isocianatos y sus desarrollos recientes. Se presentan las características de las redes dinámicas, ya que serán un tema central en los capítulos siguientes. Completamos el capítulo con la descripción de las técnicas de impresión 3D y su rol en la fabricación sostenible.

En el **Capítulo 2**, implementamos técnicas de impresión 3D por extrusión junto con materiales dinámicos de propiedades avanzadas. Desarrollamos materiales con separación de fases cuyas propiedades mecánicas pueden ajustarse espacialmente mediante calentamiento selectivo.

El **Capítulo 3** se dedica a expandir la imprimibilidad de estos materiales hacia técnicas de impresión 3D basadas en luz. Para ello, desarrollamos un nuevo procedimiento de fotocurado y realizamos una búsqueda sistemática de diluyentes (non)reactivos para ajustar la viscosidad de la resina.

## Resumen

En el **Capítulo 4**, abordamos el diseño de monómeros con el objetivo de dotar a los materiales basados en oxazolidonas de degradabilidad. Desarrollamos un nuevo tipo de enlace dinámico, estudiamos su formación y dinámica, e introducimos esta química en materiales imprimibles mediante luz con degradabilidad ajustable.

El **Capítulo 5** describe avances adicionales en el diseño de monómeros, donde implementamos oximas como nucleófilos. Esto nos permite alcanzar conversiones más altas, que no eran posibles en el capítulo anterior, además de mantener la degradabilidad. Introducimos este enlace en materiales reciclables mecánicamente, químicamente y degradables.

El último capítulo experimental, el **Capítulo 6**, describe la implementación de reticulantes dinámicos de oxazolidona en un recubrimiento resbaladizo de prueba de concepto para aplicaciones biomédicas.

Finalmente, el **Capítulo 7** presenta las principales conclusiones de los capítulos experimentales, junto con una perspectiva sobre futuros desarrollos de los materiales aquí descritos.

## Résumé

Les polyuréthanes non isocyanates sont une classe de matériaux qui suscite un intérêt croissant grâce à leur sécurité accrue par rapport à leurs homologues à base d'isocyanates. Parmi tous les polyuréthanes non isocyanates, les polyoxazolidones montrent des applications prometteuses grâce à leur réactivité chimique particulière.

Bien que prometteuse, cette classe de polymères reste relativement inexplorée, en particulier en ce qui concerne leur fabrication. Ce travail se concentre sur la recherche de nouvelles chimies impliquant des oxazolidones et leur combinaison avec des techniques de fabrication avancées, offrant ainsi une plateforme pour le développement de cette classe de polyuréthanes non isocyanates.

Dans le **chapitre 1**, nous décrivons l'état de l'art de la chimie des polyuréthanes non isocyanates et ses développements récents. Nous décrivons les caractéristiques des réseaux dynamiques, car ils seront un thème central dans les chapitres suivants. Nous concluons le chapitre par la description des techniques d'impression 3D et de leur rôle dans la fabrication plus durable.

Dans le **chapitre 2**, nous mettons en œuvre des techniques d'impression 3D basées sur l'extrusion combinées à des matériaux dynamiques présentant des propriétés avancées. Nous développons des matériaux à séparation de phases avec des propriétés mécaniques ajustées spatialement par chauffage sélectif.

Le **chapitre 3** est consacré à l'extension de l'imprimabilité de ces matériaux vers des techniques d'impression 3D basées sur la lumière. Pour ce faire, nous développons une nouvelle procédure de photocuration et recherchons systématiquement des diluants réactifs afin d'obtenir la viscosité souhaitée de la résine.

## Résumé

Le **chapitre 4** se concentre sur la conception de monomères afin d'attribuer aux matériaux à base d'oxazolidone des propriétés de dégradabilité. Nous développons un nouveau type de liaison dynamique, étudions sa formation et sa dynamique, et l'introduisons dans des matériaux imprimables par DLP avec une dégradabilité modulable.

Le **chapitre 5** décrit de nouveaux développements à travers la conception de monomères visant à augmenter la stabilité hydrolytique dans des conditions ambiantes. Cela nous permet d'obtenir des matériaux stables dans l'eau avec des rendements élevés, ce qui n'était pas possible avec la chimie développée au **chapitre 4**. Nous introduisons cette liaison dans des matériaux mécaniquement et chimiquement recyclables et hydrolytiquement dégradables.

Le dernier chapitre expérimental, le **chapitre 6**, décrit la mise en œuvre de réticulants dynamiques à base d'oxazolidone dans un revêtement glissant de preuve de concept pour des applications biomédicales.

Enfin, le **chapitre 7** présente les principales conclusions des chapitres expérimentaux, ainsi qu'une perspective sur les développements futurs des matériaux décrits ici.

## Acknowledgements

As this work's cover only shows three names, but the pages are crafted by the hands and minds of uncountable people, the next few lines are dedicated to thank some (hopefully most).

As my the main supervisor of this work, the first words will have to go Haritz Sardon. You gave me both the space and trust to develop this project fully. I thank you for showing me how to valorize my ideas to bring them to fruition.

As my co-supervisor, I want to thank Christophe Detrembleur for his keen eye and for hosting me for the first year of PhD.

As my main unofficial supervisor I want to thank Fernando Vidal, for keeping up the spirits, following papers from their inception to their publication with painstaking patience.

As an infinite source of ideas, and maybe more than anything else a friend, I want to thank Daniele. You taught me how to survive in academia, giving me the energy to follow through notwithstanding any difficulty. You and Elena make a wonderful couple, and one of the closest friends I have.

As the mainstay of the lab, I wish to thank MartaX, for keeping order in this chaotic mass.

As the backbone of this weird superorganism I want to thank every and all postdoc in the lab, starting from Lucas for being an encyclopedia you can always refer to, Gabriel for his passion, Louise for her (unfathomable) positivity, Letizia for her support, Xabi for building up 3D printing expertise and actually being a nice human being, Ion for his availability and obviously Mikel for his ability to calculate any reaction



## Acknowledgements

pathway in 30 sec time (while writing random letters on a black screen, still baffles me)

As the muscles, keeping this machine moving I want to thank each and every student who works or worked in Sardon Lab. I want to thank Gabi and Flore for their joyful energy, and Ainhoa, Alice Jon, Emelin, Paula, Emelin, Ane, Claire, Jacopo, Giulia, Gianmaria, MartaM, Shafi, Jaya, Oihane, Akshaya, Bea, Ekta and Ander for creating a working environment in which I felt welcomed. Special thanks to Aritz, for being the perfect hoodmate. Major recognition also goes to all the support staff of the lab. Thanks also to all the people from the faculty and beyond: Federica, Ilaria, Antonella, Sharon and everyone else.

As we lived a year still plagued by the remnants of a pandemic that everyone wants to forget I want to thank all the people at CERM. Especially Anna, Oscar, Lionel, Sofia and François for their company in the toughest year of PhD. Warm thanks also to Bruno and Thomas for teaching me everything I know about cyclic carbonates.

As science is an inherently collaborative struggle, I want to thank all the collaborators that gave life to the studies contained herein. A thanks goes to the people at PolymerExpert for hosting me for three months in their premises.

As we shared this experience far away in space but close in mind, I want to thank all the NIPU people. In these years we created a community that I hope will thrive after this chapter.

As all instruments were painstakingly maintained and operated, I must thank the countless technician enabling whole generation of scientist to push the boundaries of knowledge. Special thanks to Loli Martin for her support in AFM characterisation.

## Acknowledgements

As life is not only work I want to thank all the people I met outside the chemistry faculty. To Adam, Irian, Jorge, Sara and Fernando. People that make coming back to Belgium a joy: Ci, Cata and Givi. People from the past that remain more than important: Julian, Tommy, Orlando.

As the youngest brother I want to thank my siblings for paving the way, every chapter in new ways. I deeply appreciate the relationship we've constructed in the years, even at a distance you are central in my life.

As my roots I want to thank my family. You've enabled me to explore far and wide while always keeping a safe nest to where I could return.

As my life companion, I want to thank Chiara. We built and continue building a life-defining link, one that I am proud of...



## List of Acronyms and Symbols

<b>3MP</b> Methyl-3-Mercaptopropionate	<b>DVB</b> Divinylbenzene
<b>Ace</b> Acetone	<b>DVS</b> Divinyl Sulfone
<b>ACN</b> Acetonitrile	<b>E<sub>a</sub></b> Activation Energy
<b>AFM</b> Atomic Force Microscopy	<b>E<sub>c</sub></b> Critical Energy
<b>AM</b> Additive Manufacturing	<b>E<sub>flow</sub></b> Activation Energy of Flow
<b>ANT</b> Anthraquinone	<b>EtOAc</b> Ethyl Acetate
<b>BAPO</b> Phenylbis(2,4,6-trimethylbenzoyl)phosphine oxide	<b>FDM</b> Fused Deposition Modeling
<b>BnOH</b> Benzyl Alcohol	<b>FEP</b> Fluorinated Ethylene Propylene
<b>CAN</b> Covalent Adaptable Network	<b>FFF</b> Fused Filament Fabrication
<b>DBU</b> 1,8-Diazabicyclo[5.4.0]undec-7-ene	<b>FTIR</b> Fourier Transform Infrared Spectroscopy
<b>DFT</b> Density Functional Theory	<b>GC</b> Gel Content
<b>DIW</b> Direct Ink Writing	<b>HARP</b> High Area Rapid Printing
<b>DLP</b> Digital Light Processing	<b>HexOH</b> Hexanol
<b>DM</b> Diallyl Maleate	<b>HRMS</b> High Resolution Mass Spectroscopy
<b>DMSO</b> Dimethyl Sulfoxide	<b>IOD</b> Bis(4-methylphenyl)iodonium hexafluorophosphate
<b>DMTA</b> Dynamic Thermomechanical Analysis	<b>ITX</b> Isopropyl Thioxanthone
<b>D<sub>p</sub></b> Degree of Penetration	<b>LCD</b> Liquid Crystal Display
<b>DRIPS</b> Dynamic Reaction-Induced Phase Separation	<b>mDSC</b> modulated Differential Scanning Calorimetry
<b>DT</b> Diallyl Terephthalate	<b>MeOH</b> Methanol

**MIBC** 4-methyl-2-pentyl alcohol  
**MM** Multimeral  
**MSA** methanesulfonic acid  
**NIPU** Non-Isocyanate Polyurethane  
**NMR** Nuclear Magnetic Resonance  
**OM** Optical Microscopy  
**PEO** Polythelene Glycol  
**PhOH** Phenol  
**PHOXa** Polyhydroxyoxazolidone  
**PHU** Polyhydroxyurethane  
**POU** Poly(oxo)urethane  
**POXa** Polyoxazolidone  
**PPO** Polypropylene oxide  
**PU** Polyurethanes  
**RDS** Rate-Determining Step  
**SEC** Size Exclusion Chromatography  
**SEM** Scanning Electron Microscopy  
**SI** Swelling Index

**SLA** Stereolithography  
**s-NOM** Scanning near Field Optical Microscopy  
**SYMS** Sylanto 7 MS  
**tBuOH** Tert-Butyl Alcohol  
**TEA** Triethyl Amine  
**TEM** Transmission Electron Microscopy  
**TFA** Trifluoro Acetic Acid  
**T<sub>g</sub>** Glass Transition Temperature  
**TGA** Thermogravimetric Analysis  
**THF** Tetrahydrofuran  
**TPL** Two-photon Lithography  
**T<sub>ur</sub>** Temperature of Upper Transition  
**TVC** Trivinyl Cyclohexane  
**VAM** Volumetric Additive Manufacturing  
**VP** Vat Photopolymeriza

# Table of contents

Abstract.....	V
Resumen .....	VII
Résumé .....	IX
Acknowledgements .....	XI
List of Acronyms and Symbols.....	XV
Table of contents.....	XVII
Introduction.....	1
1.1. The current face of Chemistry and its future .....	3
1.2. Additive Manufacturing and its Role in Sustainability .....	4
1.2.1. Material Extrusion.....	7
1.2.2. Vat Photopolymerization .....	9
1.3. The Rise of Non-isocyanate Polyurethanes.....	21
1.3.1. Polyoxazolidones, a less famous class of NIPUs.....	24
1.4. The role of Covalent Adaptable Networks in Today's Polymer Chemistry.....	27
1.4.1. Associative CANs .....	29
1.4.2. Dissociative CANs .....	29
1.4.3. Parameters for the design of CANs .....	30
1.4.4. Applications .....	31
1.5. References .....	32
Aim of this thesis .....	47
Fully recyclable Pluripotent Networks for 3D printing enabled by dissociative dynamic bonds .....	51

2.1. Abstract .....	53
2.2. Introduction .....	55
2.3. Results and Discussion .....	59
2.3.1. Probing Thiol-Ene Reactions in a Difunctional Oxazolidone 59	
2.3.2. Reversible Thiol-Ene Dynamics in Tandem Polymer Networks .....62	
2.3.3. Attaining Pluripotent Behavior through Tempering ....66	
2.3.4. FDM of Pluripotent Materials towards Functional Builds .....71	
2.4. Conclusions .....	76
2.5. Materials And Methods .....	78
2.6. References .....	121
DLP Printing of Pluripotent Materials .....	127
3.1. Abstract .....	129
3.2. Introduction .....	131
3.3. Results and Discussion .....	133
3.3.1. 3D printing of tandem formulation .....	133
3.3.2. Developing a 2-stage curing .....	142
3.3.3. DLP printing by 2-Stage Curing .....	148
3.4. Conclusions .....	149
3.5. Materials and Methods .....	150
3.6. References .....	160
A Platform for the 3D printing of dissociative CO <sub>2</sub> -derived Networks with Tuneable Degradation .....	165

4.1.	Abstract .....	167
4.2.	Introduction .....	169
4.3.	Results and Discussion.....	171
4.3.1.	Small molecule studies .....	171
4.3.1.	Preparation of Photocurable Materials .....	177
4.3.2.	Versatility of the <i>N,O</i> -acetal chemistry .....	179
4.3.3.	Hydrolytic Degradation: From Model Compounds to Materials .....	183
4.3.4.	DLP 3D Printing .....	187
4.4.	Conclusions .....	189
4.5.	Materials and Methods .....	192
4.6.	References .....	251

## Developing the Oxime-ene dynamic chemistry towards degradable and recyclable NIPUs .....

5.1.	Abstract .....	261
5.2.	Introduction .....	263
5.3.	Results and Discussion .....	265
5.3.1.	Small molecule studies .....	265
5.3.2.	Modelling of the Oxime-ene Reaction.....	270
5.3.3.	Preparation of Materials Based on the Oxime-ene Reaction .....	271
5.3.4.	Hydrolytic Degradation .....	274
5.4.	Conclusions .....	276
5.5.	Materials and Methods .....	278
5.6.	References .....	331



General Conclusions .....	385
7.1. Conclusions .....	387
7.2. Perspective .....	394
7.3. List of Publications .....	396

# 1

Introduction

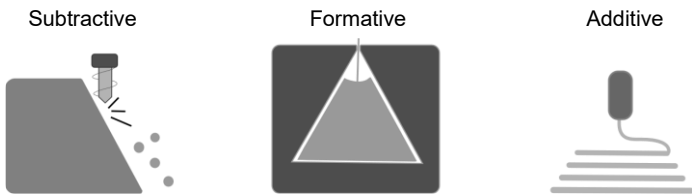


## 1.1. The current face of Chemistry and its future

Chemistry cannot be separated from the context in which it exists. Its relation and impacts unfold on the environment, society and the economy, revealing a deeply interconnected system. As one of the major branches of chemistry, polymer chemistry majorly influenced the world we live in and continues to do so to this day. Undeniably, polymers and their most recognisable form, plastics, have benefitted society, giving access to clean(er) energy and water, accessible manufacturing and medicines. Accompanying this, irresponsible, short-sighted production and aggressive lobbying have brought widespread pollution with limited understanding of the possible long-term effects, transgressing planetary boundaries and leaving us in the zone of high risk.<sup>1</sup> With foresight vision, Krief *et al*<sup>2</sup> built upon the chemistry-oriented twelve principles of green chemistry and proposed the “One World Chemistry” concept. In their work, a systems thinking approach was described for chemistry, recognising in the chemist the role not to only develop new materials, but also to act as a steward and approach their research with a holistic view.<sup>3</sup> Combining this concept with the principles of circular chemistry<sup>4</sup> enables today’s chemists to orient themselves away from short-sighted strategies in which the immediate utility is the priority over long term sustainability. Albeit this work has a marked explorative nature, we attempted to intermix these approaches, striving for interdisciplinarity and focussing on the whole materials life, from its synthesis to its manufacturing to its end-of-life potential.

## 1.2. Additive Manufacturing and its Role in Sustainability

Producing objects in a layer-by-layer fashion is not a modern thing. However, with the advent of computers its combination into what is commonly referred to as additive manufacturing (AM) or 3D printing.<sup>5</sup> This manufacturing technique is a rapidly evolving field that allows the quick preparation of metal, ceramics, glass and polymeric objects from computer-designed models. When compared to subtractive, (such as machining and drilling) or formative manufacturing (injection moulding), additive manufacturing is capable of producing parts with higher complexity and generates less waste (Scheme 1.1). Furthermore, the cost of the part is (partially) decoupled from the scale at which is produced, enabling the production of complex parts economically.<sup>6</sup> Additive manufacturing has also the ability to create objects by depositing material only where it is actually needed, allowing the use of less material per part, a concept named dematerialisation.<sup>7,8</sup>



**Scheme 1.1.** Schematic representation of subtractive, formative and additive manufacturing techniques.

AM techniques are divided into seven categories (ISO/ASTM) being binder jetting, material jetting, powder bed fusion, direct energy

deposition, sheet lamination, vat photopolymerization and material extrusion (Scheme 1.2).<sup>9</sup>

**Binder jetting** refers to an AM technique in which a binder agent is jetted through a nozzle on a bed of powdered material. After a layer has been formed, the printer deposits a new layer of powder, and the binder is again jetted. Following this, a densification process is carried out in order to give shape stability to the 3D-printed object. This technique is very versatile and can print materials ranging from ceramics to polymers, however, it requires multiple steps to arrive to the final printed part.

In **material jetting** a photopolymer is jetted through a nozzle and cured in a layer-by-layer fashion. This printing technique is fast but has limited applicability owing to the stringent viscosity requirements. Multi-material strategy can be easily implemented by using additional nozzles.

A powdered material is hit by a strong laser that melts selected regions in **Powdered bed fusion**. This technique is useful for the printing of both metals and polymers. The stringent requirements of the powder uniformity and low electrostatic charge limit its breadth, it is however the technique of choice for printing metal parts.

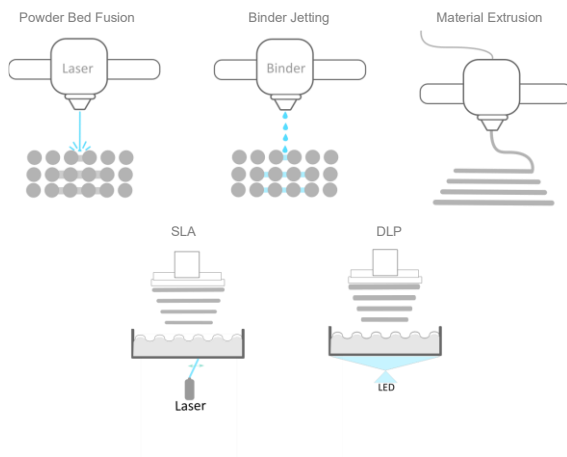
In **direct energy deposition**, a strong laser melts the material as soon as it is deposited enabling the printing of metals and alloys.

**Sheet lamination** refers to producing layers by cutting and stacking sheets of a material, useful to produce bulk objects.

**Material extrusion** refers to any technique in which the material is extruded through a nozzle. It is one of the most popular techniques for AM as it is simple and low-cost. Between all types of material extrusion, fused filament fabrication (FFF) has seen wide commercial success. In

this technique, a polymeric filament is deposited in a layer-by-layer fashion. Wider industrial adoption is still limited because of this technique's inherent anisotropic mechanical properties, given by poor interfilamentous adhesion, and poor surface quality. A more general term that is widely employed in the literature is direct ink writing (DIW), in which material the material feed is different from a polymeric filament.

Finally, **VAT photopolymerization** refers to any technique that employs a light source to cure a specific part of a photocurable resin.



*Scheme 1.2.* Representation of selected types of 3D printing techniques.

While the first five techniques were not explored in this thesis, both material extrusion and vat photopolymerization will be discussed in depth below since were a central piece in the development of the studies collected in this document.

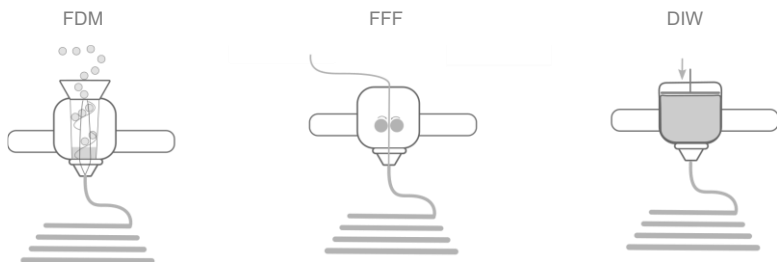
## 1.2.1. Material Extrusion

As previously said, material extrusion technologies rely on the ejection of material from a nozzle. It is mainly divided into two class, FDM in which the feedstock is heated to its melting temperature to enable the deposition and DIW, where a piston is used to extrude the material (Scheme 1.3). Generally, shear thinning resins are employed. When this kind of resin is forced through a nozzle it flows efficiently and, as soon as the shear force is stopped, turns back to its solid-like behaviour.<sup>10–13</sup> Generally, DIW has lower resolution when compared to FDM and it is mainly used in the biomedical field.<sup>14</sup>

The polymeric materials used in FMD (or fused filament fabrication, FFF, if a filament feedstock is employed) need certain parameters to enable their successful printing.<sup>15–18</sup> They require thermal transitions and viscoelastic properties that enable both the extrusion from the nozzle without clogging and the adhesion of layers between themselves by physical entanglement.<sup>19,20</sup> Hence, heating above  $T_g$  for amorphous materials and above  $T_m$  for semicrystalline polymers is necessary to have durable 3D-printed parts.<sup>21</sup> Temperature and deposition speed are essential to dampen the anisotropic properties given by the poor interfilamentous adhesion that arises from physical bonding.<sup>22–26</sup> Amorphous polymer will result in less shrinkage of the part after cooling since no crystallization occurs in the part.<sup>27,28</sup> The most popular thermoplastic filaments used in FDM are poly(lactic)acid (PLA), acrylonitrile butadiene styrene, Nylon, Polystyrene (PS), Polyethylene terephthalate, thermoplastic polyurethane, polypropylene and poly(ethyl ether ketone).<sup>28,29</sup> While most commercially available printers rely on a filament extruder, screw-based extruder also exists and can use pelletised feedstock with similar performances.<sup>30</sup> This cuts the cost of production of filament and has lower manufacturing constraints, at the expense of higher process complexity. Furthermore,



it enables the extrusion of high volumes of materials playing a key role in the AM of recycled materials.<sup>31–34</sup>



**Scheme 1.3.** Representation of FDM, FFF and DIW 3D printing techniques.

#### 1.2.1.1. Sustainability in FDM

FDM, with its thermoplastic feedstock already employs recyclable materials, however, most of them are either petro-derived or require polluting catalysts for their synthesis. Examples of alternative filaments that are biosourced and degradable exist, such as polyhydroxyalkanoates.<sup>35,36</sup> Filling is also another commonly used strategy for increasing the renewably sourced carbon in the final filament since fillers help with shape retention and often lead to increased mechanical properties. As an example, polycaprolactone could be filled up to 50% with waste coca shell powder without disrupting its printability, effectively making use of a waste stream and combining it with a biodegradable polymer.<sup>18</sup> Recycled plastics have also been employed for 3D printing with promising results and led to the commercialisation of this type of material.<sup>37</sup> CANs (*vide infra*) have also been used for FDM printing. In this case, the dynamic chemistry

requires a very quick exchange dynamic to avoid incurring in problems of melt fracturing. However, insertion of dynamic bonds returns isotropic parts, working towards breaking one of the major barriers to the adoption of the FDM technology.<sup>19,20,38–40</sup> Together with this, CANs, retain the inherent recyclability of the FDM feedstock, with a high potential for expanding its applicability to real-world scenarios.

## 1.2.2. Vat Photopolymerization

### 1.2.2.1. Photopolymerization

The foundation of VP is photopolymerization, in which light irradiation is used to promote the polymerisation of the monomers that compose the resin. Upon light irradiation, active species or initiators are generated, typically being free radicals. Reactions are typically carried out in bulk and at low temperatures, reducing the energy requirements and heightening the selectivity to carry out the reaction.<sup>41,42</sup> While less common, the use of photoacids and photobases was also successfully reported in the field of VP.<sup>43–46</sup>

### 1.2.2.2. Chain growth vs Step growth

Photopolymerization can be carried out by both chain growth and step growth mechanisms, however, chain growth mechanisms are the most commonly reported. The most established moieties employed for chain growth photopolymerization are (meth)acrylates, which, thanks to the stabilisation of the radical species, react quickly and efficiently.<sup>47,48</sup> Furthermore, (meth)acrylates are well established in the industry, hence a wide variety of structures are accessible. Chain-growth mechanisms, while preferred, generally lead to early gelation given the quick rise in molecular weight upon initiation. Although this

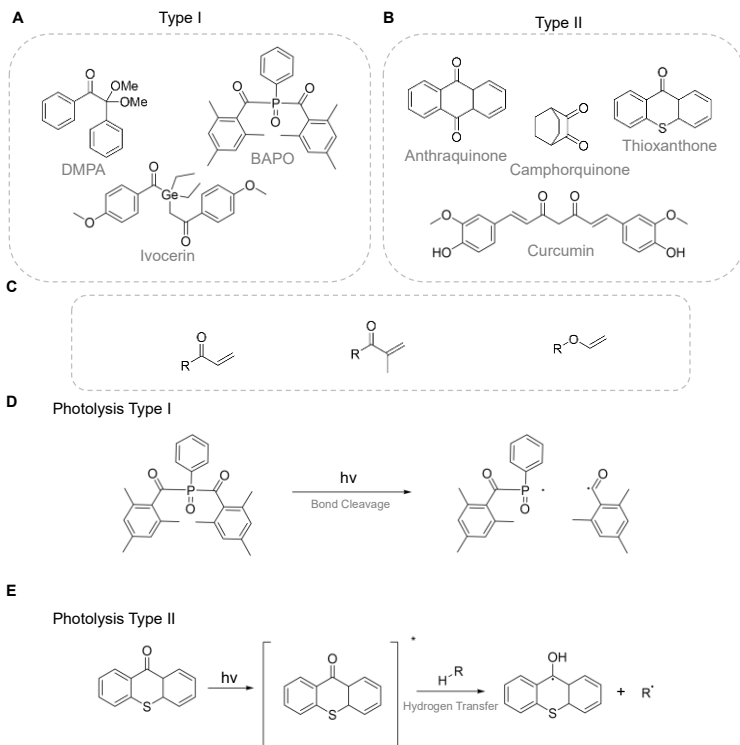
offers quick gel-points (in the order of seconds) it also yields non-uniform and often brittle materials.<sup>49</sup> In order to circumvent this limitation, step growth mechanisms are generally utilised.<sup>50</sup> The slower gel point times given by the subsequent addition of monomers towards the formation of dimers trimers and finally crosslinked polymers. This means that the gel point, at which the network is interconnected, is reached upon high conversions, hence a more uniform network result.<sup>51</sup> An intermix between the two mechanisms is also often employed, for example in the toughening of dental composites.<sup>52</sup> Furthermore, using step growth reaction enables the insertion of heteroatom-rich backbones, giving a handle for the control of the (bio)degradability of the materials.<sup>43</sup> By moving away from backbones entirely made of C-C bonds enables oneself to access recyclability through both chemical and mechanical means. See section 1.4.3 for more about sustainability in 3D printing.

### 1.2.2.3. Photoinitiators

Photopolymerization initiators come in a variety of structures. Their design aims to achieve dark stability (the active species are not liberated without irradiation) and high absorbance at the wavelength at which the photopolymerization is carried out. Furthermore, their solubility in the resin components is key to achieve homogenous reaction. Ideally, the absorbance profile and the wavelength of maximum activity should be superimposed, in order to have the highest activation.<sup>53</sup> Upon excitation by light a photocleavage or energy transfer, the photoinitiator liberates the active species. Depending on the type of active species liberated the mechanisms and structure vary greatly, hence below the three main groups of photoinitiators will be described more in depth.

#### 1.2.2.4. Radical Photoinitiators

Radical Photoinitiators liberate free radicals upon light exposure. Generally, two main classes are recognised, Type I photoinitiators in which the radical generation is given by the (homolytic) cleavage of a bond or type II in which an H-abstraction step generates the active species (Scheme 1.4-a,b,c,d,e). Type I photoinitiators employ germanium derivatives, benzyl ketals or phosphine oxide structures for the liberation of the radicals.<sup>27,54</sup> Phosphine oxide are generally preferred since are devoid of metal centres and they absorb blue light (>400 nm), hence enabling safer photopolymerizations that avoid the use of dangerous UV irradiation. Furthermore, they have desirability in most organic species. Type II photoinitiators are generally higher complexity systems, often involving two or three components, however, four component systems have also been reported.<sup>55-57</sup> In this, a chromophore in the form of benzophenone, anthraquinones, thioxanthenes or camphorquinone absorbs light to reach their excited state. An H-abstraction follows, typically from a tertiary amine or thiol-bearing molecule, leading to the generation of the initiating radical (Scheme 1.4-e).



**Scheme 1.4.** Representative structure of Type I (a) and Type II (b) photoinitiators. Monomers classically used for radical photopolymerisation (c). Mechanism of liberation of the radical species, type I (d) and Type II (e).

Radical processes generally convert double in shorter single bonds, this change at the molecular level is reflected in shrinkage at the macro scale, leading to internal stresses in the photopolymerised object.

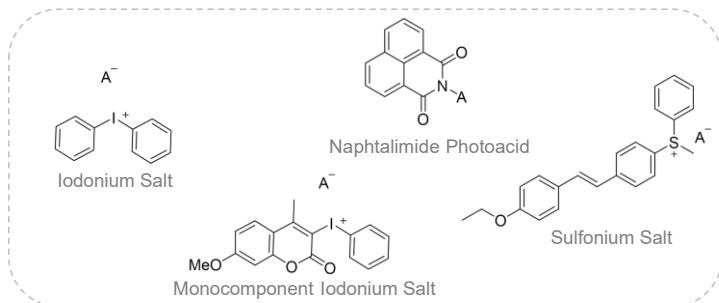
Hence, strategies for photopolymerization based on other types of reaction, such as addition or nucleophilic attacks, have been developed. To initiate these acids or bases are required, thus photoacids and photobases were developed. This expanded the possible ring opening polymerisation or step growth mechanisms portfolio accessible by photopolymerization.

#### 1.2.2.5. Photoacid Generators

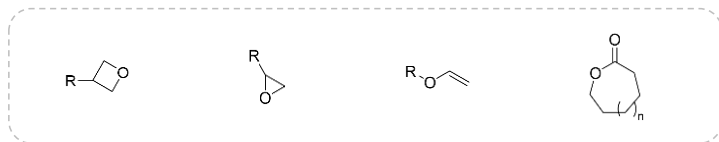
Photoacids were initially introduced as molecular tools for lithography. However, their potential for catalysing photoreactions was quickly realised. The first photoacids proposed, iodonium salts, were first developed in 1972.<sup>58</sup> This kind of species have very limited absorption spectra, often requiring UV light to liberate the acidic species (200-250 nm). Hence, they are often coupled with photosensitisers such as anthraquinones or thioxanthone derivatives.<sup>49,59-61</sup> More recent developments saw the substitution of the benzyl rings with chromophoric structures, such as coumarines (Scheme 1.5-a,c)).<sup>62-64</sup> This broadened the absorption spectra and removed the need for bimolecular systems.<sup>63-65</sup> The success of this strategy translated into the availability of photoacids that absorb at 405 nm as commercial systems. Iodonium salts are not the only photoacid structure reported, sulfoniums are also often used, however, their sensitisation is more challenging, reducing the possibility of tuning their activation.<sup>59</sup> Both Brønsted and Lewis acids can be liberated depending on the choice of anion. Covalent photoacids, based on the isomerisation of spiropyran moieties have also been introduced. These photoacids have the advantage of avoiding the formation of any radical species upon liberation of the active acid and are reversible, hence upon further light exposure they can reactivate, offering a finer control over the process.<sup>66</sup> Other non-ionic photoacids are arylsulfonates, imino and imidosulfonates, these species can irreversibly liberate mesyl- trifl- or

tosylates, giving access to a wide range of acidity of the liberated species.<sup>59,65</sup> Spatio-temporal control of the generation of acids opened up the possibility to polymerise epoxide, vinyl ethers, oxetanes and cyclic esters, enabling the synthesis of heteroatom-rich photopolymers (Scheme 1.5-b).<sup>67</sup> In fact, VP of epoxycyclohexane and divinyl ethers are well reported in the literature, although their lower curing efficiency often requires a further post-printing treatment to arrive at full conversion of the monomers.<sup>68–74</sup>

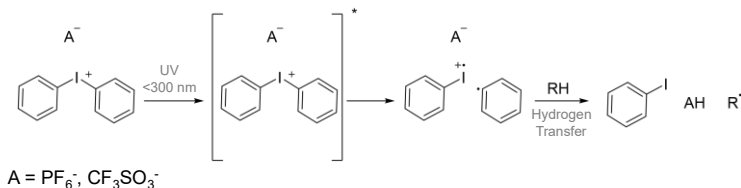
A



B



C



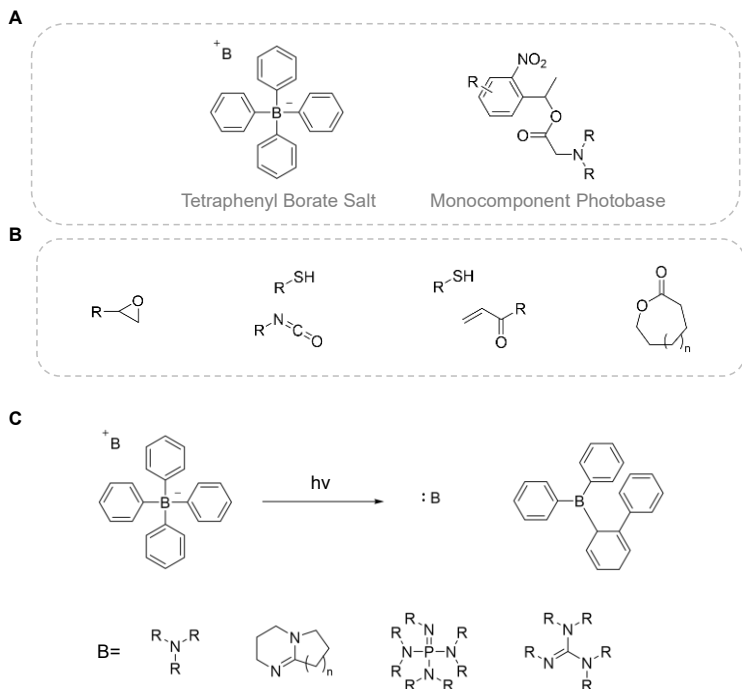
**Scheme 1.5.** Representative structure of photoacid generators (a) and monomers used in cationic photocuring (b) with respective mechanism of liberation of the acidic species (c).

#### 1.2.2.6. Photobase Generators

Photobase generators are less common in the 3D printing world. Photobases that can liberate both weak bases such as primary and



secondary amines and strong bases like amidines, phosphazenes, carbenes and guanidines have been reported.<sup>59,75–80</sup> While monocomponents system exist, they often incur in the liberation of CO<sub>2</sub> after activation (Scheme 1.6-a,b,c).<sup>81</sup> This often leads to defects in the printed parts. In order to overcome this issue for VP applications, a bimolecular system based on a type II photosensitiser (isopropyl thioxanthone) and a photobase (tetraphenylborate salts) were employed. Interestingly, thanks to the formation of dynamic thiourethane bonds from the base-catalysed isocyanate-thiol reaction, the authors could depolymerise the network and recover the resin, ultimately overcoming a major limitation of radical photopolymerization processes.<sup>43</sup> Thanks to the liberation of bases upon light irradiation the photopolymerization of epoxides, isocyanates and thiol-michael moiety was achieved.<sup>67,82</sup>



**Scheme 1.6.** Representative structure of photobase generators (a) with monomers used in anionic photocuring (b). Representative mechanism of liberation of the basic species (c).

#### 1.2.2.7. History and types of VP

Pioneered by Kodama in 1981 with his work developing stereolithography, vat photopolymerization relies on crosslinking a photopolymer in a layer-by-layer fashion. The crosslinking can be

carried out either by scanning a laser on the surface of the liquid resin (stereolithography, SLA) or by curing the entire layer using a projector (Digital Light Processing, DLP). In the years more refined techniques have been developed, naming two-photon lithography (TPL) and volumetric additive manufacturing (VAM).

In SLA the part is built using a scanning laser, hence the resolution and size of the part are heavily dependent on both the scanning speed and the laser shape. Depending on the orientation of the light, two different types of printers exist, top-down, in which the laser irradiates the resin from the top and the cured layers are then submerged in fresh resin, or bottom-up, in which the light source is placed below the resin. In this last case, the resin is stored in a vat with a transparent bottom and the resin is allowed to attach to the transparent window. When a new layer is formed the part is moved upwards, detaching it from the window. In order to ease separation and limit delamination issues, fluoropolymer-based (fluorinated ethylene propylene, FEP) or PDMS windows are generally used since they provide a flexible window with low adhesion to most polymers. Top-down models were first developed but nowadays bottom-up systems are preferred as they require less resin to fill the tank. Furthermore, the resin in a top-down system is continuously exposed to the air, incurring in issues of oxygen inhibition of the radical photocuring.<sup>83</sup>

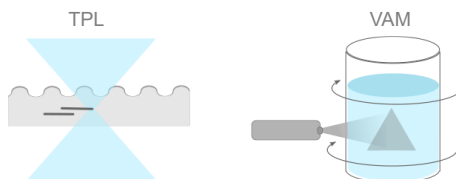
DLP printing achieves faster printing times as it does not rely on a scanning laser but can irradiate an entire 2D image thanks to a digital micromirror device (DMD) or a liquid crystal display (LCD).<sup>83–85</sup> Curing an entire layer simultaneously decouples part complexity and printing times, intensifying greatly the process. To further increase the throughput of this technology, DeSimone developed an oxygen-permeable membrane that inhibits the polymerisation on the bottom of the vat. Coined CLIP (continuous liquid interface production), allows the printer to forego entirely the step of detaching the layers from the

platform, greatly increasing printing speed (25 to 100 times) and reducing the risk of delamination.<sup>86,87</sup> Furthermore, since the platform moves upward continuously, defects originating from a layer-by-layer manufacturing method are minimised. Another limitation of DLP printing is the area of resin that can be cured at any moment. In fact, curing a large area of resin results in strong suction forces at the moment of detachment. In order to reduce this, high-area rapid printing (HARP) makes use of a liquid interface between the resin and the transparent window. The fluorinated oil does not mix with the resin, hence greatly reducing the interfacial adhesion as well as dissipating the heat generated by the exergonic photopolymerization, reducing the negative effects of scaling up DLP printing.<sup>88</sup>

*Two-photon lithography* (TPL) utilises the physical phenomena of two-photon absorption to better localise the energy shone on the sample, hence enabling the printing of  $\mu\text{m}$ -sized objects (Scheme 1.7).<sup>89,90</sup> In TPL, the absorption of two photons is rendered possible by using two different laser sources, and only where the two coincide enough energy is liberated to initiate photopolymerization. With this method, features below 100 nm can be printed. Generally, NIR lasers are used for this method, enabling the use of readily available VP inks. Furthermore, since the structures are created in the volume, no support structures are required.

*Volumetric additive manufacturing* (VAM) generates an entire object by irradiating 2D images in a photosensitive ink at different angles or using photoswitchable initiators.<sup>91-98</sup> The addition of the 2D images enables to precisely control the dose of light shone on each voxel (a volume pixel). Hence, only where the 2D images superimpose curing will occur (Scheme 1.7). While still in its infancy, VAM techniques, enable the production of bulk objects and do not suffer from the stringent viscosity requirements of other techniques. Furthermore, no support structures are needed as the objects are held in place by the surrounding resin.

However, the resin must be completely transparent to allow scanning of the entire volume, reducing the additives that can be added to VAM resins.



*Scheme 1.7.* Schematic of TPL and VAM 3D printing techniques.

#### 1.2.2.8. Sustainable Advances in DLP Printing

DLP printing is amenable to great impacts in tomorrow's circular economy. While its inherent ability to use fewer resources is an asset for the sustainability of VP, most often feedstocks for 3D printing applications are petrol-based and in most cases, unrecyclable.<sup>99</sup> Alternative strategies employ renewable resources as feedstock for the formulation of resins and filaments for AM applications. In the field of VP, double bond bearing feedstock such as terpenes<sup>100</sup> and vegetable oils have been used as resin by formulating them with thiol crosslinkers.<sup>101</sup> Other strategies rely on the derivatisation of hydroxyl-rich feedstock such as lignin<sup>102–104</sup> and carbohydrates<sup>105–107</sup> with (meth)acrylic groups in order to formulate resins with quick curing kinetics. This method was even applied to waste cooking oil, demonstrating the resilience of this chemistry towards impurities.<sup>108</sup> Another strategy to increase the renewable content in photoreins is to use biobased fillers, such as cellulose nanocrystals or lignin.<sup>109</sup> While making use of renewable resources, these strategies return crosslinked thermosets that cannot be easily recycled at the end of their life. The

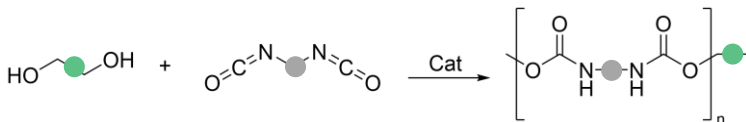
introduction of dynamic chemistries (*vide infra*) in the network enabled the realisation of recyclable thermosets.<sup>110,111</sup> Most strategies employ diacrylate monomers bearing the dynamic moiety in their structure as this gives reliable printability. However, the final product cannot be recycled back to resin and can be only reprocessed mechanically. In order to be able to recycle the object back to its monomers, chemistries that use dynamic bonds as crosslinking points are generally employed. Examples of these works include ester,<sup>112</sup> thiourethane<sup>43</sup> thiol-michael<sup>113</sup> or disulfide bonds.<sup>114</sup> These strategies generally employ non-radical processes for the photocuring of the resins.

The ability of 3D printing for reducing material usage together with the first studies on developing material amenable to circularity promises great impacts of these technologies in tomorrow's manufacturing environment.

### 1.3. Avoiding isocyanates, the rise of Non-isocyanate Polyurethanes

Polyurethanes (PU) are an important class of polymers in today's industry, accounting for around 8% of the total plastic demand.<sup>115</sup> This versatile family of polymers can be found in most application thank to their plethora of mechanical properties. The structural variability of both their two components, polyols and polyisocyanate precursors enable this class of polymer to be applied in coatings, resins, foams, elastomers and adhesives.<sup>115-119</sup> While pervasive in today's economy, their preparation is relying on recently REACH-restricted chemicals, isocyanates. These chemicals are highly reactive towards nucleophiles, both water and amines react with them rapidly and if liberated in the environment can cause long-lasting damage. One of the

worst accidents in chemical history, the Bhopal accident, originated from a leak of methyl-isocyanate and injured more than half a million people with repercussions resounding to this day after 40 years from its occurrence.



**Scheme 1.8.** Conventional synthesis of PU using a diisocyanate and a diol.

Hence, the classical step-growth polymerisation of polyol and polyisocyanates first discovered by Otto Bayer in 1937<sup>120</sup> (Scheme 1.8) is seeing increasing criticism in the scientific literature. At the same time, industries are actively researching possible alternative routes for producing this essential piece of today's economy. One of the emergent strategies to avoid the use of isocyanates for the production of PUs is the aminolysis of (five-membered) cyclic carbonates.<sup>117,119,121–128</sup> These precursors are not only isocyanate- and phosgene-free, rendering them inherently safer, but also are derived from CO<sub>2</sub> in a one-step cycloaddition with epoxides.<sup>129,130</sup> This makes use of CO<sub>2</sub> in an atom-economical way and offers the possibility of attaining the high structural variability of PU precursors since epoxides are an important part of today's economy and thus widely available. These (poly)cyclic carbonates have seen rising interest and are today commercially available at the kg scale. Their preparation involves a [3+2] cycloaddition that is frequently mediated by (organo)catalysts such as ammonium salts or more complex binary systems.<sup>120,131–143</sup> Their later aminolysis returns a hydroxy-urethane moiety.<sup>121,144,145</sup> (Scheme 1.9)

The nucleophilic attack can occur from both sides of the cyclic carbonate affording a majoritarian isomer containing a secondary alcohol and a minoritarian one bearing a primary alcohol. This type of reaction proceeds very slowly at room temperature (RT).<sup>146–149</sup> Hence most often the production of poly(hydroxy)urethane (PHU) is carried out at temperatures above 80 °C and in the presence of basic catalysts. Furthermore, the high density of hydroxyl groups in the polymer structure leads to limited diffusion in the reaction media owing to an increase in viscosity.<sup>117,150,151</sup> This greatly limits the molecular weights that can be attained through this strategy. Together with this, the tight H-bonding network reduces the ability of PHU to phase separate, a key aspect in the development of thermoplastic PU elastomers.<sup>152</sup> While hybrid strategies, such as copolymerisation, have been employed to overcome a limitation in PHU synthesis,<sup>151,153–156</sup> molecular design strategies have achieved an increased rate of polymerisation, allowing to attain the production of NIPUs at RT. Both increasing the ring size, substituting the cyclic carbonate and increasing the amine nucleophilicity have been explored to enhance the polymerisation kinetics.<sup>127,131,157</sup>



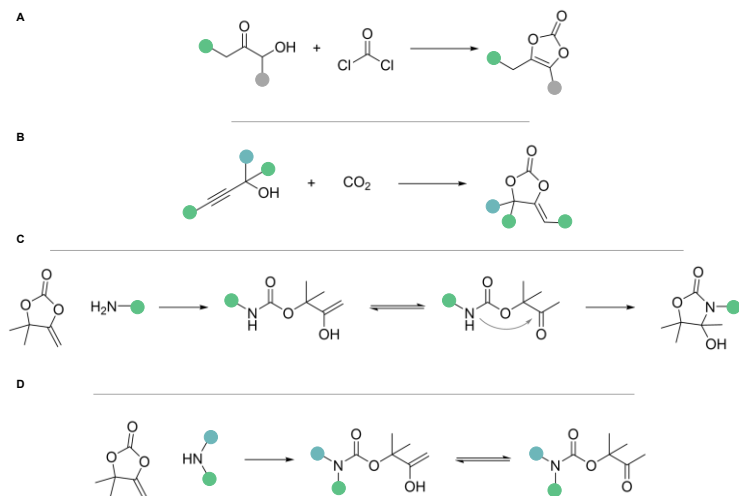
**Scheme 1.9.** [3+2] cycloaddition of CO<sub>2</sub> to epoxide for the synthesis of 5-membered cyclic carbonates and their subsequent aminolysis.



### 1.3.1. Polyoxazolidones, a less famous class of NIPUs

Between all strategies, the introduction of an exo- or endo vinylene group was shown to allow the aminolysis of cyclic carbonates in good to high yields at RT, often without a catalyst.<sup>131,137,158,159</sup> While the synthesis of endovinylene cyclic carbonates often employs phosgene or its derivatives (Scheme 1.10-a),<sup>160</sup> exovinylene cyclic carbonate can be synthesised in one step by coupling CO<sub>2</sub> to propargyl alcohols (Scheme 1.10-b).<sup>161-165</sup> The increased rate of aminolysis is attributed to the increased ring strain provided by the sp<sup>2</sup> carbon of the double bond. This, together with the tautomerisation of the enol resulting from the nucleophilic attack to the carbonyl function towards its ketone form, results in an oxo-carbamate derivative (Scheme 1.10-c).<sup>166</sup> The ketone can again be attacked by the -NH- of the carbamate, forming a five-membered cycle if a primary amine is employed. When a secondary amine is employed, the reaction will yield an oxo-urethane moiety instead (Scheme 1.10-d). Hence, by careful selection of amine Poly(hydroxy)oxazolidones (PHOxa) and poly(oxo)urethane (POU) can be prepared.<sup>166-168</sup> Both primary and secondary amines react quickly, the first one seeing a complete reaction in a matter of hours while the second often requires 24 h to have a complete reaction.<sup>137,166,168-170</sup> A limitation of the strategy is the low availability of diketone precursors for the production of difunctional exovinylene carbonate monomers. Two of the most commonly used are Hexane-2,5-dione and cyclohexanone dione. After reacting with Ethynylmagnesium bromide, the resulting propargyl alcohols can be efficiently transformed into difunctional monomers. However, these rigid structures often lead to insoluble polymers, limiting their applicability.<sup>171</sup> In order to prepare flexible polymers a multistep synthesis was developed. This strategy introduced longer alkyl chain spacers between ketone moieties.<sup>172</sup>

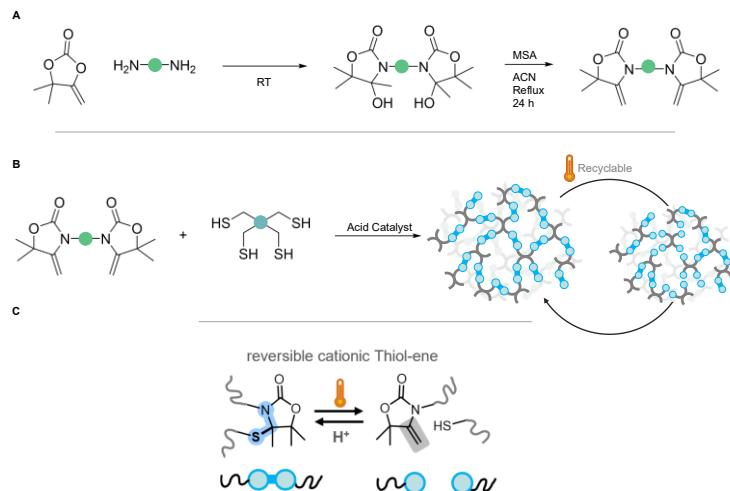
While safer, it still employed the volatile, carcinogenic and toxic methylvinyl ketone, limiting the scalability and safety of the process. It did, however, provide a powerful tool for the production of PHOxa that could be easily formulated in liquid formulations.<sup>173</sup> Before these strategies employing CO<sub>2</sub> addition, PHOxa were mainly synthesised by coupling isocyanates and epoxides, providing a safer route to this polymer class<sup>174</sup> renowned for its high thermal and chemical resistance.<sup>168,175</sup>



**Scheme 1.10.** a) Synthesis of endovinylenic cyclic carbonate by using phosgene b) Synthesis of exovinylenic cyclic carbonate by using CO<sub>2</sub> c) Reaction of an exovinylenic cyclic carbonates with a primary amine yielding a hydroxy-oxazolidone product d) Reaction of an exovinylenic cyclic carbonates with a secondary amine yielding an oxo-urethane moiety.

The pendant tertiary alcohol of PHOXa was exploited as a useful chemical handle. In fact, these polymers can undergo spontaneous dehydration at temperatures above 100 °C.<sup>166</sup> The dehydration can also be carried out at milder conditions by employing acidic catalysts or acetic acid as a solvent (Scheme 1.11-a).<sup>166</sup> This results in an electron-rich exovinylene double bond that can undergo the cationic thiol-ene reaction. This less-known thiol-ene coupling is a highly efficient reaction<sup>176</sup> that was employed by Habets *et al.* to produce thiol-crosslinked poly oxazolidones (POXa) (Scheme 1.11-b). In this case, the synthesis employed a monofunctional exovinylene cyclic carbonate and a difunctional amine linker. After nucleophilic attack and dehydration, difunctional exovinylene monomers could be prepared (Scheme 1.11-a). A variety of materials could be prepared, from elastomeric to rigid and brittle just by changing the diamine linker. Furthermore, the cationic thiol-ene adduct, the *N*, *S*-acetal bond, was found to be dynamic and could be used to depolymerise the network at high temperatures (Scheme 1.11-c). This enabled mechanical recycling by means of hot pressing, injection moulding and extrusion together with the ability to depolymerise the resin into its components, effectively recycling it chemically.<sup>177</sup> While this study revealed the potential for POXas as a versatile tool in material science, further works should concentrate on finding more sustainable monomer synthesis. In fact, the syntheses reported so far rely heavily on toxic chemicals and silica column/filtration purification, strongly affecting the scale-up potential of the monomers. Furthermore, finding ways to enhance the structural variability would further push POXa as a future-proof polymer class.<sup>175</sup>

# 1

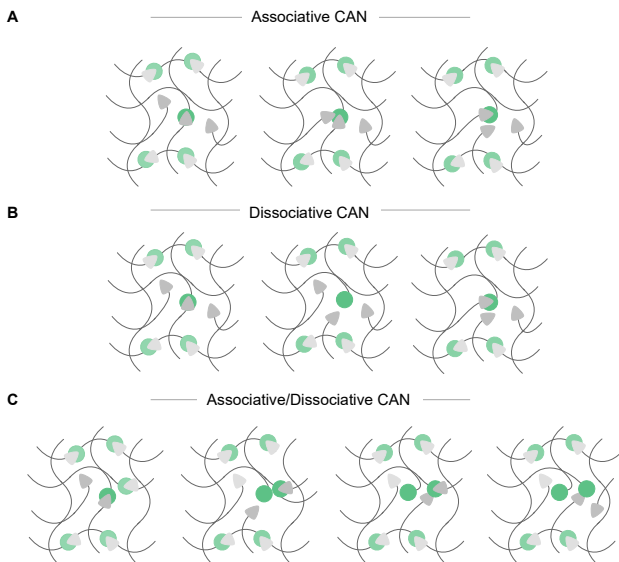


**Scheme 1.11.** a) Synthesis of Difunctional exovinylene oxazolidone monomers starting with a diamine precursor b) Preparation of crosslinked POXA networks by cationic thiol-ene c) Dynamic cationic thiol-ene reaction.

## 1.4. The role of Covalent Adaptable Networks in Today's Polymer Chemistry

Dynamic chemistry relies on the bond breaking and reforming towards the achievement of the thermodynamic equilibrium.<sup>178</sup> Two key parameters describe dynamic chemistries; reaction equilibrium and reaction rate. The first reflects the tendency of the bonds to exchange while the second describes the speed at which they do so. The introduction of dynamic chemistries in polymeric networks gave rise to

a new class of materials coined covalent adaptable networks (CAN).<sup>179–182</sup>



**Scheme 1.12.** Representation of mechanisms behind the dynamicity in associative CANs (a), dissociative CANs (b) and associative/dissociative CANs (c).

This enables CANs to exhibit flow behaviour in a manner akin to thermoplastics, however, the driving force for this phenomenon is the exchange at the molecular level, not the melting of the material. CANs have been proposed as a more sustainable alternative to retaining the thermoset's properties while achieving both mechanical and chemical recyclability. In order to do so, the dynamic reaction should reach equilibrium in relevant timeframes for the manufacturing process after

exposure to the stimulus (heat, light..) to display the dynamic features at the macroscopic level. CANs are generally divided into two classes, dissociative and associative, however, recent work highlights that associative/dissociative mechanisms exist.<sup>183</sup>

### 1.4.1. Associative CANs

Associative CANs see their crosslinking density unchanged while being able to flow thanks to their particular exchange mechanism (Scheme 1.12-a).<sup>184</sup> In this case the bond exchange happens concertedly, with a free moiety reacting onto a dynamic moiety integrated in the polymer backbone. This forms a new bond while liberating another free moiety than can continue the exchange. This type of materials has a similar viscosity profile to the one of glass over temperature increase; hence they were denominated vitrimers.<sup>185</sup> Common associative chemistries used in material science are; transesterification, transamidation, transcarbamoylation, transalkylation, disulfide and imines.<sup>184,186,187</sup>

### 1.4.2. Dissociative CANs

In contrast, dissociative networks rely on the breaking of bonds (Scheme 1.12-b), hence the crosslinking density decreases with the decreasing equilibrium constant of the dynamic reaction.<sup>183</sup> Often, heating this kind of material can lead to complete depolymerisation, enabling the processing of this kind of material with techniques that require low-viscosity liquids.<sup>39,40,188</sup> Dissociative CANs have been also proposed for their creep resistance, since at the working temperatures their crosslinking density is high, and low or no exchange is expected.<sup>183</sup> Common chemistries used to build dissociative CANs are Diels Alder, alkoxyamines, boronic esters disulfides, thioethers, hindered ureas, thiol-michael and acetals.<sup>150,189-200</sup>

Associative/Dissociative CANs undergo a mechanism that requires both dissociation of the dynamic bond and then the free moiety can exchange in an associative way (Scheme 1.12-d). They are less studied as the mechanism is of more difficult characterisation.<sup>183</sup>

### 1.4.3. Parameters for the design of CANs

A common parameter used to reflect the kinetics and mechanism of a given dynamic covalent chemistry is the activation energy  $E_{\text{flow}}$ .<sup>181,201,202</sup> This parameter is extracted from the stress relaxation dynamics of a material, generally measured by either rheology or dynamic mechanical analysis (DMA).<sup>203,204</sup> Sequential measurements at increasing temperatures reflect faster relaxation dynamics, the measurements are then fitted using a Maxwell model. The resulting values follow an Arrhenius dependence, from which the activation energy can be extracted. Often, higher-level Maxwell models are needed to account for multimodal relaxation. Furthermore, recently stretched exponential has been used to account for network inhomogeneities that would cascade into different relaxation modes.<sup>179</sup>

In order to lower the times necessary to display the dynamicity of the chemistry, catalysts are added with the effect of lowering the  $E_a$ . For example, the transesterification reaction can be accelerated to enable the processing of a crosslinked network by extrusion, after catalyst optimisation.<sup>205</sup> Together with catalyst choice, the exchange kinetics are greatly influenced by network parameters such as crosslinking density and rigidity. Crystallinity and phase separation can also influence the ability of bonds to exchange.<sup>206–208</sup> These three handles enable the creation of materials with specific properties tailored to the application. For example, localising the dynamic bonds in a phase-separated microstructure allows the preparation of high creep-resistance CANs while retaining their recyclability.<sup>206,209</sup>

#### 1.4.4. Applications

The introduction of dynamic bonds in polymer network not only endows them with the ability to be reprocessed, but it can open up the doors to multiple applications.

By exploiting the dynamicity of CANs, polymeric networks can be depolymerised to recover the initial materials, realising their chemical recycling. By adding a small molecule that would compete with the dynamic bonds, Wang *et al* showed that they could recover the fibre from an epoxy composite using ethylene glycol by leveraging the transesterification reaction. After evaporation of the ethylene glycol, they could recover a resin that was repolymerised to give a material with similar properties. Thiourethane, thioesters or imine were also demonstrated to be apt for chemical recycling in a similar manner.<sup>156,210</sup>

The presence of an active dynamic chemistry can also endow materials with the ability to self-heal upon stimulus. Both covalent and supramolecular bonds have been explored for this application. A variety of stimuli have been proposed, such as heat and light.

The introduction of dynamic chemistry can also allow the preparation of shape memory polymers together with three/four-dimensional morphing.<sup>210</sup>

As seen previously in **Section 1.2.1.1**, if the exchange is rapid it can open up CANs for use in manufacturing techniques such as additive manufacturing (AM) and injection moulding.<sup>177,211</sup>



## 1.5. References

1. Persson, L. *et al.* Outside the Safe Operating Space of the Planetary Boundary for Novel Entities. *Environ Sci Technol* **56**, 1510–1521 (2022).
2. Matlin, S. A., Mehta, G., Hopf, H. & Krief, A. One-world chemistry and systems thinking. *Nat Chem* **8**, 393–398 (2016).
3. Matlin, S. A., Cornell, S. E., Kümmerer, K., Mahaffy, P. G. & Mehta, G. Inventing a secure future: material stewardship as chemistry's mission for sustainability. *RSC Sustainability* **3**, 804–821 (2025).
4. Mutlu, H. & Barner, L. Getting the Terms Right: Green, Sustainable, or Circular Chemistry? *Macromol Chem Phys* **223**, (2022).
5. Su, A. & Al'Aref, S. J. *History of 3D Printing. 3D Printing Applications in Cardiovascular Medicine* (Elsevier Inc., 2018). doi:10.1016/B978-0-12-803917-5.00001-8.
6. Longhitano, G. A., Nunes, G. B., Candido, G. & da Silva, J. V. L. The role of 3D printing during COVID-19 pandemic: a review. *Progress in Additive Manufacturing* **6**, 19–37 (2021).
7. Mamica, L. Dematerialised and re-dematerialised economy – 3D printing as a key technological and environment-friendly innovation. *Economic and Environmental Studies* **18**, 265–291 (2018).
8. Paris, H., Mokhtarian, H., Coatanéa, E., Museau, M. & Ituarte, I. F. Comparative environmental impacts of additive and subtractive manufacturing technologies. *CIRP Ann Manuf Technol* **65**, 29–32 (2016).
9. Tofail, S. A. M. *et al.* Additive manufacturing: scientific and technological challenges, market uptake and opportunities. *Materials Today* **21**, 22–37 (2018).
10. Saadi, M. A. S. R. *et al.* Direct Ink Writing: A 3D Printing Technology for Diverse Materials. *Advanced Materials* **34**, 2108855 (2022).
11. Lügger, S. J. D., Verbroekken, R. M. C., Mulder, D. J. & Schenning, A. P. H. J. Direct Ink Writing of Recyclable Supramolecular Soft Actuators. *ACS Macro Lett* **11**, 935–940 (2022).
12. Dominguez-Alfaro, A. *et al.* 3D Printable Conducting and Biocompatible PEDOT-graft-PLA Copolymers by Direct Ink Writing. *Macromol Rapid Commun* **42**, 1–8 (2021).
13. Zhao, Y. *et al.* 3D printing of unsupported multi-scale and large-span ceramic via near-infrared assisted direct ink writing. *Nat Commun* **14**, 1–9 (2023).
14. Singh, S. & Ramakrishna, S. Biomedical applications of additive manufacturing: Present and future. *Curr Opin Biomed Eng* **2**, 105–115 (2017).
15. Ahn, S. H., Montero, M., Odell, D., Roundy, S. & Wright, P. K. Anisotropic material properties of fused deposition modeling ABS. *Rapid Prototyp J* **8**, 248–257 (2002).
16. Arif, M. F., Kumar, S., Varadarajan, K. M. & Cantwell, W. J. Performance of biocompatible PEEK processed by fused deposition additive manufacturing. *Mater Des* **146**, 249–259 (2018).

17. Arivazhagan, A., Saleem, A., Masood, S. H., Nikzad, M. & Jagadeesh, K. A. Study of Dynamic Mechanical Properties of Fused Deposition Modelling Processed Ultem Material. *American Journal of Engineering and Applied Sciences* **7**, 307–315 (2014).
18. Wasti, S. & Adhikari, S. Use of Biomaterials for 3D Printing by Fused Deposition Modeling Technique: A Review. *Front Chem* **8**, 532815 (2020).
19. Yang, K. et al. Diels–Alder Reversible Thermoset 3D Printing: Isotropic Thermoset Polymers via Fused Filament Fabrication. *Adv Funct Mater* **27**, 1700318 (2017).
20. Prasanna Kar, G., Lin, X. & Terentjev, E. M. Fused Filament Fabrication of a Dynamically Crosslinked Network Derived from Commodity Thermoplastics. *ACS Appl Polym Mater* **4**, 4364–4372 (2022).
21. Arrigo, R. & Frache, A. FDM Printability of PLA Based-Materials: The Key Role of the Rheological Behavior. *Polymers (Basel)* **14**, 1754 (2022).
22. Shaffer, S., Yang, K., Vargas, J., Di Prima, M. A. & Voit, W. On reducing anisotropy in 3D printed polymers via ionizing radiation. *Polymer (Guildf)* **55**, 5969–5979 (2014).
23. Afrose, M. F., Masood, S. H., Iovenitti, P., Nikzad, M. & Sbarski, I. Effects of part build orientations on fatigue behaviour of FDM-processed PLA material. *Progress in Additive Manufacturing* **1**, 21–28 (2016).
24. Solomon, I. J., Sevel, P. & Gunasekaran, J. A review on the various processing parameters in FDM. *Mater Today Proc* **37**, 509–514 (2020).
25. Samykano, M. et al. Mechanical property of FDM printed ABS: influence of printing parameters. *International Journal of Advanced Manufacturing Technology* **102**, 2779–2796 (2019).
26. Rodríguez-Panes, A., Claver, J. & Camacho, A. M. The influence of manufacturing parameters on the mechanical behaviour of PLA and ABS pieces manufactured by FDM: A comparative analysis. *Materials* **11**, (2018).
27. Ligon, S. C., Liska, R., Stampfl, J., Gurr, M. & Mülhaupt, R. Polymers for 3D Printing and Customized Additive Manufacturing. *Chem Rev* **117**, 10212–10290 (2017).
28. Guggenbiller, G. et al. 3D Printing of Green and Renewable Polymeric Materials: Toward Greener Additive Manufacturing. *ACS Appl Polym Mater* **5**, 3201–3229 (2023).
29. Patel, A. & Taufik, M. Extrusion-Based Technology in Additive Manufacturing: A Comprehensive Review. *Arabian Journal for Science and Engineering* **2022** 49:2 49, 1309–1342 (2022).
30. Liu, H. et al. Granule-based material extrusion is comparable to filament-based material extrusion in terms of mechanical performances of printed PLA parts: A comprehensive investigation. *Addit Manuf* **75**, 103744 (2023).
31. Duty, C. E. et al. Structure and mechanical behavior of Big Area Additive Manufacturing (BAAM) materials. *Rapid Prototyp J* **23**, 181–189 (2017).
32. Cruz Sanchez, F. A., Boudaoud, H., Camargo, M. & Pearce, J. M. Plastic recycling in additive manufacturing: A systematic literature review and opportunities for the circular economy. *J Clean Prod* **264**, 121602 (2020).

33. Additive manufacturing of heat sensitive polymer melt using a pellet-fed material extrusion.
34. Whyman, S. M. Design and development of a small-scale pellet extrusion system for 3D printing biopolymer materials and composites : submitted to the School of Engineering and Advanced Technology in partial fulfillment of the requirements for the degree of Master of Eng. **96**, 3417–3428 (2018).
35. Sardon, H., Long, T. & Le Ferrand, H. Sustainable Additive Manufacturing of Plastics. *ACS Sustain Chem Eng* **10**, 1983–1985 (2022).
36. Sanchez-Rexach, E., Johnston, T. G., Jehanno, C., Sardon, H. & Nelson, A. Sustainable Materials and Chemical Processes for Additive Manufacturing. *Chemistry of Materials* **32**, 7105–7119 (2020).
37. Schneevogt, H. *et al.* Sustainability in additive manufacturing: Exploring the mechanical potential of recycled PET filaments. <https://doi.org/10.1177/26349833211000063> **30**, 263498332110000 (2021).
38. Krishna Kumar, B. & Dickens, T. J. Dynamic bond exchangeable thermoset vitrimers in 3D-printing. *J Appl Polym Sci* **140**, 1–13 (2023).
39. Davidson, J. R., Appuhamillage, G. A., Thompson, C. M., Voit, W. & Smaldone, R. A. Design Paradigm Utilizing Reversible Diels-Alder Reactions to Enhance the Mechanical Properties of 3D Printed Materials. *ACS Appl Mater Interfaces* **8**, 16961–16966 (2016).
40. Appuhamillage, G. A. *et al.* 3D printed remendable polylactic acid blends with uniform mechanical strength enabled by a dynamic Diels-Alder reaction. *Polym Chem* **8**, 2087–2092 (2017).
41. Shao, J., Huang, Y. & Fan, Q. Visible light initiating systems for photopolymerization: Status, development and challenges. *Polym Chem* **5**, 4195–4210 (2014).
42. Lai, H., Peng, X., Li, L., Zhu, D. & Xiao, P. Novel monomers for photopolymer networks. *Prog Polym Sci* **128**, 101529 (2022).
43. Lopez de Pariza, X. *et al.* Recyclable photoresins for light-mediated additive manufacturing towards Loop 3D printing. *Nat Commun* **14**, (2023).
44. Invernizzi, M., Suriano, R., Muscatello, A., Turri, S. & Levi, M. Near-visible stereolithography of a low shrinkage cationic/free-radical photopolymer blend and its nanocomposite. *J Appl Polym Sci* **137**, 48333 (2020).
45. Zhao, B. *et al.* Fast Living 3D Printing via Free Radical Promoted Cationic RAFT Polymerization. *Small* **19**, (2023).
46. Zhao, B. *et al.* Photoinduced 3D Printing through a Combination of Cationic and Radical RAFT Polymerization. *Macromolecules* **55**, 7181–7192 (2022).
47. Schmidt, L. E., Leterrier, Y., Vesin, J. M., Wilhelm, M. & Månson, J. A. E. Photorheology of fast UV-curing multifunctional acrylates. *Macromol Mater Eng* **290**, 1115–1124 (2005).
48. Konuray, O., Fernández-Francos, X., Ramis, X. & Serra, À. State of the art in dual-curing acrylate systems. *Polymers (Basel)* **10**, 178 (2018).

49. Topa, M. & Ortyl, J. Moving towards a finer way of light-cured resin-based restorative dental materials: Recent advances in photoinitiating systems based on iodonium salts. *Materials* **13**, (2020).
50. Sycks, D. G., Wu, T., Park, H. S. & Gall, K. Tough, stable spiroacetal thiol-ene resin for 3D printing. *J Appl Polym Sci* **135**, 1–12 (2018).
51. Blasco, E., Wegener, M. & Barner-Kowollik, C. Photochemically Driven Polymeric Network Formation: Synthesis and Applications. *Advanced Materials* **29**, (2017).
52. Ligon-Auer, S. C., Schwentenwein, M., Gorsche, C., Stampfl, J. & Liska, R. Toughening of photo-curable polymer networks: a review. *Polym Chem* **7**, 257–286 (2015).
53. Irshadeen, I. M. *et al.* Action Plots in Action: In-Depth Insights into Photochemical Reactivity. *J Am Chem Soc* **143**, 21113–21126 (2021).
54. Yan, Y. *et al.* Photoinduced generation of ketyl radicals and application in C-C coupling without external photocatalyst. *Green Chemistry* **25**, 4129–4136 (2023).
55. Dietliker, K. *et al.* Advancements in photoinitiators-Opening up new applications for radiation curing. *Prog Org Coat* **58**, 146–157 (2007).
56. Yagci, Y., Jockusch, S. & Turro, N. J. Photoinitiated polymerization: Advances, challenges, and opportunities. *Macromolecules* **43**, 6245–6260 (2010).
57. Dietlin, C. *et al.* Photopolymerization upon LEDs: New photoinitiating systems and strategies. *Polym Chem* **6**, 3895–3912 (2015).
58. Crivello, J. V. The discovery and development of onium salt cationic photoinitiators. *J Polym Sci A Polym Chem* **37**, 4241–4254 (1999).
59. Zivic, N. *et al.* Recent Advances and Challenges in the Design of Organic Photoacid and Photobase Generators for Polymerizations. *Angewandte Chemie - International Edition* **58**, 10410–10422 (2019).
60. Devoe A N, R. J. *et al.* Transient intermediates in the photolysis of iodonium cations. <https://doi.org/10.1139/v87-391> **65**, 2342–2349 (2011).
61. Fouassier, J. P., Burr, D. & Crivello, J. V. Time-resolved laser spectroscopy of the sensitized photolysis of iodonium salts. *J Photochem Photobiol A Chem* **49**, 317–324 (1989).
62. Petko, F. *et al.* One-Component Stilbene-Based Iodonium Photoinitiators with Increased Photoacid Quantum Yield for Cationic Vat 3D Printing. (2024) doi:10.1021/acs.macromol.4c01692.
63. Topa, M. *et al.* One-component cationic photoinitiators based on coumarin scaffold iodonium salts as highly sensitive photoacid generators for 3D printing IPN photopolymers under visible LED sources. *Polym Chem* **11**, 5261–5278 (2020).
64. Zivic, N. *et al.* A novel naphthalimide scaffold based iodonium salt as a one-component photoacid/photoinitiator for cationic and radical polymerization under LED exposure. *Polym Chem* **7**, 5873–5879 (2016).
65. Lopez De Pariza, X. *et al.* Novel imino- And aryl-sulfonate based photoacid generators for the cationic ring-opening polymerization of  $\epsilon$ -caprolactone. *Polym Chem* **12**, 4035–4042 (2021).

66. Vozzolo, G. *et al.* Controlling associative transcarbamylation reactions by light in dynamic polyurethane networks using reversible spiropyran photoswitches. *Polymer (Guildf)* **302**, 127051 (2024).
67. Lai, H., Zhang, J., Xing, F. & Xiao, P. Recent advances in light-regulated non-radical polymerisations. *Chem Soc Rev* **49**, 1867–1886 (2020).
68. Dall'Argine, C. *et al.* Hot-Lithography SLA-3D Printing of Epoxy Resin. *Macromolecular Materials and Engineering* vol. 305 Preprint at <https://doi.org/10.1002/mame.202000325> (2020).
69. Shi, Q. *et al.* Recyclable 3D printing of vitrimer epoxy. *Mater Horiz* **4**, 598–607 (2017).
70. Choi, S. *et al.* Weldable and Reprocessable Shape Memory Epoxy Vitrimer Enabled by Controlled Formulation for Extrusion-Based 4D Printing Applications. *Adv Eng Mater* **24**, 1–10 (2022).
71. Appuhamillage, G. A. *et al.* 110th Anniversary: Vat Photopolymerization-Based Additive Manufacturing: Current Trends and Future Directions in Materials Design. *Ind Eng Chem Res* **58**, 15109–15118 (2019).
72. Enayati-gerdroodbar, A., Khayati, A. & Ahmadi, M. An Overview on Potential of Novel Photoinitiators for Vat Photopolymerization- Based 3D / 4D Printing Formulations. *Eur Polym J* 113552 (2024) doi:10.1016/j.eurpolymj.2024.113552.
73. Pierau, L. *et al.* Bio-sourced monomers and cationic photopolymerization–The green combination towards eco-friendly and non-toxic materials. *Prog Polym Sci* **127**, 101517 (2022).
74. Bagheri, A. & Jin, J. Photopolymerization in 3D Printing. *ACS Appl Polym Mater* **1**, 593–611 (2019).
75. Huang, Y., Li, L., Liu, X. & Li, Z. Photobase-catalysed anionic thiol-epoxy click photopolymerization under NIR irradiation: from deep curing to shape memory. *Polym Chem* **13**, 3048–3052 (2022).
76. Bouzrati-Zerelli, M. *et al.* Design of novel photobase generators upon violet LEDs and use in photopolymerization reactions. *Polymer (Guildf)* **124**, 151–156 (2017).
77. Zivic, N. *et al.* Thioxanthone-Based Photobase Generators for the Synthesis of Polyurethanes via the Photopolymerization of Polyols and Polyisocyanates. *Macromolecules* **53**, 2069–2076 (2020).
78. Zhang, X. *et al.* O-Nitrobenzyl-Based Photobase Generators: Efficient Photoinitiators for Visible-Light Induced Thiol-Michael Addition Photopolymerization. *ACS Macro Lett* **7**, 852–857 (2018).
79. Zhang, X., Xi, W., Wang, C., Podgórski, M. & Bowman, C. N. Visible-Light-Initiated Thiol-Michael Addition Polymerizations with Coumarin-Based Photobase Generators: Another Photoclick Reaction Strategy. *ACS Macro Lett* **5**, 229–233 (2016).
80. Sun, X., Gao, J. & Wang, Z. tetraphenylborate: A photobase generator and a photocatalyst for living anionic ring-opening polymerization and cross-linking of polymeric materials containing ester. *J. Am. Chem. Soc.* 1–11 (2008).
81. Vazquez, J. A. *et al.* Photobase-catalyzed thiol-ene click chemistry for light-based additive manufacturing. *Polym Chem* (2025) doi:10.1039/D4PY01120A.

82. Pei, H. W. *et al.* Photopolymerization activated by photobase generators and applications: from photolithography to high-quality photoresists. *Polym Chem* **15**, 248–268 (2024).
83. Pagac, M. *et al.* A Review of Vat Photopolymerization Technology : Materials. *Polymers (Basel)* **13**, 598 (2021).
84. Sampson, K. L. *et al.* Multimaterial Vat Polymerization Additive Manufacturing. *ACS Applied Polymer Materials* vol. 3 4304–4324 Preprint at <https://doi.org/10.1021/acsapm.1c00262> (2021).
85. Al Rashid, A., Ahmed, W., Khalid, M. Y. & Koç, M. Vat photopolymerization of polymers and polymer composites: Processes and applications. *Addit Manuf* **47**, 102279 (2021).
86. Lipkowitz, G. *et al.* Injection continuous liquid interface production of 3D objects. *Sci Adv* **8**, 3917 (2022).
87. Hsiao, K. *et al.* Single-digit-micrometer-resolution continuous liquid interface production. *Sci Adv* **8**, 2846 (2022).
88. Walker, D. A., Hedrick, J. L. & Mirkin, C. A. Rapid, large-volume, thermally controlled 3D printing using a mobile liquid interface. *Science* (1979) **366**, 360–364 (2019).
89. Steidl, L. *et al.* Non-ionic photo-acid generators for applications in two-photon lithography. *J Mater Chem* **19**, 505–513 (2009).
90. Harinarayana, V. & Shin, Y. C. Two-photon lithography for three-dimensional fabrication in micro/nanoscale regime: A comprehensive review. *Opt Laser Technol* **142**, 107180 (2021).
91. Regehly, M. *et al.* Xolography for linear volumetric 3D printing. *Nature* **588**, 620–624 (2020).
92. Kelly, B. E. *et al.* Volumetric additive manufacturing via tomographic reconstruction. *Science* (1979) **363**, 1075–1079 (2019).
93. Schwartz, J. J., Porcincula, D. H., Cook, C. C., Fong, E. J. & Shusteff, M. Volumetric additive manufacturing of shape memory polymers. *Polym Chem* **13**, 1813–1817 (2022).
94. Loterie, D., Delrot, P. & Moser, C. High-resolution tomographic volumetric additive manufacturing. *Nat Commun* **11**, 1–6 (2020).
95. Shusteff, M. *et al.* One-step volumetric additive manufacturing of complex polymer structures. *Sci Adv* **3**, (2017).
96. Cook, C. C. *et al.* Highly Tunable Thiol-Ene Photoresins for Volumetric Additive Manufacturing. *Advanced Materials* **32**, 1–6 (2020).
97. Thijssen, Q., Toombs, J., Li, C. C., Taylor, H. & Van Vlierberghe, S. From pixels to voxels: A mechanistic perspective on volumetric 3D-printing. *Prog Polym Sci* **147**, 101755 (2023).
98. Thijssen, Q. *et al.* Volumetric Printing of Thiol-Ene Photo-Cross-Linkable Poly( $\epsilon$ -caprolactone): A Tunable Material Platform Serving Biomedical Applications. *Advanced Materials* (2023) doi:10.1002/adma.202210136.
99. Gebler, M., Schoot Uiterkamp, A. J. M. & Visser, C. A global sustainability perspective on 3D printing technologies. *Energy Policy* **74**, 158–167 (2014).

100. Weems, A. C., Delle Chiaie, K. R., Worch, J. C., Stubbs, C. J. & Dove, A. P. Terpene- and terpenoid-based polymeric resins for stereolithography 3D printing. *Polym Chem* **10**, 5959–5966 (2019).
101. Grauzeliene, S., Valaityte, D., Motiekaityte, G. & Ostrauskaite, J. Bio-based crosslinked polymers synthesized from functionalized soybean oil and squalene by thiol-ene UV curing. *Materials* **14**, (2021).
102. Zhu, G. et al. High-performance 3D printing UV-curable resins derived from soybean oil and gallic acid. *Green Chemistry* **23**, 5911–5923 (2021).
103. Ebers, L. S. et al. 3D printing of lignin: Challenges, opportunities and roads onward. *Biopolymers* **112**, e23431 (2021).
104. Wan, Z., Zhang, H., Niu, M., Guo, Y. & Li, H. Recent advances in lignin-based 3D printing materials: A mini-review. *Int J Biol Macromol* **253**, 126660 (2023).
105. Kumari, S., Mondal, P. & Chatterjee, K. Digital light processing-based 3D bioprinting of  $\kappa$ -carrageenan hydrogels for engineering cell-loaded tissue scaffolds. *Carbohydr Polym* **290**, 119508 (2022).
106. Porwal, M. K., Hausladen, M. M., Ellison, C. J. & Reineke, T. M. Biobased and degradable thiol-ene networks from levoglucosan for sustainable 3D printing. *Green Chemistry* **25**, 1488–1502 (2023).
107. Flourat, A. L. et al. Levoglucosenone to 3D-printed green materials: synthesizing sustainable and tunable monomers for eco-friendly photo-curing. *Green Chemistry* **25**, 7571–7581 (2023).
108. Wu, B. et al. Direct Conversion of McDonald's Waste Cooking Oil into a Biodegradable High-Resolution 3D-Printing Resin. *ACS Sustain Chem Eng* **8**, 1171–1177 (2020).
109. Voet, V. S. D. et al. Sustainable Photopolymers in 3D Printing: A Review on Biobased, Biodegradable, and Recyclable Alternatives. *Macromol Rapid Commun* **42**, 2000475 (2021).
110. Durand-Silva, A. et al. Balancing Self-Healing and Shape Stability in Dynamic Covalent Photoresins for Stereolithography 3D Printing. *ACS Macro Lett* **10**, 486–491 (2021).
111. Cortés-Guzmán, K. P. et al. Recyclable, Biobased Photoresins for 3D Printing Through Dynamic Imine Exchange. *ACS Sustain Chem Eng* **10**, 13091–13099 (2022).
112. Nguyen, L. T. & Du Prez, F. E. Direct restoration of photocurable cross-linkers for repeated light-based 3D printing of covalent adaptable networks. *Mater Horiz* **11**, 6408–6415 (2024).
113. Stubbs, C. J., Khalfa, A. L., Chiaradia, V., Worch, J. C. & Dove, A. P. Intrinsically Recurable Photopolymers Containing Dynamic Thiol-Michael Bonds. *J Am Chem Soc* **144**, 11729–11735 (2022).
114. Machado, T. O. et al. A renewably sourced, circular photopolymer resin for additive manufacturing. *Nature* **2024** 629:8014 **629**, 1069–1074 (2024).
115. Engels, H. W. et al. Polyurethanes: Versatile materials and sustainable problem solvers for today's challenges. *Angewandte Chemie - International Edition* **52**, 9422–9441 (2013).

116. Hu, P., Kumar, A., Gharibi, R. & Agarwal, S. Tailor-made compostable polyurethanes. *Polym Chem* **13**, 622–630 (2022).
117. Nohra, B. et al. From petrochemical polyurethanes to biobased polyhydroxyurethanes. *Macromolecules* **46**, 3771–3792 (2013).
118. Sardon, H. et al. Synthesis of polyurethanes using organocatalysis: A perspective. *Macromolecules* **48**, 3153–3165 (2015).
119. Guillaume, S. M., Khalil, H. & Misra, M. Green and sustainable polyurethanes for advanced applications. *J Appl Polym Sci* **134**, (2017).
120. Grignard, B., Gennen, S., Jérôme, C., Kleij, A. W. & Detrembleur, C. Advances in the use of CO<sub>2</sub> as a renewable feedstock for the synthesis of polymers. *Chem Soc Rev* **48**, 4466–4514 (2019).
121. Rokicki, G., Parzuchowski, P. G. & Mazurek, M. Non-isocyanate polyurethanes: Synthesis, properties, and applications. *Polym Adv Technol* **26**, 707–761 (2015).
122. Kathalewar, M. S., Joshi, P. B., Sabnis, A. S. & Malshe, V. C. Non-isocyanate polyurethanes: From chemistry to applications. *RSC Adv* **3**, 4110–4129 (2013).
123. Khatoon, H., Iqbal, S., Irfan, M., Darda, A. & Rawat, N. K. A review on the production, properties and applications of non-isocyanate polyurethane: A greener perspective. *Progress in Organic Coatings* vol. 154 Preprint at <https://doi.org/10.1016/j.porgcoat.2020.106124> (2021).
124. Rayung, M., Ghani, N. A. & Hasanudin, N. A review on vegetable oil-based non isocyanate polyurethane: towards a greener and sustainable production route. *RSC Advances* vol. 14 9273–9299 Preprint at <https://doi.org/10.1039/d3ra08684d> (2024).
125. Maisonneuve, L., Lamarzelle, O., Rix, E., Grau, E. & Cramail, H. Isocyanate-Free Routes to Polyurethanes and Poly(hydroxy Urethane)s. *Chem Rev* **115**, 12407–12439 (2015).
126. Zhang, D. et al. Polymerization of Cyclic Carbamates: A Practical Route to Aliphatic Polyurethanes. *Macromolecules* **52**, 2719–2724 (2019).
127. Cornille, A., Auvergne, R., Figovsky, O., Boutevin, B. & Caillol, S. A perspective approach to sustainable routes for non-isocyanate polyurethanes. *Eur Polym J* **87**, 535–552 (2017).
128. Easley, A. D., Mangano, A. & Fors, B. P. Safer Polyurethane Foams with Cyclic Carbonates. *Angewandte Chemie - International Edition* **62**, (2023).
129. Vidal, F. et al. Designing a circular carbon and plastics economy for a sustainable future. *Nature* **626**, 45–57 (2024).
130. Mundo, F., Caillol, S., Ladmiral, V. & Meier, M. A. R. On Sustainability Aspects of the Synthesis of Five-Membered Cyclic Carbonates. *ACS Sustain Chem Eng* **12**, 6452–6466 (2024).
131. Ngassam Tounzoua, C., Grignard, B. & Detrembleur, C. Exovinylene Cyclic Carbonates: Multifaceted CO<sub>2</sub>-Based Building Blocks for Modern Chemistry and Polymer Science. *Angewandte Chemie - International Edition* vol. 61 Preprint at <https://doi.org/10.1002/anie.202116066> (2022).



132. Büttner, H., Longwitz, L., Steinbauer, J., Wulf, C. & Werner, T. Recent Developments in the Synthesis of Cyclic Carbonates from Epoxides and CO<sub>2</sub>. *Topics in Current Chemistry* **2017** *375*:3 **375**, 1–56 (2017).
133. Alves, M. *et al.* Organocatalyzed coupling of carbon dioxide with epoxides for the synthesis of cyclic carbonates: catalyst design and mechanistic studies. *Catal Sci Technol* **7**, 2651–2684 (2017).
134. Comerford, J. W., Ingram, I. D. V., North, M. & Wu, X. Sustainable metal-based catalysts for the synthesis of cyclic carbonates containing five-membered rings. *Green Chemistry* **17**, 1966–1987 (2015).
135. Martín, C., Fiorani, G. & Kleij, A. W. Recent advances in the catalytic preparation of cyclic organic carbonates. *ACS Catal* **5**, 1353–1370 (2015).
136. Song, B., Qin, A. & Tang, B. Z. Syntheses, properties, and applications of CO<sub>2</sub>-based functional polymers. *Cell Rep Phys Sci* **3**, 100719 (2022).
137. Siragusa, F. *et al.* Access to Biorenewable and CO<sub>2</sub>-Based Polycarbonates from Exovinylene Cyclic Carbonates. *ACS Sustain Chem Eng* **9**, 1714–1728 (2021).
138. Jeske, R. C. *et al.* Pre-Rate-Determining Selectivity in the Terpolymerization of Epoxides, Cyclic Anhydrides, and CO<sub>2</sub>: A One-Step Route to Diblock Copolymers. *Angewandte Chemie International Edition* **47**, 6041–6044 (2008).
139. Cao, H., Liu, S. & Wang, X. Environmentally benign metal catalyst for the ring-opening copolymerization of epoxide and CO<sub>2</sub>: state-of-the-art, opportunities, and challenges. *Green Chemical Engineering* **3**, 111–124 (2022).
140. Büttner, H., Longwitz, L., Steinbauer, J., Wulf, C. & Werner, T. Recent Developments in the Synthesis of Cyclic Carbonates from Epoxides and CO<sub>2</sub>. *Top Curr Chem* **375**, (2017).
141. Wang, Y. & Darensbourg, D. J. Carbon dioxide-based functional polycarbonates: Metal catalyzed copolymerization of CO<sub>2</sub> and epoxides. *Coord Chem Rev* **372**, 85–100 (2018).
142. Bhat, G. A. & Darensbourg, D. J. Progress in the catalytic reactions of CO<sub>2</sub> and epoxides to selectively provide cyclic or polymeric carbonates. *Green Chemistry* **24**, 5007–5034 (2022).
143. Song, Q. W. *et al.* Bifunctional silver(I) complex-catalyzed CO<sub>2</sub> conversion at ambient conditions: Synthesis of  $\alpha$ -methylene cyclic carbonates and derivatives. *ChemSusChem* **8**, 821–827 (2015).
144. Diakoumakos, C. D. & Kotzev, D. L. Non-isocyanate-based polyurethanes derived upon the reaction of amines with cyclocarbonate resins. *Macromol Symp* **216**, 37–46 (2004).
145. Gomez-Lopez, A., Elizalde, F., Calvo, I. & Sardon, H. Trends in non-isocyanate polyurethane (NIPU) development. *Chemical Communications* **57**, 12254–12265 (2021).
146. Monie, F. *et al.* The Multifaceted Role of Water as an Accelerator for the Preparation of Isocyanate-Free Polyurethane Thermosets. *Macromolecules* (2024) doi:10.1021/ACS.MACROMOL.4C01672.

147. Monie, F., Grignard, B. & Detrembleur, C. Divergent Aminolysis Approach for Constructing Recyclable Self-Blown Nonisocyanate Polyurethane Foams. *ACS Macro Lett* **11**, 236–242 (2022).
148. Monie, F., Vidil, T., Grignard, B., Cramail, H. & Detrembleur, C. Self-foaming polymers: Opportunities for the next generation of personal protective equipment. *Materials Science and Engineering R: Reports* **145**, 100628 (2021).
149. Monie, F. *et al.* Chemo- and Regioselective Additions of Nucleophiles to Cyclic Carbonates for the Preparation of Self-Blowing Non-Isocyanate Polyurethane Foams. *Angewandte Chemie - International Edition* **59**, 17033–17041 (2020).
150. Huang, Y.-W. & Torkelson, J. Catalyst-Free Polyhydroxyurethane Covalent Adaptable Network Exhibiting Full Cross-Link Density Recovery after Reprocessing: Facilitation by Synthesis with Sterically Hindered Secondary Amines. Preprint at <https://doi.org/10.26434/chemrxiv-2025-77gn3> (2025).
151. Ecochard, Y. & Caillol, S. Hybrid polyhydroxyurethanes: How to overcome limitations and reach cutting edge properties? *Eur Polym J* **137**, 109915 (2020).
152. Chen, X., Li, L., Wei, T. & Torkelson, J. M. Reprocessable Polymer Networks Designed with Hydroxyurethane Dynamic Cross-links: Effect of Backbone Structure on Network Morphology, Phase Segregation, and Property Recovery. *Macromol Chem Phys* **220**, 1–9 (2019).
153. Decostanzi, M., Bonneaud, C. & Caillol, S. From hydroxyurethane methacrylates to hybrid nonisocyanate polyurethanes. *J Polym Sci A Polym Chem* **57**, 1224–1232 (2019).
154. Bizet, B., Grau, E., Asua, J. M. & Cramail, H. Hybrid Nonisocyanate Polyurethanes (H-NIPUs): A Pathway towards a Broad Range of Novel Materials. *Macromolecular Chemistry and Physics* vol. 223 Preprint at <https://doi.org/10.1002/macp.202100437> (2022).
155. Zhang, T. *et al.* New kinds of lignin/non-isocyanate polyurethane hybrid polymers: Facile synthesis, smart properties and adhesive applications. *Ind Crops Prod* **199**, 116706 (2023).
156. Seychal, G. *et al.* Synergetic Hybridization Strategy to Enhance the Dynamicity of Poorly Dynamic CO<sub>2</sub>-derived Vitrimers achieved by a Simple Copolymerization Approach. *Adv Funct Mater* **35**, 2412268 (2025).
157. Quienne, B., Poli, R., Pinaud, J. & Caillol, S. Enhanced aminolysis of cyclic carbonates by  $\beta$ -hydroxylamines for the production of fully biobased polyhydroxyurethanes. *Green Chemistry* **23**, 1678–1690 (2021).
158. Ngassam Tounzoua, C. *et al.* A Catalytic Domino Approach toward Oxo-Alkyl Carbonates and Polycarbonates from CO<sub>2</sub>, Propargylic Alcohols, and (Mono- And Di-)Alcohols. *ACS Sustain Chem Eng* **8**, 9698–9710 (2020).
159. Li, X. *et al.* Cascade Transformation of Carbon Dioxide and Alkyne-1, n-diols into Densely Substituted Cyclic Carbonates. *ACS Catal* **12**, 2854–2860 (2022).
160. Qiao, C. *et al.* An Organocatalytic Route to endo-Vinylene Carbonates from Carbon Dioxide-Based exo-Vinylene Carbonates. *Adv Synth Catal* **366**, 291–298 (2024).

161. Xu, J. X., Zhao, J. W. & Jia, Z. Bin. Efficient catalyst-free chemical fixation of carbon dioxide into 2-oxazolidinones under supercritical condition. *Chinese Chemical Letters* **22**, 1063–1066 (2011).
162. Jiang, H., Zhao, J. & Wang, A. An efficient and eco-friendly process for the conversion of carbon dioxide into oxazolones and oxazolidinones under supercritical conditions. *Synthesis (Stuttg)* **5**, 763–769 (2008).
163. Song, Q. W. *et al.* Thermodynamically favorable synthesis of 2-oxazolidinones through silver-catalyzed reaction of propargylic alcohols, CO<sub>2</sub>, and 2-aminoethanols. *ChemSusChem* **9**, 2054–2058 (2016).
164. Du, M. *et al.* An efficient and recyclable AgNO<sub>3</sub>/ionic liquid system catalyzed atmospheric CO<sub>2</sub> utilization: Simultaneous synthesis of 2-oxazolidinones and  $\alpha$ -hydroxyl ketones. *J Catal* **393**, 70–82 (2021).
165. Li, X. D., Cao, Y., Ma, R. & He, L. N. Thermodynamically favorable protocol for the synthesis of 2-oxazolidinones via Cu(I)-catalyzed three-component reaction of propargylic alcohols, CO<sub>2</sub> and 2-aminoethanols. *Journal of CO<sub>2</sub> Utilization* **25**, 338–345 (2018).
166. Habets, T., Siragusa, F., Grignard, B. & Detrembleur, C. Advancing the synthesis of isocyanate-free poly(oxazolidones)s: Scope and limitations. *Macromolecules* **53**, 6396–6408 (2020).
167. Siragusa, F. *et al.* Unifying Step-Growth Polymerization and On-Demand Cascade Ring-Closure Depolymerization via Polymer Skeletal Editing. *Macromolecules* **55**, 4637–4646 (2022).
168. Razavi-Esfali, M. *et al.* Design of functional isocyanate-free poly(oxazolidone)s under mild conditions. *Polym Chem* **15**, 1962–1974 (2024).
169. Habets, T. *et al.* Facile construction of functional poly(monothiocarbonate) copolymers under mild operating conditions. *Polym Chem* **13**, 3076–3090 (2022).
170. Siragusa, F. *et al.* Continuous Flow Synthesis of Functional Isocyanate-Free Poly(oxazolidone)s by Step-Growth Polymerization. *ACS Macro Lett* **13**, 644–650 (2024).
171. Wong, A. R., Barrera, M., Pal, A. & Lamb, J. R. Improved Characterization of Polyoxazolidinones by Incorporating Solubilizing Side Chains. *Macromolecules* **55**, 11006–11012 (2022).
172. Habets, T. *et al.* Facile Access to CO<sub>2</sub>-Sourced Polythiocarbonate Dynamic Networks And Their Potential As Solid-State Electrolytes For Lithium Metal Batteries. *ChemSusChem* **16**, 1–18 (2023).
173. Habets, T. U. de L.-Ul. > C. and E. S. from A. to M. (CESAM). Advancing the use of CO<sub>2</sub>-sourced activated cyclic carbonates for the synthesis and recycling of heteroatom-rich polymers. (2024).
174. Francis, T. & Thorne, M. P. Carbamates and 2-oxazolidinones from tertiary alcohols and isocyanates. *Can J Chem* **54**, 24–30 (1976).
175. Bachmann, M., Marxen, A., Schomäcker, R. & Bardow, A. High performance, but low cost and environmental impact? Integrated techno-economic and life cycle

- assessment of polyoxazolidinone as a novel high-performance polymer. *Green Chemistry* **24**, 9143–9156 (2022).
176. Sutherland, B. P., Kabra, M. & Kloxin, C. J. Expanding the thiol-X toolbox: Photoinitiation and materials application of the acid-catalyzed thiol-ene (ACT) reaction. *Polym Chem* **12**, 1562–1570 (2021).
  177. Habets, T. *et al.* Covalent Adaptable Networks through Dynamic N,S-Acetal Chemistry: Toward Recyclable CO<sub>2</sub>-Based Thermosets. *J Am Chem Soc* **145**, 25450–25462 (2023).
  178. Yan, T., Balzer, A. H., Herbert, K. M., Epps, T. H. & Korley, L. S. T. J. Circularity in polymers: addressing performance and sustainability challenges using dynamic covalent chemistries. *Chem Sci* **14**, 5243–5265 (2023).
  179. Zhang, V., Kang, B., Accardo, J. V. & Kalow, J. A. Structure-Reactivity-Property Relationships in Covalent Adaptable Networks. *J Am Chem Soc* **144**, 22358–22377 (2022).
  180. Zhao, X. L., Tian, P. X., Li, Y. D. & Zeng, J. B. Biobased covalent adaptable networks: towards better sustainability of thermosets. *Green Chemistry* **24**, 4363–4387 (2022).
  181. Hafner, B. R., Pal, S., Lewis, B., Keten, S. & Shull, K. R. Network Topology and Percolation in Model Covalent Adaptable Networks. (2024) doi:10.1021/acsmacrolett.4c00523.
  182. Bowman, C. N. & Kloxin, C. J. Covalent adaptable networks: Reversible bond structures incorporated in polymer networks. *Angewandte Chemie - International Edition* **51**, 4272–4274 (2012).
  183. Jourdain, A. *et al.* Rheological Properties of Covalent Adaptable Networks with 1,2,3-Triazolium Cross-Links: The Missing Link between Vitrimers and Dissociative Networks. *Macromolecules* **53**, 1884–1900 (2020).
  184. Cheng, L., Zhao, X., Zhao, J., Liu, S. & Yu, W. Structure and Dynamics of Associative Exchange Dynamic Polymer Networks. *Macromolecules* **55**, 6598–6608 (2022).
  185. Montarnal, D., Capelot, M., Tournilhac, F. & Leibler, L. Silica-like malleable materials from permanent organic networks. *Science (1979)* **334**, 965–968 (2011).
  186. Krishnakumar, B. *et al.* Vitrimers: Associative dynamic covalent adaptive networks in thermoset polymers. *Chemical Engineering Journal* **385**, 123820 (2020).
  187. Porath, L., Soman, B., Jing, B. B. & Evans, C. M. Vitrimers: Using Dynamic Associative Bonds to Control Viscoelasticity, Assembly, and Functionality in Polymer Networks. *ACS Macro Lett* **11**, 475–483 (2022).
  188. Gandini, A. The furan/maleimide Diels-Alder reaction: A versatile click-unclick tool in macromolecular synthesis. *Prog Polym Sci* **38**, 1–29 (2013).
  189. Bin Rusayyis, M. A. & Torkelson, J. M. Reprocessable covalent adaptable networks with excellent elevated-temperature creep resistance: Facilitation by dynamic, dissociative bis(hindered amino) disulfide bonds. *Polym Chem* **12**, 2760–2771 (2021).

190. Orrillo, A. G. & Furlan, R. L. E. Sulfur in Dynamic Covalent Chemistry. *Angewandte Chemie - International Edition* **61**, (2022).
191. Chakma, P. & Konkolewicz, D. Dynamic Covalent Bonds in Polymeric Materials. *Angewandte Chemie* **131**, 9784–9797 (2019).
192. Urban, M. W. Dynamic materials: The chemistry of self-healing. *Nat Chem* **4**, 80–82 (2012).
193. Elizalde, F., Aguirresarobe, R. H., Gonzalez, A. & Sardon, H. Dynamic polyurethane thermosets: Tuning associative/dissociative behavior by catalyst selection. *Polym Chem* **11**, 5386–5396 (2020).
194. Boynton, N. R. *et al.* Accessing pluripotent materials through tempering of dynamic covalent polymer networks. *Science* (1979) **383**, 545–551 (2024).
195. Chen, J., Zhang, K., Zhang, K., Jiang, B. & Huang, Y. Facile preparation of reprocessable and degradable phenolic resin based on dynamic acetal motifs. *Polym Degrad Stab* **196**, 109818 (2022).
196. Shen, P., Pollard, B., Ueland, M., Lawes, D. & Connal, L. A. Rapid and Versatile Functionalization of Poly-Ethylene Imine via Dynamic Amino Formation. *Macromol Rapid Commun* 2400683 (2024) doi:10.1002/MARC.202400683.
197. Li, Q. *et al.* Facile catalyst-free synthesis, exchanging, and hydrolysis of an acetal motif for dynamic covalent networks. *J Mater Chem A Mater* **7**, 18039–18049 (2019).
198. Feng, H. *et al.* Facile synthesis of hemiacetal ester-based dynamic covalent polymer networks combining fast reprocessability and high performance. *Green Chemistry* **23**, 9061–9070 (2021).
199. Du, S. *et al.* Acetal-thiol Click-like Reaction: Facile and Efficient Synthesis of Dynamic Dithioacetals and Recyclable Polydithioacetals. *Angewandte Chemie International Edition* e202405653 (2024) doi:10.1002/ANIE.202405653.
200. Zhang, L. & You, Z. Dynamic Oxime-Urethane Bonds, a Versatile Unit of High Performance Self-healing Polymers for Diverse Applications. *Chinese Journal of Polymer Science (English Edition)* **39**, 1281–1291 (2021).
201. Van Zee, N. J. & Nicolaÿ, R. Vitrimers: Permanently crosslinked polymers with dynamic network topology. *Prog Polym Sci* **104**, 101233 (2020).
202. Isogai, T. & Hayashi, M. A simple design of a vitrimer network with various fractions of bond exchangeable units for revisiting the Arrhenius dependence of relaxation properties. *Polym Chem* **15**, 269–275 (2023).
203. Cho, J. *et al.* Stoichiometric effects on bulk stress relaxation to enhance reprocessability in covalent adaptable networks. *Polym Chem* (2025) doi:10.1039/d5py00013k.
204. Van Lijsebetten, F., De Bruycker, K., Van Ruymbeke, E., Winne, J. M. & Du Prez, F. E. Characterising different molecular landscapes in dynamic covalent networks. *Chem Sci* **32**, 12865–12875 (2022).
205. Taplan, C., Guerre, M., Winne, J. M. & Du Prez, F. E. Fast processing of highly crosslinked, low-viscosity vitrimers. *Mater Horiz* **7**, 104–110 (2020).

206. de Heer Kloots, M. H. P., Schoustra, S. K., Dijkman, J. A. & Smulders, M. M. J. Phase separation in supramolecular and covalent adaptable networks. *Soft Matter* **19**, 2857–2877 (2023).
207. Hayashi, M., Suzuki, M. & Kito, T. Understanding the Topology Freezing Temperature of Vitrimer-Like Materials through Complementary Structural and Rheological Analyses for Phase-Separated Network. *ACS Macro Lett* 182–187 (2025) doi:10.1021/acsmacrolett.4c00783.
208. Ge, S. *et al.* Unravelling the Mechanism of Viscoelasticity in Polymers with Phase-Separated Dynamic Bonds. *ACS Nano* **16**, 4746–4755 (2022).
209. Zhang, L., Chen, L. & Rowan, S. J. Trapping Dynamic Disulfide Bonds in the Hard Segments of Thermoplastic Polyurethane Elastomers. *Macromol Chem Phys* **218**, 1–10 (2017).
210. Zheng, N., Xu, Y., Zhao, Q. & Xie, T. Dynamic Covalent Polymer Networks: A Molecular Platform for Designing Functions beyond Chemical Recycling and Self-Healing. *Chem Rev* **121**, 1716–1745 (2021).
211. Montoya-Ospina, M. C., Zeng, J., Tan, X. & Osswald, T. A. Material Extrusion Additive Manufacturing with Polyethylene Vitrimers. *Polymers (Basel)* **15**, 1332 (2023).



## 1.6. Aim of this thesis

In the previous chapter, we highlighted both the research carried out in the NIPU field together with the advancements in dynamic networks and 3D printing. These three fields will be combined in this document with its main goal to **develop new chemistries based on exovinylene oxazolidones and their implementation for advanced manufacturing.**

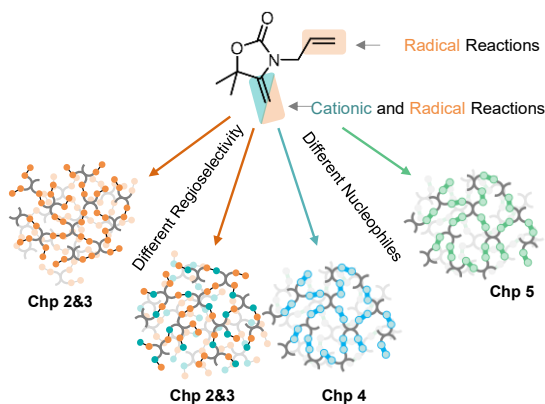


*Figure 1.1.* Representation of the palette of the materials developed in this thesis exploiting both regioselective processes and different nucleophiles.

In **Chapter 2**, we introduce a new, scalable synthesis of an oxazolidone-based monomer. This monomer will accompany the reader along the thesis, with the exploration of its chemistry in all the chapters (Figure 1.1). Its design had two moieties, one exovinylene and one allylic double bond. This offered a handle for controlling its regio- and photo-chemistry with a variety of reagents. Specifically in **Chapter 2**, we develop its photochemistry in



combination with thiols, developing a tandem photocuring procedure that enables the formation of both dynamic and non-dynamic bonds in the final network structure. We find these networks to be phase-separated and we exploit the dynamic behaviour of the material to tune its mechanical properties. We demonstrate its ability to be 3D printed by FDM to produce a simple clamp with spatially controlled mechanical properties.

We expand further on this concept in **Chapter 3**. Seeing the limited resolution of FDM, in this chapter we develop the photocuring procedure further to adapt it for DLP use. We start by optimising the photoinitiating system and develop a 2-step photocuring procedure that can produce pluripotent materials by photocuring in seconds. We explore a variety of reactive and non-reactive diluents to modulate the viscosity of the resin and find that they do not hinder the formation of a phase-separated morphology. We finish this chapter by 3D printing simple objects with good resolution, with promising developments in the field of pluripotent materials.

In **Chapter 4** we move away from thiol-based dynamic chemistry in order to attain degradability. We introduce *N,O*-acetals on oxazolidones and study their dynamicity and model their reaction pathway by density functional theory (DFT). We introduce them in materials and tune their degradability by copolymerisation. These materials photopolymerise in seconds, enabling their 3D printing by DLP.

We follow with **Chapter 5** where we again go back to monomer design and search for other nucleophiles that combine both high conversions and degradability of the bond. We find the perfect candidate in oximes. The reaction between exovinylene oxazolidones and oximes is studied, from monomer screening to its temperature dependence. We find an intermediate behaviour between *N,S*-acetals and *N,O*-acetals. We introduce this bond in both mechanically and chemically recyclable materials while maintaining their degradability, showcasing a case of monomer design towards circularity.

Aim of this thesis

As a last experimental chapter, **Chapter 6**, narrates the implementation of the dynamic *N,S*-acetal chemistry in industrially-relevant materials. We include this dynamic bond in slippery coating for application in the biomedical fields in a first proof-of-concept.

Follows **Chapter 7**, in which the main learnings from the previous chapters are recollected, and a summary of the future challenges is proposed.



# 2

Fully recyclable

Pluripotent Networks for 3D printing

Enabled by Dissociative Dynamic  
Bonds





## 2.1. Abstract

Additive manufacturing (AM) has risen in popularity due to its ability to produce complex shapes in a material-efficient way. However, to produce objects with advanced properties, complex multimaterial strategies are often employed. This one-polymer-one-property paradigm significantly slows down the application of AM, and in particular of fused deposition modelling (FDM), for manufacturing of functional objects. In this study we take advantage of pluripotency in materials, i.e. the ability to attain different properties from a single stock, to afford mechanically tuneable 3D printed dynamic thermosets (moduli from 2 MPa – 3 GPa, 1500x increase, Stress at break from 2 MPa to 70 MPa, 35x increase). To do so, we design FDM-compatible CO<sub>2</sub>-derived dissociative polymer networks that undergo a dynamic reaction-induced phase-separation (DRIPS). This strategy enables the control of the size of the rigid phase with a simple post-printing thermal treatment, cascading in spatially patterned mechanical properties. This study showcases new directions for the 3D printing communities, with deep implications in soft robotics and compliant mechanics.

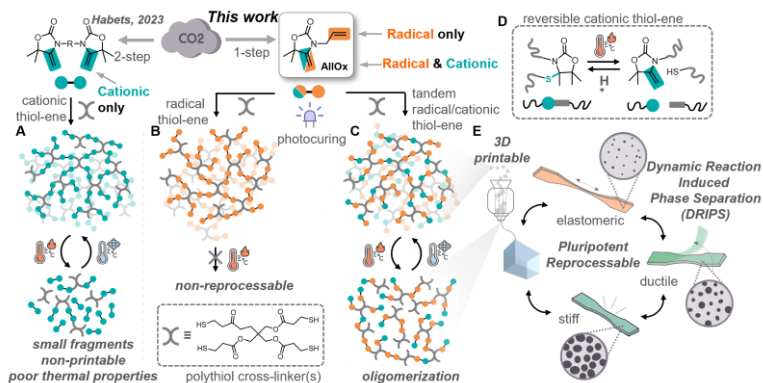


**Figure 2.1.** General strategy to attain pluripotent CO<sub>2</sub>-derived oxazolidone-based polymer networks exploiting permanent/reversible thiol-ene reactions with polythiol cross-linkers: bridged bis-oxazolidone monomers with two identical exo-vinylene groups as studied by Habets et al. (2023) formed fully depolymerizable networks via exclusive cationic thiol-ene reactions (a); a diolefinic oxazolidone monomer (AlIOx) photocured into two distinct polymer networks by choice of initiation: a photo-radical initiator created fully permanent and non-reprocessable networks (b), while a “tandem” combination of radical/cationic initiators generated a mix of permanent/dynamic bonds (c). Scheme of the reversible cationic thiol-ene (d). Thermally depolymerizable photocured resins via tandem thiol-ene displayed dynamic reaction-induced phase separation (DRIPS), which can be exploited to produce 3D printable and reprocessable materials with pluripotent characteristics, ranging from elastomeric, ductile, and stiff (e).



## 2.2. Introduction

Additive manufacturing (AM), commonly named 3D printing, has evolved from a small-size and rapid prototyping technique to a full-scale manufacturing tool widely applied in fields<sup>1,2</sup> ranging from automotive,<sup>3</sup> construction to biomedical.<sup>4,5</sup> Of all the 3D printing methods, fused deposition modelling (FDM) stands out for its simplicity, safety, and broad range of resulting materials properties.<sup>6,7</sup> In FDM, thermoplastic materials are melted through a heated nozzle and transformed into a 3D object by depositing the melted filament in a layer-by-layer fashion. However, the potential of FDM suffers from the anisotropic mechanical properties of the prints due to the poor interfilamentous adhesion as the different layers are bonded only by weak non-covalent forces.<sup>8,9</sup>

Among the different approaches to reducing the anisotropy while maintaining the sustainability of FDM, the introduction of dynamic crosslinks is one of the most promising strategies.<sup>10–13</sup> A judicious choice of the dynamic bond enabled the extrusion of networks based on the transesterification reaction,<sup>14–16</sup> disulfide metathesis,<sup>17</sup> imine exchange,<sup>18</sup> thiol anhydride exchange<sup>19</sup> and Diels alder reaction,<sup>20–22</sup> thus opening the doors to their use in FDM processes.<sup>7,8,21</sup> As an example, Smaldone and co-workers proposed a ground-up design of a dissociative network specifically designed for FDM showing isotropy up to 95% enabled by its high degree of crosslinking.<sup>20</sup> Despite the achievement of isotropic prints, these new materials needed long cooling times due to the slow recovery of crosslinks and were printed with a custom-built 3D printer. While the incorporation of these dynamic bonds does not impede their “drop-in” in current 3D printers, the introduction of a high density of crosslinks in long-chain polymers can dramatically change their processing parameters. This may result in thermal degradation side reactions and high viscosities that hinder printability.<sup>20</sup>

A recent progress in the field of dissociative networks, pluripotency, i.e. the ability to attain different properties from a single material, has been translated to the chemical space by Rowan and coworkers. In their work, they took advantage of the dynamic reaction-induced phase-separation (DRIPS) as an efficient strategy to tune the properties of polymeric materials.<sup>23–26</sup> We envision that combining adequate DRIPS morphologies, room-temperature exchange dynamics, thermal transitions ( $T_{\text{ambient}} < T_g < T_{\text{annealing}} < T_{\text{Upper Transition, } T_{\text{UT}}}$ ), and melt viscoelastic properties, would result in a powerful platform for the additive manufacturing of complex actuators with on-demand mechanical properties from a single material, a feat that is achieved in light-based 3D printing but not in FDM.<sup>27–29</sup> We decided to employ FDM printing as it is a more commonly available technique, requires little specialized equipment and would benefit majorly from the introduction of single material-multiple properties systems. To advance pluripotency into FDM, thus introducing spatially-resolved properties from a single material, three design criteria must be fulfilled: (i) appropriate melt viscosities at high temperatures; (ii) a wide “tempering” window, where the cross-linking density (i.e., the ratio at equilibrium of an open/close adduct) can be thermally modulated and topologically fixed once cooled at room temperature<sup>26</sup> and (iii) a covalent bond possessing fast reversibility at processing temperatures, which enables hot filament extrusion without incurring in melt-fracture, a common issue when working with CANs.<sup>17</sup> Applying this concept could be a further evolution in FDM 3D printing as the mechanical properties of the objects could evolve after printing by simple and localised annealing.<sup>26</sup> This could avoid other multi-material strategies for the production of complex, functional structures.<sup>7,30–32</sup>

In our search for a dynamic bond that could be amenable for pluripotency, we paid special attention to the dialkyl-substituted *N,S*-acetal group in cyclic oxazolidones. It was previously demonstrated that the reaction of terminal thiols with the exo-vinylene group ( $>\text{C}=\text{CH}_2$ ) of alkylidene oxazolidones has indeed a quick association-dissociation dynamics below 50 °C and low

activation barriers of exchange ( $\sim 16\text{--}19 \text{ kcal mol}^{-1}$ ) under catalytic amounts of methyl sulfonic acid (MSA).<sup>33,34</sup> Furthermore, this bond is sufficiently rigid ( $T_g > T_{\text{ambient}}$ ) and had previously provided materials with high transparency, no colouration or odor, a set of improved characteristics compared to other networks containing linear thioethers produced by radical thiol-ene or (anion-mediated) thia-Michael reactions.<sup>35–37</sup> However, networks comprising only reversible *N,S*-acetal bonds as crosslinking points undergo thermal depolymerization into monomeric fragments at low temperatures ( $< 100 \text{ }^\circ\text{C}$ ), resulting in rapid loss of mechanical performance and melt viscosities unfit for FDM (Figure 2.1-a,d). We hypothesized that balancing network integrity and dynamicity by combining permanent/dynamic crosslinks would enable the implementation of high-performance poly(oxazolidone)-type materials<sup>33,38–44</sup> into simultaneously pluripotent and 3D printable objects.

To achieve this, we designed a monomer structure that forms permanent *and* dynamic bonds through two concurrent reactions. We propose a bifunctional oxazolidone monomer, 3-allyl-5,5-dimethyl-4-methyleneoxazolidin-2-one (**ALIOx**, Figure 2.1), containing two C=C double bonds with divergent reactivities. The monomer is highly scalable and composed of 26 wt% of carbon dioxide ( $\text{CO}_2$ ), making use of this widely available C1 synthon.<sup>45–47</sup> In contrast, most polymer networks today that combine strong and weak bonds necessitate multiple tailored monomers or complex architectures. This strategy would greatly simplify this conundrum by enabling the introduction of dynamic and permanent bonds from a single source,<sup>48</sup> reminiscent of one-monomer two-polymer systems.<sup>49,50</sup> We further demonstrate how photoradical and photo-acid initiators are efficient UV photocuring agents to simultaneously, or in “tandem”, trigger both radical and cationic pathways of **ALIOx**, giving rise to both thermally labile and irreversible network nodes homogeneously distributed in the bulk material (Figure 2.1-b,c). More importantly, the “tandem” networks present a marked (sub) microphase-segregation via DRIPS mechanism, affording mechanically strong and tunable materials (from elastomeric to rigid and ductile to stiff and brittle,

Young's moduli ( $E_V$ ) = 2 MPa – 3 GPa, 1500x increase) that can be controlled by a thermal annealing process, with suitable viscoelastic profiles for FDM and mechanical reprocessability (Figure 2.1-e). We show that we can afford single-material 3D printed objects with spatially resolved mechanical properties and isotropy showcasing new possible directions for FDM 3D printing, with potential to actuate in soft-robotics and compliant mechanics.

## 2.3. Results and Discussion

### 2.3.1. Probing Thiol-Ene Reactions in a Difunctional Oxazolidone

The modular, highly scalable, and highly atom economical (AE=0.87) synthesis of functional oxazolidones enabled us to access the desired **AlIOx** monomer in >100-gram batches (78% yield) directly from CO<sub>2</sub>. Our adapted 1-step protocol reaction between a propargyl alcohol, allyl amine, and CO<sub>2</sub> employed readily available commercial starting materials and a cheap, heterogenous CuI catalyst (Figure 2.2-a).<sup>47</sup> The targeted transparent and liquid monomer could be easily dehydrated and purified in a distillation apparatus, overall providing a convenient preparation route for the broader applicability of **AlIOx** (see SI for experimental details, Figure S2.1-S2.2).

With the new allyl-alkylidenyl-oxazolidone monomer in hand, we set to probe the chemoselectivity of the radical vs cationic thiol-ene processes towards the two distinct C=C functional groups. Formation of the three possible S-C bonds (two thioether via radical pathways, Figure S2.3-a; one *N,S*-acetal via cationic pathways Figure S2.3-b)<sup>35</sup> was followed by sampling reactions in bulk using 3-methyl mercaptopropionate (3MP) as a model mono-functional aliphatic thiol (Figure 2.2, see SI for details). As expected, conversion data as measured by <sup>1</sup>H NMR analyses demonstrated that the chemoselectivity of the process strongly depended on the type of initiation. In the presence of isopropyl thioxanthone (ITX, 1 wt%) as an efficient type II photoinitiator (PI)

under UV irradiation (390 nm),<sup>51</sup> the reaction of the model thiol lacked complete chemoselectivity towards the allyl and exovinylene C=C double bonds over an extended period of time (Figure 2.2-b, S2.4, S2.9). In the NMR spectra, the formation of two thioether groups was evident by the disappearance of the resonances associated with the olefinic groups ( $\delta$  = 5.71, 5.18 ppm for allyl, 4.04 ppm for exo-vinylene) and the appearance of new  $-CH_2S-$  peaks ( $\delta$  = 3.55, 3.24, 2.9-2.7, and 1.88 ppm) (Figure 2.2-c, Figure S2.5). However, the reaction rates differed significantly at room temperature: within 2 minutes of UV irradiation, 86% of the allyl group had reacted while conversion of the exo-vinylene group had only reached 7% (Figure 2.2-b), suggesting that complementary reaction pathways could be possible at short reaction times. Using phenylbis(2,4,6-trimethylbenzoyl) phosphineoxide (BAPO, 1 wt%) as PI under equivalent conditions resulted in similar reactivity, albeit higher conversions of the exo-vinylene group were achieved at long reaction times (Figure 2.5, Figure S2.10-S2.11). The structure of the double thiol-ene radical adduct (**OX\_S1**) was supported by <sup>1</sup>H, <sup>13</sup>C NMR and high-resolution mass-spectrometry (HRMS) characterization of the isolated species (Figure S2.5).

Next, we investigated the cationic thiol-ene pathway between **ALLOx** and 3MP using methanesulfonic acid (MSA) as catalyst (Figure S2.3-b, mechanism). MSA was selected as was previously demonstrated to efficiently catalyze the cationic thiol/ene reaction.<sup>52</sup> As expected, we observed a high chemoselectivity towards the exovinylene moiety, leaving the allyl C=C unreacted after 40 min at room temperature (Figure 2.2-d, Figure S2.11).<sup>35</sup> Specifically, the <sup>1</sup>H NMR spectra displayed a rapid disappearance of the exovinylene peaks ( $\delta$  = 4.04 ppm) while the allyl peaks shifted to higher ppm ( $\delta$  = 5.71, 5.18 to 5.87, and 5.28-5.14 ppm) (Figure 2.2-e, Figure S2.7). Efficient formation of the *N,S*-acetal adduct (**OX\_S2**) which reached 72% conversion after just 1 min, could also be followed by new  $-Me$  resonances ( $\delta$  = 1.59, 1.40, 1.38 ppm).

Hence, to make use of the high selectivity towards distinct C=C at short periods of time, a fast “tandem” radical/cationic thiol-ene process –rather than a sequential one– needed to be devised. Inspired by previous acrylate-epoxy formulations for vat photopolymerization,<sup>53–55</sup> we investigated a combination of a photo-acid and a photoradical initiator to trigger both processes concomitantly with the switch ON of UV irradiation (~390 nm). The system consisted of ITX as photosensitizer, which served as an efficient initiator for radical thiol-ene reaction (*via* H-abstraction of the thiol)<sup>51</sup> as well as to sensitize iodonium salts-based photoacids (in this work, bis(4-methylphenyl) iodonium hexafluorophosphate (IOD)).<sup>56,57</sup> Indeed, employing 1 wt% of the photosensitizer-photoacid ITX/IOD system in a 1:1 weight ratio resulted in fast reaction kinetics and high conversions of both C=C double bonds in the same studied model reaction between **AlloX** and 3MP (Figure 2.2-f, Figure S2.13). Specifically, conversions of 99% and 85% according to the <sup>1</sup>H NMR spectra were attained for allyl and exo-vinylene groups, respectively, within 1 min at room temperature upon UV irradiation (390 nm). The simultaneous activation of both radical and cationic pathways was confirmed by the formation of the *N,S*-acetal and thioester adducts (**OX\_S3**), which presented a new –CH<sub>2</sub>S– peak ( $\delta$  = 3.50–3.26 and 1.90 ppm,) and a new –Me peak ( $\delta$  = 1.59, 1.43, 1.36 ppm), which could only form by the simultaneous radical and cationic pathways, respectively (Figure 2.2-g, Figure S2.9).

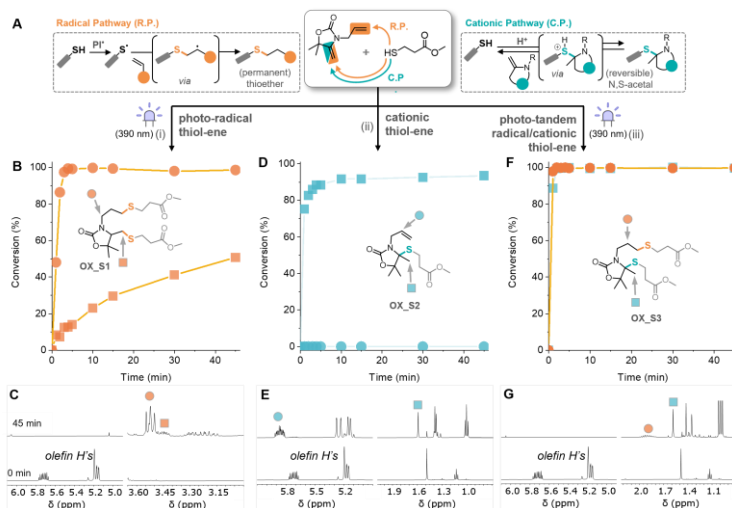


**Figure 2.2.** Model thiol-ene reaction studies and schematic representation of the radical and cationic pathways. Conversion data over time of the reaction between **ALLOx** monomer and mono-functional thiol methyl 3-mercaptopropionate in bulk with various initiators as determined by  $^1\text{H}$  NMR spectroscopy, following (b) photo-radical thiol-ene to form bis-thioether model **OX\_S1** and corresponding  $^1\text{H}$  NMR (c), (d) cationic thiol-ene to form *N,S*-acetal model **OX\_S2** with unreacted allyl group (e); and (f) photo-tandem radical/cationic thiol-ene to form thioether/*N,S*-acetal model **OX\_S3** (g). Reagents and conditions (see SI for details): (i) bulk, 1 mol% phenylbis(2,4,6-trimethylbenzoyl) phosphine oxide (BAPO), UV irradiation (390 nm), room temperature; (ii) bulk, 1 mol% methanesulfonic acid (MSA), room temperature; (iii) bulk isopropyl thioxanthone (ITX) and bis(4-methylphenyl) iodonium hexafluorophosphate (IOD) in 1:1 ratio 1 mol% UV irradiation (390 nm), room temperature. Corresponding  $^1\text{H}$  NMR spectra before and after 45 min of irradiation for radical (e), cationic (f) and tandem (g) kinetics.

### 2.3.2. Reversible Thiol-Ene Dynamics in Tandem Polymer Networks

Once the reactivity of the **AlLOx** monomer towards the radical and cationic thiol-ene pathways was established, the formation of polymer networks was investigated with equimolar amounts of tetrafunctional pentaerythritol tetrakis(3-mercaptopropionate) (**S4**). In such systems, we expected to control the extent of permanent thioether and reversible *N,S*-acetals linkages by the choice of initiator (radical vs tandem radical/cationic). In this way, we could probe the influence of cross-linking equilibrium thermodynamics (as reflected by DRIPS microstructures and the extent of dynamic bonds formed) in governing bulk materials properties. Thus, we used 1 wt% of the same photoradical (BAPO) or tandem photosensitizer-photoacid system (ITX/IOD in 1:1 weight ratio) under otherwise similar conditions (bulk, 365 nm, room temperature, 30 min) to yield solid polymer networks **R\_S4** and **T\_S4**, respectively (Figure 2.1, further details on the preparation in SI). In both cases, complete consumption of the C=C double bonds was confirmed by the disappearance of the Fourier-transform infrared (FT-IR) resonances at 1678 and 1640 cm<sup>-1</sup> corresponding to the stretching modes of the exo-vinylene and allyl groups, respectively (Figure S2.14). Due to the low dipole of the C-S bonds, the new thioether and *N,S*-thioacetal bonds provided weak, non-conclusive signals in the FT-IR spectra of the isolated network. However, both materials showed gel contents above 90% in THF, confirming their crosslinked nature (Table S1). The photocuring reaction kinetics were quick and efficient, reaching conversion of 80% with a 60 s irradiation (390 nm, 20 mW/cm<sup>2</sup>) and having a gel point of 225 s (Figure S2.15).

Despite the use of same monomeric building blocks, as well as seemingly identical C=C conversions (resulting in likely comparable network topologies), the distinct access to reversible cross-links between **R\_S4** (permanent) and **T\_S4** (dynamic) resulted in drastically different microstructures and thermal properties. First, a phase separated



— morphology was clearly present in analyses of tandem network **T\_S4**, as observed by transmission electron microscopy (TEM) (Figure 2.3-a) and optical microscopy (OM) (Figure S2.16). All these results indicated areas of higher electron density and refractive index, attributed to hard domains (~100 nm in size) in a continuous soft matrix conforming with a characteristic DRIPS microstructure. Although scanning near field optical microscopy (s-NOM) coupled with nano-FT-IR mapping and Confocal Raman Microscopy could not unambiguously distinguish chemical differences between the domain phases (Figure S2.17-18), tracing the peak intensities at  $977\text{ cm}^{-1}$  and  $1741\text{ cm}^{-1}$  revealed identical phase-separated structures as those observed by atomic force microscopy (AFM) (Figure S2.19). In stark contrast, radically crosslinked network **R\_S4** displayed no obvious features in neither TEM (Figure 2.3-b) nor OM or AFM (Figure S2.16, S2.20), suggesting a single polymer matrix with spatial homogeneity in its cross-linking density.

Secondly, modulated differential scanning calorimetry (mDSC) analysis of **T\_S4** showed two thermal transitions in the reversing heat flow curves ( $T_g = 39\text{ }^{\circ}\text{C}$ ,  $T_{UT} = 96\text{ }^{\circ}\text{C}$ , Figure 2.3-c); the broader  $T_{UT}$  (which presented an onset at  $69\text{ }^{\circ}\text{C}$ ) was accompanied by an endothermic peak in the non-reversing thermogram, a sign of the expected depolymerization reaction (*vide infra*). This temperature range provided ca.  $60\text{ }^{\circ}\text{C}$  tempering window for developing the material's mechanical properties (that is, the temperature range between  $T_g$  and  $T_{UT}$ ). In sharp contrast, **R\_S4** displayed only one glass transition at slightly lower temperatures ( $T_g = 20\text{ }^{\circ}\text{C}$ ) and no endothermic peak in the non-reversing heat flow curve, further confirming the permanent nature of the radically cross-linked network (Figure S2.21). The differences in thermal transitions observed by DSC were also paralleled in dynamic thermomechanical analyses (DMTA) of photocured rectangular strips (Figure 2.3-d). In one hand, alpha relaxations, assigned to the  $T_g$  of the materials, could be observed in both networks ( $T_a = 47\text{--}49\text{ }^{\circ}\text{C}$ ). Contrarily, **T\_S4** showed a 2-order of magnitude drop in the storage modulus ( $E'$ ) above  $100\text{ }^{\circ}\text{C}$ , while no changes in the plateau  $E'$  were observed in **R\_S4** above  $100\text{ }^{\circ}\text{C}$ .

Furthermore, **T\_S4** showed a high but accessible  $T_{\text{depolymerisation}}$  (155 °C, Figure S2.22) as determined by the final melt-flow of **T\_S4** in a temperature ramp in a shear rheology, a beneficial property that points towards its possible FDM printability.

Having observed different outcomes in the physical properties between the two modes of network photocuring, we sought to demonstrate the reversible thiol-ene bond in **T\_S4** as the acting mechanism. A combination of *ex-situ* and *in-situ* analyses by  $^1\text{H}$  NMR and FT-IR spectroscopy (Figure 2.3-e,h) provided convincing evidence of the cleavage of the thiol-ene adduct and formation of transient depolymerized structures, likely as a result of the residual protic species present upon photoacid activation. First, *ex-situ*  $^1\text{H}$  NMR spectroscopy experiments of isolated tandem model **OX\_S3** treated at various temperatures (15 min) to activate the reversible *N,S*-acetal bond and quenched with base, akin to a material annealing process, revealed a ca. 40% change in the dissociation of the *N,S*-acetal thiol-ene adduct between  $T_g$  and  $T_{UT}$  (Figure 2.3-e and 2.3-f, Figure S2.23), similar to other non-catalyzed thia-Michael networks.<sup>23,26</sup> Specifically, new resonances of the alkylidene C=C in the parent **AlLOx** ( $\delta$  = 4.19-4.13 ppm) steadily appeared with concomitant reduction of the -Me signal of the *N,S*-acetal group ( $\delta$  = 1.59, 1.43, 1.36 ppm) on raising the treatment temperature from 25 °C to 150 °C. The extent of dissociation was further supported by *in-situ* FT-IR spectroscopy at temperatures from 25 °C to 150 °C of model network **T\_S4**. As expected, the intensity of the exo-vinylene C=C double bond (1678  $\text{cm}^{-1}$ ) increased on heating, which also correlated to ca. 50% change in the dissociation of the *N,S*-acetal thiol-ene adduct (Figure 2.3-f, Figure 2.3-h). In contrast, radically photocured **R\_S4** displayed negligible increase in FT-IR resonances associated with the alkylidene C=C when the material was subjected to an identical thermal study, attesting for its non-dissociative behavior (Figure S2.24-a). Importantly, the extent of the dissociated *N,S*-acetal thiol-ene adduct was at least partially preserved upon cooling to room

temperature after the thermal treatment, as confirmed by FTIR spectroscopy (Figure S2.24-b).

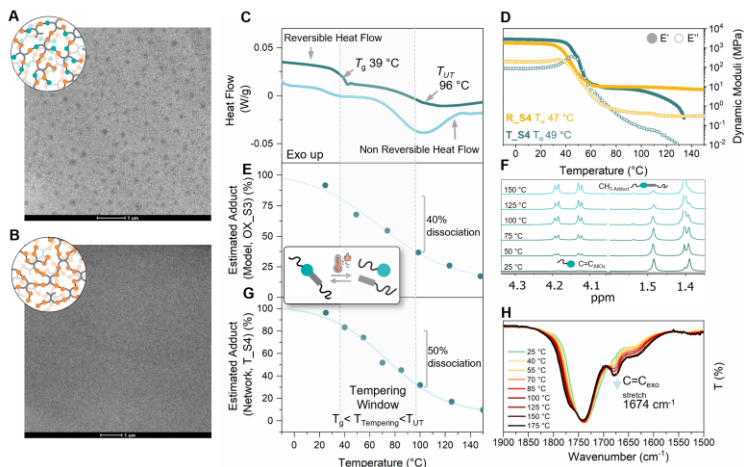


**Figure 2.3.** Transmission electron microscopy of dynamic “tandem” oxazolidone network, T<sub>S4</sub>, showing a DRIPS microstructure (a), and permanent radical oxazolidone network, R<sub>S4</sub>, without detectable features (b). (c) Reversing (teal) and non-reversing (cyan) mDSC thermograms of TS<sub>4</sub>. (d) Dynamic mechanical analyses (DMA) of T<sub>S4</sub> (teal) and R<sub>S4</sub> (yellow). Overlap of thiol-ene reaction dynamics with polymer thermal transitions: extend of adduct formation in a molecular model OX<sub>S3</sub> (e) as calculated from  $^1\text{H}$  NMR experiments of dissociated adducts by treatment at different temperatures (f); extend of adduct formation in bulk TS<sub>4</sub> polymer network (g) as determined from FT-IR experiments at 25  $^\circ\text{C}$  after thermal annealing at various temperatures. In-situ temperature-dependent FTIR spectra of tandem material at temperatures between 25 and 175  $^\circ\text{C}$  (h).

Finally, **T\_S4** was subjected to 150 °C for 10 min (>80% extent depolymerization), a point at which triethylamine was added to the resulting viscous liquid in order to quench the acid catalyst and thus, to avoid the back reaction (i.e. *N,S*-acetal formation) when cooling.<sup>33</sup> The partial solubility of this material in polar organic solvents allowed the spectroscopic and chromatographic characterization of the resulting oligomers. Specifically, <sup>1</sup>H and <sup>13</sup>C NMR analyses of the soluble fraction in DMSO-*d*<sub>6</sub> showed the presence of free exo-vinylene double bonds as indicated by the peaks at 4.22-4.16 ppm and 150 ppm in the <sup>1</sup>H and <sup>13</sup>C NMR spectra, respectively (Figure S2.25). Size exclusion chromatography (SEC) in tetrahydrofuran (THF) revealed oligomeric species with a number average molecular weight (*M<sub>n</sub>*) of 1900 g.mol<sup>-1</sup> and a dispersity (*Đ*) of 1.9 (Figure S2.26). The presence of thio-ether bond linkages ( $\delta$  = 3.63 ppm, CH) in the soluble fraction further confirmed at least partial step-growth polymerization via permanent radical thiol-ene, confirming that indeed both reactions occurred during tandem photocuring.

### 2.3.3. Attaining Pluripotent Behavior through Tempering

Having demonstrated the presence of DRIPS microstructures and the influence of temperature on the extent of thiol-ene adduct formation, we were intrigued by the effect of tempering on the observed phase separation and mechanical properties (Figure 2.4-a). Hence, dumbbell-shaped specimens (ASTM D638 TYPE V) were prepared by photocuring films of **T\_S4**, treatment for 24 h at five different temperatures (40, 60, 75, 90 and 110 °C), and finally cut to shape with a sample die. AFM studies confirmed the sea-island type morphology with quasi-spherical domains embedded in a continuous matrix previously observed with TEM, s-NOM, and OM (Figure 2.4-b, Table S2.2, Figures S2.14-S2.16, S2.17). Interestingly, samples tempered below the onset of *T<sub>UT</sub>* at 40 °C and 60 °C showcased a significant increase in domain size (84, 152, and 168 nm at 25 °C, 40 °C and 60 °C, respectively) and hard-phase area density (1.4%, 5.8%, and 25.6% at 25 °C,

40 °C and 60 °C). Tempering above 60 °C again decreased the size (118 and 100 nm, for 75 °C and 90 °C, respectively) and area coverage (16.4% and 12.1%, for 75 °C and 90 °C, respectively) of hard domains, likely as a result of the higher extent of network mobility and reduction in crosslinking density (Figure 2.3-c,e,g). Finally, tempering at temperatures above  $T_{UT}$  (110 °C) completely erased the phase-separated morphology, in line with the expected large extent depolymerization and immiscibility to miscibility change between the two phases above  $T_{UT}$  (Figure 2.5-b, Table S2.2).<sup>23</sup> Remarkably, these changes in phase separation size and density were also reversible: heat treatment at 60 °C for 24 h after phase erasing at 130 °C was capable of partially recovering the DRIPS microstructure (Figure S2.27), pointing towards a reprocessable materials with the recovery of initial morphology and mechanical properties (*vide infra*).

The effect of the thermal tempering and hard-phase volume coverage was immediately apparent in the mechanical properties of the resulting materials, enabling to target an impressive wide range of  $E$ , stresses at break ( $\sigma_b$ ), and elongations at break ( $\epsilon_b$ ) (Figure 2.4-c and Table S2.3). Initially, photocured materials stored at ambient temperature (below  $T_g$ , 1.4% hard area density) were rigid and ductile ( $E = 1.6$  GPa,  $\epsilon_b = 44$  %;  $\sigma_b = 21$  MPa;  $\epsilon_{yield} = 2.5$  %;  $\sigma_{yield} = 29$  MPa), while they became more brittle upon tempering below the onset of  $T_{UT}$  affording stiff materials ( $E$  increased by  $\times 1.1$  and  $\times 1.9$ ,  $\epsilon_b$  decreased by  $\times 0.09$  and  $\times 0.06$ , and  $\sigma_b$  increased by  $\times 2.1$  and  $\times 2.6$ , at 40 °C and 60 °C, respectively). Within this tempering window, the increased density of hard domains (5.8%, and 25.6%) restricted the mobility of the polymer network in a similar way as (nano) fillers can strengthen a matrix.<sup>58,59</sup> Mirroring the decrease of size and area coverage of hard domains above the onset of  $T_{UT}$  observed in the AFM, tempered materials at 75 °C and 90 °C were respectively softer ( $E = 1$  GPa,  $\epsilon_b = 12.5$  %;  $\sigma_b = 15.5$  MPa;  $\epsilon_{yield} = 3.3$  %;  $\sigma_{yield} = 24$  MPa) and elastomeric without a yield point ( $E = 11.7$  MPa,  $\epsilon_b = 88$  %;  $\sigma_b = 7.7$  MPa). Finally, when the material was treated at temperatures above  $T_{UT}$  (Figure 2.4-b) an even softer elastomeric material was obtained ( $E = 2$  MPa,

$\epsilon_b = 108\%$ ;  $\sigma_b = 2\text{ MPa}$ ), that displayed elastic recovery above 95% over 10 stretching cycles (Figure S2.28). This simple tempering procedure enabled us to reach properties from elastomeric to rigid plastics from a single pluripotent material in a wider range with respect to previous studies.<sup>26</sup>

Previously, locally graded mechanical properties were achieved with multimaterial design in FDM to achieve multi-performance objects.<sup>60</sup> Pluripotent materials have the potential to achieve the same feat but without the complexity of multimaterial printing.<sup>8,61</sup> To demonstrate this ability, we prepared a dogbone sample with a rigid side (60 °C, 24 h) and a softer side (110 °C, 4 h). When applying torque, only the soft side responded to the stimulus by cork-screw twisting (Figure 2.4-d). Upon release of the stress, the sample elastically returned to the initial state. A similarly treated specimen was subjected to a uniaxial tensile test. Digital image correlation was used to compute the global strain field and thus identify the difference in mechanical behaviour of the two regions (Figure 2.4-e). Upon a global strain of 4.0 %, the upper part deformation was 6.1 % while the lower rigid part was only deformed by 1.1 %. As expected, the deformation and final rupture were localized in the softer region, proving that locally controlled mechanical properties were achievable through spatially resolved annealing.

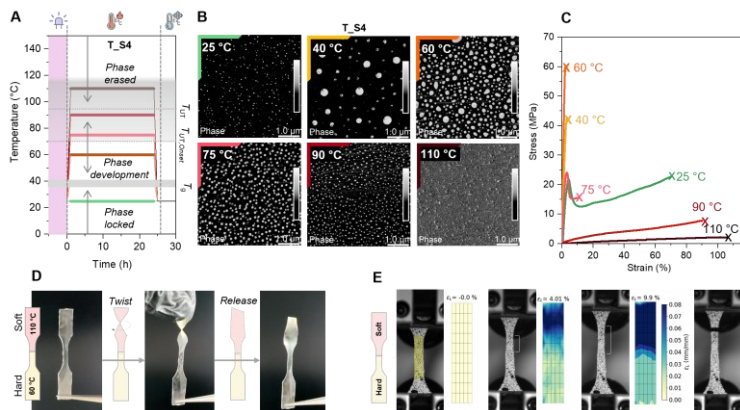


**Figure 2.4.** (a) Scheme of the applied thermal treatment to **T\_S4**: (1) UV-photocuring of the monomer resin (30 min), (2) annealing at various temperatures (25 °C (green), 40 °C (yellow), 60 °C (orange), or 110 °C (dark red) for 24 h), and (3) cooling to room temperature. (b) Atomic force microscopy (AFM) imaging of **T\_S4** after thermal annealing. (c) Representative uniaxial tensile testing data of **T\_S4** specimens (ASTM dogbone Type V) after different heat treatments (10 mm/min). (d) Demonstration of local annealing on a dogbone specimen by applying torque. (e) Application of a tensile stress to a locally annealed dogbone, displaying larger extensibility in the soft section and corresponding strain field

To further investigate the effect of cross-linking density on the mechanical properties of the materials, we extended the network synthesis to tri-functional (lower cross-linking density) and hexa-functional (higher cross-linking density) poly-thiols (Trimethylolpropane tris(3-mercaptopropionate)), S3, and dipentaerythritol hexakis(3-mercaptopropionate), S6). Using

equimolar amounts of **AlLOx** with **S3** or **S6**, both radical (**R\_S3** and **R\_S6**) and tandem (**T\_S3** and **T\_S6**) networks were photocured under identical conditions of photoinitiation as those employed with tetra-thiol **S4**. Supporting information includes a detailed explanation and thermomechanical and spectroscopic characterizations, which confirmed the consumption of all the C=C (allyl and alkylidene) groups upon irradiation (Figure S2.29). Similarly to **T\_S4**, DRIPS microstructures (a dual phase morphology with circular domains embedded in a continuous matrix as determined by AFM (Figure 2.5-a, Table S4), and two thermal transitions ( $T_g = 9\text{--}44\text{ }^\circ\text{C}$ ,  $T_{UT, \text{onset}} = 33\text{--}60\text{ }^\circ\text{C}$ ,  $T_{UT} = 80\text{--}118\text{ }^\circ\text{C}$ , for **T\_S3** and **T\_S6**, respectively; Figure S2.30) were present in both tandem materials. Again, the phase morphology was greatly dependent on the  $T_{\text{tempering}}$  and its relative position with respect to  $T_g$ ,  $T_{UT, \text{onset}}$ , and  $T_{UT}$  (Table S4). Hence, **T\_S3** displayed no detectable phase separation at ambient temperature, and only a sparse number of small spherical domains were observed (48 nm, 1.9 % of the area) after annealing at 60 °C. In contrast, **T\_S6** already showed a large number of quasi-spherical domains at ambient temperature (84 nm, 6% hard-phase area density), which greatly increased in size and area coverage upon heat treatment at 60 °C (600 nm, 15% hard-phase area density). Regardless of their  $T_{\text{tempering}}$ , **T\_S3** and **T\_S6** were found to be amorphous due to the lack of crystalline features observed in the X-Ray diffractograms (Figure S2.31). In contrast, radical networks (**R\_S3** and **R\_S6**) had no DRIPS microstructures, given the presence of a single thermal transition ( $T_g = -7^\circ\text{C}$  and  $41\text{ }^\circ\text{C}$  for **R\_S3** and **R\_S6**, respectively, Figure S2.32).

The network cross-linking density not only influenced the sub-micron morphology but as expected, gave stark differences in mechanical properties. As expected given its lower crosslinking density, **T\_S3** was softer when compared to **T\_S4** while **T\_S6** was more rigid owing to a higher network density. The effect of **T\_S3** and **T\_S6** tempering was demonstrated after annealing at three different temperatures (25, 60, 110 °C) (Figure S2.33); full mechanical characterization is presented in Table S3 (see SI). Taking all



tandem materials (**T\_S3**, **T\_S4**, **T\_S6**), the range of obtained properties expanded thanks to the combination of pluripotency and the tuning of the network density (Figure 2.5-b): 3-orders of magnitude in  $E$  (2 MPa to 3.3 GPa), 2-orders of magnitude in  $\varepsilon_b$  (2 % to 108 %), and 1-order of magnitude in  $\sigma$  (2 MPa to 70 GPa). In comparison, the range of tensile properties attained by the radical networks (**R\_S3**, **R\_S4**, **R\_S6**), which are not responsive to tempering, were substantially narrower (Table S3). The combined results from spectroscopic and mechanical analyses suggest that contrasting with previously studied thia-Michael networks, the mechanical properties of tandem oxazolidone-based crosslinked materials are governed by a combination of phase separation and crosslinking density (extent of adduct formation).<sup>26</sup>

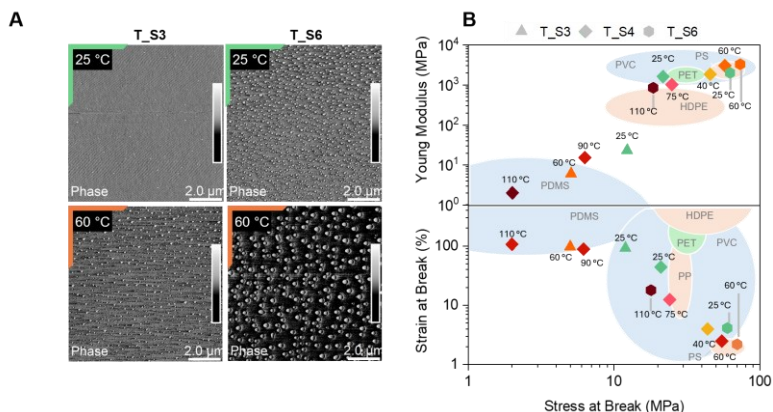


**Figure 2.5.** (a) Atomic force microscopy (AFM) imaging of **T\_S3** and **T\_S6** after thermal annealing at 25 °C (green) and 60 °C (orange) for 24 h. (b) Ashby plot of uniaxial tensile data for materials studied in this work.

While recycling has been proven for other homogenous, single-phase *N,S*-acetal-based materials based on their reversible thiol-ene reaction,<sup>33</sup> we wanted to understand the influence of the phase separation on polymer flow and potential reprocessability of the dynamic thermosets. To rationalize these effects, we first measured stress relaxation of **T\_S4** after treatment above  $T_{UT}$  (110 °C, 24 h, Figure S2.34-a), where phase separation was erased, and compared with a **T\_S4** sample with a fully developed dual phase morphology (60 °C, 24 h, Figure 2.6-a). Analyses on heating from 70 °C upwards in a timescale that would not interfere with the DRIPS microstructure, uncovered that, in fact, the flow activation energy ( $E_{flow}$ ) for both samples to be similar (74 kJ/mol, Figure 2.6-b, Figure S2.34-b), values within the range of previously reported cationic-mediated and anionic-mediated thio-ene and thio-Michael networks.<sup>26,33</sup> Importantly, while the  $E_{flow}$  did not vary between the two, we found a difference in the relaxation times (Table S5).

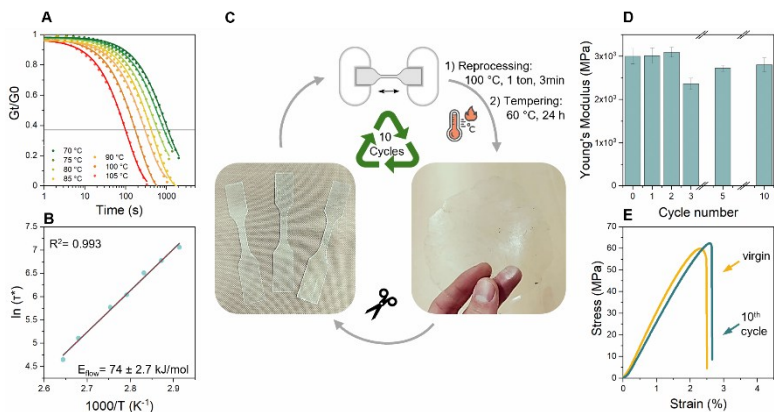


**Figure 2.6.** (a) Stress relaxation of the tandem material **T\_S4** with fully developed phase morphology (previously tempered at 60 °C, 24 h), lines are fitted first order Maxwellian. (b) Arrhenius plot of relaxation times vs

temperature for tempered tandem material **T\_S4**. (c) recycling process (d) Evolution of Young's Modulus over 10 recycling cycles. (e) Stress-Strain curves of virgin and recycled tandem material.

Indeed, the phase separated material displayed  $\times 1.3$ – $1.6$  slower relaxation times at the measured temperatures, a phenomenon previously reported for other phase separated systems.<sup>62</sup> This behavior can be explained on the basis of hard domains hindering bond exchange by trapping part of the dynamic linkages and/or acting as a physical barrier for exchange.<sup>63,64</sup>

We then studied the mechanical recyclability of the tandem materials by grinding a sample of photocured **T\_S4** and hot pressing for 3 min at 100 °C under 1 ton of pressure. Under these conditions, colourless, transparent, and homogeneous films were obtained (Figure 2.7-c). To re-introduce a developed DRIPS microstructure, the films were then subsequently treated at 60 °C for 24 h. After 10 recycling cycles, the mechanical properties remained practically unchanged with  $E$  remaining between 3.0–2.8 GPa (Figure 2.7-d,e). The material did not show any discolouration, and its IR spectrum and DSC trace were unchanged after 10 cycles (Figure S2.35-a,b), suggesting that the material did not degrade during reprocessing. This result is quite remarkable, as it implies that the cationic-mediated mechanism necessary for the reversible thiol-ene reaction remained functioning after many reprocessing cycles, suggesting no decomposition of any catalytic protic species.

#### 2.3.4. FDM of Pluripotent Materials towards Functional Builds

The melt-flow properties of depolymerized networks above  $T_{UT}$  ( $>100$  °C), which enabled the reprocessing of solid films, enticed the prospect of applying the tandem dynamic networks in filament-based additive manufacturing. For adequate printability, materials are required to display: (i) complex viscosities below  $10^3$  Pa·s at reasonable printing temperatures,

and (ii) significant shear thinning, since it allows exiting the nozzle easily and retaining the shape after deposition, resulting in high-definition and controlled flow.<sup>17,65</sup> Viscosity measurements by shear-rheology determined that **T\_S4** and **T\_S6** displayed shear thinning in all tested temperatures, ranging from 100–150 °C and 160–190 °C, respectively (Figure 2.7-a, and Figure S2.36, S2.37). Moreover, complex viscosities at high frequencies (at 100 Hz) were well within the printability region, revealing a desirable rheological behaviour for FDM.<sup>66</sup>

While pellet extrusion has some inherent challenges such as the need for a consistent material flow,<sup>67</sup> we selected this technology as it is closer to commercial models and has been regarded as a strong tool in the industrialization of FDM printing.<sup>68–71</sup> As a proof of concept, pieces of photocured **T\_S6** were extruded through a twin screw extruder at 165 °C into filaments of 2 mm in diameter, which were subsequently pelletized into fragments between 3-5 mm in size (Figure S2.38). A minor change in colouration from yellow to dark yellow was noted, possibly due to thermal degradation of the materials. The pellets were fed into a modified Ender 3 NEO printer fitted with a v4 universal pellet extruder and a 0.4 mm nozzle heated to 150 °C (Figure 2.7-b, Figure S2.39). Under these printing conditions (0.2 mm layer, 7.5 mm/s, 50% infill), a single-walled geometric vase structure, a complex spiral vase, and a pyramid were printed measuring several centimetres (Figure 2.7-c, top, Figure S2.40 for a zoomed version). The selected infill had reasonable resolution; small variations were observed in the Z-axis as a result of inconsistent flow due to the complex single-screw system that fed the nozzle.<sup>70</sup> Importantly, the printed objects displayed significant interlayer cohesion as shown in scanning electron microscopy (SEM) images (Figure 2.7-c, bottom), highlighting the bridging ability of **T\_S6** after deposition.

This observation prompted us to investigate the ability of printed tandem materials to produce isotropic prints. In traditional FDM, weak non-covalent forces between different layers result in poor interfilamentous adhesion and

significant anisotropic mechanical properties.<sup>8,9</sup> This has significantly limited the industry adoption of FDM to small-scale and bespoke prototyping tool. Addressing this challenge has been highlighted as a key advancement towards expanding 3D printing towards functional applications, in a market that is projected to grow to 1\$ trillion by 2030.<sup>21</sup> To demonstrate this, 2.5D rectangular structures of **T\_S4** were printed with a single-filament direction and subsequently rigidified at 60 °C for 24 h. Analyses by DMTA showed no significant difference in  $E'$  as measured in the 0° and 90° orientation with respect to the filaments highlighting its isotropic behaviour (Figure 2.5-d).<sup>17</sup>

As a final proof of the ability of thiol-ene based printed thermosets to display localized mechanical properties, a simple gripper was printed and locally heated to have a soft junction that connected two rigid arms (Figure 2.5-e). First, the object was tempered at 60 °C for 24 hours to completely rigidify it; then, the connecting bar was locally heated over a hot plate at 110 °C for 1 h to provide the elastic section. As a result of this treatment, the gripper was able to open and close effortlessly when actuated manually through the bending of the middle section and hold and lift a weight of 100 g with the tip of the rigid arms. The ability to have spatially-resolved mechanical properties has a high potential to impact the fields of compliant mechanics and soft robotics.<sup>72</sup>

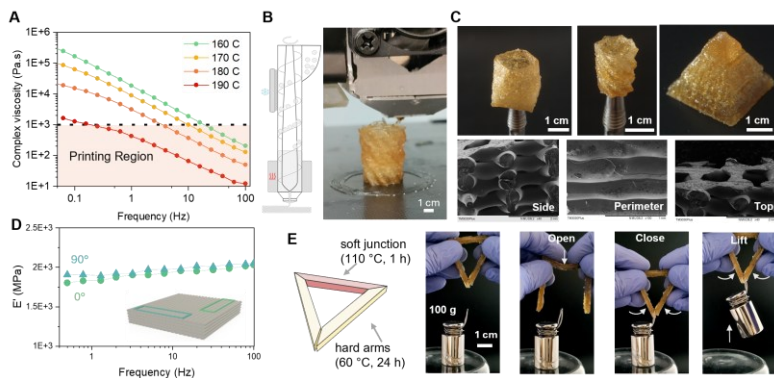


**Figure 2.7.** (a) Plot of complex viscosity vs frequencies of **T\_S6** at temperatures ranging from 160 to 190 °C obtained by melt shear rheology. (b) Diagram of the FDM printing head with pellet extrusion and photography of the printing process of **T\_S6**. (c) Top: photographs of 3D printed single-walled geometric vase (left), spiraling vase (center), and pyramid (right) with 50% infill. Bottom: scanning electron microscopy (SEM) images of cut sections of **T\_S6** printed object by extrusion FDM. (d) Frequency sweeps of 3D printed specimens (**T\_S4**) perpendicular and parallel to the bead orientation (e) Scheme of functional gripper with spatially resolved mechanical properties, and demonstration of a 3D-printed functional gripper that exploits areas of distinct rigidity to lift a weight (arrows show the direction and location of the applied forces).

## 2.4. Conclusions

We have presented a new strategy for the production of pluripotent materials that enables their introduction in the field of additive manufacturing. With this strategy we attain properties ranging from Young's Moduli of 2 MPa and elongation at break of 100% toward moduli of 3 GPa and stress at break of 55 MPa with a single resin. By exploiting two double bonds with different

reactivity, the monomer could form a mixture of dynamic *N,S*-acetals and non dynamic thioether moieties that cascaded towards desirable viscoelastic properties showing both shear thinning behavior and complex viscosity apt for FDM printing. Furthermore, they gave isotropic prints owing to the strong covalent bonding between filaments. Importantly, the materials presented a dynamic reaction-induced phase-separation (DRIPS) mechanism that could be exploited to tune the properties by simple thermal annealing in a fully reversible manner. As a proof of concept we created a functional gripper with spatially resolved mechanical properties by simple localized heating, presenting a new paradigm for achieving functionality in 3D printing. The efficient reprocessability of the *N,S*-acetal moiety was further demonstrated by mechanical recycling the material for 10 cycles, resulting in a minor reduction in mechanical properties. The wide window of mechanical properties reveals the potential of the concept of pluripotency for the production of next-gen 3D printing materials, with deep implication in compliant mechanics and soft robotics.

## 2.5. Materials And Methods

### 2.5.1. Materials

2-Methyl-3-butyn-2-ol (Sigma, 98%), Allylamine (Sigma, 98%), Copper Iodide (Sigma, 98%), Methyl 3-mercaptopropionate (Sigma, 98%, 3MP), Phenylbis(2,4,6-trimethylbenzoyl) phosphine oxide (BAPO, Ciba), Methanesulfonic acid (Sigma, >99%), Bis(4-methylphenyl)iodonium Hexafluorophosphate (IOD, Sigma, >99%, electronic grade), Isopropyl Thioxanthone (ITX, TCI, >98%), 1,3,5-trimethoxy benzene (Sigma) Trimethylolpropane tris(3-mercaptopropionate) (S3, Sigma, ≥95%), Pentaerythritol tetrakis(3-mercaptopropionate) (S4, Sigma, ≥95%), Dipentaerythritol Hexakis(3-mercaptopropionate) (S6, TCI, >93%), Triflic Acid (Sigma, >99%) and Sulfuric Acid (Sigma, >95%), Triethylamine (Sigma, 99.5%) were used without further purification.

### 2.5.2. Synthesis of Compounds

#### 2.5.2.1. Synthesis of **AlloX**

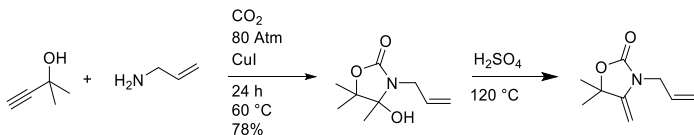


**Figure S2.1.** Synthesis of **AlloX**.

3-allyl-5,5-dimethyl-4-methyleneoxazolidin-2-one (**AlloX**) was prepared by adapting Jiang *et al.* procedure.<sup>73</sup> 2-Methyl-3-butyn-2-ol (84.1 g, 100 mmol, 1 eq), allyl Amine (60 g, 105 mmol, 1.05 eq) and copper iodide (10 g, 5 mol%) were loaded in a stainless-steel autoclave. CO<sub>2</sub> was injected at a pressure of



## 2

80 atm and a temperature of 60 °C under mechanical stirring. After 24 h the reaction vessel was depressurized, and the deep red mixture was distilled with a short path distillation apparatus at 120 °C over sulfuric acid (0.5 mL) under vacuum. The target material was obtained as a colourless oil (130 g, 78% yield) and stored in a freezer (-18 °C).

**<sup>1</sup>H-NMR** (300 MHz, DMSO-*d*<sub>6</sub>) δ 5.76 (m, 1H), 5.26 – 4.99 (m, 2H), 4.22 – 4.10 (m, 3H), 4.02 (dt, *J* = 5.0, 1.7 Hz, 2H), 1.47 (s, 9H). **<sup>13</sup>C-NMR** (75 MHz, DMSO) δ 154.48, 149.72, 131.17, 116.58, 81.92, 80.31, 42.82, 27.52. **IR**: 2980, 1760, 1680, 1642. **Mp (DSC)**: 6 °C.

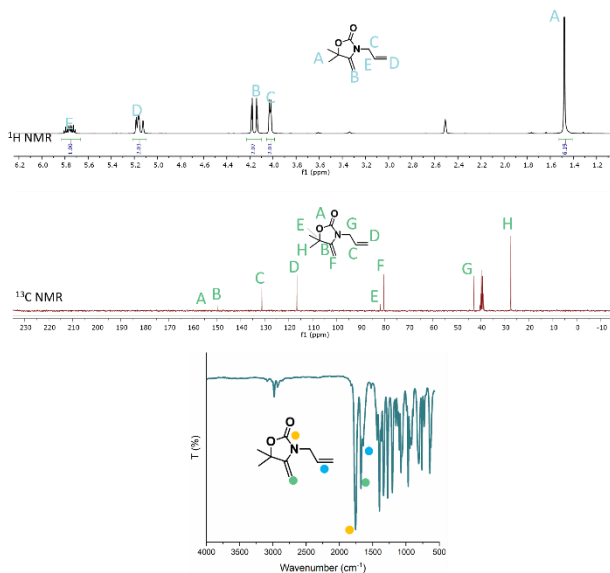
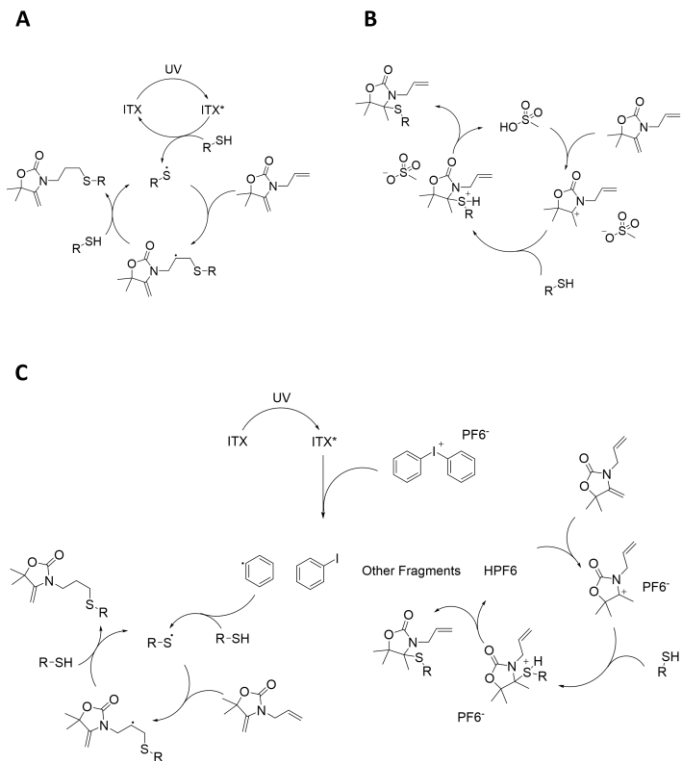


Figure S2.2. Characterisation of Allox: <sup>1</sup>H-NMR, <sup>13</sup>C-NMR, IR.

## 2.5.2.2. Thiol ene reaction mechanism



**Figure S2.3.** Reaction mechanism of radical thiol ene (a) and cationic thiol ene (b) and tandem thiol-ene (c) on **Allox**. In (a) and (c) the reaction with the exovinylene double bond was omitted for brevity.

## 2

### 2.5.2.3. Synthesis radical model compounds (OX\_S1)

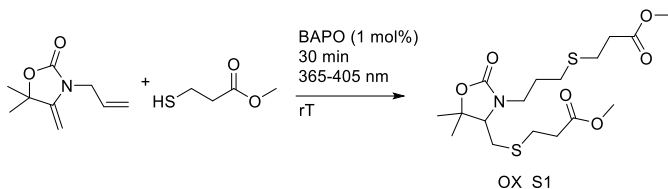


Figure S2.4. Synthesis of OX\_S1.

**Allox** (0.6 mmol, 1 eq) was mixed with methyl-3-mercaptopropionate (1.2 mmol, 2 eq) in a glass vial. BAPO (1 mol%) was dissolved in a small amount of dichloromethane and then added to the mixture. The homogenous yellow mixture was irradiated in an asiga flash curing chamber for 30 min under stirring (Low pressure mercury lamp, 365-405 nm, 36 Watts). The resulting transparent mixture was diluted in EtOAc and was washed twice with subsaturated brine. The organic phases were dried over  $\text{MgSO}_4$  and evaporated using rotary evaporation. The resulting yellow viscous liquid was subjected to column chromatography (Hex:EtOAc 7:3, vanillin stain). The organic solvent was removed *via* rotary evaporation and the resulting product was obtained as a transparent viscous liquid (yield = 54%).

**$^1\text{H-NMR}$**  (300 MHz, Chloroform- $d$ )  $\delta$  3.71 (s, 3H), 3.69 (s, 3H), 3.55 (m, 1H), 3.51 – 3.16 (m, 2H), 2.96 – 2.48 (m, 10H), 2.01 – 1.77 (m, 2H), 1.48 (s, 3H), 1.39 (s, 3H).  **$^{13}\text{C-NMR}$**  (75 MHz, Chloroform- $d$ )  $\delta$  173.16, 172.91, 157.90, 81.37, 64.50, 52.75 (d,  $J = 9.8$  Hz), 42.31, 35.45, 32.27, 30.07, 29.41, 29.13, 28.36, 27.87, 22.55. **HRMS (ESI)**  $m/z$ :  $[\text{M-Na}]^+$  calcd for  $\text{C}_{17}\text{H}_{30}\text{NO}_6\text{S}_2$ , 430.1329; found, 430.1330

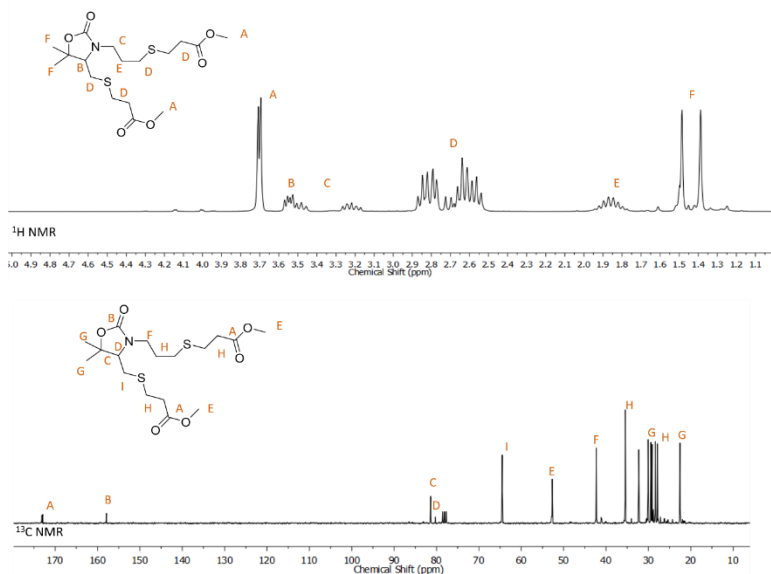


Figure S2.5.  $^1\text{H}$ -NMR (top) and  $^{13}\text{C}$ -NMR (bottom) spectra of **OX\_S1** ( $\text{CDCl}_3$ ).

#### 2.5.2.4. Synthesis Cationic model compounds (**OX\_S2**)

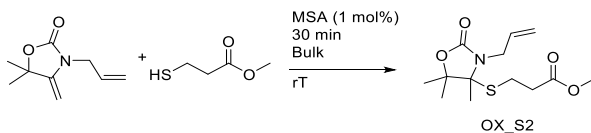


Figure S2.6. Synthesis of **OX\_S2**.

**Allox** (0.6 mmol, 1 eq) was mixed with methyl-3-mercaptopropionate (0.6 mmol, 1 eq) in a glass vial. MSA (1 mol%) was added to the mixture. The homogenous yellow mixture was stirred for 30 min. The resulting transparent mixture was diluted in EtOAc and was washed twice with subsaturated brine. The organic phases were dried over  $\text{MgSO}_4$  and evaporated using rotary evaporation. The resulting yellow viscous liquid was subjected to column chromatography (Hex:EtOAc 8:2, vanillin and iodine stain). The organic solvent was removed *via* rotary evaporation and the resulting product was obtained as a transparent viscous liquid (yield = 74%).

**$^1\text{H-NMR}$**  (300 MHz,  $\text{DMSO-d}_6$ )  $\delta$  6.01 – 5.81 (m, 1H), 5.35 – 5.02 (m, 2H), 3.85 (dddt, 2H), 3.61 (s, 3H), 2.86 – 2.33 (m, 4H), 1.55 (s, 3H), 1.40 (s, 3H), 1.34 (s, 3H).  **$^{13}\text{C-NMR}$**  (75 MHz,  $\text{DMSO}$ )  $\delta$  171.50, 155.91, 134.34, 116.50, 85.38, 78.15, 51.55, 42.58, 40.33, 40.06, 39.78, 39.50, 39.22, 38.94, 38.66, 32.58, 24.92, 24.01, 23.01, 20.57 **HRMS (ESI)**  $m/z$ :  $[\text{M-H}]^+$  calcd for  $\text{C}_{17}\text{H}_{30}\text{NO}_6\text{S}_2\text{H}^+$ , 288.3740; found, 288.3742

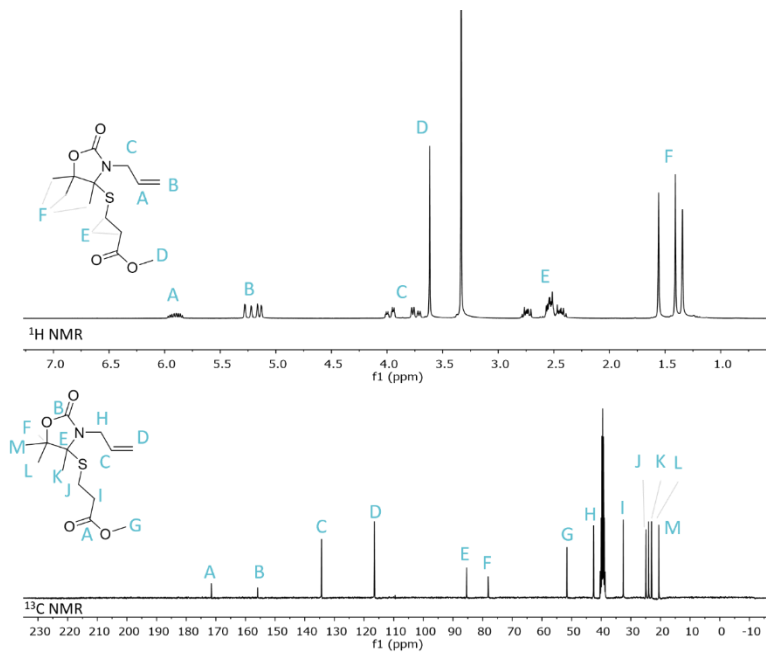


Figure S2.7. <sup>1</sup>H-NMR (top) and <sup>13</sup>C-NMR (bottom) spectra of **OX\_S2** (DMSO-*d*<sub>6</sub>).

## 2

### 2.5.2.5. Synthesis Tandem model compounds (OX\_S3)

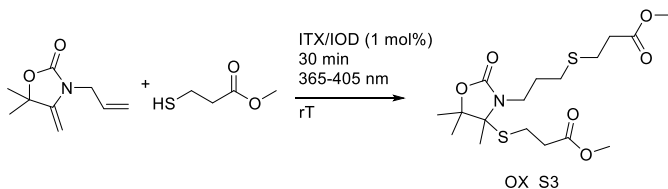


Figure S2.8. Synthesis of OX\_S3.

**Allox** (0.6mmol, 1 eq) was mixed with methyl-3-mercaptopropionate (1.2 mmol, 2eq) in a glass vial. ITX and IOD (1 mol %) were added and the mixture was stirred until homogenous. The yellow mixture was irradiated in an asiga flash curing chamber for 30 min under stirring (low pressure mercury lamp, 365-405 nm, 36 Watts). The resulting viscous yellow mixture was diluted in ethyl acetate and was washed twice with subsaturated brine. The organic phases were dried over  $\text{MgSO}_4$  and evaporated using rotary evaporation. The resulting yellow viscous liquid was subjected to column chromatography (Hex:EtOAc 7:3, vanillin stain). The organic solvent was removed *via* rotary evaporation and the resulting product was obtained as a yellowish viscous liquid (yield = 74%)

**$^1\text{H-NMR}$**  (300 MHz, Chloroform- $d$ )  $\delta$  3.67 (s, 3H), 3.66 (s, 3H), 3.56 – 3.18 (m, 2H), 2.86 – 2.68 (m, 4H), 2.63 – 2.30 (m, 8H), 1.99 – 1.75 (m, 2H), 1.59 (s, 3H), 1.43 (s, 3H), 1.36 (s, 3H).  **$^{13}\text{C-NMR}$**  (75 MHz, Chloroform- $d$ )  $\delta$  172.26, 171.60, 157.20, 85.57, 79.33, 78.49, 51.89, 40.08, 34.56, 33.12, 29.48, 26.97, 25.33, 24.47, 23.42, 21.08. **HRMS (ESI)**  $m/z$ :  $[\text{M-Na}]^+$  calcd for

$C_{17}H_{30}NO_6S_2Na^+$ , 430.1329; found, 430.1336

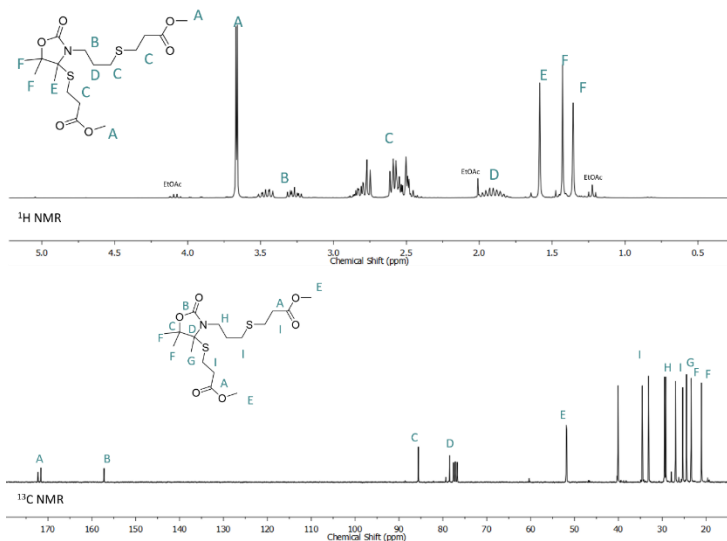


Figure S2.9.  $^1H$  (top) and  $^{13}C$ -NMR (bottom) spectra of OX\_S3 ( $CDCl_3$ ).

### 2.5.3. Methods

**Nuclear magnetic resonance (NMR) spectroscopy.**  $^1H$ - and  $^{13}C$ -NMR analyses were performed on a Bruker Avance 300 MHz spectrometer at 25 °C in the Fourier transform mode using  $CDCl_3$  or  $DMSO-d_6$  as solvents.

**SEC.** The samples were first dried in an oven at 60 °C under vacuum and then redissolved in THF to achieve a concentration of about 1 mg·mL<sup>-1</sup>. The solutions were filtered with a PTFE filter (pore size = 0.2 μm) before injection. The SEC (Agilent PL-GPC 50 integrated system) consisted of an autosampler, a pump and a differential refractometer as detector. A guard column (Agilent



## 2

PLGel 5  $\mu$ M, 50x1.5mm and two columns (PLGel  $\mu$ M, 30x7.5mm) were used for the fractionation at 40 °C using THF as eluent. The flow rate of THF through the columns was 1 mL·min<sup>-1</sup>. The reported molar masses are referred to polystyrene standards and the data was processed with PL-GPC software control v.2.3.0 (Agilent).

**HRMS (ESI)** data were acquired in SCAN mode, using a mass range 50–1000 u in resolution mode (FWHM  $\approx$  20,000) and a scan time of 0.1 s. The source temperature was set to 120 °C and the desolvation temperature to 350 °C. The capillary voltage was 0.7 kV and the cone voltage 15 V. Nitrogen was used as the desolvation and cone gas at flow rates of 600 L/h and 10 L/h, respectively. Before analysis, the mass spectrometer was calibrated with a sodium formate solution. A leucine-enkephalin solution was used for the lock mass correction, monitoring the ions at mass-to-charge ratio (m/z) 556.2771 and 278.1141. All of the acquired spectra were automatically corrected during acquisition based on the lock mass. The samples were dissolved in the corresponding solvent at a concentration of 1 mg/ml and diluted to 20  $\mu$ g/mL for the analysis.

**Atom Economy Calculation** Atom economy was calculated as described in<sup>74</sup> briefly. Eq 1 was employed:

$$AE = \frac{Mass_{Product}}{\sum Mass_{Reactants}} * 100 \quad (1)$$

**Gel content (GC).** Films prepared as described in the experimental section were cut in rectangular shapes and weighted ( $m_1$ ) before immersing 48 h in tetrahydrofuran. After weighing, the swelled films ( $m_2$ ) were dried in a vacuum oven at 60 °C for 24 h. The films were weighed once again ( $m_3$ ). Swelling (SI) and Gel content (GC) were calculated with equation 2 and 3, respectively:

$$SI = 100 * m_2 / m_1 \quad (2)$$

$$GC = 100 * m_3 / m_1 \quad (3)$$

**Tensile tests** were carried out on dogbone samples (see Preparation of Films below) (ASTM D638 TYPE V) in an Instron 5569 tensile tester (Instron, Norwood, MA, USA). Young's modulus, Tensile strength ( $\sigma_t$ ), Yield strength ( $\sigma_y$ ), and strain at break ( $\epsilon_b$ ) were determined using Bluehill software from the load-displacement curves at a crosshead speed of 10 mm/min. A minimum of three tensile specimens were tested for each reported value. Cyclic tensile tests were conducted to 20% strain at a rate of 10 mm min<sup>-1</sup>. 10 Cycles were measured. Calculation of elastic recovery was carried out following previous works.<sup>3</sup>

**Finite Element Digital Image Correlation (FE-DIC)** To efficiently measure and discriminate the differences between the upper (soft) part and lower (rigid) part of the locally heat-treated dogbone sample, full field strain measurements were performed. Indeed, direct measurements from the tensile testing apparatus will lead to mistake in the strain value due to the assumption of a homogeneous material, which is not anymore the case. Digital image correlation (DIC) allows to compute globally the strain field of a sample and thus differences can be observed compared to a general extensometer measurements. A Baumer® Vexu-24M camera was used with an in-house python software to record images at a 2 Hz frequency. A white and black speckle pattern was laid on specimen with a spray-paint. A white layer was firstly spread on the sample, black paint was then projected to generate random pattern composed of black dots. Images were post-processed with Pyxel,<sup>75</sup> a finite-element DIC Python software developed at the Clément Ader Institute (Toulouse, France). This method relies on

minimising distance between two functions linked to reference and deformed images respectively by analysing grey level of finite element's degree of freedom (dof) environment. Since the displacement obtained for each dof is linked to a finite element mesh, deformation field can be obtained by derivation using a Gauss-Newton algorithm.<sup>76</sup> The Region of Interest (ROI) was set for the global sample to 20 mm x 3 mm window placed in the narrower area of the sample. Finite-Element Mesh is composed of 50 elements of 0.6 mm x 2 mm size each with 8 dofs per element. To also compute and compare completely the upper and lower part of the sample, two different ROI were used, localized manually on the respective upper and lower part of the sample (CF IMAGES (if needed)). The ROI was set at 3 x 10 mm with 25 elements 0.2 x 2 mm size elements. In order to avoid computational costs and divergences at high displacement, the DIC measurements were only performed up to 10 % strain.

**Fourier Transform Infrared Spectroscopy (FT-IR) spectra** were recorded on a Nicolet iS20 Spectrometer using Attenuated Total Reflection (ATR) at a resolution of 4 cm<sup>-1</sup> and a total of 32 interferograms. The spectra at high temperature were obtained on a Nicolet 6700FT-IR spectrophotometer equipped with a specap variable temperature transmission cell. Spectra were recorded in the range of 4000 and 400 cm<sup>-1</sup> with a spectrum resolution of 4 cm<sup>-1</sup>, and a total of 64 interferograms. Samples were prepared by photocuring the resins composed of equimolar amounts of **Allox**, S4 and photoinitiator system (0.5 wt%) on KBr windows. The spectra were then acquired at each temperature after 5 min of equilibration. To calculate the amount of adduct at a given temperature the peak at 1678 cm<sup>-1</sup> was integrated. Conversion was calculated assuming that the integral of the peak at 175 °C was 83% of dissociation (from <sup>1</sup>H NMR experiments) using eq 4:

$$\text{Estimated Adduct bulk material (\%)} = \frac{\text{Area}_{\text{Temperature}}}{\text{Area}_{100\% \text{ adduct}}} * 100 \quad (4)$$

**Modulated Differential Scanning Calorimetry** was performed on a TA Instruments DSC 250 calibrated with indium, and the curves were analyzed using the Trios software. A period of 60 seconds with an amplitude of 1 °C was used. A ramp of 3 °C per minute from -20 °C to 175 °C.

**Dynamic Mechanical Analysis (DMA)** was performed on a DMA Q800. A 10 mm x 2 mm x 0.7 mm (l x w x t) was placed in a tension film clamp. An oscillation amplitude of 15 µm and a static force of 0.01 N were employed. A ramp of 3 °C/min was used from -20 to 175 with a frequency of 1 Hz.  $T_a$  was measured as the peak in the Tan delta curve.

**Isothermal stress relaxation** was conducted on a DMAQ800 in tension mode. Rectangular samples of 15×6×0.5 mm were used. The sample was held at the desired temperature for 10 min before a 1% strain was applied. The strain was kept constant for 60 min. Stress-relaxation of the dynamic cross-linked network was defined using a first order Maxwell model (Equation 4). The Flow Activation Energy ( $E_{flow}$ ) was then extracted by plotting an Arrhenius relationship (Equation 5) with  $\tau^*$  as a function of  $1/T$  (eq).

$$\frac{G(t)}{G_0} = e^{-t/\tau^*} \quad (5)$$

$$\tau^* = \tau_0 e^{E_a/RT} \quad (6)$$

**TEM** was acquired on a TECNAI G2 20 TWIN FEI transmission electron microscope equipped with LaB6 filament operated at an accelerating voltage of 120 kV in bright-field image mode at magnifications between ×6500 and ×50k. The samples were about 80 nm thick and were obtained by cutting at -90°C using a Leica EMFC6 cryoultramicrotome device equipped with a

—

diamond knife. These ultrathin sections were placed on a 300 mesh-formvar Cu grids for imaging. No staining was carried out.

**AFM** was acquired in tapping mode using a Dimension ICON (Bruker) with Nanoscope VI (Bruker) as software. A TESP-V2 cantilever was used at 320 kHz frequency (Spring constant: 37 N/m, radius 7 nm, length 125  $\mu\text{m}$ , silicon, repulsive mode, 25  $^{\circ}\text{C}$ ). Images were elaborated using Nanoscope Software. A first order background was removed, and the images were coloured with the standard colour palette. To compare images of different materials the same scale was used. The Nanoscope plugin “particle analysis” was used to estimate size and area % of the hard phase.

**Nano-FTIR and s-NOM** were recorded with a neaSNOM system (Neaspec GmbH, Germany) comprising both s-SNOM and nano-FTIR capabilities. Pt-Si coated AFM tips were used. IR s-SNOM imaging was performed with illumination from a tunable quantum cascade laser. Nano-FTIR spectroscopy was performed with illumination from amid-infrared laser supercontinuum. The final nano-FTIR spectra were obtained by averaging 25 individual spectra. The total acquisition time was 15 min and the spectral resolution 17  $\text{cm}^{-1}$ . The spectra were normalized to that obtained on a clean gold surface (reference measurements). Data were analyzed using Gwyddion.

**Temperature Sweep Rheology** was performed on an Ares G2 rheometer with a 12 mm plate-plate geometry. A ramp of 3  $^{\circ}\text{C}/\text{min}$  was used with a 1% strain and 0.5 Hz frequency. A 0.2 N normal force was applied to the material before starting to measurement to ensure good contact with the plates.

**Frequency Sweep Rheology** was performed on an Ares G2 rheometer with a 12 mm plate-plate geometry. A 5% strain was applied after isothermal for 10 min at the desired temperature. Then a frequency sweep from 0.01 to 100 Hz was performed. A 0.2 N normal force was applied to the material before starting to measurement to ensure good contact with the plates.

**Photorheology** was performed on an ARG2. A LED UV-curing accessory centered at 365 nm (20 mW/cm<sup>2</sup>) was used together with an acrylic transparent bottom plate and a single use aluminum parallel plate (20 mm). The measurement was performed in the linear viscoelastic regimen with frequency of 1 Hz with a gap of 400 μm.

**Optical Microscopy and Confocal raman** Raman spectra were collected using a Witec alpha300RA equipment. An excitation wavelengths of 785 nm was used with typical integration time per point of around 500 ms and 50 accumulations. Reported data correspond to average values after removing cosmic ray artifacts. A 100x objective was used for confocal measurements. Additionally, Raman images were taken over sample areas of about 100 micrometers squared with data points measured every 200 nm.

**Radical, Tandem and Cationic Model Reactions.** Model reactions between **AlLOx** and 3-methyl mercaptopropionate were carried out with 3 different initiators. The two components were mixed in equal SH to double bond ratio in bulk with the photoinitiator. The samples were irradiated at 390nm (20 mW/cm<sup>2</sup>) and aliquots of the reaction mixture were sampled over time. The reactions were monitored by <sup>1</sup>H-NMR spectroscopy to determine the conversion in the product.

For all reaction the conversion was calculated with Equation 7 (where  $I_t$  is the integral at time t and  $I_0$  the integral at time 0) by taking into consideration the signal of the CH<sub>2</sub> of the allyl bond (5.16 ppm), CH<sub>2</sub> of exovinylene double bond (3.98 ppm). The signal were normalized using the signal of the internal standard (1,3,5-trimethoxy benzene, signal at 6.06 ppm, singlet). For the cationic thiol ene kinetics the signal of the methyl of 3MP was used as internal standard (3.68 ppm, singlet)

$$Conversion (\%) = \frac{I_t}{I_0} * 100 \quad (7)$$

## 2

**Radical Model Reaction:** **AlLOx** (4 mmol, 1 eq.), 1,3,5-trimethoxy benzene (10 mg) and 3-methyl mercaptopropionate (8 mmol, 2 eq.) were added to a vial. ITX (1 mol%) was added and the mixture was stirred until complete dissolution. The mixture was then irradiated with a 390 nm light (Kessil, PR160L, 390nm, 20 mW/cm<sup>2</sup>). The NMR sample were prepared by dissolving 10  $\mu$ L of the reaction medium in 500  $\mu$ L CDCl<sub>3</sub> and were stored in the dark before measurement.

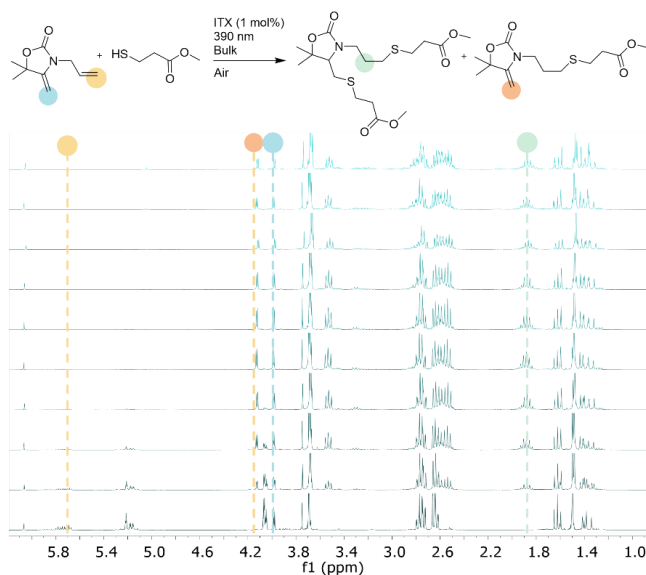


**Figure S2.10.** <sup>1</sup>H NMR kinetics of model radical thiol ene using ITX as photoinitiator

**Radical Model Reaction:** **AlLOx** (4 mmol, 1 eq.), 1,3,5-trimethoxy benzene (10 mg) and 3-methyl mercaptopropionate (8 mmol, 2 eq.) were added to a vial. BAPO (1 mol%) was added and the mixture was stirred until complete

dissolution. The mixture was then irradiated with a 390 nm light (Kessil, PR160L, 390nm, 20 mW/cm<sup>2</sup>). The NMR sample were prepared by dissolving 10  $\mu$ L of the reaction medium in 500  $\mu$ L CDCl<sub>3</sub> and were stored in the dark before measurement.

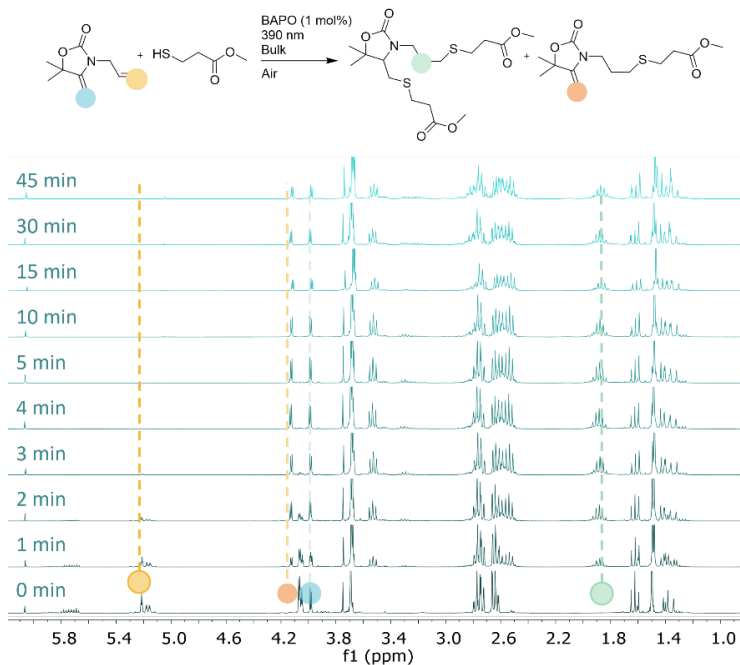


**Figure S2.11.** <sup>1</sup>H NMR kinetics of model radical thiol-ene using BAPO as photoinitiator

**Cationic Model Reaction:** **Allox** (4 mmol, 1 eq) and 3-methyl mercaptopropionate (8 mmol, 2 eq.) were added to a vial. MSA (1 mol%) was



## 2

added. The NMR sample were prepared by quenching 10  $\mu\text{L}$  of the reaction medium in 500  $\mu\text{L}$  of  $\text{CDCl}_3$  with 5  $\mu\text{L}$  of Triethylamine.

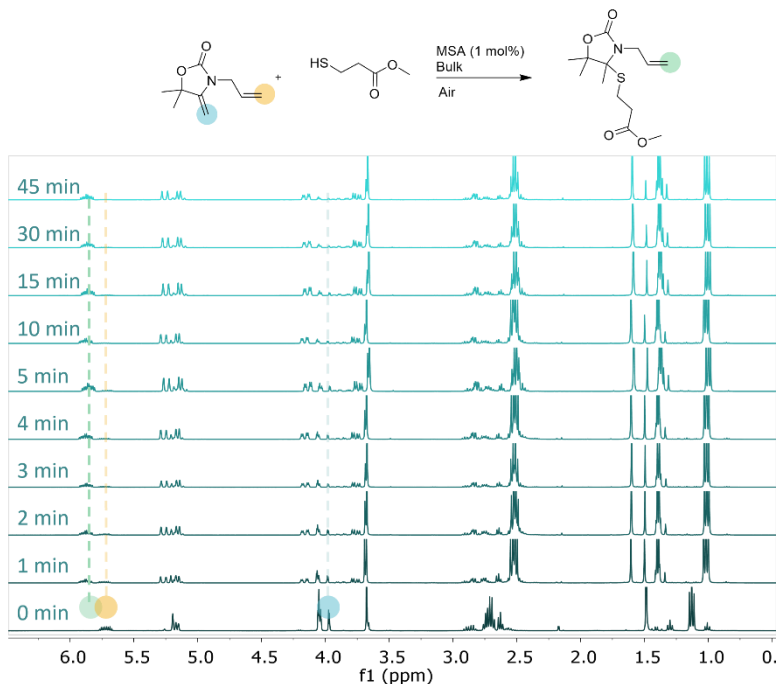


Figure S2.12. <sup>1</sup>H NMR kinetics of model cationic thiol ene

**Tandem Model Reaction:** **AlLOx** (4 mmol, 1 eq.), 1,3,5-trimethoxy benzene (10 mg) and 3-methyl mercaptopropionate (8 mmol, 2 eq.) were added to a vial. IOD/ITX (1 mol% of each component) was added and the mixture was stirred until complete dissolution. The mixture was then irradiated with a 390 nm light (Kessil, PR160L, 390nm, 20 mW/cm<sup>2</sup>). The NMR sample were prepared

by dissolving 10  $\mu\text{L}$  of the reaction medium in 500  $\mu\text{L}$   $\text{CDCl}_3$  with 5  $\mu\text{L}$  of Triethylamine and were stored in the dark before measurement.

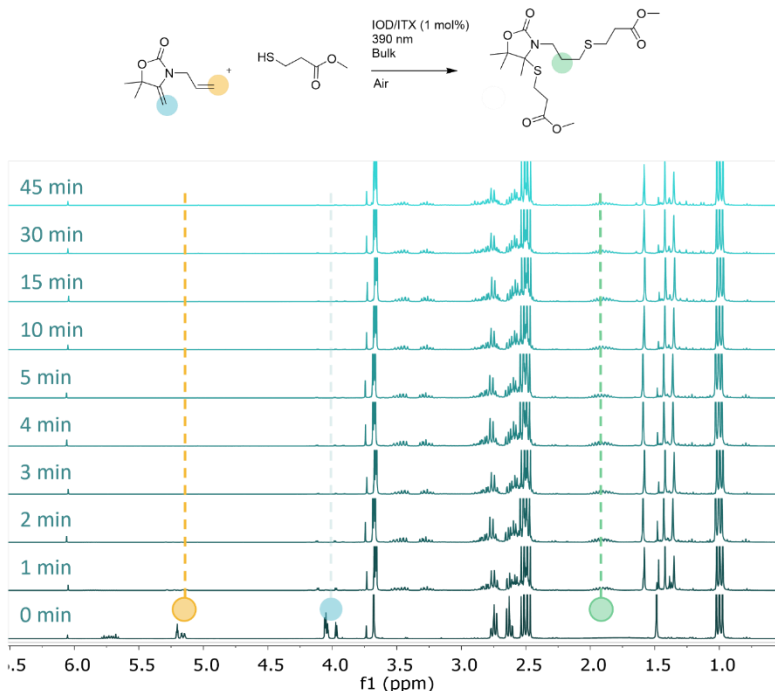


Figure S2.13. <sup>1</sup>H NMR kinetics of model tandem thiol-ene.

**Preparation of Crosslinked Networks and Films.** The photoinitiators were first dissolved in **Allox** (0.5 wt%). The mixture was mixed with a vortex mixer for 30 s before adding the crosslinker (equimolar amount of SH to double bond functionality). As an example, T\_S4 was prepared by mixing IOD/ITX (12.5 mg, 0.5 wt%) in **Allox** (1 g, 6 mmol, 2 eq), to which S4 (1.5 g, 3 mmol, 1

eq) were added via pipette. Other networks were prepared in an analogous manner. The resulting mixture was again vortexed for 1 min. The liquid was then poured into moulds and cured for 30 min in an Asiga post-cure chamber (Low pressure mercury lamp with a broad emission in the UV and visible). For the various heat treatments, films were placed in a temperature control oven at the desired temperature for 16-20 hours, then cooled quickly to room temperature, and finally stored for 24 h at room temperature before testing their properties. The materials are named R\_Sn for radical materials and T\_Sn for tandem materials with n being the number of functionality of the thiol crosslinked used. Films with spatially-resolved annealing were prepared by first treating the entire dogbone at 60 °C for 24 h. Then half of the dogbone was placed on a hot plate at 110 °C for 4 h to erase the phase separated structure.

**Reprocessing of Films** The material was grinded and then hot-pressed in a Collin P200E hydraulic press for 3 min at 100 °C with an applied pressure of 10 tons. The resulting film was cooled down for 10 min before cutting dogbone samples (ASTM D638 TYPE V) with a die cutter. The resulting dogbone shapes were heat treated 24 h, cooled quickly to room temperature and then stored for 24 h at room temperature before testing.

**Preparation of Films for AFM analysis** The photoinitiator system was first dissolved in **AlLOx** (0.5 wt%). The mixture was mixed with a vortex mixer for 30 s before adding the crosslinker (equimolar amount of SH to double bond functionality). The resulting mixture was again vortexed for 1 min. The resin was then brought into a Glovebox to avoid dust contamination (Argon atmosphere). The liquid was then drop casted on a glass slide and cured for 5 min with a 365 nm lamp at 20 mW/cm<sup>2</sup>. The cured films were placed in an airtight container under normal atmosphere before being heat treated and then cooled quickly to room temperature. The samples were stored for 24 h at room temperature in a desiccator before testing their properties.

**3D Printing** The material was grinded and then extruded through a twin-screw extruder at 165 °C and 30 rpm to obtain a homogenous filament. The filament was let to rest for 30 min at room temperature and then cut into pellets using a pelletizer. The resulting pellets were stored in a desiccator to avoid any humidity absorption. They were then charged in an Ender 3 NEO retrofitted with a V4 Pellet extruder and a 0.4 mm nozzle. The nozzle was set at 185 °C and a speed of 5 mm/s was employed. Layers of 0.2 mm were printed. A skirt of 6 lines was used to reach a stable filament deposition.

After optimization it was found that a low speed and a more pronounced thermal gradient were necessary to fully depolymerize the polymer as the melting was given by a chemical reaction. Hence slow printing speed, coupled with a fan that is located further away from the nozzle helped with the deposition of a homogenous filament. A consistent size of pellets was also fundamental in having consistent material flow.

## 2

### 2.5.4. Photocuring and Materials Properties

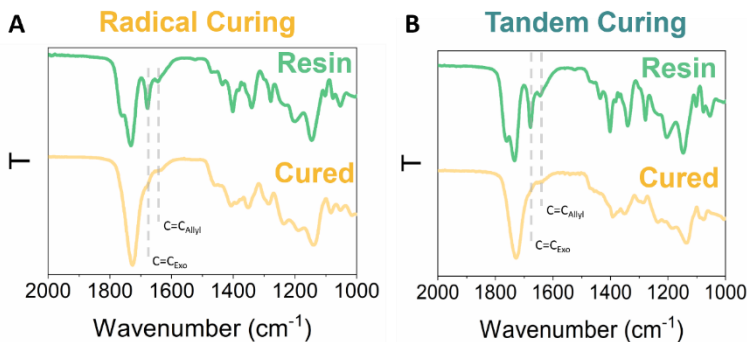


**Figure S2.14.** IR spectra of the resin and photocured radical material (Radical\_S4) (b) IR spectra of the resin and photocured tandem material (Tandem\_S4). The thiol band was not used to estimate the conversion as its signal to noise ratio was unsatisfactory.

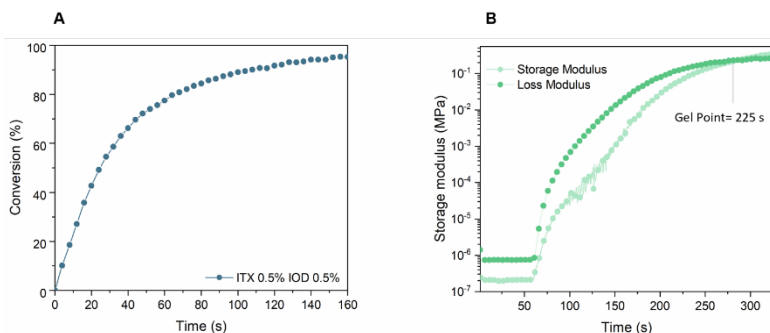


**Figure S2.15.** Conversion over time as calculated by RT FTIR analysis (a) Photorheology of T\_S4 (b).

**Table S2.1.** Gel Content and Swelling in THF of Tandem and radical material

PI	Crosslinker	SI (THF)	GC (THF)
Tandem	S4	156 $\pm$ 4	95 $\pm$ 3
Radical	S4	146 $\pm$ 0.5	98 $\pm$ 0.3

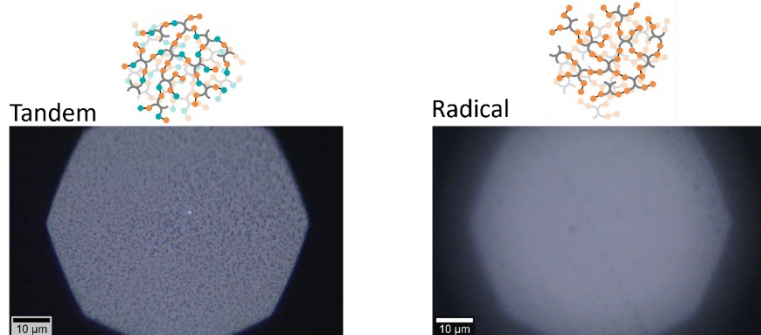


**Figure S2.16.** OM of Tandem material (T\_S4) and Radical material (R\_S4).

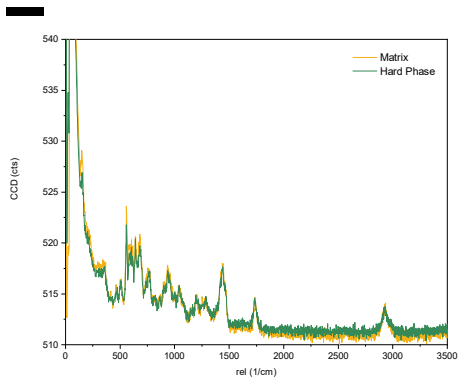


Figure S2.17. Confocal Raman spectra of hard phase and matrix of **T\_S4**.

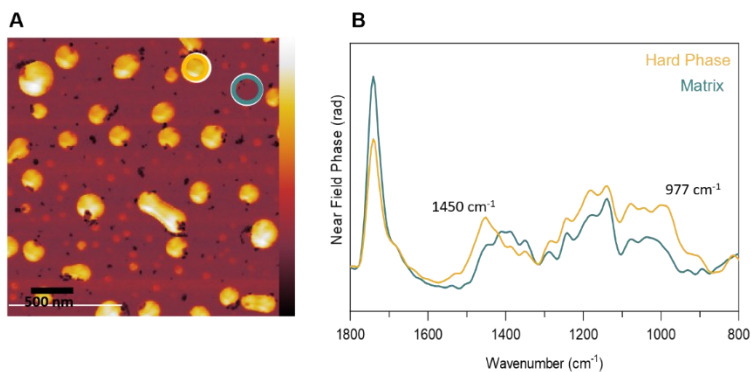


Figure S2.18. AFM Phase Imaging of **T\_S4** and corresponding Nano-FTIR spectra of the hard phase and matrix.

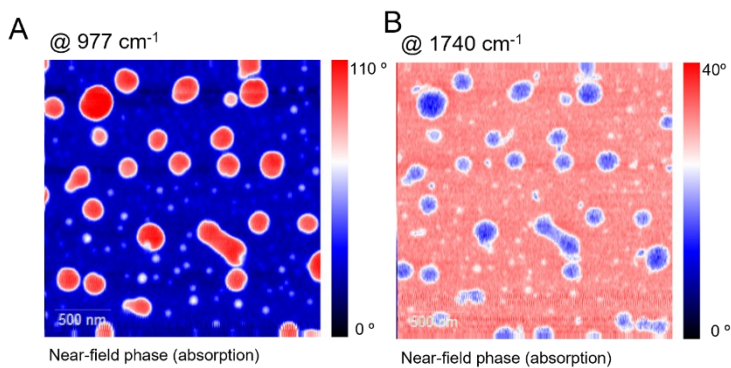


Figure S2.19. s-NOM imaging at  $977\text{ cm}^{-1}$  (A) and  $1740\text{ cm}^{-1}$  (B) of the tandem material (T\_S4).

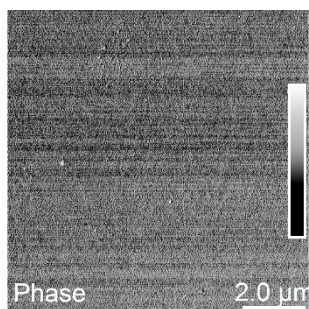


Figure S2.20. AFM of R\_S4.



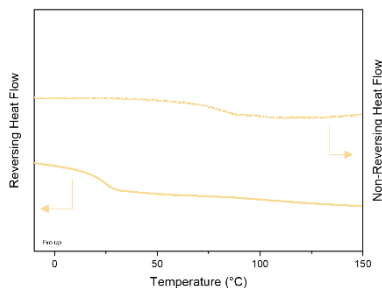


Figure S2.21. mDSC of radical material (**R\_S4**).

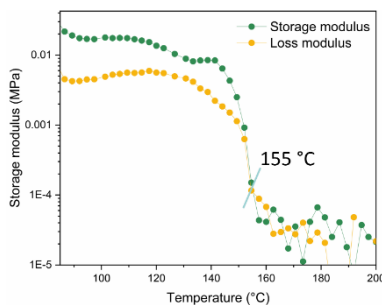


Figure S2.22. Temperature Sweep of **Tandem\_S4**.

### Estimation of Adduct Dissociation

Ox\_S3 was mixed with MSA (1 mol%) and placed in a vial under N<sub>2</sub> atmosphere. The mixture was heated at the desired temperature for 15 min, a small aliquot (1  $\mu$ L) was then sampled and quenched with TEA (2  $\mu$ L). The mixture was diluted in DMSO-*d*<sub>6</sub> (0.5 mL) and its <sup>1</sup>H NMR recorded. The conversion was estimated by the disappearance of the methyl signals of OX\_S3 (1.59 ppm) using Equation 5.

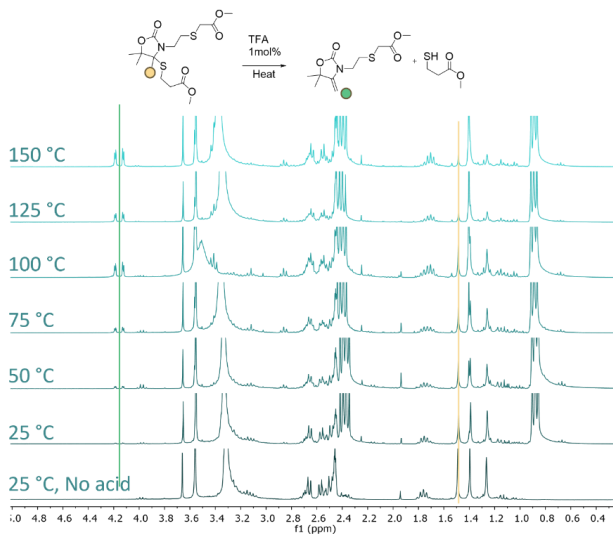


Figure S2.23.  $^1\text{H}$  NMR experiment of Adduct Dissociation (Ox\_S3) at different temperatures (DMSO  $d_6$ ).

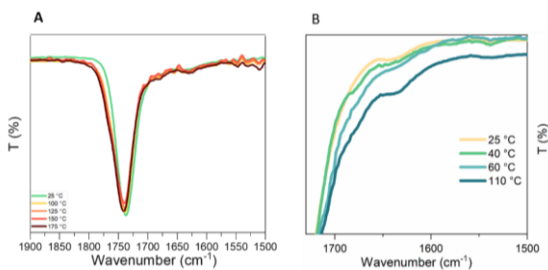
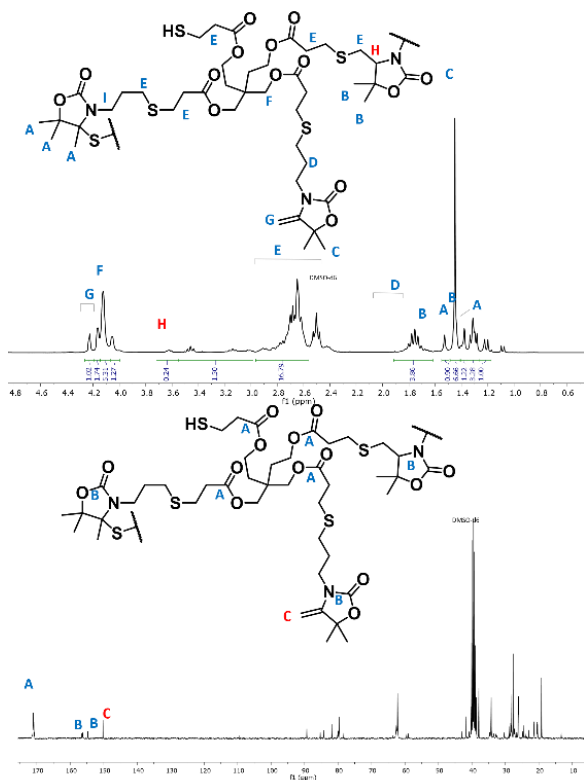


Figure S2.24. Temperature Dependent IR spectroscopy of Radical material (R\_S4, a) and spectra of T\_S4 after thermal treatment (b).



**Figure S2.25.**  $^1\text{H}$ - (top) and  $^{13}\text{C}$ -NMR (bottom) spectra of the depolymerised tandem material (Tandem\_S4). **AlloX** was used as a model compound to assign signals C, G while the tandem and radical compound (OX\_S1) helped for resonances A, D and H ( $^1\text{H}$ ).

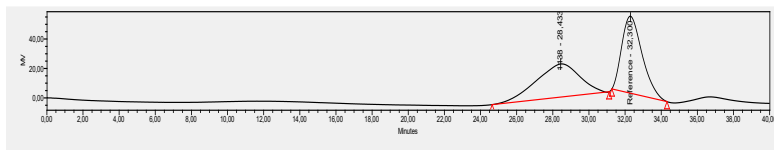
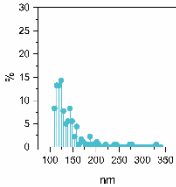
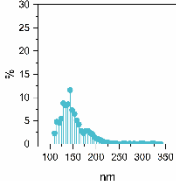
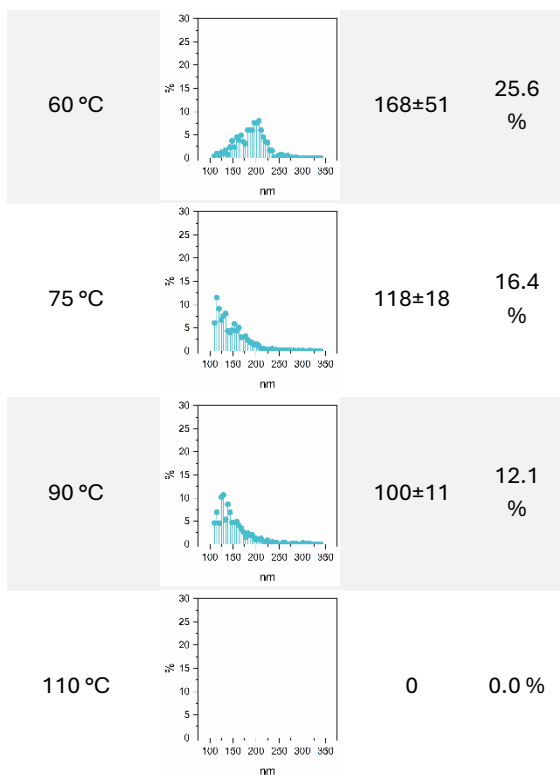


Figure S2.26. SEC trace of **T<sub>S4</sub>** after thermal depolymerisation.

### 2.5.5. Phase Separation

Table S2.2. AFM Characterisation of Hard phase in Tandem\_S4 with different heat treatments.

Heat treatment	Particle Distribution	Mean Particle size (nm)	Area Hard Phase
25 °C		84±25	1.4 %
40 °C		152±92	5.8 %



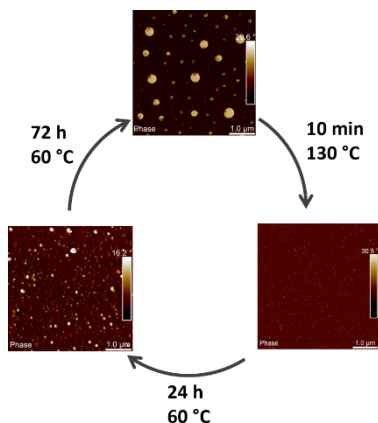


**Figure S2.27.** Cyclability of Phase separation. Heat treatment at 130 °C completely erases phase separation. Heat treatment at 60 °C for 24 h partially recovers the morphology. A fully developed morphology was found for 72 h of heat treatment at 60 °C.

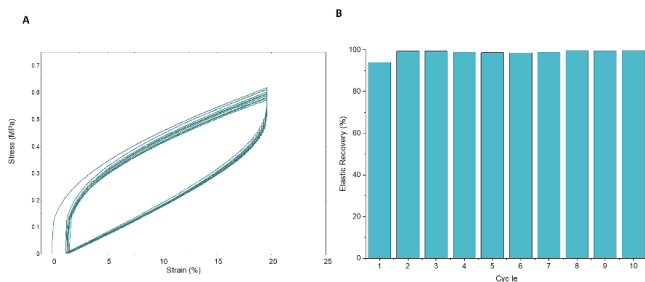


**Figure S2.28.** Histeresis of T<sub>S4</sub> treated at 110 °C for 24 h over 10 cycles at 20% strain and elastic recovery.

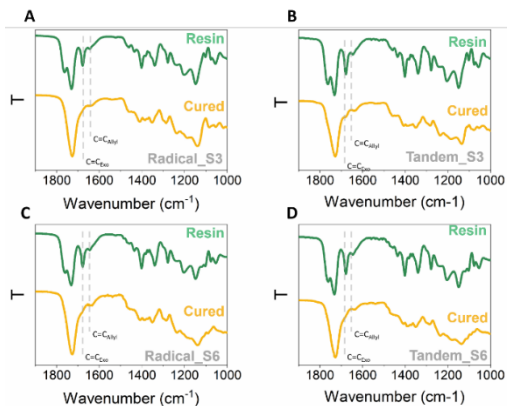
## 2

**Table S2.3.** Mechanical properties of radical and tandem materials with a variety of crosslinkers.

<i>Material</i>	<i>Crosslinker</i>	<i>T<sub>Anneal</sub></i>	<i>E (MPa)</i>	<i>ε<sub>break</sub> (%)</i>	<i>σ<sub>break</sub> (MPa)</i>
Tandem	S3	25 °C	22.9 ± 2.7	92 ± 6	12.4 ± 3.3
	S3	60 °C	6±0.3	97±10	5±1
	S4	25 °C	1640 ± 75	44 ± 3	21 ± 1
	S4	40 °C	1840±130	3.8±0.2	44±2
	S4	60 °C	3000±180	2.5±0.3	55±6
	S4	75 °C	1010±140	12.5±2.1	15.5±1.5
	S4	90 °C	11.7±1.6	88±2	7.7±1.1

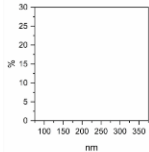
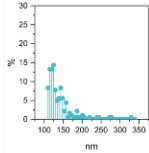
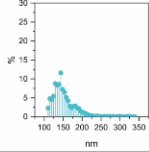
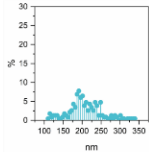
	S4	110 °C	2.0±0.3	108±8	2±0.2
	S6	25 °C	1980 ± 224	4.1 ± 0.4	60 ± 5
	S6	60 °C	3300±220	2.2±0.4	70±4
Radical	S3	60 °C	8±1.5	75±9	3.9±0.2
	S4	60 °C	750±80	26±2	13±3
	S6	60 °C	1720±70	4±1	27±5





*Figure S2.29.* (a) IR pre and post curing of **Radical\_S3** (b) IR pre and post curing of **Tandem\_S3** (c) IR pre and post curing of **Radical\_S6** (d) IR pre and post curing of **Tandem\_S6**.

**Table S2.4.** AFM Characterization of Tandem Material prepared with Tri- and Hexathiol crosslinkers together with morphological details.

Thiol	Heat Treatment (24 h)	Particle Distribution	Mean Domain diameter (nm)	Area Hard Domain (%)
Trithiol	25		-	-
	60		47±9	2%
Hexathiol	25		84±11	6 %
	60		267±54	15 %

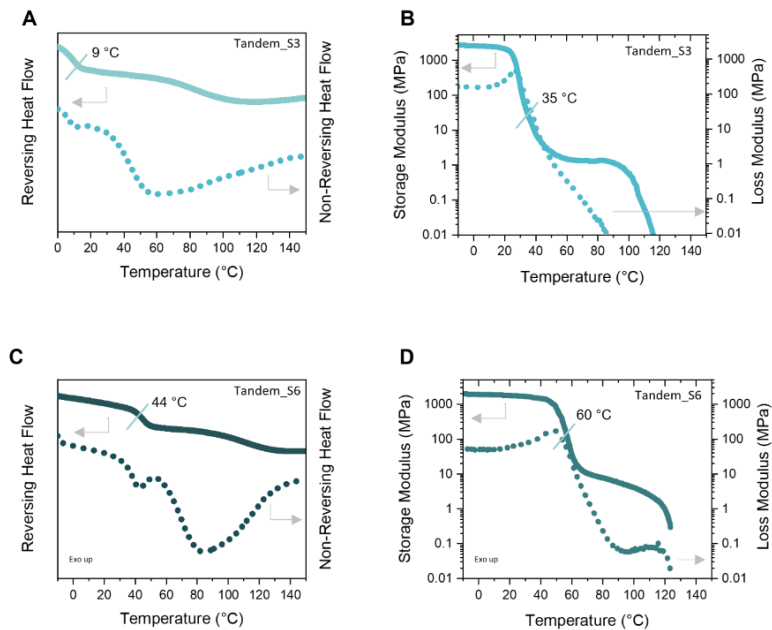


Figure S2.30. (a) mDSC trace of Tandem\_S3 (b) DMTA trace Tandem\_S3 (c) mDSC trace of Tandem\_S3 T\_S6 (d) DMTA trace Tandem\_S6.

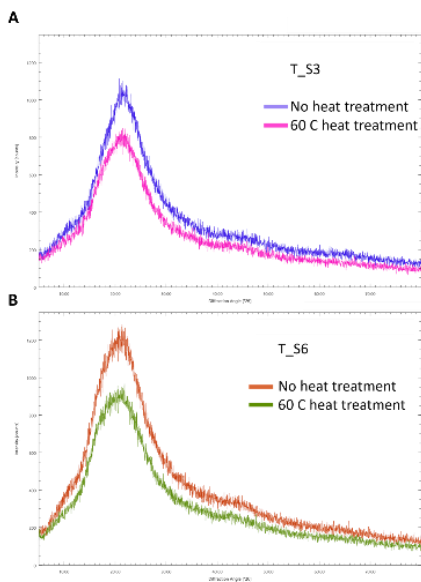


Figure S2.31. XRD diffractograms of **T\_S3** (top) and **T\_S6** (Bottom).

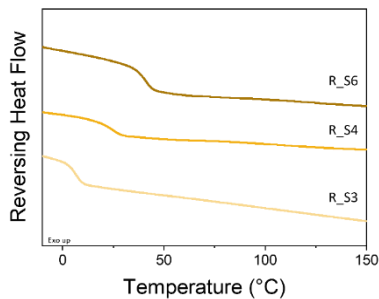
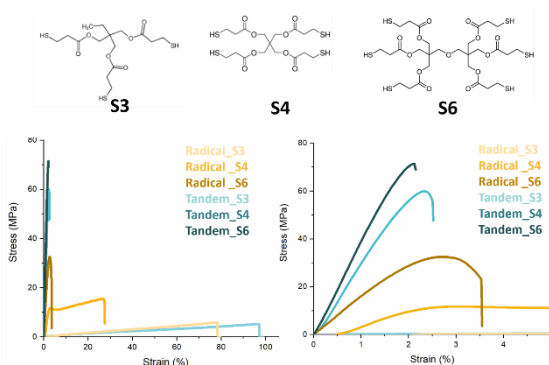
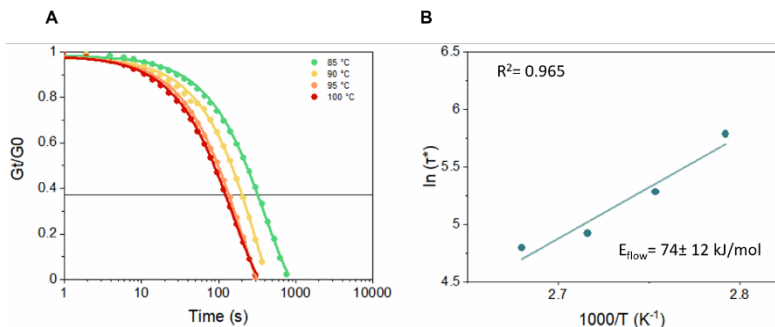


Figure S2.32. mDSC of **R\_S3**, **R\_S4** and **R\_S6**.



**Figure S2.33.** Top, Structures of used crosslinkers; Bottom, (left) Mechanical properties of tandem and radical materials; (right) Zoom of left graph. All materials were annealed at 60 °C for 24 h and then stored at 25 °C for 24 h before testing.



**Figure S2.34.** (a) Stress relaxation curves and first order Maxwellian fitting of **Tandem\_S4** after heat treatment at 110 °C (b) Arrhenius plot of Tandem\_S4 heat treated at 110 °C for 24 h.

**Table S2.5.** Stress relaxation data for **T\_S4** for different heat treatments and relative  $R^2$  (first order Maxwellian fitting).

Sample	T (°C)	$\tau$ (s)	$R^2$
T_S4 60 °C, 24 h	70	1161	0.999
T_S4 60 °C, 24 h	75	872	0.998
T_S4 60 °C, 24 h	80	670	0.998
T_S4 60 °C, 24 h	85	418	0.997
T_S4 60 °C, 24 h	90	320	0.997
T_S4 60 °C, 24 h	100	165	0.999
T_S4 60 °C, 24 h	105	104	0.998
T_S4 110 °C, 24 h	85	324	0.999
T_S4 110 °C, 24 h	90	196	0.998
T_S4 110 °C, 24 h	95	136	0.999
T_S4 110 °C, 24 h	100	121	0.999

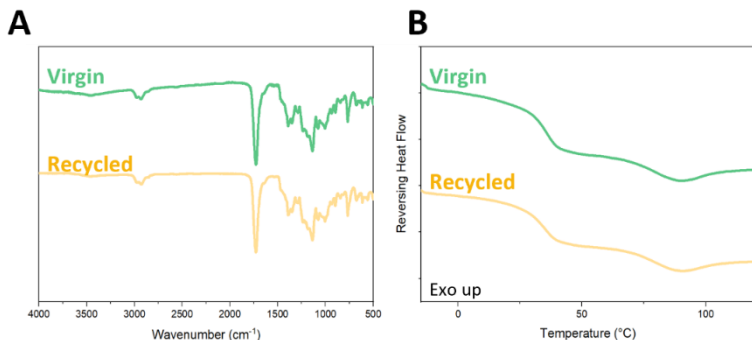


Figure S2.35. (a) IR Spectra of virgin and recycled materials (**Tandem\_S4**) (b) and mDSC traces of virgin and recycled materials (**Tandem\_S4**).

### 2.5.6. 3D printing

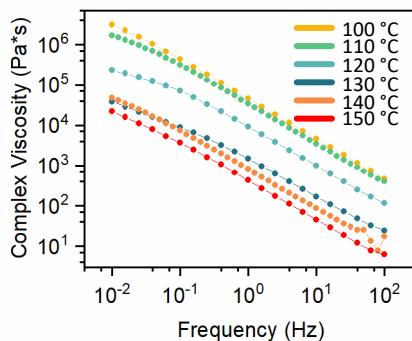


Figure S2.36. Frequency Sweep Rheometry (SAOS) of **T\_S4** at temperatures ranging from 100 to 150 °C.

T\_S6

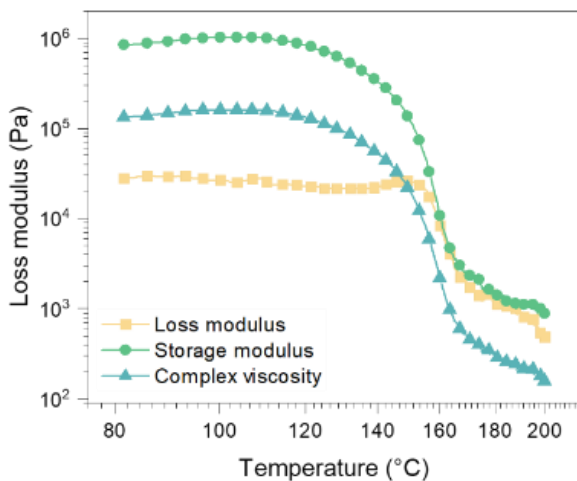
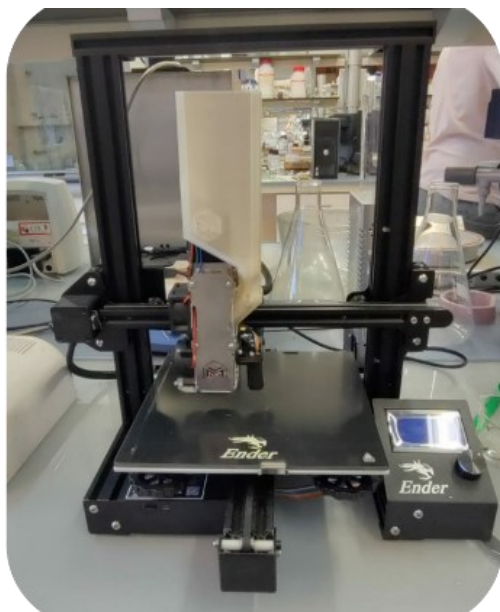


Figure S2.37. Temperature Sweep of Tandem\_S6.

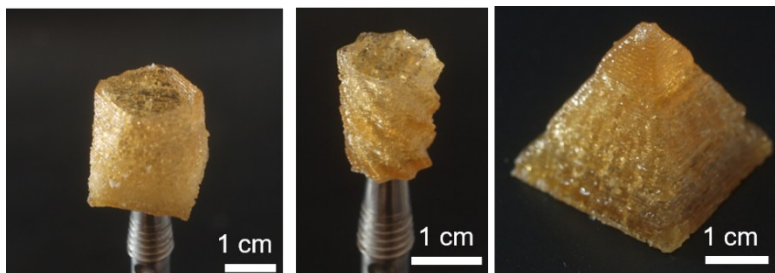


Figure S2.38. Filament produced from the twin screw extruder and pellets (T\_S6).





*Figure S2.39.* Ender 3 NEO 3D printer with a v4 Universal Pellet Extruder mount.





*Figure S2.40.* 3D printed structures using T\_S6.

## 2.6. References

1. Pal, A. K., Mohanty, A. K. & Misra, M. Additive manufacturing technology of polymeric materials for customized products: Recent developments and future prospective. *RSC Adv* 11, 36398–36438 (2021).
2. Tofail, S. A. M. et al. Additive manufacturing: scientific and technological challenges, market uptake and opportunities. *Materials Today* 21, 22–37 (2018).
3. Shahrubudin, N., Lee, T. C. & Ramlan, R. An overview on 3D printing technology: Technological, materials, and applications. *Procedia Manuf* 35, 1286–1296 (2019).
4. Melchels, F. P. W. et al. Additive manufacturing of tissues and organs. *Prog Polym Sci* 37, 1079–1104 (2012).
5. Singh, S. & Ramakrishna, S. Biomedical applications of additive manufacturing: Present and future. *Curr Opin Biomed Eng* 2, 105–115 (2017).
6. Solomon, I. J., Sevel, P. & Gunasekaran, J. A review on the various processing parameters in FDM. *Mater Today Proc* 37, 509–514 (2020).
7. Jiang, Z. et al. Extrusion 3D Printing of Polymeric Materials with Advanced Properties. *Advanced Science* 7, 1–32 (2020).
8. Bijalwan, V. et al. 3D Printing of Covalent Adaptable Networks: Overview, Applications and Future Prospects. *Polymer Reviews* 64, 36–79 (2024).
9. Ahn, S. H., Montero, M., Odell, D., Roundy, S. & Wright, P. K. Anisotropic material properties of fused deposition modeling ABS. *Rapid Prototyp J* 8, 248–257 (2002).
10. Lucherelli, M. A., Duval, A. & Averous, L. Biobased vitrimers: Towards sustainable and adaptable performing polymer materials. *Prog Polym Sci* 127, 101515 (2022).
11. Zheng, J. et al. Vitrimers: Current research trends and their emerging applications. *Materials Today* 51, 586–625 (2021).
12. Van Zee, N. J. & Nicolay, R. Vitrimers: Permanently crosslinked polymers with dynamic network topology. *Prog Polym Sci* 104, 101233 (2020).
13. Krishna Kumar, B. & Dickens, T. J. Dynamic bond exchangeable thermoset vitrimers in 3D-printing. *J Appl Polym Sci* 140, 1–13 (2023).
14. Joe, J. et al. A 4D Printable Shape Memory Vitriimer with Repairability and Recyclability through Network Architecture Tailoring from Commercial Poly( $\epsilon$ -caprolactone). *Advanced Science* 8, 1–11 (2021).
15. Choi, S. et al. Weldable and Reprocessable Shape Memory Epoxy Vitriimer Enabled by Controlled Formulation for Extrusion-Based 4D Printing Applications. *Adv Eng Mater* 24, 1–10 (2022).
16. Prasanna Kar, G., Lin, X. & Terentjev, E. M. Fused Filament Fabrication of a Dynamically Crosslinked Network Derived from Commodity Thermoplastics. *ACS Appl Polym Mater* 4, 4364–4372 (2022).

17. Montoya-Ospina, M. C., Zeng, J., Tan, X. & Osswald, T. A. Material Extrusion Additive Manufacturing with Polyethylene Vitrimers. *Polymers (Basel)* 15, 1332 (2023).
18. Kim, S. et al. Closed-loop additive manufacturing of upcycled commodity plastic through dynamic cross-linking. *Sci Adv* 8, 1–9 (2022).
19. Saed, M. O., Lin, X. & Terentjev, E. M. Dynamic Semicrystalline Networks of Polypropylene with Thiol-Anhydride Exchangeable Crosslinks. *ACS Appl Mater Interfaces* 13, 42044–42051 (2021).
20. Yang, K. et al. Diels–Alder Reversible Thermoset 3D Printing: Isotropic Thermoset Polymers via Fused Filament Fabrication. *Adv Funct Mater* 27, 1700318 (2017).
21. Davidson, J. R., Appuhamillage, G. A., Thompson, C. M., Voit, W. & Smaldone, R. A. Design Paradigm Utilizing Reversible Diels–Alder Reactions to Enhance the Mechanical Properties of 3D Printed Materials. *ACS Appl Mater Interfaces* 8, 16961–16966 (2016).
22. Appuhamillage, G. A. et al. 3D printed remendable polylactic acid blends with uniform mechanical strength enabled by a dynamic Diels–Alder reaction. *Polym Chem* 8, 2087–2092 (2017).
23. Herbert, K. M. et al. Dynamic reaction-induced phase separation in tunable, adaptive covalent networks. *Chem Sci* 11, 5028–5036 (2020).
24. Sivakova, S., Bohnsack, D. A., Mackay, M. E., Suwanmala, P. & Rowan, S. J. Utilization of a combination of weak hydrogen-bonding interactions and phase segregation to yield highly thermosensitive supramolecular polymers. *J Am Chem Soc* 127, 18202–18211 (2005).
25. Herbert, K. M. et al. Controlling the Morphology of Dynamic Thia-Michael Networks to Target Pressure-Sensitive and Hot Melt Adhesives. *ACS Appl Mater Interfaces* 13, (2021).
26. Boynton, N. R. et al. Accessing pluripotent materials through tempering of dynamic covalent polymer networks. *Science* (1979) 383, 545–551 (2024).
27. Jia, Y. et al. New Prospects Arising from Dynamically Crosslinked Polymers: Reprogramming Their Properties. *Advanced Materials* 2313164 (2024) doi:10.1002/ADMA.202313164.
28. Ehrmann, K. & Barner-Kowollik, C. Colorful 3D Printing: A Critical Feasibility Analysis of Multi-Wavelength Additive Manufacturing. *J Am Chem Soc* 145, 24438–24446 (2023).
29. Schwartz, J. J. & Boydston, A. J. Multimaterial actinic spatial control 3D and 4D printing. *Nat Commun* 10, 1–10 (2019).
30. Zhou, L. Y., Fu, J. & He, Y. A Review of 3D Printing Technologies for Soft Polymer Materials. *Adv Funct Mater* 30, 1–38 (2020).
31. Saadi, M. A. S. R. et al. Direct Ink Writing: A 3D Printing Technology for Diverse Materials. *Advanced Materials* 34, 2108855 (2022).
32. Sampson, K. L. et al. Multimaterial Vat Polymerization Additive Manufacturing. *ACS Appl Polym Mater* 3, 4304–4324 (2021).
33. Habets, T. et al. Covalent Adaptable Networks through Dynamic *N,S*-acetal Chemistry: Toward Recyclable CO<sub>2</sub>-Based Thermosets. *J Am Chem Soc* 145, 25450–25462 (2023).

34. Laviéville, S. et al. Trifluoromethylated *N,S*-acetal as a Chemical Platform for Covalent Adaptable Networks: Fast Thiol Exchange and Strong Hydrostability for a Highly Transparent Material. *Macromolecules* (2024) doi:10.1021/ACS.MACROMOL.4C01359.
35. Sutherland, B. P., Kabra, M. & Kloxin, C. J. Expanding the thiol-X toolbox: Photoinitiation and materials application of the acid-catalyzed thiol-ene (ACT) reaction. *Polym Chem* 12, 1562–1570 (2021).
36. Uchiyama, M., Osumi, M., Satoh, K. & Kamigaito, M. Thiol-Ene Cationic and Radical Reactions: Cyclization, Step-Growth, and Concurrent Polymerizations for Thioacetal and Thioether Units. *Angewandte Chemie - International Edition* 59, 6832–6838 (2020).
37. Li, Q. et al. Concurrent thiol-ene competitive reactions provide reprocessable, degradable and creep-resistant dynamic-permanent hybrid covalent networks. *Green Chemistry* 22, 7769–7777 (2020).
38. Habets, T., Siragusa, F., Grignard, B. & Detrembleur, C. Advancing the synthesis of isocyanate-free poly(oxazolidones)s: Scope and limitations. *Macromolecules* 53, 6396–6408 (2020).
39. Grignard, B., Gennen, S., Jérôme, C., Kleij, A. W. & Detrembleur, C. Advances in the use of CO<sub>2</sub> as a renewable feedstock for the synthesis of polymers. *Chem Soc Rev* 48, 4466–4514 (2019).
40. Gennen, S., Grignard, B., Tassaing, T., Jérôme, C. & Detrembleur, C. CO<sub>2</sub>-Sourced  $\alpha$ -Alkylidene Cyclic Carbonates: A Step Forward in the Quest for Functional Regioregular Poly(urethane)s and Poly(carbonate)s. *Angewandte Chemie - International Edition* 56, 10394–10398 (2017).
41. Habets, T. et al. Facile construction of functional poly(monothiocarbonate) copolymers under mild operating conditions. *Polym Chem* 13, 3076–3090 (2022).
42. Pal, A., Wong, A. R. & Lamb, J. R. Chemically Recyclable, High Molar Mass Polyoxazolidinones via Ring-Opening Metathesis Polymerization. *ACS Macro Lett* 13, 502–507 (2024).
43. Maes, S. et al. Unprecedented associative exchange in CO<sub>2</sub>-sourced cyclic S,O-acetals based covalent adaptable networks. *Polym Chem* 8, 5255–5446 (2024).
44. Razavi-Esfali, M. et al. Design of functional isocyanate-free poly(oxazolidone)s under mild conditions. *Polym Chem* 15, 1962–1974 (2024).
45. Vidal, F. et al. Designing a circular carbon and plastics economy for a sustainable future. *Nature* 626, 45–57 (2024).
46. Hepburn, C. et al. The technological and economic prospects for CO<sub>2</sub> utilization and removal. *Nature* 575, 87–97 (2019).
47. Jiang, H., Zhao, J. & Wang, A. An efficient and eco-friendly process for the conversion of carbon dioxide into oxazolones and oxazolidinones under supercritical conditions. *Synthesis (Stuttg)* 5, 763–769 (2008).

48. Stubbs, C. J., Khalfa, A. L., Chiaradia, V., Worch, J. C. & Dove, A. P. Intrinsically Recurable Photopolymers Containing Dynamic Thiol-Michael Bonds. *J Am Chem Soc* 144, 11729–11735 (2022).
49. Shi, C., Clarke, R. W., McGraw, M. L. & Chen, E. Y. X. Closing the ‘one Monomer-Two Polymers-One Monomer’ Loop via Orthogonal (De)polymerization of a Lactone/Olefin Hybrid. *J Am Chem Soc* 144, 2264–2275 (2022).
50. Ebert, T., Wollbrink, A., Seifert, A., John, R. & Spange, S. Multiple polymerization-formation of hybrid materials consisting of two or more polymers from one monomer. *Polym Chem* 7, 6826–6833 (2016).
51. Uygun, M., Tasdelen, M. A. & Yagci, Y. Influence of type of initiation on thiol-ene ‘click’ Chemistry. *Macromol Chem Phys* 211, 103–110 (2010).
52. Habets, T. et al. Covalent Adaptable Networks through Dynamic *N,S*-acetal Chemistry: Toward Recyclable CO<sub>2</sub>-Based Thermosets. *J Am Chem Soc* 145, 25450–25462 (2023).
53. Crivello, J. V. The discovery and development of onium salt cationic photoinitiators. *J Polym Sci A Polym Chem* 37, 4241–4254 (1999).
54. Konuray, O., Fernández-Francos, X., Ramis, X. & Serra, À. State of the art in dual-curing acrylate systems. *Polymers (Basel)* 10, 178 (2018).
55. Invernizzi, M., Suriano, R., Muscatello, A., Turri, S. & Levi, M. Near-visible stereolithography of a low shrinkage cationic/free-radical photopolymer blend and its nanocomposite. *J Appl Polym Sci* 137, 48333 (2020).
56. Yagci, Y., Jockusch, S. & Turro, N. J. Photoinitiated polymerization: Advances, challenges, and opportunities. *Macromolecules* 43, 6245–6260 (2010).
57. Pierau, L. et al. Bio-sourced monomers and cationic photopolymerization–The green combination towards eco-friendly and non-toxic materials. *Prog Polym Sci* 127, 101517 (2022).
58. Crosby, A. J. & Lee, J. Y. Polymer nanocomposites: The ‘nano’ effect on mechanical properties. *Polymer Reviews* 47, 217–229 (2007).
59. López-Barrón, C. R., Lu, J., Throckmorton, J. A., Passino, H. & Gopinadhan, M. Microstructure, Viscoelasticity, and Extensional Rheology of Ethylene-Propylene Copolymer Vitrimers. *Macromolecules* 57, 2729–2745 (2024).
60. Espalin, D., Ramirez, J. A., Medina, F. & Wicker, R. Multi-material, multi-technology FDM: Exploring build process variations. *Rapid Prototyp J* 20, 236–244 (2014).
61. Nazir, A. et al. Multi-material additive manufacturing: A systematic review of design, properties, applications, challenges, and 3D printing of materials and cellular metamaterials. *Mater Des* 226, 111661 (2023).
62. Ricarte, R. G., Tournilhac, F. & Leibler, L. Phase Separation and Self-Assembly in Vitrimers: Hierarchical Morphology of Molten and Semicrystalline Polyethylene/Dioxaborolane Malei-mide Systems. *Macromolecules* 52, 432–443 (2019).

63. de Heer Kloots, M. H. P., Schoustra, S. K., Dijksman, J. A. & Smulders, M. M. J. Phase separation in supramolecular and covalent adaptable networks. *Soft Matter* 19, 2857–2877 (2023).
64. Han, H. & Xu, X. Poly(methyl methacrylate)–epoxy vitrimer composites. *J Appl Polym Sci* 135, 1–5 (2018).
65. Dominguez-Alfaro, A. et al. Electroactive 3D printable poly(3,4-ethylenedioxythiophene)-: Graft -poly( $\epsilon$ -caprolactone) copolymers as scaffolds for muscle cell alignment. *Polym Chem* 13, 109–120 (2022).
66. Arrigo, R. & Frache, A. FDM Printability of PLA Based-Materials: The Key Role of the Rheological Behavior. *Polymers (Basel)* 14, 1754 (2022).
67. Boyle, B. M., Xiong, P. T., Mensch, T. E., Werder, T. J. & Miyake, G. M. 3D printing using powder melt extrusion. *Addit Manuf* 29, 100811 (2019).
68. Duty, C. E. et al. Structure and mechanical behavior of Big Area Additive Manufacturing (BAAM) materials. *Rapid Prototyp J* 23, 181–189 (2017).
69. Cruz Sanchez, F. A., Boudaoud, H., Camargo, M. & Pearce, J. M. Plastic recycling in additive manufacturing: A systematic literature review and opportunities for the circular economy. *J Clean Prod* 264, 121602 (2020).
70. Liu, H. et al. Granule-based material extrusion is comparable to filament-based material extrusion in terms of mechanical performances of printed PLA parts: A comprehensive investigation. *Addit Manuf* 75, 103744 (2023).
71. Patti, A. Challenges to Improve Extrusion-Based Additive Manufacturing Process of Thermoplastics toward Sustainable Development. *Macromol Rapid Commun* 2400249 (2024) doi:10.1002/MARC.202400249.
72. Whitesides, G. M. Soft Robotics. *Angewandte Chemie - International Edition* 57, 4258–4273 (2018).





# 3

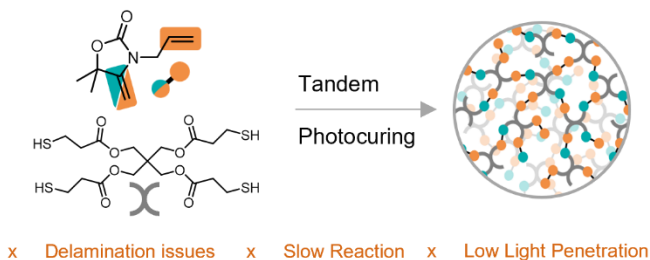
DLP Printing of  
Pluripotent Materials



### 3.1. Abstract

3D printing technology delivers manufacturing of complex objects in a material efficient way; however, single material strategies reduce the scope of its application. Researchers have developed multimaterial strategies (MM) to enable the production of objects with spatially resolved properties. However, these strategies either require complex setups or incur in stability issues. We hypothesised that we could apply the pluripotent materials developed in Chapter 2 as a candidate for MM 3D printing, where a post-printing treatment would enable the introduction of different properties. Herein, we study their photocuring and develop a new curing procedure that enable the production of pluripotent materials in seconds. We explore a variety of reactive and nonreactive diluents and their effect on the pluripotent behaviour of the materials. We find that diluents do not hinder the formation of a phase separated structure and realise the 3D printing of a complex objects.

### A Previous Chapter



### B Chapter 3

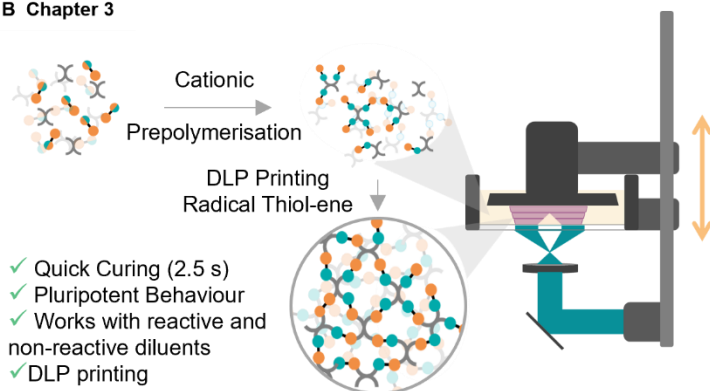


**Figure 3.1.** General Scheme of this chapter. Above the strategy employed in **Chapter 2** is described and its limitations highlighted. Below a, 2-step curing approach developed in this chapter leading to decreased printing times with retention of the pluripotent behaviour.

## 3.2. Introduction

Additive manufacturing has grown to be a centrepiece of research owing to its ability to create high-resolution structures with limited material waste. However, 3D printing is generally using a single material, incurring in inherent limitations given by the properties of the material employed. Hence researchers developed multimaterial (MM) strategies, i.e. strategies that implement the use of multiple materials in a single print, achieving spatially patterned properties, from mechanical to optical.<sup>1</sup> This endows printed samples with diverse properties ranging from environmental adaptability to improved mechanical properties. While MM strategies in FDM are established and commercial,<sup>2</sup> DLP printing sees limited MM applications. This type of 3D printing stands out for its high resolution and excellent interfacial compatibility between different resins since during printing they are connected by covalent bonds, however, it offers a different set of challenges from FDM printing.<sup>3</sup>

Research on MM DLP printing started with resin change systems.<sup>3-5</sup> These sophisticated strategies include systems that automatically move the VAT and clean and dry the part before immersing it in the new resin.<sup>4,6,7</sup> While this technique enabled production of MM prints, its reliance on custom-built printers severely limited its application and lengthened printing times. Furthermore, by using multiple resins, this technique incurs in cross contamination, increasing the amount of waste per print produced and limiting MM only in the Z direction, severely limiting its outlook. While systems relying on pumps for resin switching have been developed, the inherent mixed resin waste produced reduces their applicability.<sup>8</sup>

A strategy that avoids the engineering hurdles of vat switching relies on the chemical design of the formulation to achieve MM prints. By using orthogonal reactions, different networks can be grown from a single

resin in a spatially controlled manner.<sup>9,10</sup> Often, this kind of strategy employs different chromophores that absorb at distinct wavelengths. A prime example is the work from Schwartz *et al.* in which a mixture of acrylates and epoxy resin was used.<sup>11</sup> The acrylates could polymerise by initiation with a long wavelength-absorbing radical photoinitiator (BAPO, 450 nm) while the epoxide portion of the resin could initiate polymerisation only when irradiated at 365 nm by activation of a photoacid generator (triarylsulfonium salt). Similar strategies were also applied to thiol acrylate mixtures in which radical thiol-ene and Michael addition were controlled by spatially activating a radical photoinitiator and a photobase generator.<sup>9</sup> Another variation of this strategy comes from the use of a photobleaching front based on photoswitches in a technique named Small (Solution Mask Liquid Lithography), greatly speeding up printing times.<sup>12</sup> All the strategies described insofar using orthogonal chemistries rely on modification of the printer to enable printing at least at two different wavelengths since most commercially-available printers are single-wavelength.<sup>12</sup>

To avoid the hurdles of multiple wavelengths, grayscale strategies have been developed in place of resin switching. In this strategy, the controlling factor is not the resin formulation, but the light intensity employed for curing the resin. By regulating the light dose that every voxel receives, different crosslinking densities are achieved, returning spatially controlled mechanical properties. Grayscale strategies are executed by changing the slicing parameters; hence they are applicable to commercial printers. With this technique, impressive ranges from 1.4 MPa to 1.2 GPa moduli were achieved.<sup>13</sup> While successful in modulating the mechanical properties, this strategy returns objects that contain potentially hazardous unreacted (meth)acrylate monomers.<sup>14</sup> Furthermore, the difference in shrinkage between regions results in stress accumulation and problems with ageing.<sup>6</sup> In fact, the uncured monomers could still react under light exposure, changing the object's properties over time. Another technique based on different light

dosages was recently proposed by the group of Fors.<sup>15</sup> In this study, a mixture of acrylates and epoxides was employed. In the resin, a photosensitiser (Camphorquinone) and a photoacid generator were added together with a buffer. When irradiated by light, the photosensitiser activated the photoacid and consequently initiated the polymerisation of the acrylates. The acidic species immediately reacted with the basic buffer. Cationic polymerisation could only be achieved after long exposure, affording a handle for controlling the mechanism by light dosage. This strategy offers the possibility to modulate the properties of the printed material without modifying the printer, however, it still suffers from the same limitation as grayscale strategies, i.e., the residual unreacted monomers trapped in the material led to ageing and environmental concerns.

In this chapter, we apply the strategy of pluripotent materials developed in the previous chapter to DLP printing, with the objective of achieving multiple properties from a single material. We first explore the printability of the resin developed in Chapter 2 and realise their limitations for DLP printing. We develop a new curing strategy that enables the DLP printing of pluripotent materials and study their behaviour. With this strategy, we aimed to avoid the formation of organogels as the final product and streamline the production of printed objects with varied properties from a single material.

## 3.3. Results and Discussion

### 3.3.1. 3D printing of tandem formulation

#### 3.3.1.1. First study with ITX/IOD

Encouraged by the tandem photocuring <sup>1</sup>H NMR kinetics investigated in Chapter 2, we investigate their potential for DLP 3D printing. In order to

thoroughly characterise the curing kinetics in bulk, we employed three different techniques: real-time Fourier transform infrared spectroscopy (RT-FTIR), photo-differential scanning calorimetry (Photo-DSC) and time-sweep photo-rheology. As can be seen in Figure 3.2-a, upon light irradiation, the reaction started immediately as observed by the reduction of both the  $\text{C}=\text{C}_{\text{exo}}$  stretching ( $1684\text{ cm}^{-1}$ ) and the  $\text{C}=\text{C}_{\text{allyl}}$  stretching ( $1648\text{ cm}^{-1}$ ) resonances in the RT-FTIR (Figure 3.2-a) when using 0.5 wt% of both ITX and IOD. While maintaining stoichiometric amounts of -SH and double bonds in the resin, we explored different ratios of ITX and IOD in order to understand how that would influence the curing kinetics. From now on, the resulting resins will be named  $\text{T}_{\text{S}_n}\text{ITX}_m\text{IOD}_y$  where  $n$  is the functionality of the thiol employed,  $x$  is the weight percentage of ITX and  $y$  is the weight percentage of IOD employed. While decreasing the ratio IOD ITX from 4:1 to 1:1 ( $\text{T}_{\text{S}_4}\text{ITX}_2\text{IOD}_{0.5}$ ,  $\text{T}_{\text{S}_4}\text{ITX}_2\text{IOD}_1$ ,  $\text{T}_{\text{S}_4}\text{ITX}_2\text{IOD}_2$ ) did not strongly influence the kinetics, adding an excess of IOD ( $\text{T}_{\text{S}_4}\text{ITX}_2\text{IOD}_4$ , ratio 1:2) clearly showed slower kinetics (Figure 3.2-b). This is in line with the mechanism of activation of IOD, which requires a photoinduced electron transfer between IOD and the excited ITX to liberate the active species.<sup>16-21</sup> A similar kinetics was observed when using BAPO as initiator ( $\text{R}_{\text{S}_4}\text{BAPO}_{0.5}$ ), indicating that the bulk reactivity is markedly different than the reactivity in solution presented in **Chapter 2** as BAPO was provided slower reaction rates since the exovinylene double bond reacted slowly in radical thiol ene.<sup>22</sup> Considering that the reaction reached conversions above 80% below a minute (390 nm LED, 20 mW/cm<sup>2</sup>), we expected to be able to employ the tandem photocuring to 3D print, introducing a new cationic reaction in the world of DLP printing.<sup>23-25</sup> Further insights into the kinetics of the reaction came from PhotoDSC studies,<sup>26,27</sup>  $\text{T}_{\text{S}_4}\text{ITX}_2\text{IOD}_2$  had a  $t_{\text{max}}$  of 13 s. The trend observed by RT-FTIR was seen in PhotoDSC as well with slower reaction using excess IOD ( $\text{T}_{\text{S}_4}\text{ITX}_2\text{IOD}_4$ ,  $t_{\text{max}} = 18.2\text{ s}$ ) or lower amount of photoinitiators ( $\text{T}_{\text{S}_4}\text{ITX}_{0.5}\text{IOD}_{0.5}$   $t_{\text{max}} = 20.0\text{ s}$ ). The same trend was followed by the enthalpy of curing with  $\text{T}_{\text{S}_4}\text{ITX}_2\text{IOD}_2$  showing the



highest enthalpy of 193 J/g when compared to T\_S4\_ITX<sub>2</sub>\_IOD<sub>4</sub> and T\_S4\_ITX<sub>0.5</sub>\_IOD<sub>0.5</sub> that had an enthalpy of 170 J/g and 163 J/g, respectively. This implies that T\_S4\_ITX<sub>2</sub>\_IOD<sub>2</sub> affords a more complete curing, in accordance with RT-FTIR analysis (Figure 3.2-c).

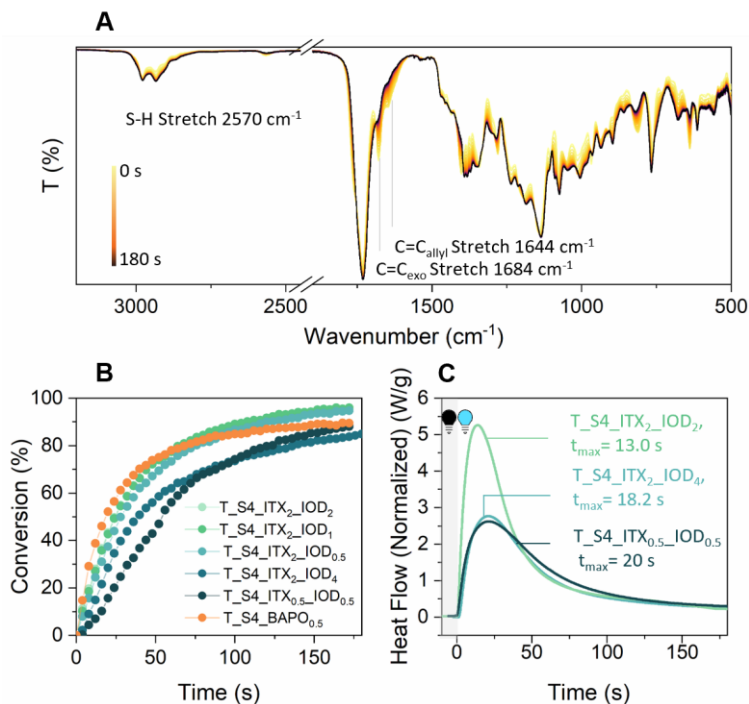


**Figure 3.2.** a) RT-FTIR monitoring of the photocuring reaction of T\_S4\_ITX<sub>0.5</sub>\_IOD<sub>0.5</sub> with a 390nm LED with a power of 20  $\text{mW}/\text{cm}^2$ ; b) Conversion vs time as calculated from RT-FTIR monitoring; c) Photo-DSC traces of T\_S4\_ITX<sub>0.5</sub>\_IOD<sub>0.5</sub>, T\_S4\_ITX<sub>2</sub>\_IOD<sub>4</sub>, T\_S4\_ITX<sub>2</sub>\_IOD<sub>2</sub> photocured with a LED centred at 390 nm with a power of 20  $\text{mW}/\text{cm}^2$ .

We set off to explore the photo-rheological behaviour of T\_S<sub>4</sub>\_ITX<sub>2</sub>\_IOD<sub>2</sub> since it showed the fastest kinetics in both RT-FTIR and PhotoDSC. Unfortunately, the photo-rheology kinetics could not be measured as the resin absorbed too much light (Figure S3.1). We found that the resin cured on the bottom plate but the cured layer did not reach the upper geometry, rendering the registration of the rheological behaviour impossible. Expecting a lower light absorption, we tried analysing the photo-rheological kinetics of T\_S<sub>4</sub>\_ITX<sub>0.5</sub>\_IOD<sub>2</sub> and could measure a gel point of 225 s (Figure 3.3-a). Together with photo-rheological information, we measured the viscosity of the resin to be 0.08 Pa·s (Figure 3.3-b), ideal for DLP printing as viscosities below 10 Pa·s are suitable for DLP printing applications. Furthermore, the resin was stable for multiple hours, with a slight increase from 0.08 to 0.24 Pa·s in the course of 6 hrs (Figure 3.3-c).

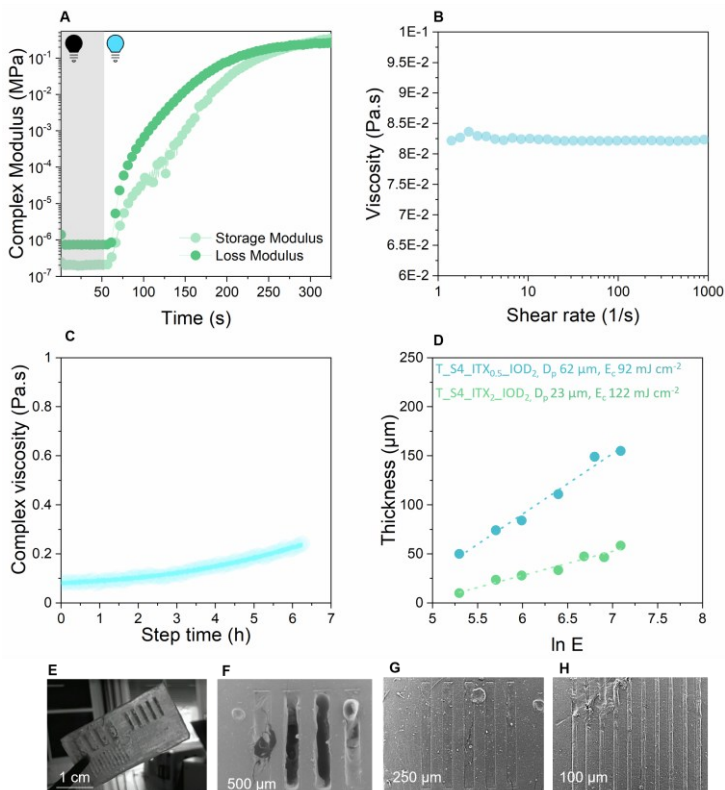


**Figure 3.3.** a) Photo-rheology trace of  $T\_S4\_ITX_{0.5\_IOD_2}$  (365nm LED with a power of 20 mW/cm<sup>2</sup>); b) Amplitude sweep Rheometry of  $T\_S4\_ITX_{0.5\_IOD_2}$  showing a viscosity of 0.082 Pa·s; c) Time sweep rheology monitoring the evolution of the complex viscosity over time (6 hrs); d) Jacobs Working curve of  $T\_S4\_ITX_{0.5\_IOD_2}$  and  $T\_S4\_ITX_{2\_IOD_2}$ ; e) Digital photograph of a structure 3D printed using  $T\_S4\_ITX_{0.5\_IOD_2}$  (Burn in 60 s, Layer 40 s) and SEM photographs of the f) 500 μm grooves g) 250

µm grooves and h) 100 µm grooves, a noticeable overcuring can be observed in all SEM micrographs, accentuated in smaller features.

With this in mind, we analysed the curing depth ( $D_p$ ) and critical energy ( $E_c$ ) by registering the Jacob's working curve of the resins. As expected, both T\_S4\_ITX<sub>0.5</sub>\_IOD<sub>2</sub> and T\_S4\_ITX<sub>2</sub>\_IOD<sub>2</sub> had very low  $D_p$  (62 and 23 µm, Figure 3.3-d). This was accompanied by high critical energy, indicating that these resins would require long irradiation times to form layers. We tried 3D printing T\_S4\_ITX<sub>0.5</sub>\_IOD<sub>2</sub> with limited success. The optimal irradiation times were found to be a burn-in of 60 s (4 layers 50 µm) and layer exposure of 40 s with a power of 20 mW/cm<sup>2</sup> with a 380 nm LED. These times were needed to avoid delamination issues of the resin, a common defect in DLP printing. Further analysis of the attainable resolution showed that these long irradiation times gave clear overcuring defects, with the lines below 250 µm being completely cured over (Figure 3.3-e,f,g,h). This was accompanied by the resin sticking strongly to the bottom transparent window of the 3D printer (FEP film), resulting in delamination of the print (figure S3.2) and deformation of the window after few trials of printing with these resins. Hence, it was clear that this type of photoinitiator was not working well with bottom-up type of printers, the most commonly used in the world of DLP printing.

### 3.3.1.2. Changing the Photoinitiating System

Two clear issues needed to be addressed to render the resin printable; first, the penetration depth had to be increased to enable curing of thicker layers, second the adhesion of the resin to the FEP film had to be reduced. In order to address the low penetration depth, we changed the photoinitiating system. We identified two different strategies, one was to exchange ITX, responsible for the high absorption at 380 nm (the working wavelength at which the Asiga max UV's LED are centred at) for the less absorbing ethyl anthraquinone (Figure 3.4-a, ANT, selected the

ethyl derivative to have solubility as Anthraquinone is not soluble in **AlIOx**).<sup>28</sup> The other was to change the photoinitiating system from bimolecular to monomolecular, employing a commercially available photoacid that could absorb at 380 nm (Sylanto 7-MS, SYMS) (Figure 3.4-a). We expected this monomolecular photoacid to enable faster liberation of the acidic species as the electron transfer occurs intramolecularly, not intermolecularly as for multicomponent photoinitiating systems.<sup>16,29-32</sup>

Encouragingly, the photo-rheology using ANT (T\_S4\_ANT2\_IOD<sub>2</sub>) returned a clear gel point at 142 s mark, showing that using this less-absorbing photosensitiser addressed the issue of light penetration (Figure 3.4-b). When measuring the RT-FTIR kinetics of photocuring using both 2 and 1 wt% of the two photoinitiators, we observed very similar behaviours as the ITX/IOD system (Figure 3.4-c). We did not observe a noticeable acceleration of the reaction using the monomolecular system as we expected. Notwithstanding this, SYMS underwent noticeable photobleaching, resulting in transparent materials when compared to both ITX/IOD and ANT/IOD systems (Figure S3.3).

While SYMS seemed well performing, storage for longer than 1 h in dark conditions at RT gave stability issues, with a noticeable increase in viscosity, hence making this system unsuitable for the long printing times required for DLP printing.<sup>32</sup> This observation was further supported by PhotoDSC measurements in which the enthalpy of reaction was noticeably smaller than the one from ITX/IOD and ANT/IOD (Figure 3.4-d,e). Gratifyingly, the ANT/IOD system had both lower  $t_{\text{max}}$  than ITX/IOD and higher enthalpy of reaction, indicating that a more complete curing was achieved. We also noticed that the PhotoDSC curve had two different peaks, a sharp one given by the radical reaction that is faster and a second one from the slower cationic thiolene reaction, indicating a mismatch in velocity of the two reactions (Figure 3.3-d).<sup>22,33</sup>

The Jacobs Working Curve of T\_S<sub>4</sub>\_ANT<sub>2</sub>\_IOD<sub>2</sub> had a stark difference with curves from the ITX/IOD system (Figure 3.4-f). As expected, the D<sub>p</sub> was much higher (324 vs 23 μm for the same wt% of photoinitiating system) while with higher E<sub>c</sub> (122 vs 356 for ANT/IOD and ITX/IOD, respectively). This indicated that we could cure much thicker layers thanks to the increased light penetration, however the high E<sub>c</sub> meant that long irradiation time were needed to do so. We could print a test structure to assess resolution with 100 μm layers with a burn-in of 50 s (4 layers) and a layer of 45 s, effectively speeding up the printing times by a factor of two. The resolution was enhanced thanks to the reduced curing times, with lines up to 250 μm being well resolved, while smaller lines showed clear overcuring (Figure 3.4-g). However, the issue of adhesion to the FEP film was not solved, with the resin sticking strongly and deforming the FEP film after few trials. We tried reducing this issue by spraying a silicon-based lubricant spray on the FEP film with little success. When printing any structure more complex than the structure used for resolution studies, we incurred in problems of delamination rendering the resin difficult to 3D print.

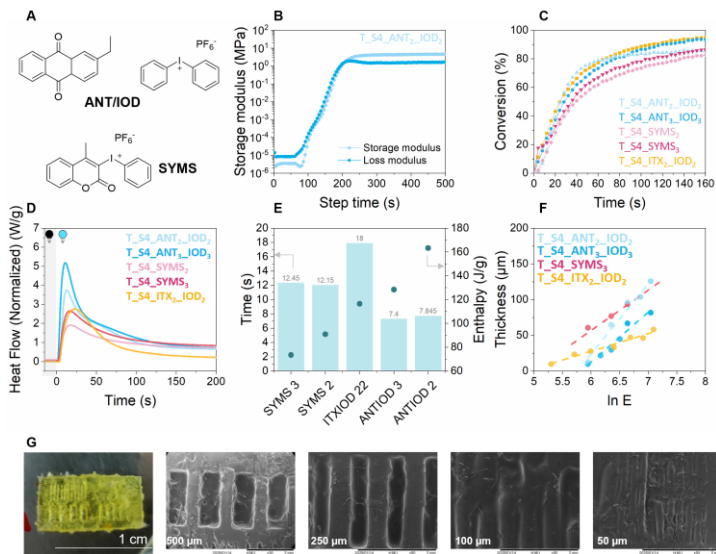


**Figure 3.4.** a) Structure of the ANT/IOD system and SYMS ; b) Photo-rheology of T\_S4\_ANT<sub>2</sub>\_IOD<sub>2</sub>; c) RT-FTIR kinetics of photocuring of resins employing ANT/IOD and SYMS (T\_S4\_ANT<sub>2</sub>\_IOD<sub>2</sub>, T\_S4\_ANT<sub>3</sub>\_IOD<sub>3</sub>, T\_S4\_SYMS<sub>2</sub>, T\_S4\_SYMS<sub>3</sub>) and T\_S4\_ITX<sub>2</sub>\_IOD<sub>2</sub> for comparison; d) PhotoDSC of resins employing ANT/IOD and SYMS (T\_S4\_ANT<sub>2</sub>\_IOD<sub>2</sub>, T\_S4\_ANT<sub>3</sub>\_IOD<sub>3</sub>, T\_S4\_SYMS<sub>2</sub>, T\_S4\_SYMS<sub>3</sub>) and T\_S4\_ITX<sub>2</sub>\_IOD<sub>2</sub> for comparison; e) column plot of t<sub>max</sub> and enthalpy of curing derived from PhotoDSC curves (T\_S4\_ANT<sub>2</sub>\_IOD<sub>2</sub>, T\_S4\_ANT<sub>3</sub>\_IOD<sub>3</sub>, T\_S4\_SYMS<sub>2</sub>, T\_S4\_SYMS<sub>3</sub>) and T\_S4\_ITX<sub>2</sub>\_IOD<sub>2</sub> for comparison; f) Jacobs working curves of T\_S4\_ANT<sub>2</sub>\_IOD<sub>2</sub> (Dp=109 μm Ec= 356 mJ/cm<sup>2</sup>), T\_S4\_ANT<sub>3</sub>\_IOD<sub>3</sub> (Dp=70 μm Ec= 346 mJ/cm<sup>2</sup>), T\_S4\_SYMS<sub>3</sub> (Dp=325 μm Ec= 170 mJ/cm<sup>2</sup>) and T\_S4\_ITX<sub>2</sub>\_IOD<sub>2</sub> (Dp=22 μm Ec= 121 mJ/cm<sup>2</sup>); g) Grooved 3D printed structure of T\_S4\_ANT<sub>2</sub>\_IOD<sub>2</sub> with SEM images of the four quadrants bearing grooves of 500, 250, 100 and 50 μm.

### 3.3.2. Developing a 2-stage curing

We hypothesized that the issues of adhesion on the FEP film were mainly caused by the asymmetrical reactivity of **AlLOx**. In fact, the allyl bond reacted faster than the exovinylene double bond, forming first a gelled matrix and then a solid (Figure 3.5-a). This rendered the printing difficult as the partially cured layer would adhere to the FEP film. Hence, we thought that making the reactivity symmetrical could reduce this issue. In order to do so, we split the tandem curing in two. We reacted the exovinylene double bond cationically before curing the resin radically using BAPO. While this strategy would ensure the presence of (almost) solely allyl bonds available for radical thiol ene curing, it strongly increased the viscosity of the resin. Hence, using reactive or non-reactive diluents became essential to ensure printability.

As can be seen in Figure 3.5-b when **AlLOx** and **S4** were mixed in an equimolar ratio between -SH and double bond in presence of 1 mol% of MSA, a stark reduction of the **AlLOx**'s CH<sub>3</sub> signal (1.48 ppm) was observed by <sup>1</sup>H NMR attesting for a 95% conversion of the exovinylene double bond (Figure 3.5-b). With this, we observed the appearance of three singlets (1.55, 1.45, 1.43 ppm) coherent with the expected structure (See Figure S3.4 for further characterisation). The transparent mixture increased in viscosity. FTIR analysis led to the same conclusion, with a stark reduction of the C=C<sub>Exo</sub> resonance (1682 cm<sup>-1</sup>) upon addition of MSA (0.5 wt%) (Figure 3.5-c). This is in line with what was observed in **Chapter 2**, in which the cationic thiol ene reaction is selective towards the exovinylene double bond, leaving the allyl double bonds unreacted. After photocuring *via* radical thiol ene (BAPO 0.5 wt%, 390 nm, 20 mW/cm<sup>2</sup>), the material was completely cured with a high gel content of the material (93±1%) and low swelling (148±3%) in THF. The resulting resin, after addition of a photoinitiator (BAPO, 0.5 wt%), showed increased curing kinetics as exemplified by its RT-FTIR



kinetics (Figure 3.5-d), reaching 75% conversion in 10 s. Additionally, its Photo-DSC shows a stark decrease in  $t_{\max}$  from 8 s of T\_S4\_ANT<sub>2</sub>\_IOD<sub>2</sub> to 6 s of C\_S4\_BAPO<sub>0.5</sub> with similar enthalpy of curing when compared to previously developed resins (125 J/g, Figure 3.5-e). The mDSC trace of the resulting cured material (C\_S4\_BAPO<sub>0.5</sub>) still showed the two key parameters for the development of pluripotent materials. It presented a  $T_g$  above room temperature (34 °C) and the presence of a  $T_{UT}$  (82 °C), a parameter that indicates the presence of two different phases (Figure 3.5-f).<sup>34,35</sup> This indicated that the cationic and radical reactions did not need to happen at the same time for the formation of a phase-separated structure. The faster curing kinetics, coupled with the retention of the pluripotent material behaviour encouraged us to further explore the DLP printing of these resins.

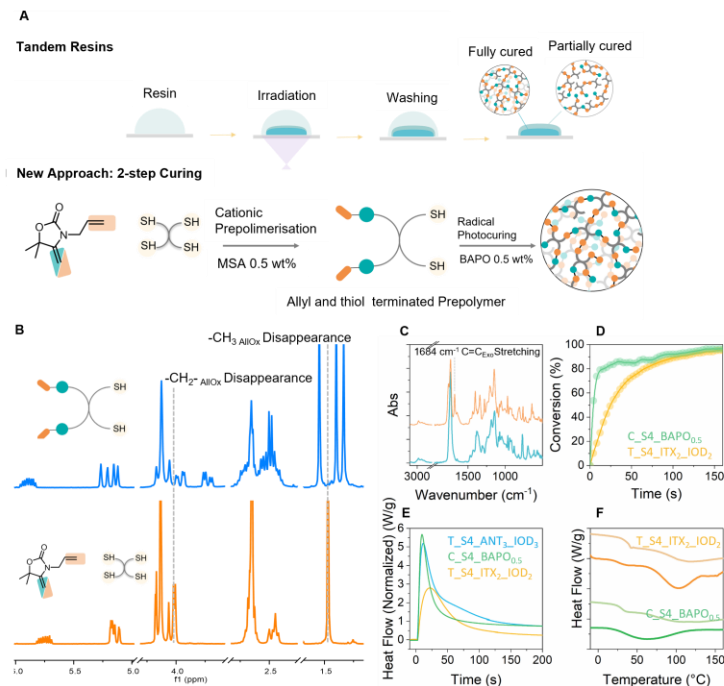


**Figure 3.5.** a) Scheme of the limitations of tandem resins and alternative 2-step curing procedure b)  $^1\text{H}$  NMR of Allox/S4 mixture (orange) and its cationic prepolymerisation (blue); c) FTIR of cationic prepolymerisation of Allox and S4; d) RT FTIR photocuring kinetics of the prepolymerised  $\text{C\_S4\_BAPO}_{0.5}$  compared to  $\text{T\_S4\_ITX}_2\text{\_IOD}_2$ ; e) PhotoDSC photocuring kinetics of  $\text{C\_S4\_BAPO}_{0.5}$  compared to  $\text{T\_S4\_ANT}_2\text{\_IOD}_2$  and  $\text{T\_S4\_ITX}_2\text{\_IOD}_2$ ; f) mDSC of  $\text{C\_S4\_BAPO}_{0.5}$  compared to  $\text{T\_S4\_ITX}_2\text{\_IOD}_2$ . All formulations had an equimolar ratio between SH and double bonds.

### 3.3.2.1. Screening reactive and non-reactive diluents for pluripotency

The high viscosity did not make this new resin suitable for 3D printing. Hence, we first formulated it using a series of reactive diluents and nonreactive diluents. Addition of diluents is a common practice to lower the viscosity of 3D printing resins.<sup>36</sup> For this study, we selected small reactive molecule diluents that had more than two functionalities per molecule and would not participate in the cationic thiol-ene prepolymerisation reaction. Specifically, we aimed at; TrivinylCyclohexane (TVC), Diallyl Terephthalate (DT), Divinylbenzene (DVB), DivinylSulfone (DVS) and Diallyl Maleate (DM). We avoided using (meth)acrylates as their homopolymerisation could have an unwanted impact on the formation of a phase-separated structure. As a non-reactive diluent, we employed acetone as it is easily removed from the prints by simple drying at room temperature.<sup>36</sup> From now, the resins are named C\_S<sub>n</sub>\_ReactiveDiluent<sub>x</sub>\_BAPO<sub>y</sub> (with n being the functionality of the thiol and x the molar percentage of reactive diluent and y being the weight percentage of BAPO).

A main concern of adding diluents to the resin was their influence on the pluripotent behaviour of the material. We started to screen different amounts of reactive diluents using DT. We started our investigation from reactive diluents as these are included in the final print, leading to reduced shrinkage and the possibility to lower the final price of the resin. When employing 30% DT we could observe that the double bond resonance in FTIR completely disappeared, indicating full curing (Figure S3.5-a). mDSC evidenced a clear decrease in  $T_g$  (from 39 to 22) but the  $T_{UT}$ , together with an endothermic peak was still retained, indicating that the addition of a reactive diluent did not interfere strongly with the formation of two phases in this kind of materials (Figure S3.5-b). While this statement holds for C\_S<sub>4</sub>\_DT<sub>50</sub>\_BAPO<sub>0.5</sub>, a further increase to C\_S<sub>4</sub>\_DT<sub>70</sub>\_BAPO<sub>0.5</sub> evidenced a single  $T_g$ , implying

that the phase-separated structure was lost (Figure S3.5-b). Furthermore, increasing the amount of DT in the resin lowered the  $T_g$  sensibly, from 22 °C for a 30% content of DT to 12 to 5 °C for a 50% and 70% content in DT, respectively. The same trend was followed by the  $T_{UT}$  that decreased from 98 to 60 °C when increasing the mole percentage of DT from 30 to 50%. This first investigation showed that the addition of the reactive diluent did not disrupt the formation of two phases when the diluent was used in percentages below 70%, indicating that retaining the connectivity between dynamic bonds is essential for the development of two-phase systems.<sup>37</sup> We set on to explore different diluents to find one that offered a material with a  $T_g$  above RT while still retaining a phase-separated morphology.

All reactive diluents explored gave materials that cured quickly and with an FTIR spectra that showed complete curing (Figure S3.5-c,e,g, i). While the FTIR seemed promising, the mDSC evidenced  $T_g$  lower than rt when used in mol% of 30, 40 and 50 for DM, DVS and DVB as shown in Figure 3.6-b, Figure S3.5-d,f,h,j. The only material that had  $T_g$  above RT (34 °C) was C\_S4\_TVC30\_BAPO<sub>0.5</sub> (Figure 3.6-c), however, its viscosity was still very high. Further increase in TVC content resulted in immiscibility of the components and gave an opaque liquid. Hence, a small percentage of acetone was added to homogenise the mixture (from now on named C\_S4\_TVC30\_Ace5\_BAPO<sub>0.5</sub>, 5% Acetone added). The AFM of the material after photocuring evidenced the presence of phase separation, with spherical domains populating the surface (surface coverage of 2%) and with a median diameter of 50 nm (Figure 3.6-d,e), smaller than the material obtained by tandem photocuring in **Chapter 2** (84 nm).

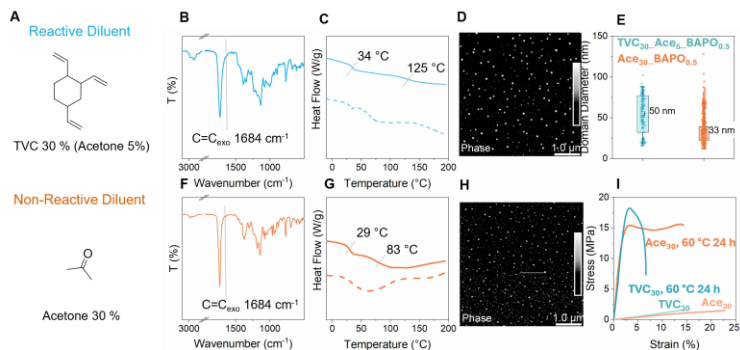


**Figure 3.6.** a) Structure of reactive diluent (TVC) and non-reactive diluent (Ace) and their percentage in the formulation presented in this image; b) FTIR spectra of photocured  $C_{S_4}TVC_{30}Ace_{5}BAPO_{0.5}$ ; c) mDSC trace of photocured  $C_{S_4}TVC_{30}Ace_{5}BAPO_{0.5}$  evidencing the presence of both  $T_g$  and  $T_{UT}$ ; d) AFM of photocured  $C_{S_4}TVC_{30}BAPO_{0.5}$ ; e) Box overlap graph of the distribution of domain size of  $C_{S_4}TVC_{30}Ace_{5}BAPO_{0.5}$  (Blue) and  $C_{S_4}Ace_{30}BAPO_{0.5}$  (Orange); f) FTIR spectra of photocured  $C_{S_4}Ace_{30}BAPO_{0.5}$ ; g) mDSC trace of photocured  $C_{S_4}Ace_{30}BAPO_{0.5}$  evidencing the presence of both  $T_g$  and  $T_{UT}$ ; h) AFM of photocured  $C_{S_4}Ace_{30}BAPO_{0.5}$ ; i) Stress-strain curves of  $C_{S_4}TVC_{30}Ace_{5}BAPO_{0.5}$  and  $C_{S_4}Ace_{30}BAPO_{0.5}$  before and after heat treatment at  $60\text{ }^{\circ}C$  for 24 h.  $C_{S_4}TVC_{30}Ace_{5}BAPO_{0.5}$  was shortened to  $TVC_{30}Ace_{5}$  and  $C_{S_4}Ace_{30}BAPO_{0.5}$  was shortened to  $Ace_{30}$  to save space.

While exploring reactive diluents, we started a parallel investigation on acetone as a non-reactive diluent (Figure 3.6-a). By using 30 wt% acetone, we could prepare a low-viscosity resin that cured completely within 60 s of irradiation (Figure 3.6-f). Its mDSC, after acetone removal (vacuum overnight), showed a  $T_g$  of  $29\text{ }^{\circ}C$  and a  $T_{UT}$  of  $83\text{ }^{\circ}C$  (Figure 3.6-g) showing that a non-reactive diluent did not obstruct the formation of phase-separated domains and did not strongly change the curing kinetics. The AFM of  $C_{S_4}Ace_{30}BAPO_{0.5}$  showed domains of

decreased size when compared to tandem materials, with a median of 33 nm (Figure 3.6-e,h).

We then studied the possibility to vary the mechanical properties of the material by heat treatment, to quantify the range of mechanical properties attainable. Both materials (C\_S4\_TVC<sub>30</sub>\_Ace<sub>5</sub>\_BAPO<sub>0.5</sub> and C\_S4\_Ace<sub>30</sub>\_BAPO<sub>0.5</sub>) showed a rigidification after heat treatment at 60 °C (Figure 3.6-i), further supporting the hypothesis that reactive diluent did not disrupt the pluripotent behaviour. Accordingly, the Young's Modulus of C\_S4\_Ace<sub>30</sub>\_BAPO<sub>0.5</sub> was tuned from 5.4±0.9 MPa to 985±123 MPa depending on the thermal treatment, while the material containing TVC was more rigid, going from 12±0.3 MPa to a modulus of 1180±95 MPa. The range of achievable properties was lower compared to the material prepared using the Tandem photocuring procedure from **Chapter 2**. This may be due to less efficient curing, as some exovinylene double bonds remained unreacted during prepolymerisation and could not react during photocuring due to the rapid increase in viscosity. Another hypothesis could be that the different connectivity of the network could lead to macroscopically different mechanical properties. However, further characterisation should be carried out to rationalise this difference in properties. Furthermore, the drying step, in which acetone was removed by drying under vacuum, could produce bubbles in the dogbone samples, giving rise to defects that negatively bias the mechanical properties values. Nonetheless, the increase in modulus was still more than 100x for both materials, confirming that this strategy is valuable for the preparation of pluripotent materials.

### 3.3.3. DLP printing by 2-Stage Curing

Having spotted two formulations that retained the pluripotent behaviour while having a viscosity that allowed printing, we set on to investigate their additive manufacturing. Encouraged by the quick and

complete curing kinetics of C\_S4\_Ace<sub>30</sub>\_BAPO<sub>0.5</sub>, we set off to explore its printability. The Jacobs Working Curve immediately showed promising results when compared to the previously developed tandem resins. In fact, the  $D_p$  was much higher (260  $\mu\text{m}$  for C\_S4\_Ace<sub>30</sub>\_BAPO<sub>0.5</sub>, Figure 3.7-a, Entry 1) together with a very low  $E_c$  (1.02  $\text{mJ}/\text{cm}^2$ ), meaning that curing thick films could be carried out in fractions of a second (Figure 3.7-a,b). This resin could cure a 200  $\mu\text{m}$  layer with an exposure of 0.5 s with a nonlinear behaviour, making the Jacobs curve's results inaccurate.<sup>38</sup> To regulate the  $D_p$ , with the final objective of improving the Z resolution in the prints, we employed a photoabsorbing dye (Sudan I) in both 0.05 wt% and 0.1 wt%. This resulted in slower photopolymerization, with an increase of  $E_c$  from 1.02 to 18.5 and 18.7 for 0.05 and 0.1 wt% content in Sudan I, respectively. Together with this, we observed a reduction of  $D_p$ , from 350 to 260 for 0.05 wt% Sudan I (Figure 3.7-a, Entry 2,3). Further increase in content of Sudan I (0.1 wt%) gave a  $D_p$  of 140  $\mu\text{m}$ , ideal for 3D printing (Figure 3.7-a,b). Together with this, C\_S4\_TVC<sub>30</sub>\_BAPO<sub>0.5</sub> (with 0.1 wt% Sudan I) showed a similar  $D_p$  to C\_S4\_Ace<sub>30</sub>\_BAPO<sub>0.5</sub>, however, it showed higher  $E_c$  (66  $\text{mJ}/\text{cm}^2$ ) meaning that it required longer times to form layers (Figure 3.7-a, Entry 4, Figure 3.7-b). We could print a structure for optimisation of the resolution with C\_S4\_Ace<sub>30</sub>\_BAPO<sub>0.5</sub> by using a burn-in exposure of 3.5 s and a layer exposure of 2 s (Figure 3.7-c). The 100  $\mu\text{m}$  grooves were well defined, with vertical walls, sharp edges and no signs of overcuring (Figure 3.7-d). Satisfyingly, we did not observe the adhesion problem that previous **AlIOx**-based resin had. C\_S4\_TVC<sub>30</sub>\_Ace<sub>5</sub>\_BAPO<sub>0.5</sub> could also be printed similarly, however, the division between layers was found to be more evident, hence further optimisation of the printing parameters is probably needed (Figure S3.6). We employed C\_S4\_Ace<sub>30</sub>\_BAPO<sub>0.5</sub> to 3D print a gyroid cube with good resolution using a layer exposure time of only 2 s (Table S3.1, Figure 3.7-e), a complex structure that can be manufactured only by additive manufacturing.

The ability to 3D print pluripotent materials by DLP printing opens the door to single-material, multiple properties strategies in DLP printing, avoiding the presence of unreacted monomers in the 3D printed object.

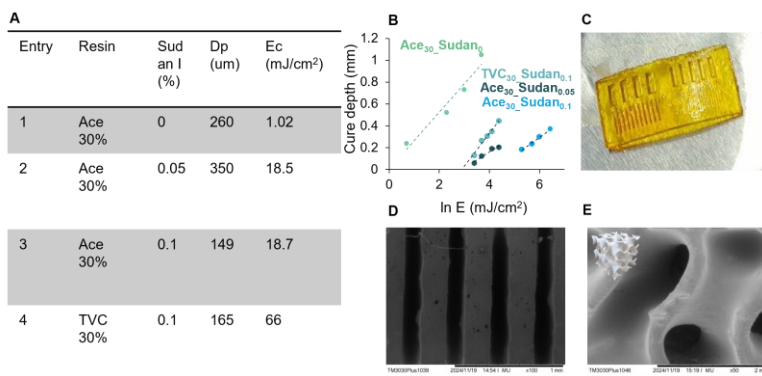


**Figure 3.7.** a) Table containing the resins studied for 3D printing application and their Jacob/s curve parameters; b) Jacob's curves of resin containing Sudan I as photoabsorber; c) 3D printed structure for optimisation of resolution; d) SEM photograph of 3D printed structure for optimisation of resolution; e) SEM picture of a 3D printed Gyroid cube, internal structure using C\_S4\_Ace<sub>30</sub>BAPO<sub>0.5</sub>.

## 3.4. Conclusions

In this Chapter, we introduced new strategies to prepare pluripotent materials and achieve their additive manufacturing by DLP printing. First, we evaluated the possibility to use the tandem formulations developed in **Chapter 2**, however, we encountered problems of limited light penetration, together with slow kinetics and strong adhesion to the bottom window of the printer. We attempted to circumvent these issues by using both a monomolecular photoacid and a different



photosensitiser (anthraquinone). This returned resin with a better light penetration that effectively sped up their 3D printing by 2x times. However, the issue of adhesion was still present, hence, we changed strategy and developed a 2-step curing procedure, in which we first prepolymerised the formulation by cationic thiol-ene reaction and then we used the faster radical thiol ene for photocrosslinking. This returned curing times of few seconds, compared to 60 seconds required to cure previous resins. We regulated the resin viscosity with a variety of non-reactive and reactive diluents finding that both did not disrupt the formation of a phase-separated structure liable to develop a pluripotent behaviour. However, only 2 resins had adequate viscosity, together with a  $T_g$  higher than RT, C\_S4\_Ace<sub>30</sub>\_BAPO<sub>0.5</sub> and C\_S4\_TVC<sub>30</sub>\_Ace<sub>5</sub>\_BAPO<sub>0.5</sub>. These resins could form layers with great resolution in less than 6 seconds, enabling the 3D printing of a complex gyroid cube in a quick manner. Further studies should focus on the influence of the phase separation on mechanical properties, together with more studies on the range of attainable properties by this 2-step strategy. With this, studies enabling the localisation of heat by more precise means, such as electrothermal or photothermal effects, should be carried out, in order to expand the applicability of the materials developed in this study. This would enable precise spatial control of the mechanical properties, with potential impacts in the field of soft robotics, compliant mechanisms and metamaterials.

## 3.5. Materials and Methods

### 3.5.1. Materials

Ethyl Anthraquinone (Sigma, 97%), Sylanto 7 MS (Synthos S.A.), Phenylbis(2,4,6-trimethylbenzoyl) phosphine oxide (BAPO, Ciba), Methanesulfonic acid (Sigma, >99%), Pentaerythritol tetrakis(3-mercaptopropionate) (S4, Sigma, ≥95), Triethylamine (TEA, Sigma,

99.5%), Sudan I (TCI, 95%) and all solvents were used without further purification. The preparation of **AlIOx** was described in **Chapter 2 (Section 2.4.1)**

### 3.5.2. Methods

**Nuclear magnetic resonance (NMR) spectroscopy.**  $^1\text{H}$ -NMR analyses were performed on a Bruker Avance 300 MHz spectrometer at 25 °C in the Fourier transform mode using  $\text{CDCl}_3$  or  $\text{DMSO}-d_6$  as solvents.

**Gel content (GC).** Films prepared as described in the experimental section were cut into rectangular shapes and weighted ( $m_1$ ) before immersing 48 h in tetrahydrofuran. After weighing, the swelled films ( $m_2$ ) were dried in a vacuum oven at 60 °C for 24 h. The films were weighed once again ( $m_3$ ). Swelling (SI) and Gel content (GC) were calculated with equations 2 and 3, respectively:

$$SI = 100 * m_2 / m_1 \quad (2)$$

$$GC = 100 * m_3 / m_1 \quad (3)$$

**Tensile tests** were carried out on dogbone samples (see Preparation of Films below) (ASTM D638 TYPE V) in an Instron 5569 tensile tester (Instron, Norwood, MA, USA). Young's modulus, Tensile strength ( $\sigma_t$ ), Yield strength ( $\sigma_y$ ), and strain at break ( $\epsilon_b$ ) were determined using Bluehill software from the load-displacement curves at a crosshead speed of 10 mm/min. A minimum of three tensile specimens were tested for each reported value.

**Fourier Transform Infrared Spectroscopy (FT-IR) spectra** were recorded on a Nicolet iS20 Spectrometer using Attenuated Total Reflection (ATR) at a resolution of  $4\text{ cm}^{-1}$  and a total of 32 interferograms. The same instrument was used to acquire real-time FTIR data. Spectra were acquired every 5 seconds by averaging 4 spectra.

**Modulated Differential Scanning Calorimetry** was performed on a TA Instruments DSC 250 calibrated with indium, and the curves were analyzed using the Trios software. A period of 60 seconds with an amplitude of  $1\text{ }^{\circ}\text{C}$  was used. A ramp of  $2\text{ }^{\circ}\text{C}$  per minute from  $-20\text{ }^{\circ}\text{C}$  to  $200\text{ }^{\circ}\text{C}$ .

**Photo DSC** was performed on a TA Instruments DSC 250 calibrated with indium. A LED source centered at 390 nm was employed as light source ( $20\text{ mW/cm}^2$ ). The resin was placed in an indium pan (1-5 mg) and measured against a empty open pan. The light was turned on after 60 s of equilibration and the reaction was monitored for 5 minutes.

**AFM** was acquired in tapping mode using a Dimension ICON (Bruker) with Nanoscope VI (Bruker) as software. A TESP-V2 cantilever was used at 320 kHz frequency (Spring constant:  $37\text{ N/m}$ , radius 7 nm, length 125  $\mu\text{m}$ , silicon, repulsive mode,  $25\text{ }^{\circ}\text{C}$ ). Images were elaborated using Nanoscope Software. A first-order background was removed, and the images were coloured with the standard colour palette. To compare images of different materials the same scale was used. ImageJ was used to estimate the particle size distribution and area coverage after colour thresholding the image.

**Photorheology** was performed on an ARG2. A LED UV-curing accessory centered at 365 nm ( $20\text{ mW/cm}^2$ ) was used together with an acrylic transparent bottom plate and a single use aluminum parallel plate (20 mm). The measurement was performed in the linear viscoelastic regimen with frequency of 1 Hz with a gap of 400  $\mu\text{m}$  (or

different if specified). To determine the viscosity of the formulated resins, a 1° 40 mm cone geometry was used. The shear rate window was from 1 to 100 s<sup>-1</sup>.

**Jacobs Curve** were obtained by placing a drop of resin on a glass coverslip and irradiated directly from below at different exposure times with a 2 mm circular beam using the spot timer of the ASIGA MAX-UV DLP 3D printer centered at 380 nm, giving an irradiance of ~20 mW/cm<sup>2</sup>. The thickness of the photocured resin was then measured with an Evanem Dloett electronic micrometer and the depth of cure was plotted against the logarithm of the light intensity for irradiation time.

**DLP Printing** A commercial Asiga Max-UV DLP 3D printer with a LED source centred at 380 nm (20 mW/cm<sup>2</sup>) was used to 3D print the resin. The 3D objects were sliced on the Asiga composer printed at an intensity of 20 mW/cm<sup>2</sup>. The printed objects were washed thoroughly with Isopropanol to remove unreacted monomers and postcured using a low-pressure mercury vapor lamp (2 mW/cm<sup>2</sup>, centred around 365 nm). The optimised parameters used for each resin are reported below:

*Table S3.1.* Parameters employed for the 3D printing of the resins developed in this chapter.

Resin	Sudan I (%)	Layer Thickness (μm)	Burn in (s)	Layer (s)
T_S4_ITX <sub>2</sub> _IOD <sub>2</sub>	-	50	60	40
T_S4_ANT <sub>2</sub> _IOD <sub>2</sub>	-	100	50	45
C_S4_Ace <sub>30</sub> _BAPO <sub>0.5</sub>	0.1	100	3.5	2
C_S4_TVC <sub>30</sub> _BAPO <sub>0.5</sub>	0.1	100	5	3

**Preparation of Materials.** The photoinitiator was first dissolved in **AlLOx**. The mixture was mixed with a vortex mixer for 30 s before adding the crosslinker together with the reactive diluent (equimolar amount of

SH to double bond functionality, See table S3.2). MSA was then added (0.5 wt%) and the mixture was left to react for 15 min under stirring. The liquid was then poured into moulds and cured for 30 min in an Asiga post-cure chamber (Low pressure mercury lamp with a broad emission in the UV and visible, centered at 365 nm, 2 mW/cm<sup>2</sup>). The samples were then dried at ambient condition for one day before being dried in a vacuum oven at RT overnight. For the heat treatments, films were placed in a temperature control oven at the desired temperature for 16-20 hours, then cooled quickly to room temperature, and finally stored in a desiccator for 24 h at room temperature before testing their properties.

Table S3.2. Composition of resins developed in this chapter.

Code	Diluent	Formulation						Diluent Mole%
		AllOx (mg)	AllOx (mol)	Diluent (mg)	Diluent (mol)	Crosslinker (mg)	Mol	
C_S4	-	700	4.2	-	-	1022		
C_S_Ace30	Acetone	700	4.2	140	2.45	1610	3.3	30 wt%
CS4_DT30	DT	70	0.4	30	0.18	147	0.3	30
CS4_DT50	DT	50	0.3	50	0.30	148	0.3	51
CS4_DT70	DT	30	0.2	70	0.43	149	0.3	70
CS4_DVB40	DVB	100	0.6	52	0.4	243	0.5	40
CS4_DVB50	DVB	100	0.6	80	0.61	296	0.6	51
CS4_DVB60	DVB	100	0.6	115	0.88	361	0.7	60
CS4_DVS40	DVS	100	0.6	50	0.42	249	0.5	41
CS4_DVS50	DVS	100	0.6	75	0.63	301	0.6	50
CS4_DVS60	DVS	100	0.6	105	0.88	363	0.7	60
CS4_DM40	DM	100	0.6	80	0.40	294	0.6	41
CS4_DM50	DM	100	0.6	120	0.61	344	0.7	51
CS4_DM60	DM	100	0.6	170	0.86	406	0.8	60
C_S_TCV <sub>10</sub>	TVC	100	0.6	10	0.06	209	0.4	10
CS4_TCV <sub>20</sub>	TVC	500	3.0	100	0.61	1124	2.3	17
CS4_TC30_Ac e <sub>a</sub>	TVC	500	3.0	200	1.23	1132	2.3	29

### 3.5.3. Supporting Characterization

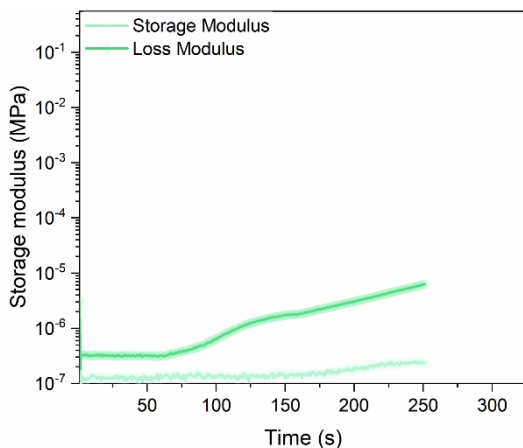


Figure S3.1. Photo-rheology trace of  $T\_S4\_ITX_2\_IOD_2$  (365nm LED with a power of  $20 \text{ mW/cm}^2$ ).

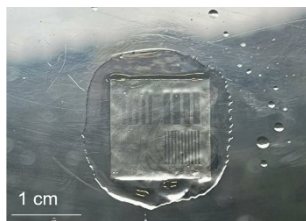
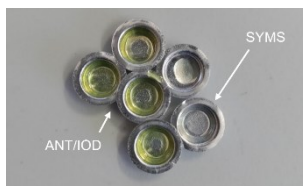
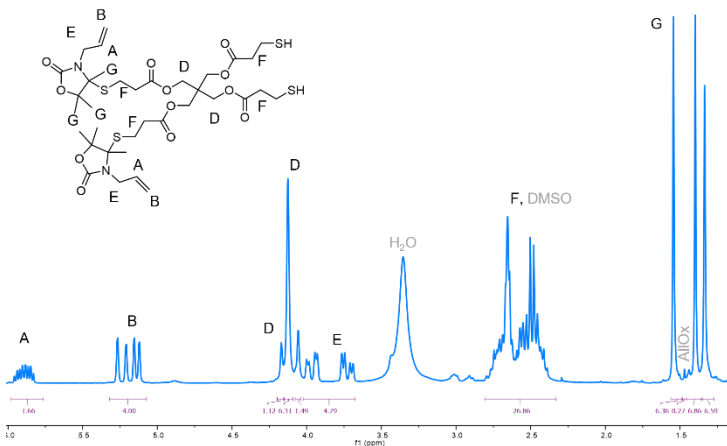


Figure S3.2. Delamination issues of  $T\_S4\_ITX_2\_IOD_2$ , adhesion to the FEP film. Pictured a delaminated structure for optimisation of photocuring time.



**Figure S3.3.** PhotoDSC pans containing  $T\_S4\_ANT_2\_IOD_2$  (Yellow) and of  $T\_S4\_SYMS_2$  (Transparent).



**Figure S3.4.**  $^1H$  NMR of the prepolymerised  $C\_S4$  with the main signals assigned. The singlet at 1.46 ppm ( $-CH_3$  AlOX) was employed to calculate conversion by comparing it to its integral before prepolymerisation. Average structure shown, the resin is composed on mono-, di- tri- and tetrasubstituted species.



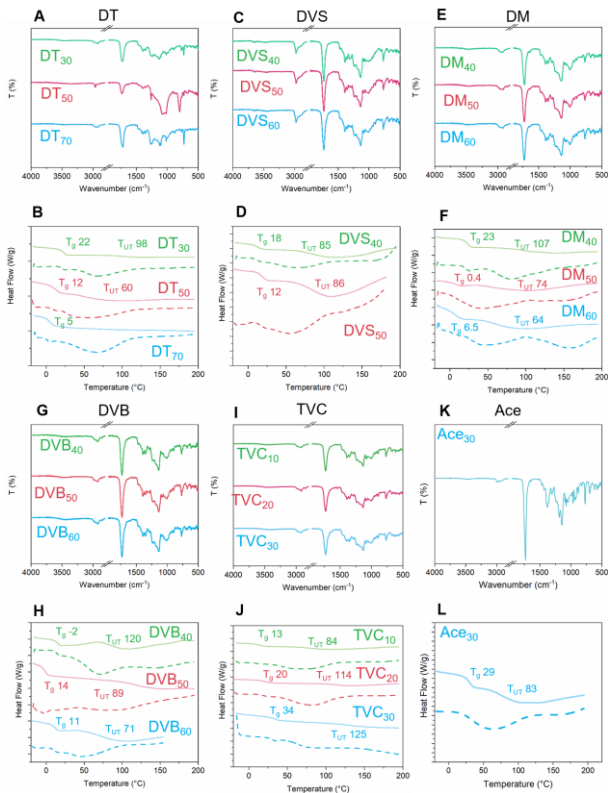
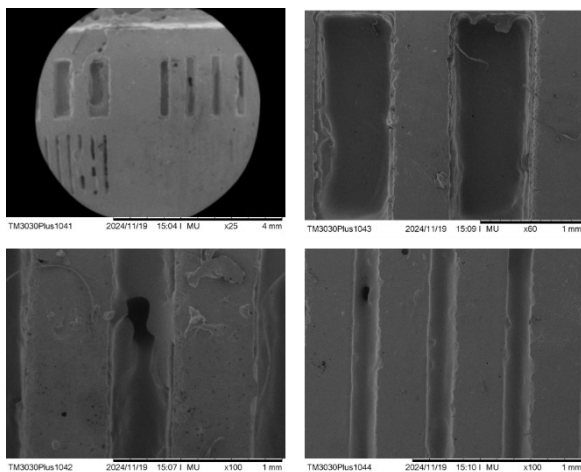


Figure S3.5. FTIR of and mDSC traces of materials prepared using DT (a,b), DVS (c,d), DM (e,f), DVB (g,h), TVC (i,j) as reactive diluent and Acetone (k,l) as non-reactive diluent.



*Figure S3.6. Structure for the optimisation of resolution printed using  $C_{S4\_TVC30\_BAPO0.5}$ .*

## 3.6. References

1. Han, D. & Lee, H. Recent advances in multi-material additive manufacturing: methods and applications. *Curr Opin Chem Eng* 28, 158–166 (2020).
2. Rafiee, M., Farahani, R. D. & Theriault, D. Multi-Material 3D and 4D Printing: A Survey. *Advanced Science* 7, 1902307 (2020).
3. Sampson, K. L. *et al.* Multimaterial Vat Polymerization Additive Manufacturing. *ACS Appl Polym Mater* 3, 4304–4324 (2021).
4. Wu, L. & Dong, Z. Interfacial Regulation for 3D Printing based on Slice-Based Photopolymerization. *Advanced Materials* 35, 1–15 (2023).
5. Nam, J. & Kim, M. Advances in materials and technologies for digital light processing 3D printing. *Nano Convergence* 2024 11:1 11, 1–25 (2024).
6. Shaukat, U., Rossegger, E. & Schlögl, S. A Review of Multi-Material 3D Printing of Functional Materials via Vat Photopolymerization. *Polymers* 2022, Vol. 14, Page 2449 14, 2449 (2022).
7. Nazir, A. *et al.* Multi-material additive manufacturing: A systematic review of design, properties, applications, challenges, and 3D printing of materials and cellular metamaterials. *Mater Des* 226, 111661 (2023).
8. Cheng, J., Yu, S., Wang, R. & Ge, Q. Digital light processing based multimaterial 3D printing: challenges, solutions and perspectives. *International Journal of Extreme Manufacturing* 6, 042006 (2024).
9. Kiker, M. T., Recker, E. A., Uddin, A. & Page, Z. A. Simultaneous Color- and Dose-Controlled Thiol–Ene Resins for Multimodulus 3D Printing with Programmable Interfacial Gradients. *Advanced Materials* 2409811, 1–8 (2024).
10. Ehrmann, K. & Barner-Kowollik, C. Colorful 3D Printing: A Critical Feasibility Analysis of Multi-Wavelength Additive Manufacturing. *J Am Chem Soc* 145, 24438–24446 (2023).
11. Schwartz, J. J. & Boydston, A. J. Multimaterial actinic spatial control 3D and 4D printing. *Nat Commun* 10, 1–10 (2019).
12. Dolinski, N. D. *et al.* Solution Mask Liquid Lithography (SMaLL) for One-Step, Multimaterial 3D Printing. *Advanced Materials* 30, 1800364 (2018).
13. Yue, L. *et al.* Single-vat single-cure grayscale digital light processing 3D printing of materials with large property difference and high stretchability. *Nat Commun* 14, 1–12 (2023).
14. M., T. *et al.* Effect of acrylate chemistry on human health. *International Archives of Occupational and Environmental Health* 2002 75:1 75, 67–72 (2002).
15. Ma, Y. *et al.* Multimaterial Thermoset Synthesis: Switching Polymerization Mechanism with Light Dosage. *ACS Cent Sci* 10, (2024).
16. Dumur, F. Recent advances on diaryliodonium-based monocomponent photoinitiating systems. *Eur Polym J* 195, 112193 (2023).

17. Topa, M. & Ortyl, J. Moving towards a finer way of light-cured resin-based restorative dental materials: Recent advances in photoinitiating systems based on iodonium salts. *Materials* 13, (2020).
18. Fouassier, J., Burr, D. & Crivello, J. V. Photochemistry and Photopolymerization Activity of Diaryliodonium Salts. *Journal of Macromolecular Science—Pure and Applied Chemistry* 31, 677–701 (1994).
19. Devoe A N, R. J. *et al.* Transient intermediates in the photolysis of iodonium cations. <https://doi.org/10.1139/v87-391> 65, 2342–2349 (2011).
20. Crivello, J. V. & Lam, J. H. W. Diaryliodonium Salts. A New Class of Photoinitiators for Cationic Polymerization. *Macromolecules* 10, 1307–1315 (1977).
21. Crivello, J. V. & Lam, J. H. W. Photoinitiated cationic polymerization with triarylsulfonium salts. *Journal of Polymer Science: Polymer Chemistry Edition* 17, 977–999 (1979).
22. Sutherland, B. P., Kabra, M. & Kloxin, C. J. Expanding the thiol-X toolbox: Photoinitiation and materials application of the acid-catalyzed thiol-ene (ACT) reaction. *Polym Chem* 12, 1562–1570 (2021).
23. Maines, E. M., Porwal, M. K., Ellison, C. J. & Reineke, T. M. Sustainable advances in SLA/DLP 3D printing materials and processes. *Green Chemistry* 23, 6863–6897 (2021).
24. Zhao, B. *et al.* Fast Living 3D Printing via Free Radical Promoted Cationic RAFT Polymerization. *Small* 19, (2023).
25. Topa, M. *et al.* One-component cationic photoinitiators based on coumarin scaffold iodonium salts as highly sensitive photoacid generators for 3D printing IPN photopolymers under visible LED sources. *Polym Chem* 11, 5261–5278 (2020).
26. Williams, R. M., Khudyakov, I. V., Purvis, M. B., Overton, B. J. & Turro, N. J. Direct and sensitized photolysis of phosphine oxide polymerization photoinitiators in the presence and absence of a model acrylate monomer: A time resolved EPR, cure monitor, and photoDSC study. *Journal of Physical Chemistry B* 104, 10437–10443 (2000).
27. Jiang, F. & Drummer, D. Curing kinetic analysis of acrylate photopolymer for additive manufacturing by photo-DSC. *Polymers (Basel)* 12, 1–11 (2020).
28. Dumur, F. Recent advances on anthracene-based photoinitiators of polymerization. *Eur Polym J* 169, 234–250 (2022).
29. Zivic, N. *et al.* A novel naphthalimide scaffold based iodonium salt as a one-component photoacid/photoinitiator for cationic and radical polymerization under LED exposure. *Polym Chem* 7, 5873–5879 (2016).
30. Zivic, N. *et al.* Recent Advances and Challenges in the Design of Organic Photoacid and Photobase Generators for Polymerizations. *Angewandte Chemie - International Edition* 58, 10410–10422 (2019).

- 
31. Petko, F. *et al.* One-Component Stilbene-Based Iodonium Photoinitiators with Increased Photoacid Quantum Yield for Cationic Vat 3D Printing. (2024) doi:10.1021/acs.macromol.4c01692.
  32. Lopez De Pariza, X. *et al.* Novel imino- And aryl-sulfonate based photoacid generators for the cationic ring-opening polymerization of  $\epsilon$ -caprolactone. *Polym Chem* 12, 4035–4042 (2021).
  33. Nguyen, L. T. T., Gokmen, M. T. & Du Prez, F. E. Kinetic comparison of 13 homogeneous thiol-X reactions. *Polym Chem* 4, 5527–5536 (2013).
  34. Boynton, N. R. *et al.* Accessing pluripotent materials through tempering of dynamic covalent polymer networks. *Science* (1979) 383, 545–551 (2024).
  35. de Heer Kloots, M. H. P., Schoustra, S. K., Dijkman, J. A. & Smulders, M. M. J. Phase separation in supramolecular and covalent adaptable networks. *Soft Matter* 19, 2857–2877 (2023).
  36. Lopez de Pariza, X. *et al.* Recyclable photoresins for light-mediated additive manufacturing towards Loop 3D printing. *Nat Commun* 14, (2023).
  37. Chen, L. *et al.* Impact of Dynamic Bond Concentration on the Viscoelastic and Mechanical Properties of Dynamic Poly(alkylurea-co-urethane) Networks. *Macromol Chem Phys* 221, 1900440 (2020).
  38. Kolibaba, T. J. *et al.* Results of an interlaboratory study on the working curve in vat photopolymerization. *Addit Manuf* 84, 104082 (2024).



# 4

A Platform  
for the 3D printing of dissociative  
CO<sub>2</sub>-derived Networks with  
Tuneable Degradation





## 4.1. Abstract

Modern-day polymers should be designed with circular economy principles in mind, considering both their recyclability and end-of-life options. In previous Chapters, Polyoxazolidones, a promising class of non-isocyanate polyurethanes, were shown to afford highly recyclable materials. However, their content in non-degradable *N,S*-acetal moiety prevented their degradation, a key factor in the end-of-life scenarios of a material. Herein we report the development of a new type of dynamic bond, the *N,O* acetal. This bond is hydrolytically degradable while endowing materials with recyclability. We report the synthesis of a diallyl monomer bearing the *N,O* acetal moiety and realise its photocuring. Thanks to the fast rate we realise its 3D printing towards the tuning of the hydrolytic degradation of the materials by changing the ratio of hydrolysable bonds in the material, highlighting a high potential for these materials for cargo delivery or degradable materials.

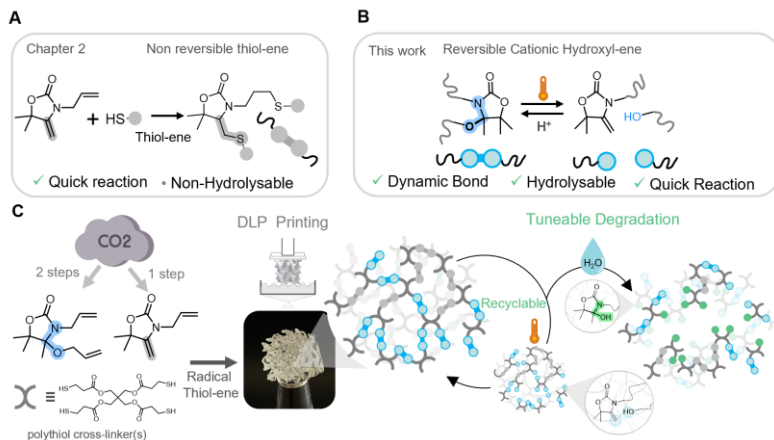


**Figure 4.1.** a) Scheme of the thiol ene reaction on **AlloX** giving origin to two thio-ether bonds; b) Scheme of the dynamic *N,O*-acetal chemistry developed in this work; c) General scheme of the study in which a diallyl monomer containing *N,O*-acetal together with a allyl-bearing alkylidene oxazolidone monomer could be 3D printed into polyoxazolidone dissociative thermoset bearing varying amounts of hydrolytically degradable bonds. The network could be recycled thanks to the reversible hydroxyl-ene reaction and degraded through hydrolysis; the rate of hydrolysis could be adjusted by varying the content in hydrolysable moiety.

## 4.2. Introduction

Worldwide plastic production is still heavily linked to the petrochemical industry. While it uses only about 6% of the global oil production,<sup>1</sup> plastics heavily impact the environment and human health by breaking down into microplastics and leaching additives into the environment.<sup>2,3</sup> Their non-renewable origin, together with their limited end-of-life options make plastic sustainability a centrepiece of today's research in polymeric materials. Mitigation strategies for the non-renewable origin of plastics include the use of bio-based feedstock, recirculated plastic wastes, or captured CO<sub>2</sub>.<sup>4–8</sup> For instance, biomass-derived alternatives to traditional petrochemical-based plastics have been on the rise.<sup>9</sup> On the other hand, CO<sub>2</sub>-based strategies<sup>10–12</sup> have been highlighted as a key step towards a circular plastic economy.<sup>13,14</sup> Indeed, CO<sub>2</sub> uptake in plastics has already seen some commercial success for the production of polycarbonate polyols in certain polyurethane applications.<sup>15–18</sup>

Another approach to enhance the sustainability of polymeric materials is the design of circular approaches to facilitate the reutilization and recycling of polymeric materials.<sup>19,20</sup> Thermosets are in dire need of such revolutionizing technologies, as their highly crosslinked structures do not allow their reprocessability via mechanical means to adopt new shapes, and thus end-up being discarded or incinerated. Alternatively, the introduction of dynamic covalent bonds in polymer networks, also named “covalent adaptive networks” or CANs,<sup>21–23</sup> has been proposed as one strategy to break this vicious cycle. Specifically, CANs enable the achievement of both the high mechanical performances and chemical resistance of crosslinked thermosets as well as the ability to be reprocessed by heat-based techniques such as extrusion or injection moulding, generally limited to thermoplastics.<sup>24</sup>

The combination of these two strategies, i.e., the introduction of captured CO<sub>2</sub> as renewable feedstock for the development of CAN

thermosets, has been highlighted as an enticing step towards more sustainable plastics.<sup>25,26</sup> An especially interesting class of CO<sub>2</sub>-derived polymers with the possibility to introduce CANs is non-isocyanate polyurethanes or NIPUs.<sup>10,27–31</sup> Recently, a new class of NIPUs has been developed by the step-growth polymerisation of CO<sub>2</sub>-derived oxazolidones bearing exo-vinylene groups with thiols. These materials have the added benefit that includes an unprecedented dynamic bond in the form of reversible *N,S*-acetals *via* reaction of the C=C with thiols, a feature that is exploited to reprocess thermosets.<sup>25</sup> Moreover, their fast and efficient exchange dynamics further enabled unparalleled recyclability and processability by multiple industrially-relevant techniques such as extrusion, injection moulding and compression moulding.

While the recyclability of materials containing the *N,S*-acetal bond was demonstrated for the pure material in a laboratory setting,<sup>25</sup> it is important to envision the end-of-life options of these new plastics in case they escape from the plastic sorting.<sup>32,33</sup> Hence, the development of degradable scaffolds that ideally turn into harmless chemical fragments is an essential piece for the sustainability of any plastic material and of NIPUs in particular, especially when posed for applications that present difficult or non-existent recoverability.<sup>11,34</sup> While sulphur-based acetals (*S,S*-) are known to display high stability towards hydrolysis,<sup>35–37</sup> oxygen-based acetals (*O,O*-) and nitrogen-based hemiaminal (*N,O*-) and amins (*N,N*-) are more prone to this type of chemical degradation into monomer or oligomeric units under acidic conditions.<sup>38,39</sup> In fact, *O,O*-acetals have been previously used to enable the degradation of polyolefins to enhance their sustainability.<sup>40,41</sup> Furthermore their degradation was controlled by the addition of a protic species, enabling on-demand degradation.<sup>42,43</sup>

In this work, we took inspiration from the degradability of *O,O*-acetals and the reversibility of *N,S*-acetals towards nucleophiles to propose a

new type of dynamic and cleavable bond, *N,O*-acetals embedded in the polymer repeat-unit heterocycle (Figure 4.1). First, we demonstrate that this type of moiety can be easily installed on a functional oxazolidone precursor at room temperature in minutes under acidic catalysis. Secondly, mechanistic insight from computational and kinetic studies indicate that this bond is dissociative with quick exchange dynamics. With this knowledge, a diallyl monomer containing a cleavable *N,O*-acetal moiety was prepared and photocured, leading to recyclable materials with controlled degradation in water (Figure 4.1). Finally, we show that these materials could be easily 3D printed by VAT enabling the production of 3D scaffolds with on-demand hydrolytic degradation (Figure 4.1). This study highlights the potential of this new degradable bond to expand the applicability of oxazolidone-based NIPU networks.

## 4.3. Results and Discussion

### 4.3.1. Small molecule studies

As we have shown previously, alkylidene-oxazolidones react efficiently with thiols under acidic catalysis to form *N,S*-acetals by addition of the thiol to the C=C double bond in a reversible manner.<sup>25,44–46</sup> Inspired by the possibility of using other common, cheap nucleophiles, we investigated the potential of alcohols to form *N,O*-acetals in an analogous fashion. The abundance of alcohols and polyols from bio-renewable origin offers an additional motivation for the potential application of this reactivity.<sup>47</sup> As a first proof-of-concept, we simply dissolved a model alkylidene-oxazolidone (3-allyl-5,5-dimethyl-4-methyleneoxazolidin-2-one, **AlIOx**) in dry deuterated methanol. As shown in Figure S4.1, the two components did not react without catalyst. However, we observed an instantaneous, exothermic reaction of **AlIOx** upon addition of 1 mol% of methanesulphonic acid (MSA) as catalyst. Under these conditions, the reaction was almost quantitative

after 15 min reaction, with conversion reaching 95% as determined by  $^1\text{H}$ -NMR spectroscopy (see ESI, Figure S4.1 for details).

We then explored the full potential of this reaction by selecting a series of alcohols with increasing steric hindrance, from primary to tertiary, and comprising phenolic and benzylic moieties. All reactions were carried out in bulk under equimolar conditions (1:1 [**AlloX**]/[R-OH]) in an argon-filled glovebox to avoid possible hydrolysis, as we previously observed that alkylidene oxazolidones hydrated into the corresponding hydroxyoxazolidone under acidic conditions (Figures S4.2,3). When reacted with alcohols, we observed a plateau in the conversion of **AlloX** in less than one minute in all cases, indicating fast reactions. However, the conversion reached at this plateau was strongly influenced by the steric hindrance and nucleophilicity of the alcohol (Figure S4.4-S4.11). Most nucleophilic and least sterically hindered alcohols displayed the highest conversions, albeit always under 50% (namely, 37.%, 45.5% and 46.7% for benzyl-, hexyl-, and methyl- alcohol, respectively). Further increases in steric hindrance and lower nucleophilicity brought down the conversion even further, well under 15% (0%, 3.9%, 8.2% and 14% for *tert*-butyl, phenyl-, 4-methyl-2-pentyl- and phenyl-ethyl alcohol).

The reaction was pushed to the formation of the *N,O*-acetal by addition of excess alcohol, as demonstrated by >80% conversion with 25 equivalents of methanol (Figure S4.12). Hence, the potential of this strategy for the production of novel oxazolidone scaffolds incorporating novel *N,O*-acetals was explored by synthesising and characterising ( $^1\text{H}$  NMR,  $^{13}\text{C}$  NMR and HRMS) five different model compounds (Figure 4.1-a,b, Figure S4.14-S4.18). These molecules were obtained in low to moderate yields (15-60%) after standard organic work-up and column chromatography separation without noticeable degradation, serving as an example of a novel library of compounds that could have potential applications in pharma, agriculture and organic synthesis.<sup>48-51</sup> The

reaction thermodynamics were then probed by analysing the reaction equilibria at temperatures ranging from 25 to 55 °C and using the **AlLOx**/hexanol system as model in 1:1 ratio (bulk) with 1 mol% of MSA (Figures S4.20-S4.24). Consistent with an exergonic process, higher temperatures resulted in lower C=C conversions at equilibrium. Indeed, a Van't Hoff plot of the equilibrium constant,  $K_{eq}$ , obtained at different temperatures provided thermodynamic parameters of  $\Delta H = -10.7 \text{ kJ}\cdot\text{mol}^{-1}$  and  $\Delta S = -8.9 \text{ J}\cdot\text{K}^{-1}\text{mol}^{-1}$  (Figure 4.2-c).

In order to further understand the reaction dynamics, we performed Density Functional Theory (theory level WB97XD/6-31+G(d)) of the model reaction between **AlLOx** and methanol, using MSA as catalyst to eliminate differences with the experimentally observed data. A conductor-like polarizable continuum solvation model ( $\epsilon=4.7113$ , chloroform) was employed, and the substituents were replaced by methyl groups mimicking the aliphatic chains of the synthesised model compounds to enable faster calculations (Figure 4.2-d, Figure S4.25). Similar to previously reported mechanisms,<sup>25</sup> the starting reactant complex is stabilised by hydrogen bonding and the interaction between the acidic MSA and the electron-rich alkene ( $\Delta G=-44.4 \text{ kJ/mol}$ ). The delocalization of the charge through the oxazolidone ring further stabilises the ring. Next, the rate-determining step (RDS) has a very low activation barrier of 12.6 kJ/mol, pointing towards the reason behind the quick reaction dynamics in all experimental conditions explored. In this step, the acidic proton of the MSA is donated to the oxazolidone ring, forming a delocalised carbocation. The then-formed Intermediate 2a is characterised by the formation of a new  $\pi$  bond between the nitrogen and the carbocation, leading to a stabilisation of the species (-42.3 kJ/mol) and a shortening of the N-C bond (from 1.320 to 1.292 Å, Table S4.1). A minor reorganization leads to Intermediate 2b, then the carbocation is attacked by the nucleophilic hydroxyl with an energy barrier of 12.1 kJ/mol leading to the formation of transition state 2 and breaking the  $\pi$  bond, signalled by the lengthening of the N-C bond

(1.292 to 1.318 Å, Table S4.1). In a concerted step, the hydrogen of the hydroxyl is transferred to the catalyst, regenerating it (intermediate 3, -46.0 kJ/mol). The little stabilisation of this intermediate with respect to the other reaction steps explains the reaction's tendency to plateau at 46.7% conversion as the product is not strongly stabilised (-50.2 kJ/mol) in confront to the starting reactants. This lower stabilisation also explains the lower efficiency of this reaction compared to its thiol counterpart ( $\Delta G_{N,O\text{-acetal}} = -50.2$  kJ/mol,  $\Delta G_{N,S\text{-acetal}} = -73.2$  kJ/mol).<sup>25</sup> In summary, DFT calculations helped us explain the behaviour of the reaction. Low stabilisation energy and small  $\Delta G^{\ddagger}_{\text{RDS}}$  led to quick reaction with low conversions, as observed experimentally.



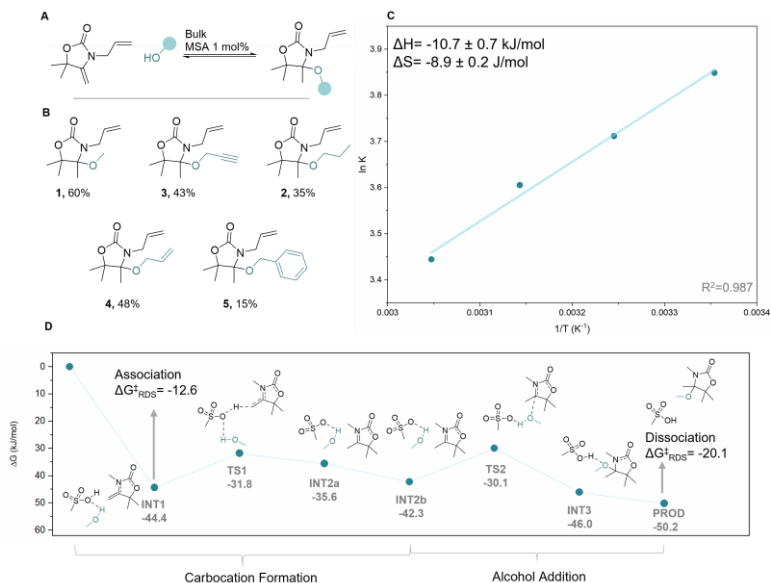


**Figure 4.2.** a) General reaction scheme between **Allox** and an alcoholic partner; b) Scope of *N,O*-acetal derivatives with isolated yields; c) Van't Hoff graph extracted from kinetics carried out at different temperatures with corresponding  $\Delta H$  (-10.7 kJ/mol) and  $\Delta S$  (-8.9 J/mol) of reaction; d) Gibbs-free energy profile of the reaction pathway for the formation of the *N,O*-acetal moiety between a model oxazolidone and a model alcohol (methanol) catalysed by MSA. Vertical arrows show the energy barriers for rate-determining steps.

The thermal reversibility of the process was investigated by *in-situ* NMR spectroscopy, in which a solution of *N,O*-acetal **4** in dry DMSO-*d*<sub>6</sub> was equilibrated at various temperatures (25–100 °C for 15 min) and subsequently their <sup>1</sup>H NMR spectra were recorded. Again, whilst no reaction was observed in a neutral environment or in the presence of a

base (1 mol% of triethylamine, TEA, Figure S4.26), the addition of acidic MSA (1 mol%) triggered the dissociation of the model compound into free **Allox** and allyl alcohol, even at room temperature (4% of dissociation). Elevating the temperature increased the dissociation to reach 86% at 100 °C (Figures S4.27-S4.29), further corroborating the role of protic species in the mechanism of association/dissociation of these *N,O*-acetals.<sup>52,53</sup>

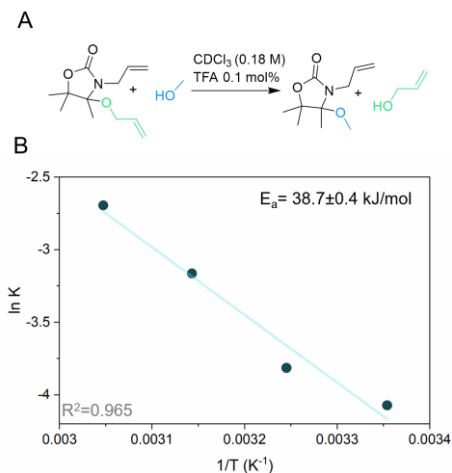


**Figure 4.3.** a) Scheme of the model exchange reaction. Reaction conditions: [4]/[methanol] = 1/10, CDCl<sub>3</sub> (0.18M), 0.1 mol% TFA); b) Arrhenius plot extracted from exchange kinetics carried out at temperatures between 25 and 55 °C.

To gain further insight into this mechanism, we probed the reaction kinetic barrier of exchange between alcohols by determining the activation energy. Thus, a 0.2 M solution of **4** and a tenfold excess of MeOH (Figure 4.3-a) was mixed with MSA (1 mol%) in dry CDCl<sub>3</sub> and the exchange reaction was monitored. Unfortunately, this resulted in a

reaction that was too quick to monitor the exchange (completed below 1 min), even with 0.1 mol% MSA. Hence, we employed a weaker acid (trifluoroacetic acid, TFA) as we previously saw that it showed reduced reaction rates (Figure S4.30). The extent of the alcohol exchange at equilibrium was found to be strongly influenced by temperature, increasing from 8% to 40% on going from 25 °C to 55 °C (Figure 4.3-c, Figure S4.31-35), which led to a calculated activation energy ( $E_a$ ) of  $38.87 \pm 0.4$  kJ/mol (Figure 4.3-c, Table S4.2). This result confirmed that the covalent exchange dynamics were quick in the presence of protic species, promising easy recyclability, with a lower  $E_a$  than previously reported *N,S*-acetal compounds (64.85 kJ/mol).<sup>25</sup>

#### 4.3.1. Preparation of Photocurable Materials

We decided to incorporate the *N,O*-acetal functionality in a polymeric matrix since this was expected to endow the network with both recyclability and degradability. Monomer **4** was selected for the preparation of the material as it already possesses two photocurable allyl bonds that can participate in step-growth polymerization via radical thiol-ene reaction with polythiols.<sup>54</sup> In order to do so, **4** was mixed with a tetrafunctional thiol crosslinker; pentaerythritol tetrakis(3-mercaptopropionate), **S4**. Finally, we chose phenylbis(2,4,6-trimethylbenzoyl)phosphine oxide (BAPO) as radical photoinitiator (0.5 wt%), and thin-films of the liquid, clear mixture were casted and irradiated with 390 nm light ( $20 \text{ mW} \cdot \text{cm}^{-2}$ ) for 60 s.

Surprisingly, a transparent and soft material with a sticky surface was obtained after irradiation rather than a self-standing object (Figure 4.4-a). Analysis of this material by FT-IR revealed that, in addition to the consumption of the allyl C=C, an intense –OH stretching band (Figure 4.4-b) together with a shoulder ( $1682 \text{ cm}^{-1}$ ) of the carbonyl stretching peak ( $1729 \text{ cm}^{-1}$ ) appeared, indicative of the presence of free exovinylene double bonds. These results indicated that the reverse

reaction (elimination of the alcohol from the oxazolidone ring) was being catalysed under these photoreaction conditions. To gain a better insight into this reaction, a mixture of 4 and a mono-functional thiol similar to our crosslinker (methyl-3-mercaptopropionate) was reacted and the reaction was followed by  $^1\text{H}$  NMR spectroscopy. After 60 s at room temperature without any irradiation, 12 mol% of **Allox** was liberated, as indicated by the presence of new resonances at 5.21 ppm (dd,  $\text{C}=\text{CH}_2$ ), 1.46 ppm (singlet  $-\text{CH}_3$ ) (Figure S4.36-a). We attributed this reactivity to the high sensitivity of *N,O*-acetal to acidic species, including weakly acidic thiols, in promoting the release of the alcohol unit and the formation of the exovinyl  $\text{C}=\text{C}$ . As a further proof of the role of acidic species in catalysing the liberation of **Allox** from 4, the use of basic triethylamine (TEA) as a pH regulator indeed prevented any side reaction between 4 and methyl-3-mercaptopropionate and provided quick reaction kinetics (Figures S36-b, S4.37).

Satisfyingly, using 0.5 wt% of TEA as a pH regulator, enabled the photocuring of the resin in a rapid manner, resulting in a fully crosslinked transparent, self-standing film after only 60 s of irradiation. The FT-IR spectra showed complete consumption of the double bond resonance ( $1644\text{ cm}^{-1}$ , Figure 4.5-d) together with a markedly lower intensity of the  $-\text{OH}$  resonance ( $3460\text{ cm}^{-1}$ , Figure 4.5-d). The successful preparation of a fully crosslinked matrix was further supported by high gel contents in THF ( $95\pm 2\%$ ) and low swelling degrees ( $135\pm 2\%$ , Table S4.3, entry 10). Photo-rheology showed a fast gel point (4.4 s) and real time FTIR (Figure S4.38) highlighted quick curing with the double bond band ( $1644\text{ cm}^{-1}$ ) being fully consumed after 20 s ( $390\text{ nm}$ ,  $20\text{ mW/cm}^2$ ). Photo-rheology further supported the occurrence of side reactions in the absence of the basic additive with a final moduli that was found to be lower than the resin prepared in the presence of the base additive (0.19 MPa without basic additive, 0.33 MPa using TEA, Figure 4.4-c,e). Hence, from this point on all materials were prepared using TEA (0.5 wt%) as additive.

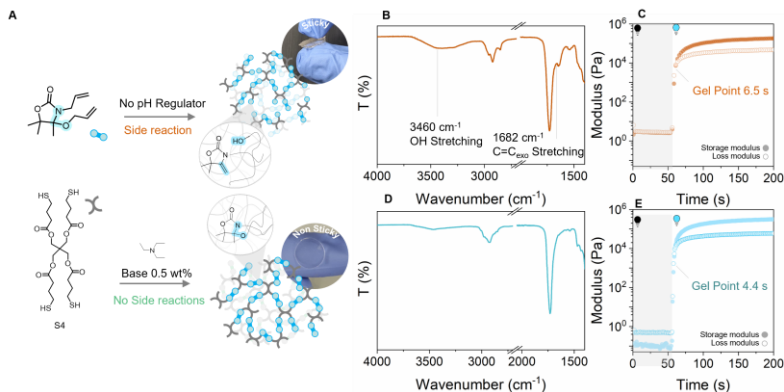


**Figure 4.4.** a) Scheme of the preparation of materials containing *N,O*-acetal moieties with and without pH regulator; b) IR spectra of the material without addition of a pH regulator; c) Photorheology results for **P(S4,100)** without pH regulator d) b) IR spectra of the material using a pH regulator (TEA 0.5 wt%); e) Photorheology results for **P(S4,100)** with pH regulator (TEA, 0.5 wt%).

#### 4.3.2. Versatility of the *N,O*-acetal chemistry

With a reliable photocrosslinking platform, we tuned the properties of the materials by changing the concentration of cleavable functionalities within the polymer network. Given the ability of **Allox** to participate efficiently in the radical thiol-ene reaction,<sup>55</sup> we mixed **Allox** and **4** in 1:1 ratio. By doing so, we could prepare thermosets featuring a combination of hydrolysable (*N,O*-acetal) and non-hydrolyzable (thioether linkages) bonds, resulting in a convenient platform to study the influence of the structural connectivity on the material's properties and hydrolytic degradation (Figure 4.5-a). For comparison, mixtures of only

**AlLOx** and thiol crosslinkers were also prepared, providing only non-hydrolyzable thiol-ether crosslinks. In order to further tune the properties, materials with varying crosslinking densities were prepared (Figure 4.5-b,c). In order to do so, **4** was mixed with a multifunctional thiol crosslinker trifunctional trimethylolpropane tris(3-mercaptopropionate), **S3**, tetrafunctional pentaerythritol tetrakis(3-mercaptopropionate), **S4**, or hexafunctional dipentaerythritol hexakis(3-mercaptopropionate), **S6** (Figure 4.5-b). Hence, the materials were labelled P(X,Y), where X denotes the thiol crosslinker (S3, S4, or S6) and Y represents the mol% of **4** in the mixture of **4** and **AlLOx** (0, 50, or 100%) (Figure 4.5-c). Finally, we chose phenylbis(2,4,6-trimethylbenzoyl)phosphine oxide (BAPO) as radical photoinitiator (0.5 wt%), and thin-films of the blends were casted and irradiated with 390 nm light ( $20 \text{ mW}\cdot\text{cm}^{-2}$ ) for 60 s. All materials were prepared using TEA (0.5 wt%) as pH regulator to avoid side reactions during photocuring.

Gratifyingly, all materials showed efficient curing, with a steep reduction of the double bond stretching resonance at  $1644 \text{ cm}^{-1}$  (Figure 4.5-d). Thermal characterisation of the materials by differential scanning calorimetry (DSC) revealed two important characteristics. First, a clear trend of raising  $T_g$  with increased crosslinking density, as clearly demonstrated by increasing the thiol functionality on going from **P(S3,50)**, **P(S4,50)**, to **P(S6,50)** and attaining  $T_g$ 's of  $-0.2 \text{ }^\circ\text{C}$ ,  $2 \text{ }^\circ\text{C}$ , and  $18 \text{ }^\circ\text{C}$  respectively (Figure 4.5-d, Table S3 entry 5,6,7). The same trend was followed by materials using 100 % of **4** (**P(S3,100)**  $T_g = 1.4 \text{ }^\circ\text{C}$ , **P(S4,100)**  $T_g = 8.8 \text{ }^\circ\text{C}$ , **P(S6,100)**  $T_g = 19.5 \text{ }^\circ\text{C}$ , Table S3, entry 9,10,11). Secondly, an endothermic peak was observed for all networks containing **4** attributed to the depolymerization of the *N,O*-acetal linkages. While no protic species were deliberately added that could have catalysed the network dissociation reaction, the protic character of the photodegradation products of BAPO (phosphonic acid-like fragments) could not be ruled out.<sup>56</sup> To study this possibility, we mixed **4** with the photodegradation products of BAPO (dissolved in DCM and

irradiated for 30 min at 390 nm, 20 mW/cm<sup>2</sup>). After 15 min of reaction, we could observe the characteristic signals of the **Allox**, proving that indeed the reaction was catalysed by the photodegradation products of BAPO (Figure S4.39).

Further support for the ability to depolymerise the materials came from dynamic mechanical analysis (DMA), variable temperature in-situ FT-IR traces, and reprocessing studies. Comparing the traces of two networks, **P(S4,50)**, and **P(S4,100)**, during a heating ramping of a DMA test, we observed a lower onset of the depolymerization reaction in the network with the highest number of reversible crosslinks (from 139 °C to 117 °C, respectively, Figure S4.40), in accordance with DSC analyses (Figure S4.40). The depolymerization could also be observed in situ in the FT-IR traces of both **P(S4, 100)** and **P(S4,50)** on heating the sample from 25 to 150 °C with the increase in the band of the exovinylene C=C double bond (1682 cm<sup>-1</sup>, Figure S4.41-a,b), consistently with the rupture of the *N,O*-acetal bond that released **Allox**. Notable, the sample containing only 50% of *N,O* acetal bonds embedded in the network showed a lower intensity of this resonance, coherently with its lower content in dynamic bonds. The ability to depolymerize **P(S4,100)** was further confirmed by hot-pressing and remoulding various fragments. Upon applying 1 ton of pressure at 90 °C for 5 min, a transparent film was obtained with similar FTIR spectra, and *T<sub>g</sub>* (7.9 °C) to the virgin material (*T<sub>g</sub>* = 8.8 °C, Figure S4.42). Its storage moduli lowered from *E'*<sub>virgin</sub> at -10 °C = 2549 MPa to *E'*<sub>reprocessed</sub> at -10 °C = 1926 MPa showing that the material only partially recovered its mechanical properties after reprocessing.

Next, we studied the mechanical properties of the materials. As expected, increasing the crosslinking density increased the Young's modulus, ranging from 3.0 ± 0.2 MPa (**P(S3,50)**) to 27.4 ± 1.5 MPa (**P(S6,50)**, Figure 4.5-f, Table S4.3, entry 5,6,7). Together with this marked stiffening, the stress at break rose as well, from 1.3 MPa to 11.4

MPa. On the other hand, the elongation at break remained within a similar order of magnitude, at  $60.8 \pm 2.9\%$  and  $45.5 \pm 1.5\%$  for **P(S4,50)** and **P(S3,50)**, respectively. While a clear trend was seen when varying the crosslinking density, materials derived from mixing **AlLOx** and **4** gave starkly different materials. **P(S4,0)** showed a clear yield point at 4.5% elongation with a modulus of 737 MPa followed by plastic deformation until 25% elongation and a stress at break of 11.9 MPa (Figure 4.5-f, Table S4.3, entry 2). The material made by mixing **AlLOx** and **4** in 1:1 ratio was much softer, with a modulus of 2.8 MPa and a stress at break of 1.77 MPa. Curiously, **P(S4,100)** was stronger, with a 3-fold increase in modulus (10.4 MPa) as well as stress at break (5.97 MPa). This was attributed to the fact that allyl bonds react much faster in the thiol-ene reaction when compared to the electron-rich exovinylene bond.<sup>57-59</sup> Thus, when photocuring, the allyl bond reacted quicker, rising the viscosity and hindering the thiol-ene reaction on the exovinylene double bond. This in turn gives origin to a network with more defects. This hypothesis was supported by the lower gel content (THF) of **P(S4,50)** when compared with **P(S4,0)** and **P(S4,100)** (Table S4.3, entry 2,6,10).



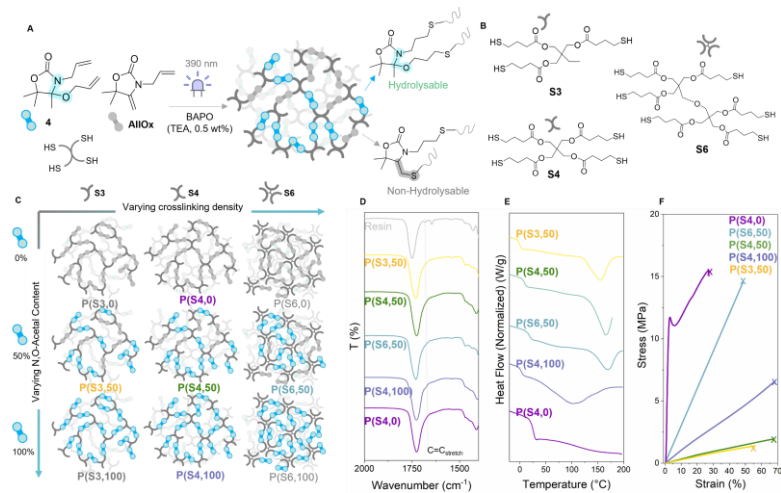


**Figure 4.5.** a) Scheme of the preparation of material mixing **4** and **AlIOx** to insert varying amounts of cleavable bonds in the network structure; b) structures of the thiol crosslinkers used to vary the crosslinking density of the materials; c) Scheme of the preparation of materials with varying crosslinking density and varying content of *N,O*-acetal moieties; d) IR spectra of the resin and material showing effective curing; e) DSC traces of materials prepared in this study; f) Stress-Strain curves of the materials prepared in this study (Young's modulus, Elongation at break and Stress at break data are summarized in Table S4.3).

### 4.3.3. Hydrolytic Degradation: From Model Compounds to Materials

Next, we hypothesized that the structural differences between *N,S*- and *N,O*-acetals derived from oxazolidones, which give markedly different exchange dynamics in the bulk when catalyzed by acids (*vide supra*), would also result in distinct reactivities towards hydrolysis. Indeed, as

with many other acid-cleavable bonds (imines, hydrazones, acetals, ketals, orthoesters, etc.),<sup>39,42</sup> the choice of heteroatom and substituent plays a key role in the pH sensitivity to hydrolytic cleavage, and thus in the hydrolysis rate constants.<sup>39</sup> When installed in a polymer network of the right topology, the hydrolysis of the *N,S*- or *N,O*-acetal bond would then offer a chemical handle for the disassembly of the polymer structure, leading to its possible (bio)degradation.

To assess the hydrolysis of our newly synthesized model *N,O*-acetals, we investigated the reaction of **4** in H<sub>2</sub>O (0.2 M) under neutral or acidic conditions (1 mol% MSA), and we compared it with the one of the *N,S*-acetal counterpart (Figure 4.6-a). As expected, the reaction rate and hydrolysis degree were markedly different between the two compounds (Figure S4.43). Specifically, when the reaction was carried out in neutral environment, 24% hydrolysis was reached after 4 days, while it only required 30 min to hydrolyse quantitatively in acidic media (Figures S4.43-S4.45). On the other hand, *N,S*-acetal model **6** displayed much higher resistance to hydrolysis, with no hydrolysis products observed after 4 days under neutral conditions, and reaching only 24% in acidic media (1 mol% MSA, Figures S4.46-S4.47). In comparison, a classic *O,O*-acetal (1,1-Dimethoxyethane) degraded to methanol and acetaldehyde much more readily than the *N,O*- or *N,S*-acetal (albeit through a slightly different set of reaction intermediates), reaching full or near full conversions in less than 1 hour or 24 hours, in acidic or neutral conditions, respectively (Figures S4.48-S4.50). These results suggested the potential of *N,O*-acetals based on oxazolidone building blocks to control the degradation of polymer materials.<sup>39</sup>

We thus investigated the hydrolytic degradation rate of our thermoset materials in water in the presence of MSA (1.0 M MSA; Figure 4.6-b). To increase the range of materials with tuneable degradability, we prepared two new materials with 25% cleavable bonds (**P(S4,25)**) and one with 75% (**P(S4,75)**) (Table S4.3). Together with the previous

materials prepared with 0, 50 and 100% cleavable bonds, a large set of thermoset materials with controlled degradability was thus available for this study. As can be seen in Figure 4.6-b,c, the material composed of solely thioether functionalities did not degrade at 25 and 60 °C, nor in neutral nor in acidic media (Figure S4.51-a,b). When exposed to higher temperatures (100 °C), the material was degraded in acidic environment, possibly by hydrolysis of the ester functionalities present in the tetrathiol crosslinker (Figure S4.51-c,d, S4.52). On the contrary, about 15% and 85% of the material containing exclusive *N,O*-acetal bonds degraded at 25°C in neutral and acidic environments after 4 days, respectively. Higher temperature (60 °C) led to an acceleration of the process, with complete degradation in minutes in acidic environment and complete degradation in 4 days in neutral environment (Figure 4.6-c,d). At 100 °C the material was degraded below 5 minutes in both acidic and neutral environments (Figure S4.51-c,d). While the material comprising a ratio of 25:75 *N,O*-acetals to thioethers behaved as expected, with degradation faster than the material with 0% *N,O*-acetals and slower than the material with 100% *N,O* acetals, the materials with 50 and 75% *N,O*-acetals were found to degrade faster than the material with 100 % *N,O*-acetals (Figure 4.6--c,d, Figure S4.51). This was attributed to the lower crosslinking density of this material as discussed above. The ability to control the speed and efficiency of the materials degradation shows the potential for these materials to be used as cargo delivery and their hydrolytic degradation.

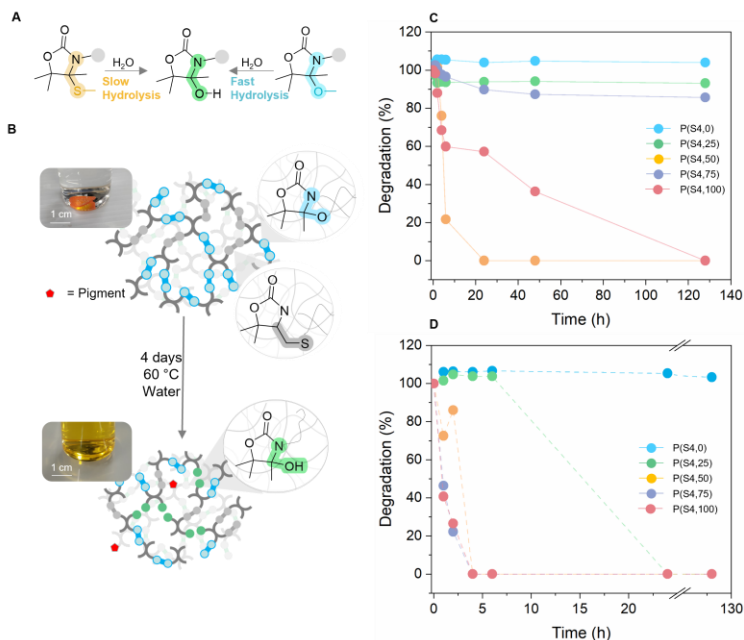


**Figure 4.6.** a) Scheme of the hydrolytic degradation of *N,S*-acetal and *N,O*-acetal moiety b) Scheme of the hydrolytic degradation of a material containing both *N,O*-acetal moieties and thioether bonds. Degradation of materials with 0 to 100% content in *N,O*-acetal linkages (**P(S4,0)** to **P(S4,100)**) under neutral (c) and acidic conditions (1M MSA) at 60 °C (d).

#### 4.3.4. DLP 3D Printing

Taking advantage of the fast-photocuring behaviour of the resins, we studied the printability of **P(S4,100)**. We analysed the photocuring behaviour of the resin using a Jacobs curve, a commonly used technique in the vat photopolymerization field to estimate the degree of light penetration and critical energy of a given resin.<sup>60</sup> The resin behaved well, with low critical energy and good light penetration (Figure 4.6-a), being able to form a 50  $\mu\text{m}$  layer in 2.5 s of exposure. 2.5D structures bearing grooves of 500, 250 and 100  $\mu\text{m}$  could be prepared by irradiating each layer for 2.5 s. The lines were found to be sharp, returning a satisfying resolution (Figure 4.7-b,c). A 3D printed gyroid (Figure 4.6-d,e,f) cube could be vat-3D printed using **P(S4,100)** as the formulation resin, proving the printability of these kinds of materials. While the XY resolution is satisfactory, the Z resolution should be optimised, by using commonly available light absorbers.<sup>61</sup> **P(S4,50)** behaved as well in 3D printing, with good resolution (Figure S4.53-a,b) and similar degree of penetration and critical energy to **P(S4,100)** (Figure S4.53-c,d,e), demonstrating the potential to print structures with tuneable degradation.

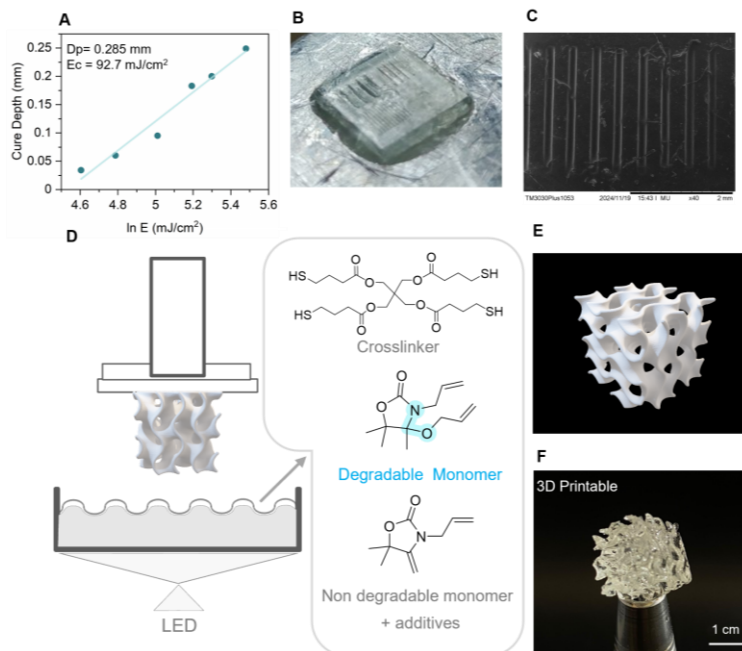


**Figure 4.7.** a) Jacobs curve for **P(S4,100)** d) Scheme of DLP printer; b) 3D printed structure for resolution optimisation; c) SEM images of 100  $\mu\text{m}$  lines; d) Scheme of the 3D printer and resin formulation; e) 3D structure of a gyroid cube; f) 3D printed gyroid cube manufactured using a MAX UV asiga DLP printer.

## 4.4. Conclusions

In this study, we presented a new type of CO<sub>2</sub>-derived CAN that enables the introduction of hydrolytic degradation in oxazolidone-based materials and their manufacturing through 3D printing. We first characterise the kinetics of bond formation via <sup>1</sup>H-NMR and find quick reactivity, with the reaction plateauing in under 1 minute although with low to medium conversions (below 50%). The conversion was found to be mainly influenced by the steric hindrance of the alcoholic partner, and it could be increased by adding excess alcohol. DFT supported the experimental results, highlighting a low stabilisation of the product compared to the starting materials (-50.2 kJ/mol) and small  $\Delta G_{\text{RDS}}^\ddagger$  (-12.6 kJ/mol), attesting to the fast kinetics. The dynamic behaviour of the bond was then clarified to be dissociative with an activation energy of 38.9 kJ/mol. With this knowledge in mind the *N,O*-acetal bond was installed in a series of materials with a fast-photocuring procedure (curing time below 60 s), enabling their 3D printing. We studied their thermal and mechanical properties, finding  $T_g$  ranging from -0.2 to 19.5 °C and Young's Moduli from 2.8 to 27.4 MPa. Exploiting the dissociative character of the *N,O* acetal bond, we recycled the material, with retention of similar IR spectra and  $T_g$  value ( $T_{g, \text{virgin}} = 8.8$  °C,  $T_{g, \text{reprocessed}} = 7.9$  °C), however we observed a loss in mechanical properties ( $E'_{\text{virgin}} = 2549$  MPa,  $E'_{\text{reprocessed}} = 1926$  MPa). A key property of *N,O*-acetal, when compared to previously reported CO<sub>2</sub>-derived CANs, is that they can be hydrolytically degraded. We studied this behaviour using both small molecules and materials and found a tuneable degradation rate promising application in cargo delivery and degradable polymers. Further work is now focusing on improving the recyclability and accessibility of this type of material.

## 4.5. Materials and Methods

### 4.5.1. Materials

2-Methyl-3-butyn-2-ol (Sigma, 98%), 4-methyl-2-pentanol (>99%, Sigma), Allylamine (Sigma, 98%), Copper Iodide (Sigma, 98%), Methyl 3-mercaptopropionate (Sigma, 98%), Phenylbis(2,4,6-trimethylbenzoyl) phosphine oxide (BAPO, Ciba), Methanol (HPLC grade, Sigma), Allyl Alcohol (anhydrous, >99%, Sigma), Benzyl Alcohol (Anhydrous, >99%, Sigma), 1-Propanol (Anhydrous, >99%, Sigma), 1-Hexanol (Anhydrous, >99%, Sigma), Methanesulfonic acid (Sigma, >99%), Trimethylolpropane tris(3-mercaptopropionate) (S3, Sigma, ≥95%), Pentaerythritol tetrakis(3-mercaptopropionate) (S4, Sigma, ≥95%), Dipentaerythritol Hexakis(3-mercaptopropionate) (S6, TCI, >93%), and Sulfuric Acid (Sigma, >95%), Triethylamine (TEA, Sigma, 99.5%), 1,8-Diazabicyclo[5.4.0]undec-7-ene (DBU, Sigma, 98%) were used without further purification

### 4.5.2. Methods

**Nuclear magnetic resonance (NMR) spectroscopy.**  $^1\text{H}$ - and  $^{13}\text{C}$ -NMR analyses were performed on a Bruker Avance 300 MHz spectrometer at 25 °C in the Fourier transform mode using  $\text{CDCl}_3$  or  $\text{DMSO}-d_6$  as solvents. High temperature  $^1\text{H}$  NMR experiments were carried out on a Bruker Avance 500 MHz.

**HRMS (ESI)** data were acquired in SCAN mode, using a mass range 50–1000 u in resolution mode ( $\text{FWHM} \approx 20,000$ ) and a scan time of 0.1 s. The source temperature was set to 120 °C and the desolvation temperature to 350 °C. The capillary voltage was 0.7 kV and the cone voltage 15 V. Nitrogen was used as the desolvation and cone gas at flow rates of 600 L/h and 10 L/h, respectively. Before analysis, the mass



## 4

spectrometer was calibrated with a sodium formate solution. A leucine-enkephalin solution was used for the lock mass correction, monitoring the ions at mass-to-charge ratio ( $m/z$ ) 556.2771 and 278.1141. All of the acquired spectra were automatically corrected during acquisition based on the lock mass. The samples were dissolved in the corresponding solvent at a concentration of 1 mg/ml and diluted to 20  $\mu\text{g/mL}$  for the analysis.

**Gel content (GC).** Films prepared as described in the experimental section were cut in rectangular shapes ( $\sim 120$  mg) and weighted ( $m_1$ ) before immersing 48 h in tetrahydrofuran. After weighing, the swelled films ( $m_2$ ) were dried in a vacuum oven at 60  $^{\circ}\text{C}$  for 24 h. The films were weighed once again ( $m_3$ ). Swelling (SI) and Gel content (GC) were calculated with equation 2 and 3, respectively:

$$SI = 100 * m_2 / m_1 \quad (2)$$

$$GC = 100 * m_3 / m_1 \quad (3)$$

**Tensile tests** were carried out on dogbone samples (see Preparation of Films below) (ASTM D638 TYPE V) in an Instron 5569 tensile tester (Instron, Norwood, MA, USA). Young's modulus, Tensile strength ( $\sigma_t$ ), Yield strength ( $\sigma_y$ ), and strain at break ( $\epsilon_b$ ) were determined using Bluehill software from the load-displacement curves at a crosshead speed of 10 mm/min. A minimum of three tensile specimens were tested for each reported value.

**Fourier Transform Infrared Spectroscopy (FT-IR) spectra** were recorded on a Nicolet iS20 Spectrometer using Attenuated Total Reflection (ATR) at a resolution of 4  $\text{cm}^{-1}$  and a total of 32 interferograms. The same instrument was used to acquire real/time

FTIR data. Spectra were acquired every 5 seconds by averaging 4 spectra. The spectra at high temperature were obtained on a Nicolet 6700FT-IR spectrophotometer equipped with a specap variable temperature transmission cell. Spectra were recorded in the range of 4000 and 400  $\text{cm}^{-1}$  with a spectrum resolution of 4  $\text{cm}^{-1}$ , and a total of 64 interferograms.

**Photorheology** was performed on an ARG2. A LED UV-curing accessory centered at 365 nm ( $20 \text{ mW/cm}^2$ ) was used together with an acrylic transparent bottom plate and a single use aluminum plate (20 mm). The measurement was performed in the linear viscoelastic regimen with frequency of 1 Hz with a gap of 400  $\mu\text{m}$ . To determine the viscosity of the formulated resins, a 1° 40 mm cone geometry was used. The shear rate window was from 1 to 100  $\text{s}^{-1}$ .

**Jacobs Curve** were obtained by placing a drop of resin on a glass coverslip and irradiated directly from below at different exposure times with a 2 mm circular beam using the spot timer of the ASIGA MAX-UV DLP 3D printer centered at 385 nm, giving an irradiance of  $\sim 20 \text{ mW/cm}^2$ . The thickness of the photocured resin was then measured with an Evanem Dloett electronic micrometer and the depth of cure was plotted against the logarithm of the light intensity for irradiation time.

**DLP Printing** A commercial Asiga Max-UV DLP 3D printer with a LED source centered at 385 nm ( $20 \text{ mW/cm}^2$ ) was used to 3D print the resin. The 3D objects were sliced on the Asiga composer with 6.5 s burn-in layer, 2.5 s exposure time and 50  $\mu\text{m}$  layer thickness at an intensity of  $20 \text{ mW/cm}^2$ . The printed objects were washed thoroughly with Isopropanol to remove unreacted monomers and postcured using a low-pressure mercury vapor lamp ( $2 \text{ mW/cm}^2$ , centered around 365 nm)

**Differential Scanning Calorimetry** was performed on a TA Instruments DSC 250 calibrated with indium, and the curves were

## 4

analyzed using the Trios software. A ramp of 10 °C/min from -20 to 200 was used.

**Dynamic Mechanical Analysis (DMA)** was performed on a DMA Q800. A 10 mm x 2 mm x 0.7 mm (l x w x t) was placed in a tension film clamp. An oscillation amplitude of 15  $\mu$ m and a static force of 0.01 N were employed. A ramp of 3 °C/min was used from -20 to 175 with a frequency of 1 Hz.  $T_g$  was measured as the peak in the Tan delta curve.

### 4.5.3. Small molecule studies

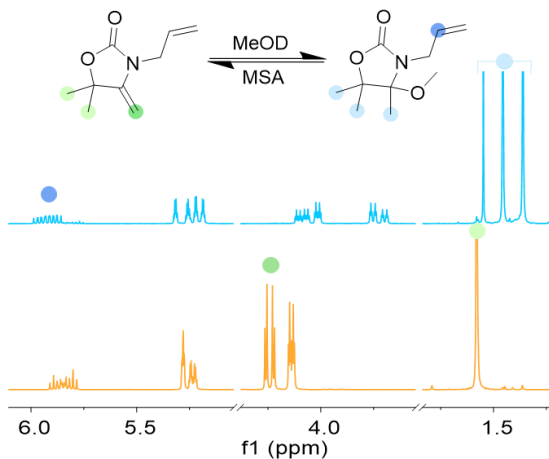


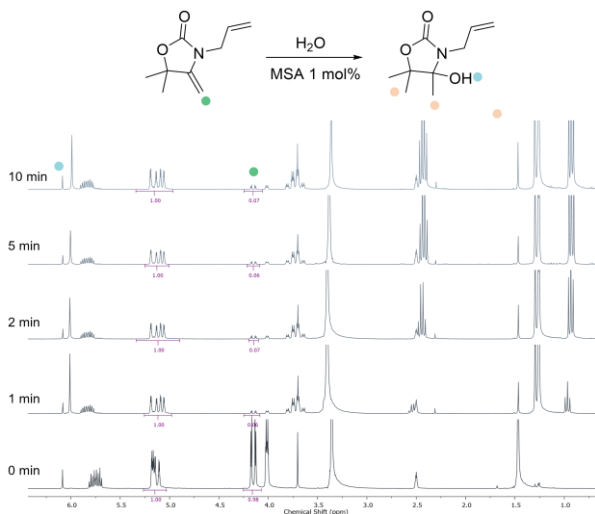
**Figure S4.1.**  $^1\text{H}$  NMR spectra pre and post addition of MSA of Allyl Oxazolidone in MeOD (0.18 M, 1 mol% MSA).

The conversion was calculated with Equation 1 (where  $I_t$  is the integral at time  $t$  and  $I_0$  the integral at time 0) by taking into consideration the signal of the  $\text{CH}_3$  of **AlLOx** (1.55 ppm). The signals were normalized using the signal of the allyl bond (multiplet, 5.16 ppm).

$$\text{Conversion (\%)} = \frac{I_t}{I_0} * 100 \quad (1)$$

#### 4.5.4. Hydration of **AlLOx**

**AlLOx** (1 eq) was mixed with water (1 eq). MSA (1 mol%) was added to the reaction and the reaction was stirred at rt. Aliquots were sampled at time 0, 1, 2, 5 and 10 min, quenched with TEA (10  $\mu\text{L}$ ) before being dissolved in deuterated  $\text{DMSO}-d_6$  (0.5 mL).



## 4

**Figure S4.2.**  $^1\text{H}$  NMR kinetics of hydration of **AlLOx** (conditions:  $[\text{AlLOx}]/[\text{H}_2\text{O}] = 1:1$ , 1 mol% MSA,  $25^\circ\text{C}$ ).

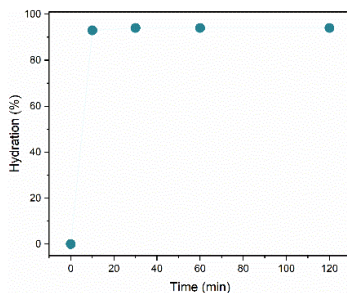


**Figure S4.3.** Hydration over time of **AlLOx** (conditions:  $[\text{AlLOx}]/[\text{H}_2\text{O}] = 1:1$ , 1 mol% MSA,  $25^\circ\text{C}$ ).

### 4.5.5. Alcohol Screening Model Reactions

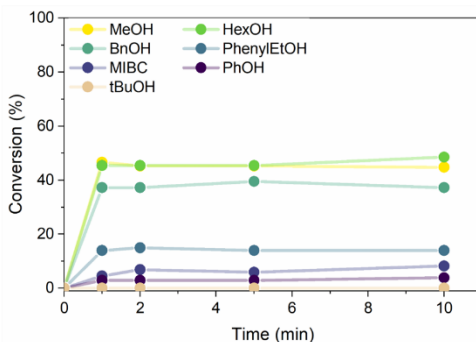


**Figure S4.4.** a)  $^1\text{H}$  NMR kinetics of the reaction between **AlLOx** and a variety of alcoholic partners (MeOH=methanol, HexOH= Hexanol, BnOH=Benzyl Alcohol, MIBC= 4-methyl-2-pentanol, tBuOH= tert-

butanol, PhenyleTOH= Phenyl Ethyl Alcohol, PhOH=Phenol) (conditions:  $[AlIOx]/[ROH] = 1:1$ , 1 mol% MSA, 25°C).

Model reactions between **AlIOx** and a set of alcohols were carried out. The two components were mixed in an argon-filled glovebox in equal OH to double bond ratio in bulk with the catalyst. Aliquots of the reaction mixture were sampled over time. The reactions were monitored by  $^1H$ -NMR spectroscopy to determine the conversion in the product.

For all reaction the conversion was calculated with Equation 1 (where  $I_t$  is the integral at time  $t$  and  $I_0$  the integral at time 0) by taking into consideration the signal of the  $CH_2$  of exovinylene double bond (3.98 ppm). The signals were normalized using the signal of the allyl bond (multiplet, 5.16 ppm).

*Methanol kinetics:* **AlIOx** (1 eq), anhydrous methanol (1.0 eq) and MSA (1 mol%) were mixed in a glass vial under argon atmosphere. The mixture was sampled at 0, 1, 2, 5, 10 min and immediately quenched with 10  $\mu$ L of DBU before being dissolved in  $DMSO-d_6$ .

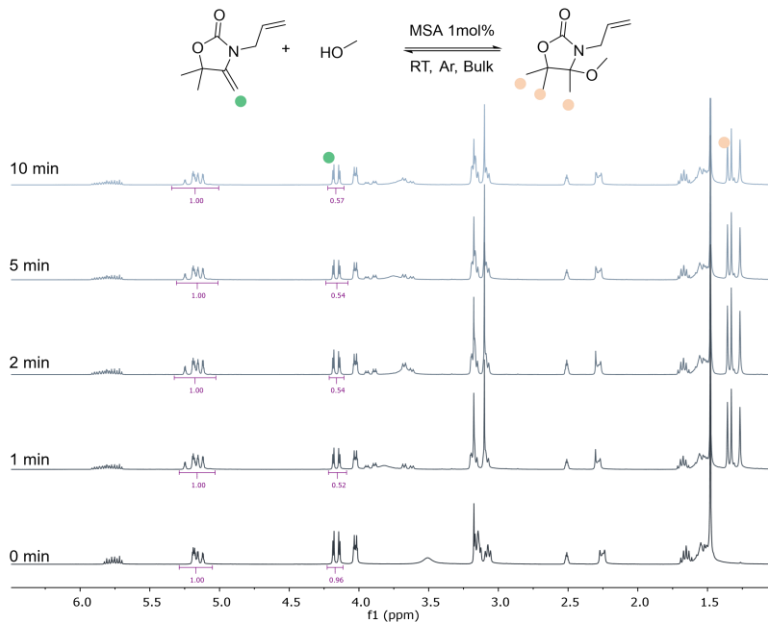


**Figure S4.5.**  $^1\text{H}$  NMR kinetics of the reaction between **Allox** and Methanol (conditions:  $[\text{Allox}]/[\text{ROH}] = 1:1$ , 1 mol% MSA,  $25^\circ\text{C}$ ).

**1-Hexanol kinetics:** **Allox** (1 eq), anhydrous 1-hexanol (Distilled over  $\text{CaH}_2$ , 1.0 eq) and MSA (1 mol%) were mixed in a glass vial under argon atmosphere. The mixture was sampled at 0, 1, 2, 5, 10 min and immediately quenched with 10  $\mu\text{L}$  of DBU before being dissolved in  $\text{DMSO-}d_6$ .

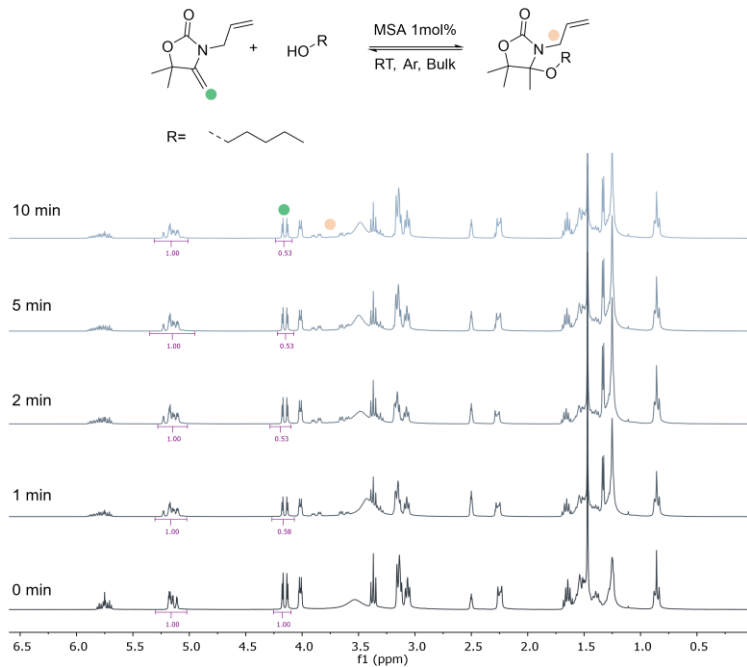


**Figure S4.6.**  $^1\text{H}$  NMR kinetics of the reaction between **AlLOx** and Hexanol (conditions:  $[\text{AlLOx}]/[\text{ROH}] = 1:1$ , 1 mol% MSA,  $25^\circ\text{C}$ ).



## 4

**Benzyl Alcohol kinetics:** **AlloX** (1 eq), anhydrous Benzyl Alcohol (Distilled over  $\text{CaH}_2$ , 1.0 eq) and MSA (1 mol%) were mixed in a glass vial under argon atmosphere. The mixture was sampled at 0, 1, 2, 5, 10 min and immediately quenched with 10  $\mu\text{L}$  of TEA before being dissolved in  $\text{DMSO}-d_6$ .

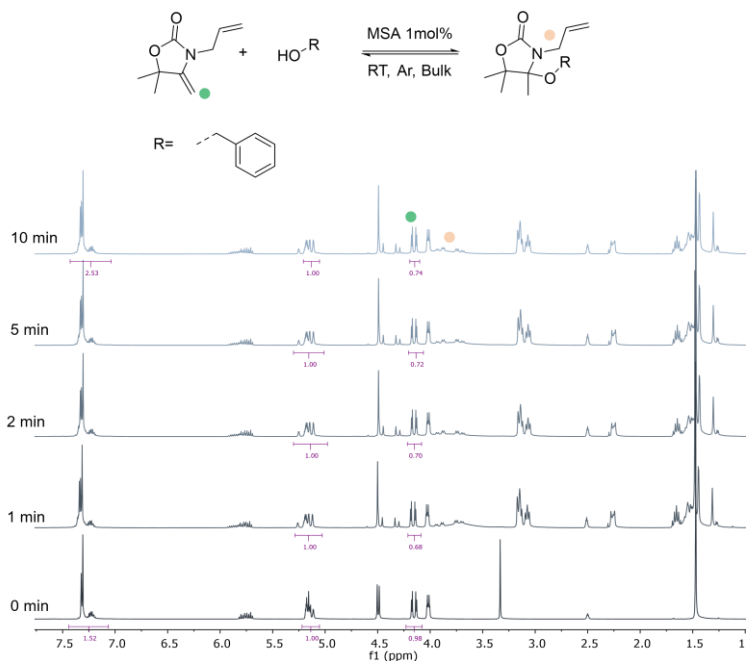


**Figure S4.7.**  $^1\text{H}$  NMR kinetics of the reaction between **AlloX** and Benzyl alcohol (conditions:  $[\text{AlloX}]/[\text{ROH}] = 1:1$ , 1 mol% MSA,  $25^\circ\text{C}$ ).

**Benzyl Ethyl Alcohol kinetics:** **AlLOx** (1 eq), anhydrous Benzyl Ethyl Alcohol (Distilled over  $\text{CaH}_2$ , 1.0 eq) and MSA (1 mol%) were mixed in a glass vial under argon atmosphere. The mixture was sampled at 0, 1, 2, 5, 10 min and immediately quenched with 10  $\mu\text{L}$  of TEA before being dissolved in  $\text{DMSO-}d_6$ .

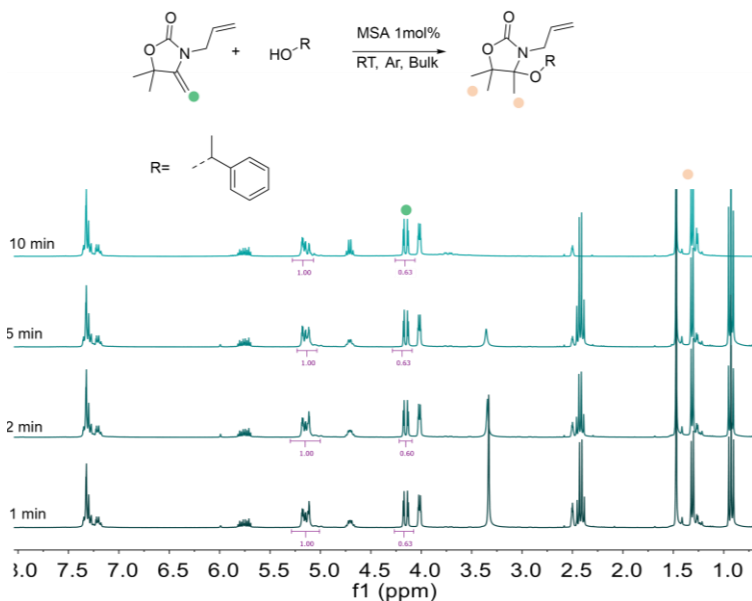


**Figure S4.8.**  $^1\text{H}$  NMR kinetics of the reaction between **AlLOx** and Benzyl Ethyl alcohol (conditions:  $[\text{AlLOx}]/[\text{ROH}] = 1:1$ , 1 mol% MSA,  $25^\circ\text{C}$ ).

**2-Methyl-4-Pentanol kinetics:** **AlLOx** (1 eq), anhydrous 2-Methyl-4-Pentanol (Distilled over CaH<sub>2</sub>, 1.0 eq) and MSA (1 mol%) were mixed in a glass vial under argon atmosphere. The mixture was sampled at 0, 1, 2, 5, 10 min and immediately quenched with 10  $\mu$ L of TEA before being dissolved in DMSO-*d*<sub>6</sub>.

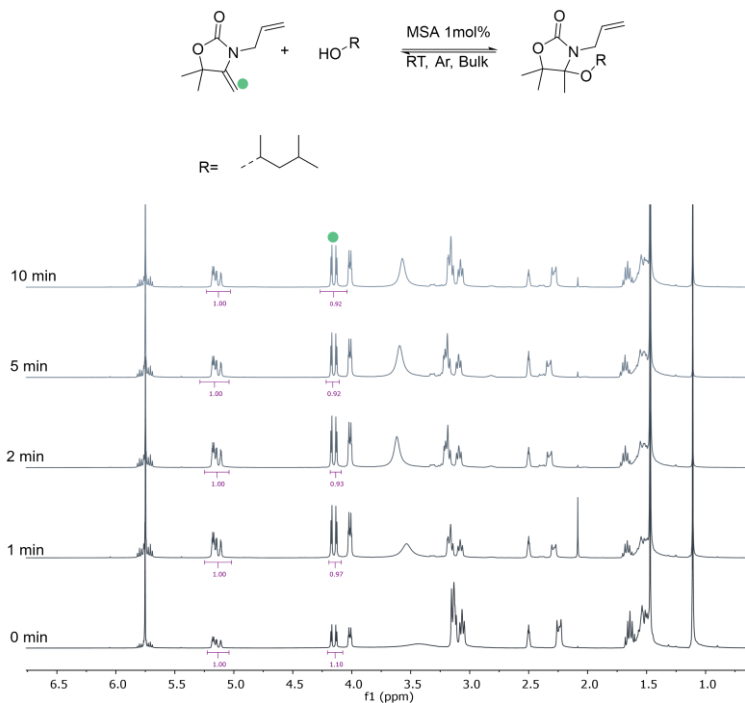


**Figure S4.9.** <sup>1</sup>H NMR kinetics of the reaction between **AlLOx** and MIBC (conditions: [AlLOx]/[ROH] = 1:1, 1 mol% MSA, 25°C).

**Phenol kinetics:** **AlLOx** (1 eq), phenol (recrystallised from Toluene, 1.0 eq) and MSA (1 mol%) were mixed in a glass vial under argon atmosphere. The mixture was sampled at 0, 1, 2, 5, 10 min and immediately quenched with 10  $\mu$ L of TEA before being dissolved in DMSO- $d_6$ .

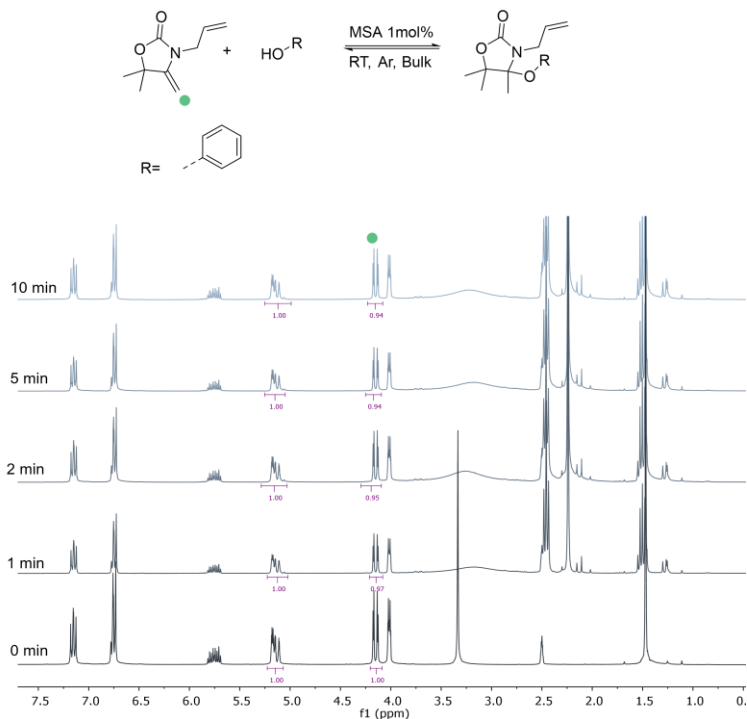


**Figure S4.10.**  $^1\text{H}$  NMR kinetics of the reaction between **AlLOx** and Phenol (conditions:  $[\text{AlLOx}]/[\text{ROH}] = 1:1$ , 1 mol% MSA,  $25^\circ\text{C}$ ).

# 4

**Tert-Butanol kinetics:** **AlLOx** (1 eq), anhydrous Tert-Butanol (Distilled over  $\text{CaH}_2$ , 1.0 eq) and MSA (1 mol%) were mixed in a glass vial under argon atmosphere. The mixture was sampled at 0, 1, 2, 5, 10 min and immediately quenched with 10  $\mu\text{L}$  of TEA before being dissolved in  $\text{DMSO}-d_6$ .

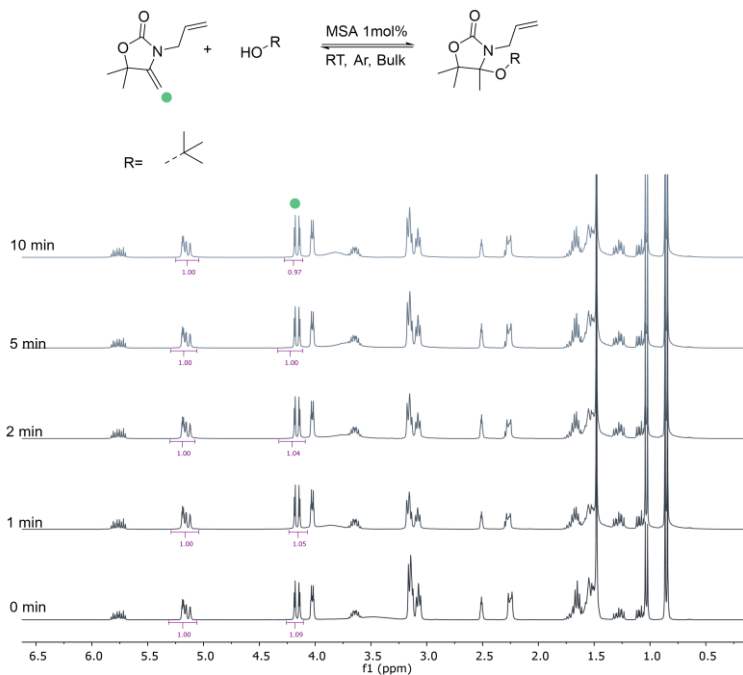


**Figure S4.11.**  $^1\text{H}$  NMR kinetics of the reaction between **AlLOx** and Tert butanol (conditions:  $[\text{AlLOx}]/[\text{ROH}] = 1:1$ , 1 mol% MSA,  $25^\circ\text{C}$ ).

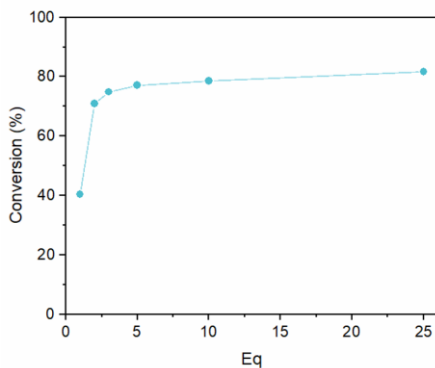
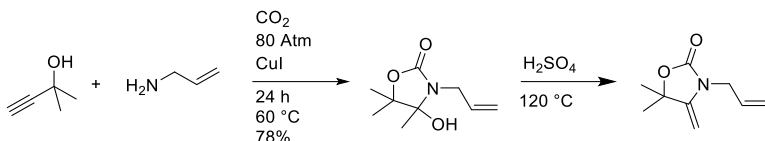


**Figure S4.12.** Conversion vs equivalent of methanol for the reaction between **AlLOx** and Methanol (dry). Conditions: Glovebox, 25 °C, 1 mol% MSA, 15 min reaction.

## 4

### 4.5.6. Synthetic Procedures

#### 4.5.6.1. Synthesis of **AlIOx**



*Scheme S4.1.* Synthesis of **AlIOx**.

3-allyl-5,5-dimethyl-4-methyleneoxazolidin-2-one (**AlIOx**) was prepared by adapting Jiang *et al.* procedure.<sup>62</sup> 2-Methyl-3-butyn-2-ol (84.1 g, 100 mmol, 1 eq), allyl Amine (60 g, 105 mmol, 1.05 eq) and copper iodide (10 g, 5 mol%) were loaded in a stainless-steel autoclave. CO<sub>2</sub> was injected at a pressure of 80 atm and a temperature of 60 °C under mechanical stirring. After 24 h the reaction vessel was depressurized, and the deep red mixture was distilled with a short path distillation apparatus at 120 °C over sulfuric acid (0.5 mL) under vacuum. The target material was obtained as a colourless oil (130 g, 78% yield) and stored in a freezer (-18 °C).

<sup>1</sup>H-NMR (300 MHz, DMSO-*d*<sub>6</sub>) δ 5.76 (m, 1H), 5.26 – 4.99 (m, 2H), 4.22 – 4.10 (m, 3H), 4.02 (dt, *J* = 5.0, 1.7 Hz, 2H), 1.47 (s, 9H). <sup>13</sup>C-NMR (75 MHz, DMSO) δ 154.48, 149.72, 131.17, 116.58, 81.92, 80.31, 42.82, 27.52. IR: 2980, 1760, 1680, 1642. Mp (DSC): 6 °C.

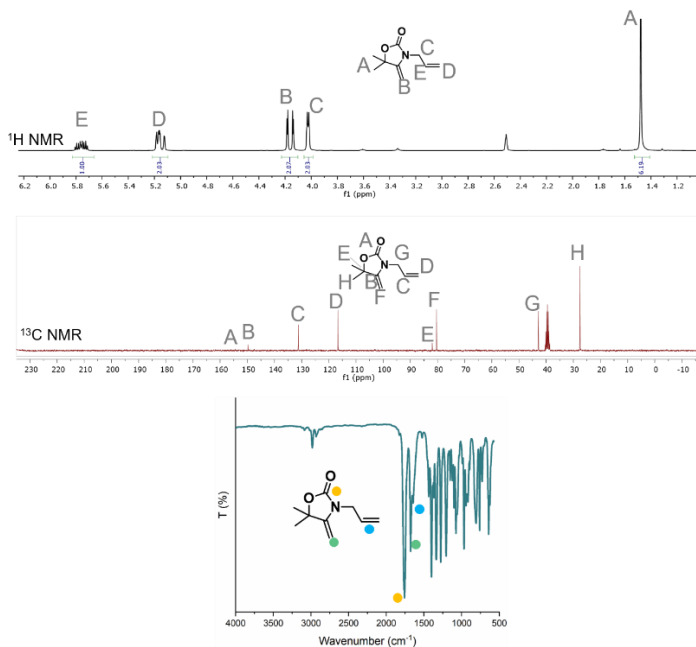
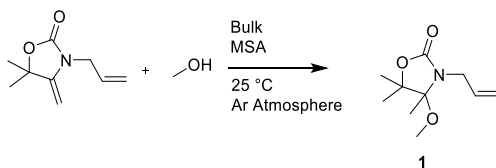


Figure S4.13. Characterisation of **Allox**: <sup>1</sup>H-NMR, <sup>13</sup>C NMR, IR.

#### 4.5.6.2. Synthesis of **1**



Scheme S4.2. Synthesis of **1**.



## 4

3-allyl-5,5-dimethyl-4-methyleneoxazolidin-2-one (**AlLOx**) (0.5 g, 3 mmol, 1 eq), anhydrous methanol (0.5 g, 15 mmol, 5 eq) and MSA (3 mg, 1 mol%) were mixed in a glass vial under argon atmosphere. The mixture was stirred for 15 min before being quenched with TEA (50  $\mu$ L). The resulting mixture was diluted with ethyl acetate (25 mL) and washed thrice with water (3x25 mL), once with brine (25 mL). The organic phase was separated and dried over  $\text{MgSO}_4$  before being evaporated *via* rotary evaporation. The resulting transparent oil was purified by column chromatography (8.5:1.5 Hexane:Ethyl Acetate,  $\text{I}_2$  and Vanillin stain,  $\text{I}_2$  was used as it selectively stains **AlLOx** but not its derivatives), a colourless oil was obtained (0.36g, 60% yield)

**$^1\text{H}$  NMR** (300 MHz,  $\text{DMSO-d}_6$ )  $\delta$  5.85 (m, 1H), 5.35 – 4.98 (m, 2H), 3.78 (m, 2H), 3.10 (s, 3H), 1.35 (s, 3H), 1.33 (s, 3H), 1.26 (s, 3H);  **$^{13}\text{C}$  NMR** (75 MHz,  $\text{MeOD}$ )  $\delta$  187.15, 159.50, 134.81, 131.94, 117.52, 117.35, 95.03, 87.17, 49.85, 49.57, 49.28, 49.00, 48.72, 48.43, 48.15, 44.45, 43.97, 28.12, 26.37, 19.90, 18.93. **HRMS (ESI)**  $m/z$ :  $[\text{M-H}]^+$  calcd for  $\text{C}_{10}\text{H}_{17}\text{NO}_3$ , 200.183; found, 200.112

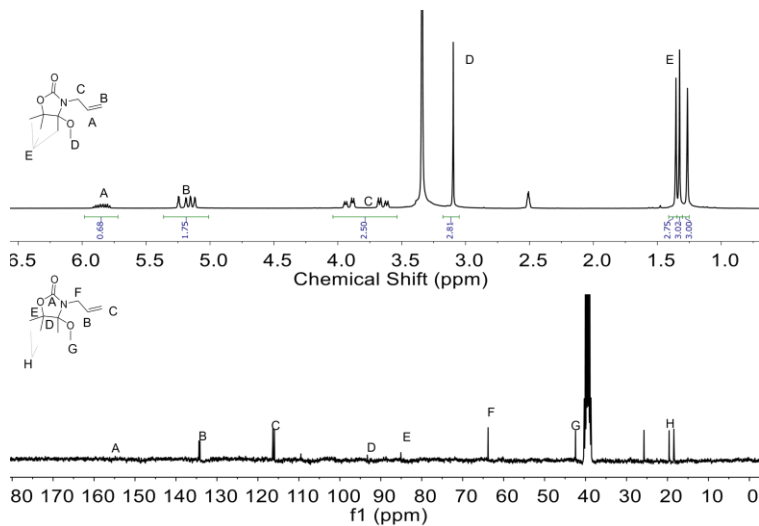
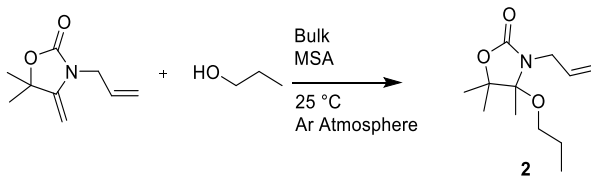


Figure S4.14. <sup>1</sup>H NMR of **1** (top) and <sup>13</sup>C NMR (bottom).

#### 4.5.6.3. Synthesis of **2**



Scheme S4.3. Synthesis of **2**.

**Allox** (0.5 g, 3 mmol, 1 eq), anhydrous 1-propanol (distilled over CaH<sub>2</sub>, 0.190 g, 3.1 mmol, 1.05 eq) and MSA (3 mg, 1 mol%) were mixed in a glass vial under argon atmosphere. The mixture was stirred for 15 min before being quenched with TEA (50 uL). The resulting mixture was diluted with ethyl acetate (25 mL) and washed thrice with water (3x25 mL), once with brine (25 mL). The organic phase was separated and dried over MgSO<sub>4</sub> before being evaporated *via* rotary evaporation. The resulting transparent oil was purified by column chromatography (8.5:1.5 Hexane:Ethyl Acetate, I<sub>2</sub> and Vanillin stain), a slight yellow oil was obtained (0.25g, 35% yield)

**<sup>1</sup>H NMR** δ 5.84 (m, 1H), 5.42 – 4.96 (m, 2H), 4.11 – 3.53 (m, 2H), 3.29 – 2.96 (m, 2H), 1.49 (q, *J* = 7.0 Hz, 2H), 1.35 (s, 3H), 1.34 (s, 3H), 1.26 (s, 3H), 0.87 (t, *J* = 7.4 Hz, 3H). **<sup>13</sup>C NMR** δ 156.30, 134.24, 116.20, 92.89, 84.98, 64.13, 42.33, 25.76, 22.52, 19.46, 18.53, 10.50. **HRMS (ESI)** *m/z*: [M-Na]<sup>+</sup> calcd for C<sub>12</sub>H<sub>21</sub>NO<sub>3</sub>, 250.289; found, 250.142

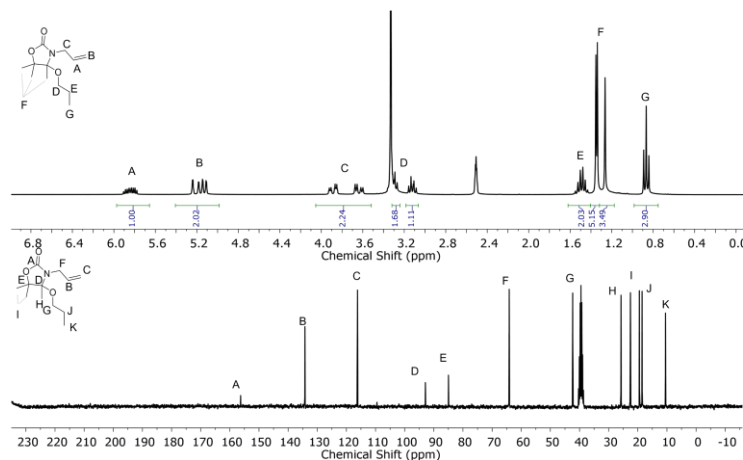
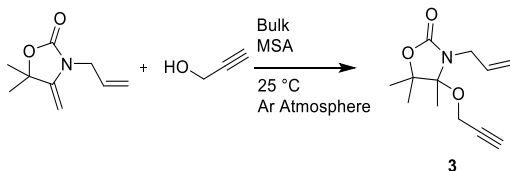


Figure S4.15. <sup>1</sup>H NMR of **2** (top) and <sup>13</sup>C NMR (bottom).

#### 4.5.6.4. Synthesis of 3-allyl-4,5,5-trimethyl-4-(prop-2-yn-1-yloxy)oxazolidin-2-one (**3**)



*Scheme S4.4.* Synthesis of **3**.

**AlLOx** (0.5 g, 3 mmol, 1 eq), anhydrous propargylic alcohol (distilled over  $\text{CaH}_2$ , 0.175 g, 3.1 mmol, 1.05 eq) and **MSA** (3 mg, 1 mol%) were mixed in a glass vial under argon atmosphere. The mixture was stirred for 15 min before being quenched with TEA (50  $\mu\text{L}$ ). The resulting mixture was diluted with ethyl acetate (25 mL) and washed thrice with water (3x25 mL), once with brine (25 mL). The organic phase was separated and dried over  $\text{MgSO}_4$  before being evaporated *via* rotary evaporation. The resulting transparent oil was purified by column chromatography (8.5:1.5 Hexane:Ethyl Acetate,  $\text{I}_2$  and Vanillin stain,  $\text{I}_2$ ), a yellow oil was obtained (0.288 g, 43% yield)

$^1\text{H}$  NMR (300 MHz,  $\text{DMSO-d}_6$ )  $\delta$  6.07 – 5.68 (m, 1H), 5.39 – 4.96 (m, 2H), 4.09 (qd,  $J$  = 15.6, 2.4 Hz, 2H), 3.82 (dddt,  $J$  = 59.8, 16.6, 6.0, 1.6 Hz, 2H), 3.45 (t,  $J$  = 2.4 Hz, 2H), 1.41 (s, 3H), 1.37 (s, 3H), 1.26 (s, 3H).  $^{13}\text{C}$  NMR (75 MHz,  $\text{DMSO}$ )  $\delta$  155.91, 134.07, 116.52, 93.96, 85.17, 80.16, 76.66, 51.66, 42.66, 40.34, 40.06, 39.78, 39.50, 39.22, 38.95, 38.67, 25.48, 19.75, 17.63. **HRMS (ESI)**  $m/z$ :  $[\text{M-H}]^+$  calcd for  $\text{C}_{12}\text{H}_{17}\text{NO}_3$ , 224.1282; found, 224.1281

4

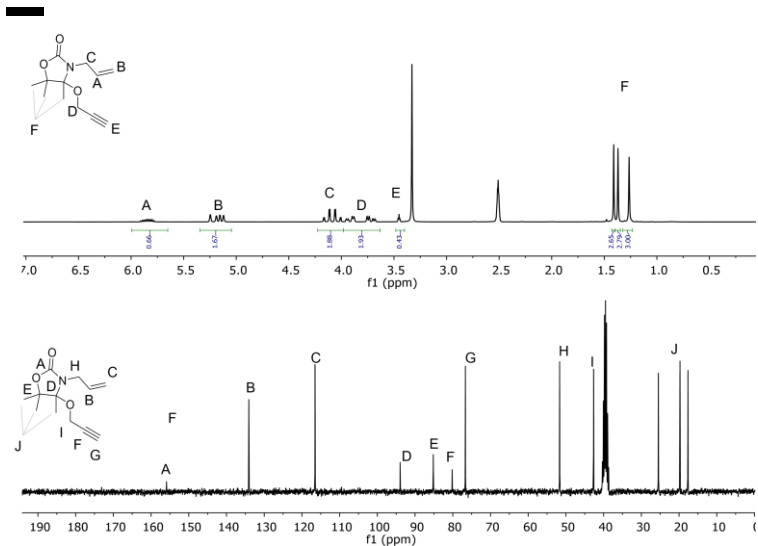
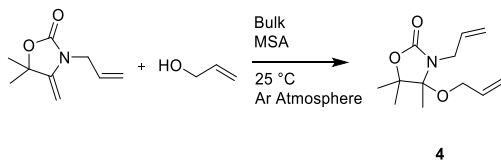


Figure S4.16. <sup>1</sup>H NMR of **3** (top) and <sup>13</sup>C NMR (bottom).

#### 4.5.6.5. Synthesis of 3-allyl-4-(allyloxy)-4,5,5-trimethyloxazolidin-2-one (**4**)



Scheme S4.5. Synthesis of **4**.

**AlLOx** (0.5 g, 3 mmol, 1 eq), anhydrous allyl alcohol (distilled over  $\text{CaH}_2$ , 0.181 g, 3.1 mmol, 1.05 eq) and MSA (3 mg, 1 mol%) were mixed in a glass vial under argon atmosphere. The mixture was stirred for 15 min before being quenched with TEA (50  $\mu\text{L}$ ). The resulting mixture was diluted with ethyl acetate (25 mL) and washed thrice with water (3x25 mL), once with brine (25 mL). The organic phase was separated and dried over  $\text{MgSO}_4$  before being evaporated *via* rotary evaporation. The resulting transparent oil was purified by column chromatography (8.5:1.5 Hexane:Ethyl Acetate,  $\text{I}_2$  and Vanillin stain), a colourless oil was obtained (0.324g, 48% yield)

**$^1\text{H}$  NMR** (300 MHz,  $\text{DMSO-d}_6$ )  $\delta$  6.10 – 5.66 (m, 2H), 5.40 – 4.89 (m, 4H), 4.02 – 3.58 (m, 4H), 1.38 (s, 3H), 1.36 (s, 3H), 1.28 (s, 3H).  **$^{13}\text{C}$  NMR** (75 MHz,  $\text{DMSO-d}_6$ )  $\delta$  156.21, 134.42, 134.17, 116.37, 115.99, 93.32, 85.12, 63.83, 42.47, 25.76, 19.63, 18.46. **HRMS (ESI)**  $m/z$ :  $[\text{M}-\text{H}]^+$  calcd for  $\text{C}_{12}\text{H}_{19}\text{NO}_3$ , 226.1440; found, 226.1438

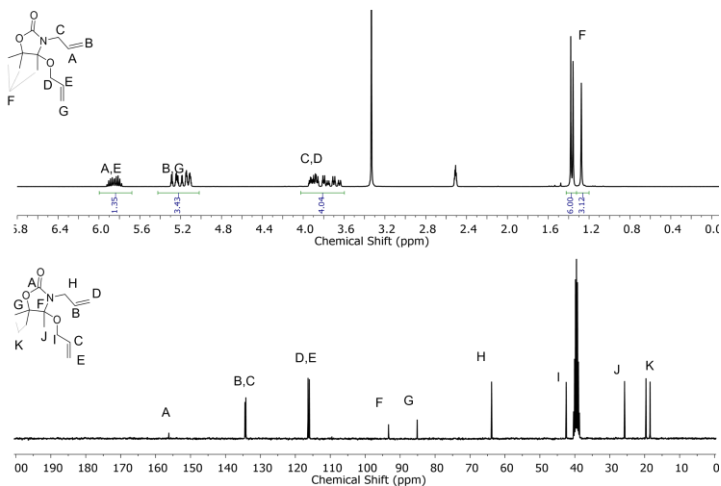
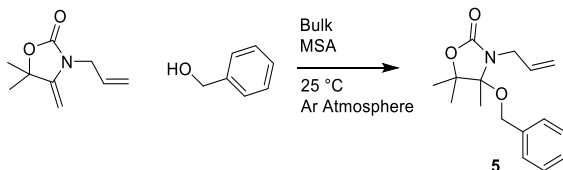


Figure S4.17.  $^1\text{H}$  NMR of **4** (top) and  $^{13}\text{C}$  NMR (bottom).

## 4

### 4.5.6.6. Synthesis of 3-allyl-4-(benzyloxy)-4,5,5-trimethyloxazolidin-2-one (**5**)



*Scheme S4.6.* Synthesis of **5**.

3-allyl-5,5-dimethyl-4-methyleneoxazolidin-2-one (**ALLOx**) (0.5 g, 3 mmol, 1 eq), anhydrous benzyl alcohol (distilled over  $\text{CaH}_2$ , 0.34 g, 3.1 mmol, 1.05 eq) and MSA (3 mg, 1 mol%) were mixed in a glass vial under argon atmosphere. The mixture was stirred for 15 min before being quenched with TEA (50  $\mu\text{L}$ ). The resulting mixture was diluted with ethyl acetate (25 mL) and washed thrice with water (3x25 mL), once with brine (25 mL). The organic phase was separated and dried over  $\text{MgSO}_4$  before being evaporated *via* rotary evaporation. The resulting transparent oil was purified by column chromatography (8.5:1.5 Hexane:Ethyl Acetate,  $\text{I}_2$  and Vanillin stain), a yellow oil was obtained (0.12 g, 15% yield)

**$^1\text{H}$  NMR** (300 MHz,  $\text{DMSO}-d_6$ )  $\delta$  7.51 – 7.13 (m, 5H), 6.03 – 5.70 (m, 1H), 5.42 – 4.97 (m, 2H), 4.61 – 4.21 (m, 2H), 3.96 – 3.63 (m, 2H), 1.44 (s, 6H), 1.31 (s, 3H).  **$^{13}\text{C}$  NMR** (75 MHz,  $\text{DMSO}$ )  $\delta$  156.21, 137.78, 134.16, 128.23, 127.43, 127.26, 116.57, 116.42, 93.53, 85.18, 80.29, 64.74, 42.81, 42.49, 40.34, 40.06, 39.78, 39.50, 39.22, 38.94, 38.66, 27.51, 25.73, 19.68, 18.36. **HRMS (ESI)**  $m/z$ :  $[\text{M}-\text{H}]^+$  calcd for  $\text{C}_{16}\text{H}_{22}\text{NO}_3$ , 276.1597; found, 276.1594

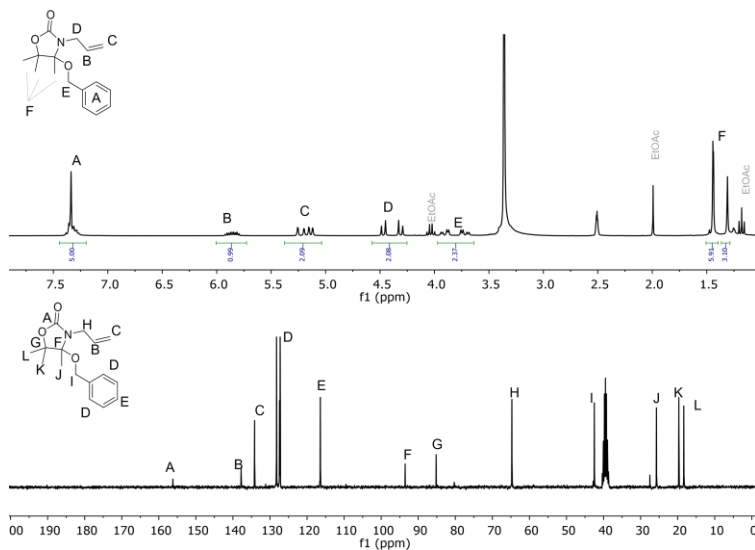
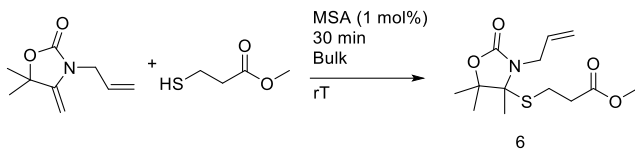


Figure S4.18.  $^1\text{H}$  NMR of **5** (top) and  $^{13}\text{C}$  NMR (bottom).

#### 4.5.6.7. Synthesis *N,S*-acetal model compound (**6**)



Scheme S4.7. Synthesis of **6**.



—

**Allox** (0.6 mmol, 1 eq) was mixed with methyl-3-mercaptopropionate (0.6 mmol, 1 eq) in a glass vial. MSA (1 mol%) was added to the mixture. The homogenous yellow mixture was stirred for 30 min. The resulting transparent mixture was diluted in EtOAc and was washed twice with subsaturated brine. The organic phases were dried over  $\text{MgSO}_4$  and evaporated using rotary evaporation. The resulting yellow viscous liquid was subjected to column chromatography (Hex:EtOAc 8:2, vanillin and iodine stain). The organic solvent was removed *via* rotary evaporation and the resulting product was obtained as a transparent viscous liquid (yield = 74%).

**$^1\text{H}$ -NMR** (300 MHz, DMSO- $d_6$ )  $\delta$  6.01 – 5.81 (m, 1H), 5.35 – 5.02 (m, 2H), 3.85 (dddt, 2H), 3.61 (s, 3H), 2.86 – 2.33 (m, 4H), 1.55 (s, 3H), 1.40 (s, 3H), 1.34 (s, 3H).  **$^{13}\text{C}$ -NMR** (75 MHz, DMSO)  $\delta$  171.50, 155.91, 134.34, 116.50, 85.38, 78.15, 51.55, 42.58, 40.33, 40.06, 39.78, 39.50, 39.22, 38.94, 38.66, 32.58, 24.92, 24.01, 23.01, 20.57 **HRMS (ESI)**  $m/z$ :  $[\text{M}-\text{H}]^+$  calcd for  $\text{C}_{17}\text{H}_{30}\text{NO}_6\text{S}_2\text{H}^+$ , 288.3740; found, 288.3742

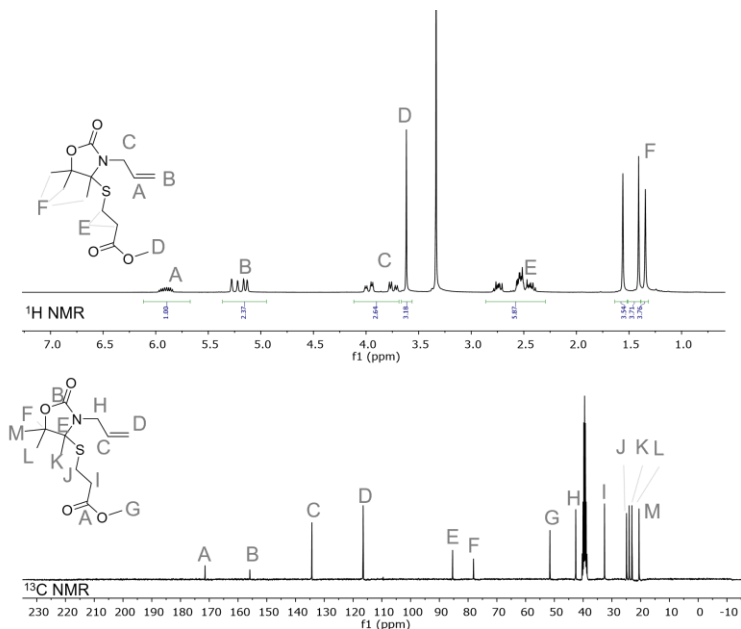


Figure S4.19. <sup>1</sup>H NMR of **6** (top) and <sup>13</sup>C NMR (bottom).

#### 4.5.7. Temperature Screening Model Reactions

Model reactions between **AlloX** and hexanol at different temperatures were carried out. The two components were mixed in an argon-filled glovebox in equal OH to double bond ratio in bulk with the catalyst. Aliquots of the reaction mixture were sampled over time and quenched with a base. The reactions were monitored by <sup>1</sup>H-NMR spectroscopy to determine the conversion in the product. For all reaction the conversion was calculated with Equation 1 by taking into consideration the signal of the CH<sub>2</sub> of exovinylene double bond (3.98 ppm). The signals were

## 4

normalized using the signal of the allyl bond (multiplet, 5.16 ppm). A Van't Hoff plot was built as previously reported.<sup>52</sup>

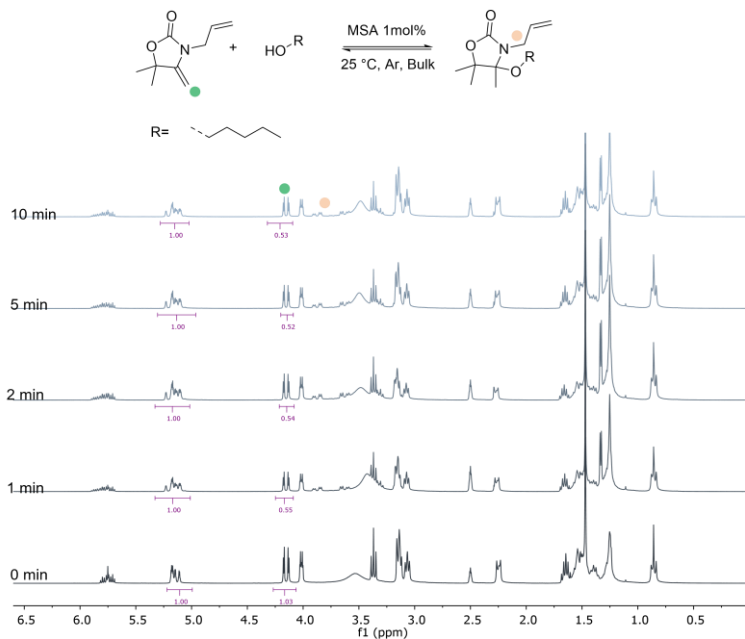


**Figure S4.20.** <sup>1</sup>H NMR kinetics of the reaction between **AlLOx** and Hexanol at 25 °C. (conditions: [AlLOx]/[HexOH] = 1:1, 1 mol% MSA, 25°C).

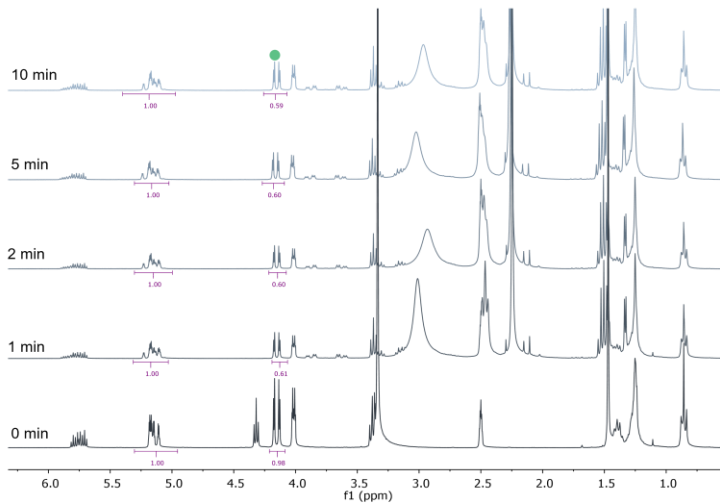
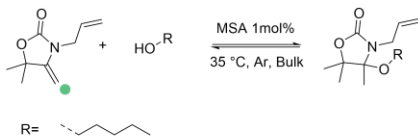


**Figure S4.21.**  $^1\text{H}$  NMR kinetics of the reaction between **Allox** and Hexanol at 35 °C (conditions:  $[\text{Allox}]/[\text{HexOH}] = 1:1$ , 1 mol% MSA, 35°C).

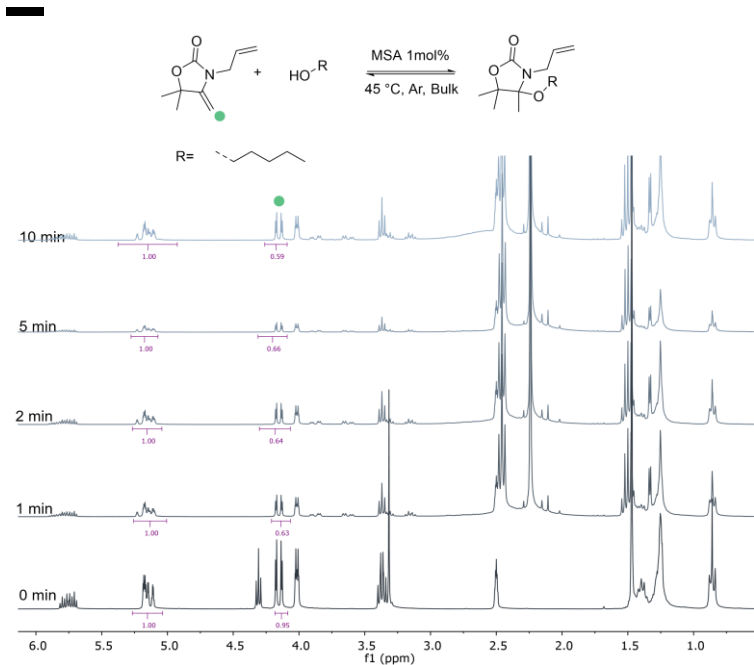


**Figure S4.22.**  $^1\text{H}$  NMR kinetics of the reaction between **Allox** and Hexanol at 45 °C. (conditions:  $[\text{Allox}]/[\text{HexOH}] = 1:1$ , 1 mol% MSA, 45 °C).

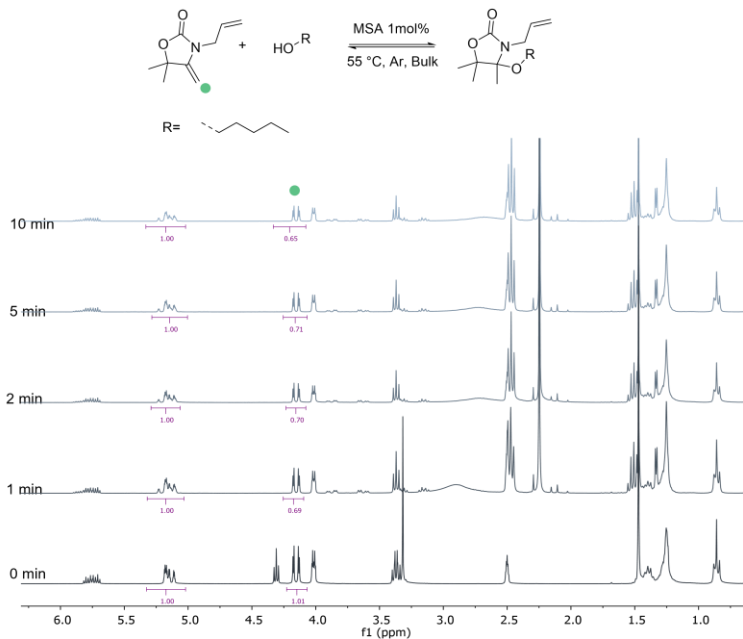


**Figure S4.23.**  $^1\text{H}$  NMR kinetics of the reaction between **AlLOx** and Hexanol at 55 °C. (conditions:  $[\text{AlLOx}]/[\text{HexOH}] = 1:1$ , 1 mol% MSA, 55°C).

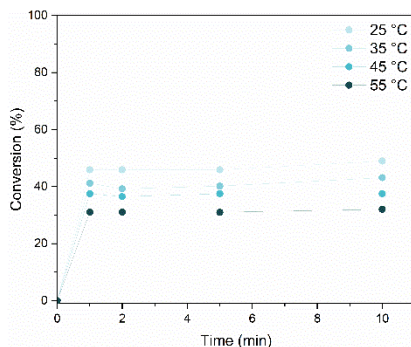


*Figure S4.24.* Kinetics of the reaction between Hexanol and **AlOx** at temperature ranging from 25 to 55 °C.

#### 4.5.8. DFT Modelling

All geometry optimizations were executed within density functional theory (DFT) using the  $\omega$ B97XD<sup>63</sup> functional combined with the 6-31+G(d)<sup>64</sup> basis set for all atoms. Frequency calculations were carried out at the same level of theory to validate that the optimized structures were minima or transition states on the potential energy surfaces. These frequencies were then used to evaluate the zero-point vibrational energy (ZPVE) and the thermal corrections to the enthalpy (H) and Gibbs free energy (G), at  $T = 298.15$  K, in the harmonic oscillator approximation. To refine the electronic energies, single-point calculations using the 6-311++G(2df,2p) basis set<sup>65</sup> were performed on the optimized structures. All the calculations were performed with the Gaussian 16 suite of programs. The molecular models used in the simulations compounds are depicted below.

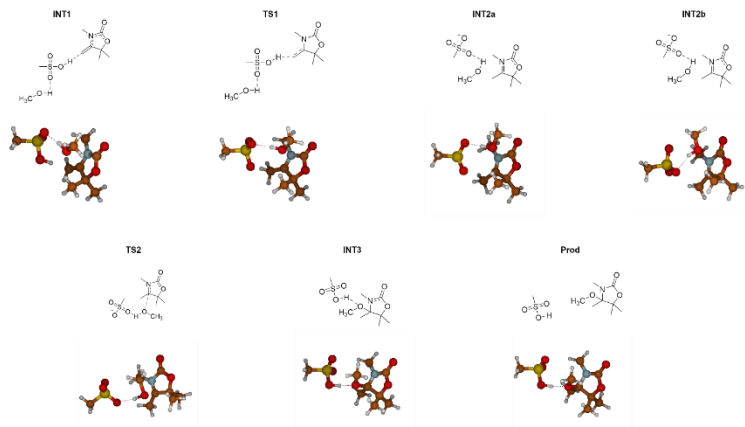


**Figure S4.25.** 2D and 3D structures of optimised intermediate and transition states of the modelled reaction path.

**Table S4.1.** Bond Length evolution along the reaction path for intermediates and transition states.



	SR	Int1	TS1	Int2a	Int2b	TS2	Int3	SP
C-C (1)	1.335	1.346	1.403	1.467	1.464	1.497	1.519	1.519
C-N (2)	1.384	1.368	1.320	1.293	1.292	1.318	1.431	1.431
N-C (3)	1.382	1.389	1.422	1.457	1.456	1.418	1.357	1.375
C-O (4)	1.205	1.203	1.195	1.189	1.189	1.192	1.206	1.207
C-O (5)	1.349	1.345	1.333	1.326	1.327	1.334	1.358	1.358



## 4

### 4.5.9. In situ NMR of dissociation of **4** with temperature

**4** was placed in a vial under argon atmosphere and its  $^1\text{H}$  NMR spectrum was measured at temperature interval of  $20^\circ\text{C}$  from  $20$  to  $100^\circ\text{C}$ . It was then dissolved in dry  $\text{DMSO}-d_6$ . The sample was given  $15$  min to equilibrate at each temperature before measuring its  $^1\text{H}$  NMR spectrum. For the sample containing  $1$  mol% MSA, the  $^1\text{H}$  NMR spectra was measured in situ by heating the same tube at different temperatures. A stock solution MSA was previously prepared and added directly to an NMR tube containing **4** and dry  $\text{DMSO}-d_6$  ( $0.18$  M).

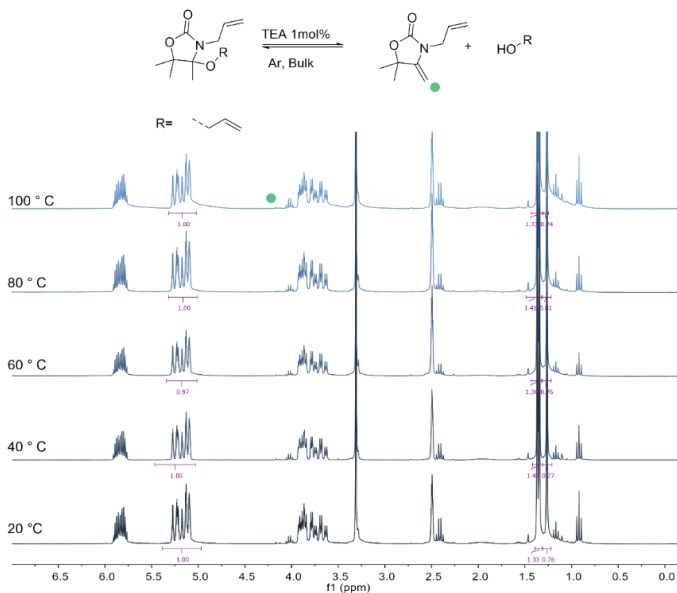


**Figure S4.26.**  $^1\text{H}$  NMR spectra of **4** at different temperatures in dry DMSO- $d_6$  with 1 mol% TEA.

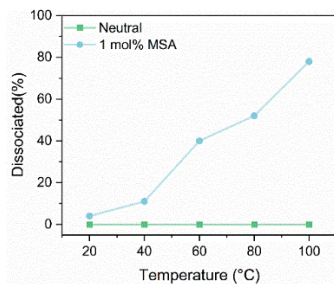
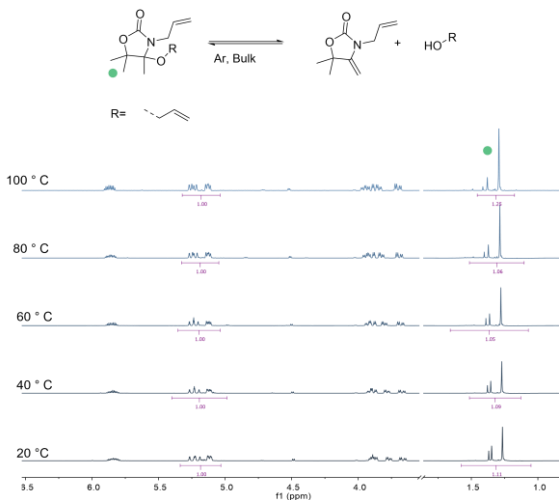


**Figure S4.27.** Dissociation of **4** at different temperatures in dry DMSO- $d_6$ .



# 4

**Figure S4.28.**  $^1\text{H}$  NMR spectra of **4** at different temperatures in dry  $\text{DMSO}-d_6$ .

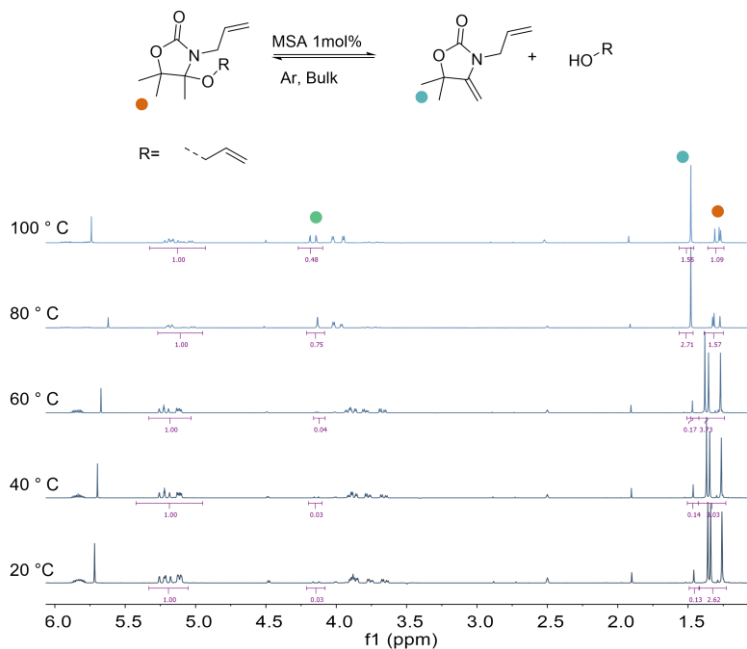


**Figure S4.29.**  $^1\text{H}$  NMR spectra of **4** at different temperatures in dry  $\text{DMSO}-d_6$  with 1 mol% MSA.

#### 4.5.10. Catalyst Screening

Model reactions between **AlLOx** and hexanol with different amounts of catalyst were carried out. MSA, TFA were screened at 1 mol% and 0.1 mol% concentration. The two components were mixed in an argon-filled glovebox in equal ROH to double bond ratio in bulk with the catalyst. Aliquots of the reaction mixture were sampled over time. The reactions were monitored by  $^1\text{H}$ -NMR spectroscopy to determine the conversion in the product.

For all reaction the conversion was calculated with Equation 1 by taking into consideration the signal of the  $\text{CH}_2$  of exovinylene double bond (3.98 ppm). The signals were normalized using the signal of the allyl bond (multiplet, 5.16 ppm).

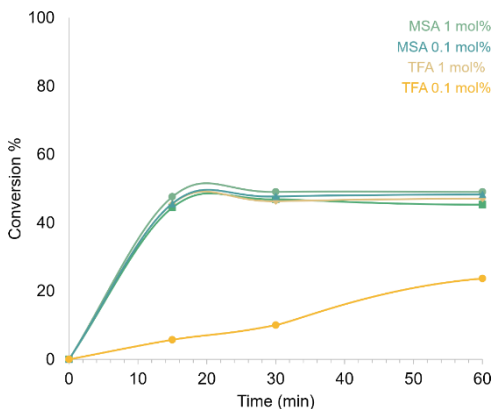


**Figure S4.30.** Conversion of the reaction between hexanol and **AlLOx** against time of a variety of catalyst (MSA, TFA) in two different concentrations (1 mol% and 0.1 mol%).

## 4.5.11. Exchange Reaction

Exchange reactions between **4** and methanol were carried out. The two components were mixed in an argon-filled glovebox with a ten-fold excess of methanol to **4**. The reaction was carried out in dry  $\text{CDCl}_3$  using TFA (0.1mol%) as catalyst. Aliquots of the reaction mixture were sampled over time. The reactions were monitored by  $^1\text{H}$ -NMR spectroscopy to determine the conversion in the product.

For all reaction the conversion was calculated with Equation 2 (where  $I_t$  is the integral at time  $t$  and 3 is the value of the integral when 100% exchange occurred) by taking into consideration the singlet of the  $\text{CH}_3$  of **1** (3.18 ppm). The signals were normalized using the signal of the allyl bond (multiplet, 5.16 ppm).

$$\text{Conversion (\%)} = \frac{I_t}{3} * 100 \quad (2)$$

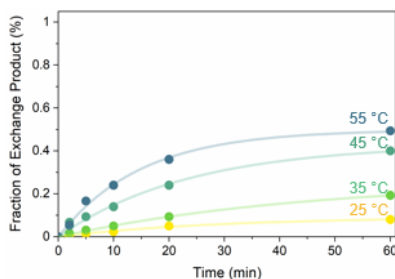


**Figure S4.31.** Fraction of exchanged product calculated from  $^1\text{H}$  NMR of the exchange reaction between **4** and methanol at temperature between 25 and 55 °C.

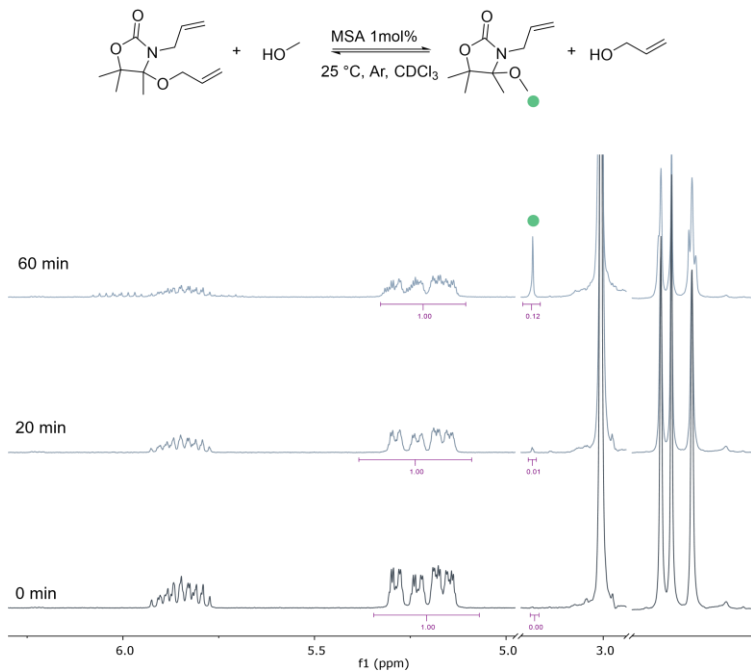


**Figure S4.32.** <sup>1</sup>H NMR kinetics of the exchange reaction between **4** and methanol at 25 °C.

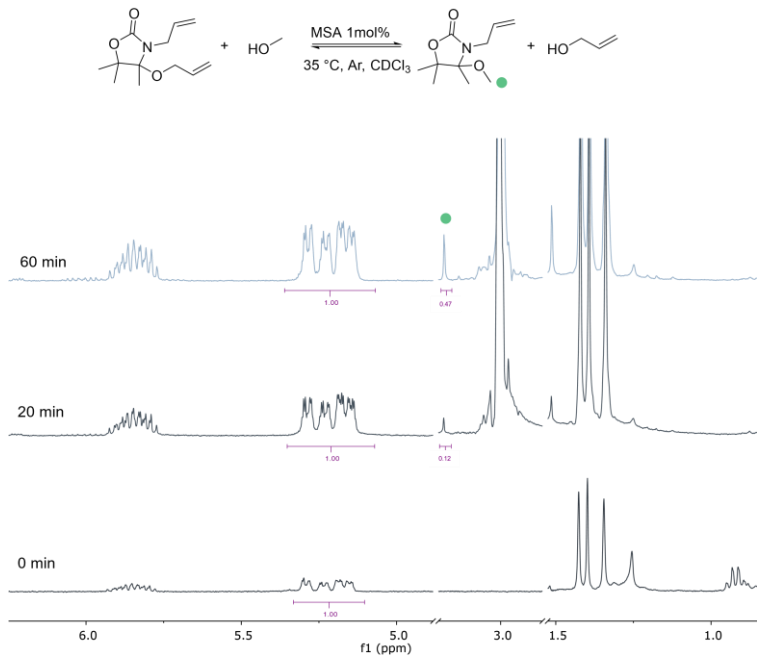


**Figure S4.33.** <sup>1</sup>H NMR kinetics of the exchange reaction between **4** and methanol at 35 °C.

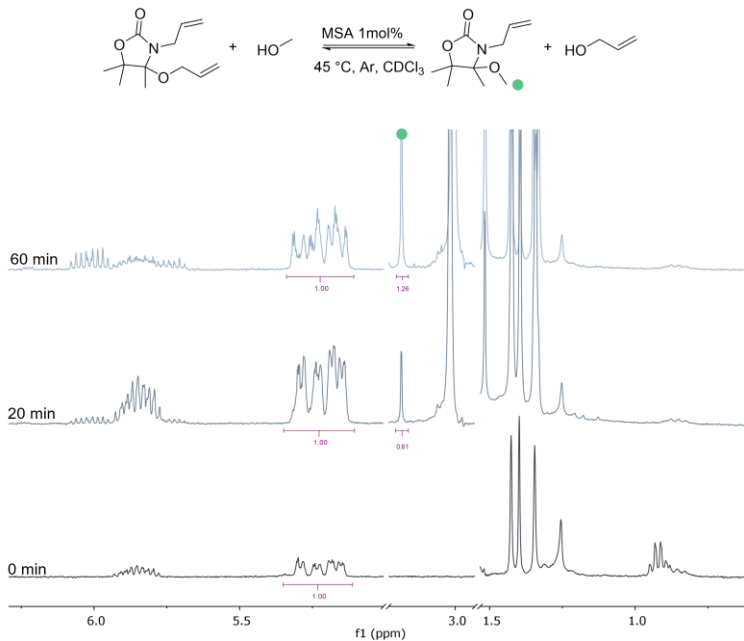


**Figure S4.34.**  $^1\text{H}$  NMR kinetics of the exchange reaction between **4** and methanol at 45 °C.



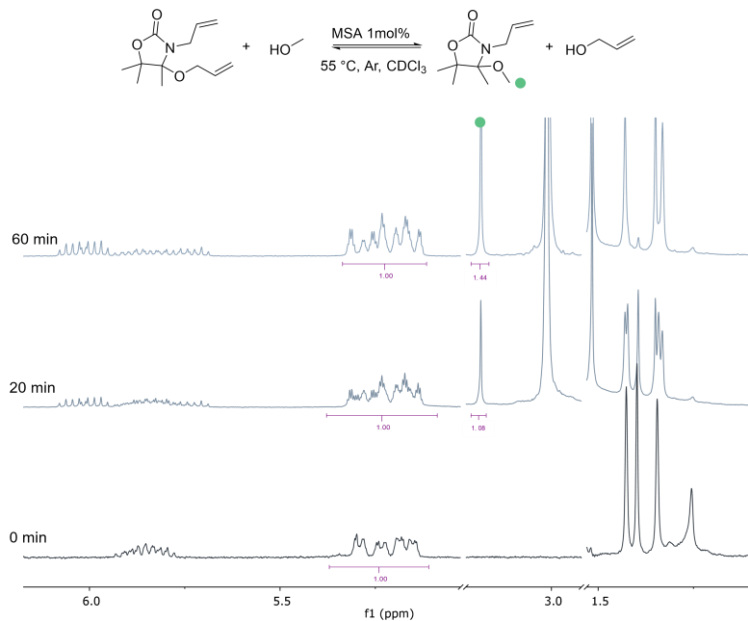


**Figure S4.35.**  $^1\text{H}$  NMR kinetics of the exchange reaction between **4** and methanol at 55 °C.

**Table S4.2.** Fitting parameters of exchange kinetics of **4** and methanol at different temperatures.

T	R <sup>2</sup>
25 °C	0.991
35 °C	0.992
45 °C	0.979
55 °C	0.994

#### 4.5.12. Materials preparation

Mixture of **AlLOx** and **4** was mixed with TEA (if applicable, 0.5 wt%). After homogenisation, a stoichiometric amount of crosslinker together with BAPO (0.5 wt%) were added. The clear, pale-yellow mixture was casted onto silicone moulds before being irradiated with light (390 nm, 20 mW/cm<sup>2</sup>). After 60 second the films were demoulded and stored in a desiccator before testing.

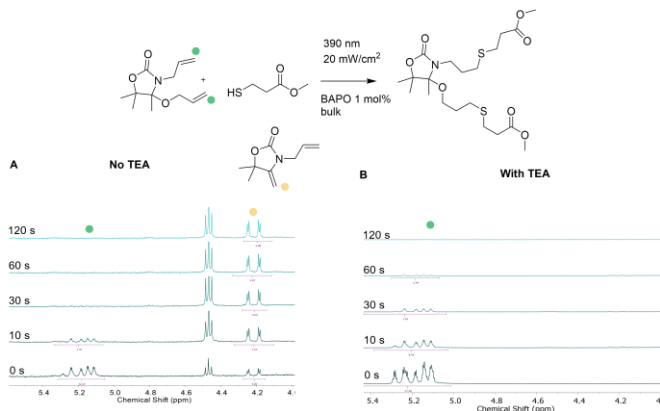


**Figure S4.36.** <sup>1</sup>H NMR kinetics in DMSO-*d*<sub>6</sub> of thiol ene kinetics between **4** and 3-methyl-mercaptopropionate with (a) and without TEA (b) (reaction conditions: bulk, 25 °C, stoichiometric under ambient conditions. Light 390 nm at 20 mW/cm<sup>2</sup>. BAPO 1 mol%, TEA 1 mol%).

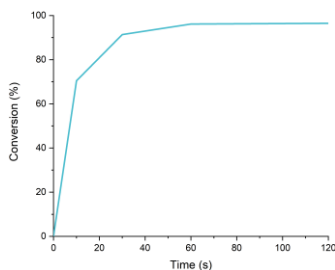


**Figure S4.37.** Conversion over time of thiol ene reaction between **4** and 3-methyl-mercaptopropionate with TEA. The conversion was calculated with Equation 1 (where  $I_t$  is the integral at time  $t$  and  $I_0$  the integral at time 0) by taking into consideration the signal of the CH<sub>2</sub> of Allyl double bond (5.2 ppm, m). The signals were normalized using the signal of CH<sub>3</sub> (1.4 ppm, s).

**Table S4.3.** Thermomechanical properties of materials prepared in this study.

Entry	Sample	Swelling (THF, %)	Gel Content (THF, %)	T <sub>g</sub> (DSC)	Endothermic peak (DSC)	Young's Modulus (Mpa)	Elongation at Break (%)	Stress at Break (MPa)
1	P(S3,0)	195±2	97.0±0.3	9	-	8±0.3	75±9	3.9±0.2
2	P(S4,0)	146.2±0.5	98±0.3	24.8	-	737±26	28.1±2.1	11.9±1.2
3	P(S6,0)	142±5	97±3	41	-	1720±70	4±0.4	27±0.9
4	P(S4,25)	151±3	98.2±0.3	19.5	145	n.d.	n.d.	n.d.
5	P(S3,50)	205±0.7	90.7±0.8	-0.2	154.6	3.0±0.2	45.5±1.5	1.3±0.2
6	P(S4,50)	149±2	94±2	2	164	2.8±0.2	60.8±2.9	1.77±0.2
7	P(S6,50)	155.3±0.9	98.0±0.1	18	169	27.4±1.5	47.2±2.3	11.4±1.1
8	P(S4,75)	161±2	95.5±0.4	4.2	141	n.d.	n.d.	n.d.
9	P(S3,100)	172.4±2.5	94.7±0.8	1.4	145	n.d.	n.d.	n.d.
10	P(S4,100)	135±2	95±2	8.8	106	10.4±0.3	64.3±3.2	5.97±0.5
11	P(S6,100)	146.3±1.5	97.2±0.5	19.5	99	n.d.	n.d.	n.d.

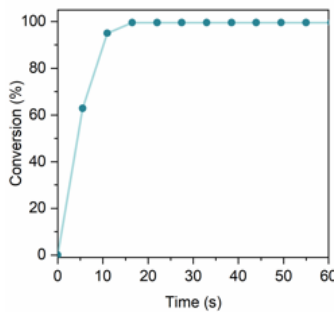


Figure S4.38. Real time FTIR of curing of **P(S4,100)**.

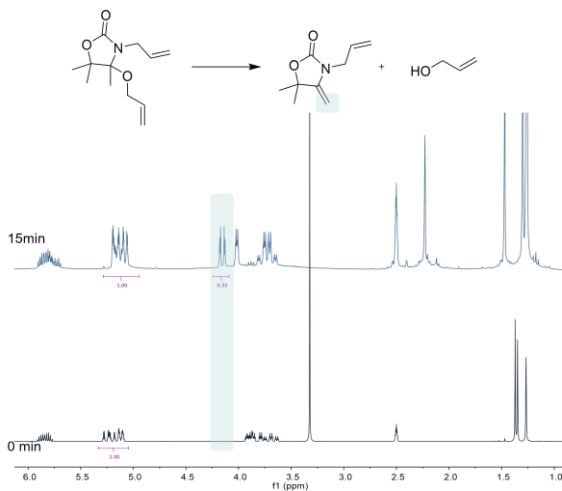


Figure S4.39. Reaction between **4** and BAPO photodegradation products (reaction conditions: stoichiometric, 25 °C, bulk, Argon atmosphere).

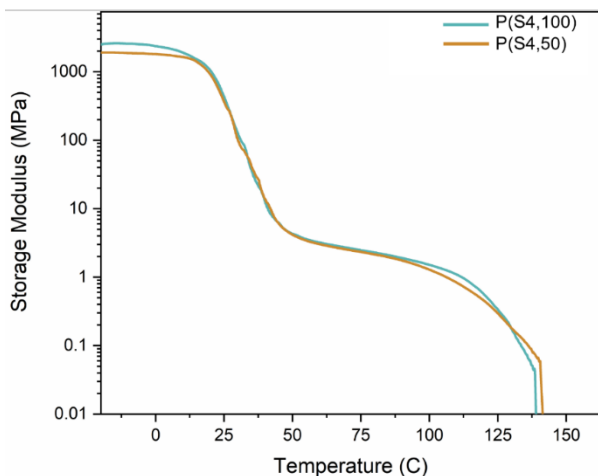


Figure S4.40. DMA trace of **P(S4,50)** and **P(S4,100)**.

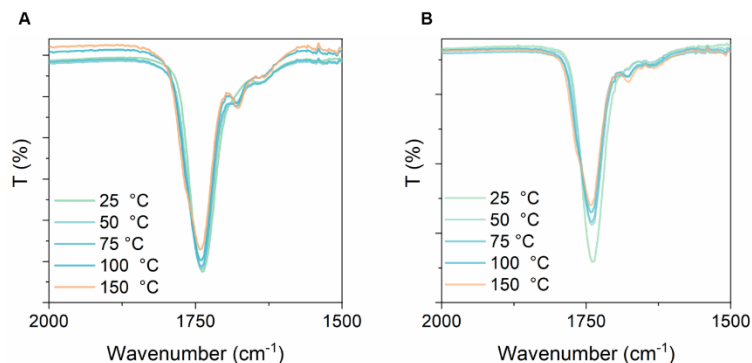


Figure S4.41. Temperature dependant FTIR spectra of **P(S4,100)** (a) and **P(S4,50)** (b) at temperature ranging from 25 to 150 °C.

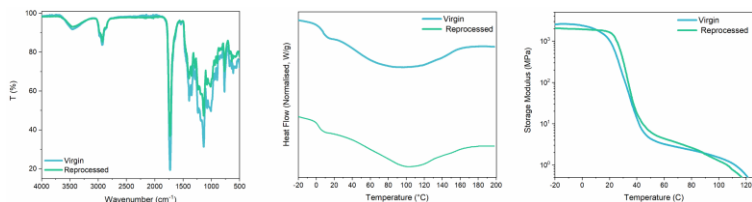


Figure S4.42. IR spectra, DSC and DMA trace of virgin and reprocessed P(S4,50).

#### 4.5.13. Hydrolytic Stability of Model Compounds

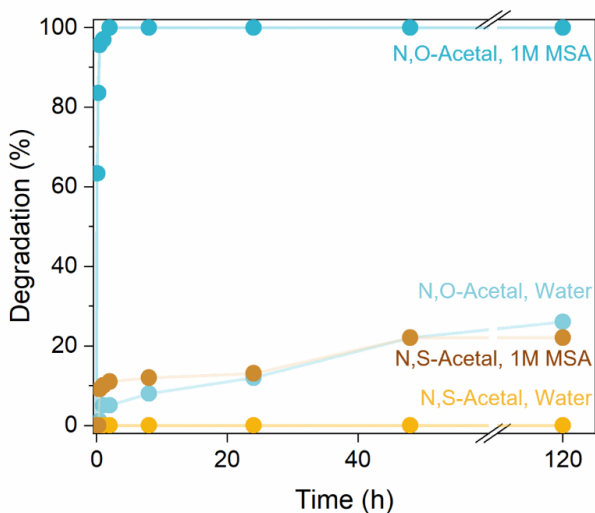
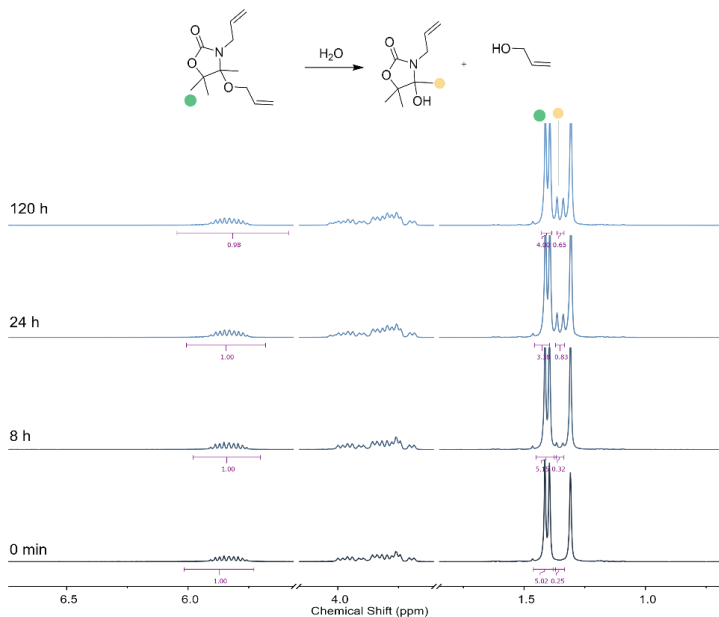


Figure S4.43. Kinetics of the hydrolysis of **4** at 25  $^{\circ}\text{C}$  and **6**. (0.2 M  $\text{D}_2\text{O}/\text{H}_2\text{O}$ , watergated  $^1\text{H}$  NMR, 1mol% MSA for acid environment).

#### 4.5.13.1. Hydrolytic degradation of an *N,O*-acetal Model Compound

**4** was mixed with H<sub>2</sub>O (0.2M, 1 mol% MSA) and stirred vigorously. Aliquots were samples and immediately quenched with TEA before being diluted in D<sub>2</sub>O:H<sub>2</sub>O (9:1) and their <sup>1</sup>H<sub>watergate</sub> NMR spectra being measured. The conversion was calculated on the ratio between methyl signal of **4** and its hydrolysis products (1.41, 1.37 ppm) using Equation 1



**Figure S4.44.** <sup>1</sup>H NMR kinetics of the hydrolytic degradation of **4** at 25 °C (0.2 M D<sub>2</sub>O/H<sub>2</sub>O, watergate <sup>1</sup>H NMR).



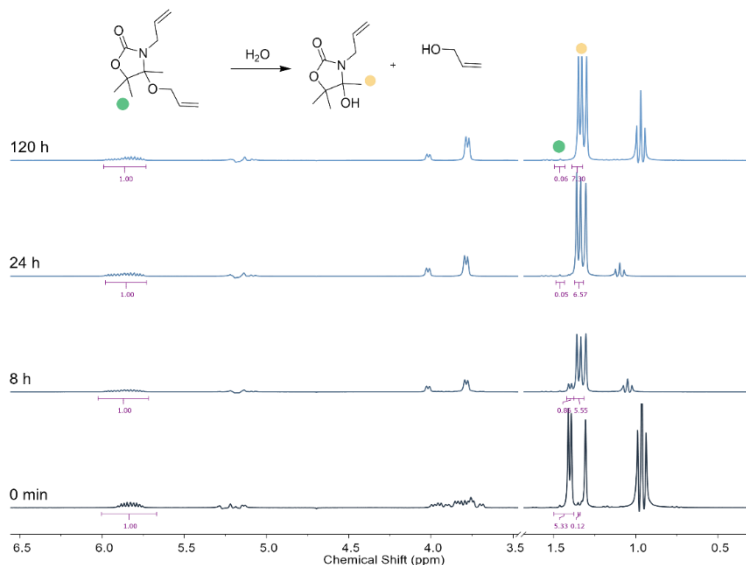


**Figure S4.45.**  $^1\text{H}$  NMR kinetics of the hydrolytic degradation of **4** at 25 °C with MSA 1 mol% (0.2 M  $\text{D}_2\text{O}/\text{H}_2\text{O}$ , TEA quench 10  $\mu\text{L}$ , watergate  $^1\text{H}$  NMR)

#### 4.5.13.2. Hydrolytic degradation of an *N,O*-acetal Model Compound

**6** was mixed with water (0.2M) and stirred vigorously. Aliquots were samples and immediately quenched with TEA before being diluted in  $\text{DMSO-}d_6$  and their  $^1\text{H}$  NMR spectra being measured. The conversion was calculated on the reduction of the singlet at 3.62 ppm (terminal methyl of thiol) using Equation 1.

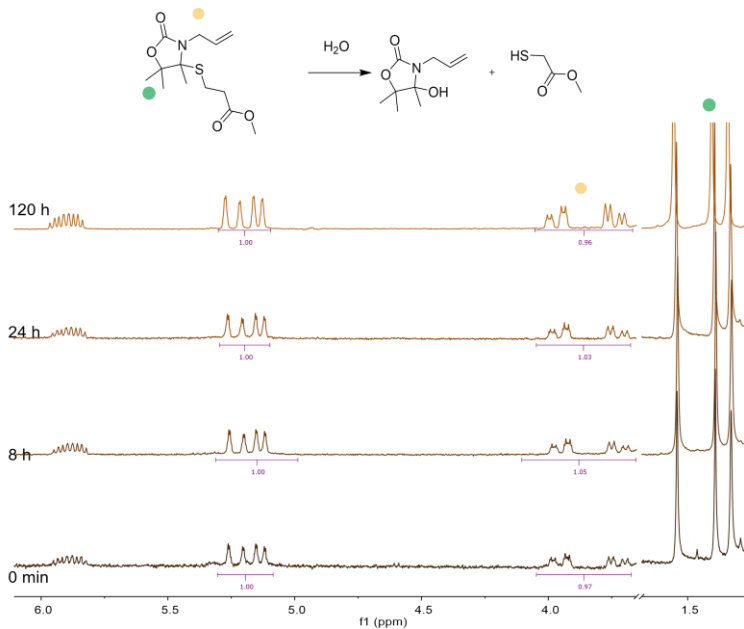


**Figure S4.46.**  $^1\text{H}$  NMR kinetics of the hydrolytic degradation of **5** at 25 °C (0.2 M in  $\text{H}_2\text{O}$ , quench TEA 10  $\mu\text{L}$ ,  $\text{DMSO-}d_6$  0.5 mL).

**6** was mixed with water (0.2M, 1 mol% MSA) and stirred vigorously. Aliquots were sampled and immediately quenched with TEA before being diluted in  $\text{DMSO-}d_6$  and their  $^1\text{H}$  NMR spectra being measured. The conversion was calculated on the reduction of the singlet at 3.62 ppm (terminal methyl of thiol)

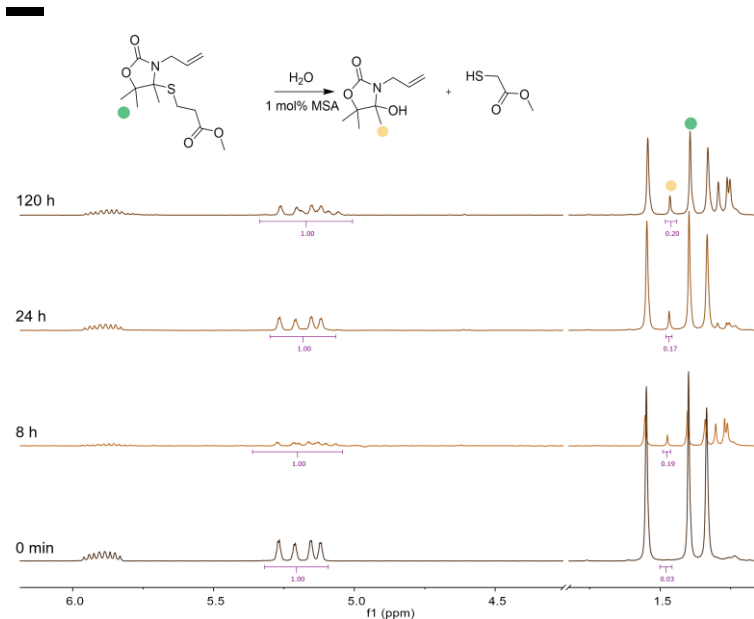


**Figure S4.47.**  $^1\text{H}$  NMR kinetics of the hydrolytic degradation of **5** at 25 °C with MSA 1 mol% (0.2 M in  $\text{H}_2\text{O}$ , quench TEA 10  $\mu\text{L}$ ,  $\text{DMSO}-d_6$  0.5 mL).

#### 4.5.13.3. Hydrolytic degradation of an O,O-acetal Model Compound

1,1-Dimethoxyethane was mixed with water (0.2M) and stirred vigorously. Aliquots were samples and immediately quenched with TEA before being diluted in  $\text{DMSO}-d_6$  and their  $^1\text{H}$  NMR spectra being measured. The conversion was calculated on the disappearance of multiplet at 4.5 ppm. For all reaction the conversion was calculated with Equation 1.

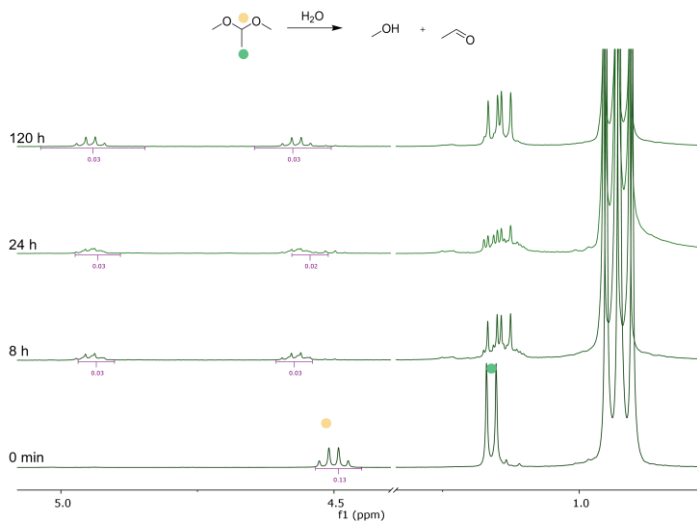


**Figure S4.48.**  $^1\text{H}$  NMR kinetics of the hydrolytic degradation of 1,1-Dimethoxyethane at 25 °C (0.2 M in  $\text{H}_2\text{O}$ , quench TEA 10  $\mu\text{L}$ ,  $\text{DMSO}-d_6$  0.5 mL).

1,1-Dimethoxyethane was mixed with water (0.2M, 1 mol% MSA) and stirred vigorously. Aliquots were samples and immediately quenched with TEA before being diluted in  $\text{DMSO}-d_6$  and their  $^1\text{H}$  NMR spectra being measured. The conversion was calculated on the disappearance of multiplet at 4.5 ppm.

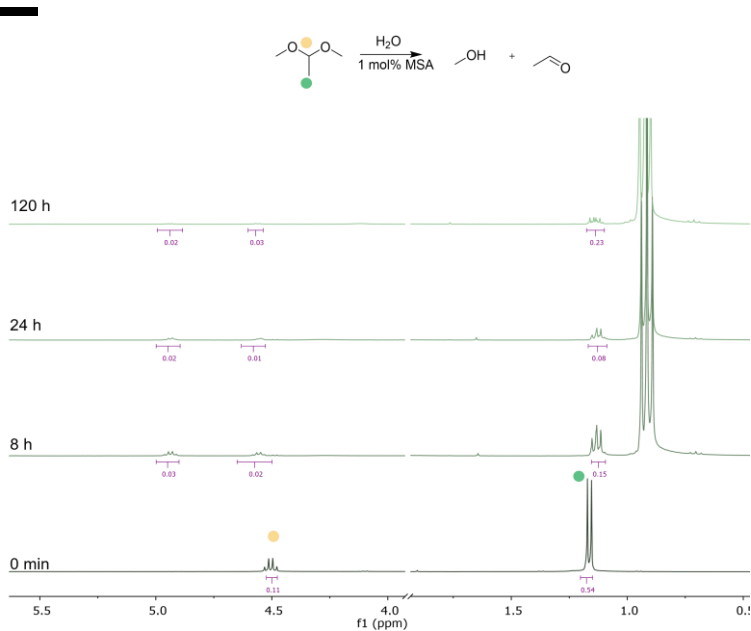


**Figure S4.49.** <sup>1</sup>H NMR kinetics of the hydrolytic degradation of 1,1-Dimethoxyethane at 25 °C with MSA 1 mol% (0.2 M in H<sub>2</sub>O, quench TEA 10 μL, DMSO-*d*<sub>6</sub> 0.5 mL).

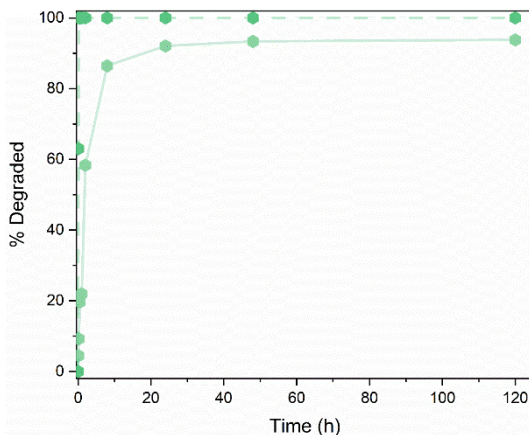


*Figure S4.50.* Kinetics of Degradation of an O,O-acetal model compound.

#### 4.5.14. Determination of degradation kinetics in materials

Circular films of the material (~250 mg) were placed in water or a 1M solution of MSA. Their degradation % was determined gravimetrically measuring the weight loss over time.

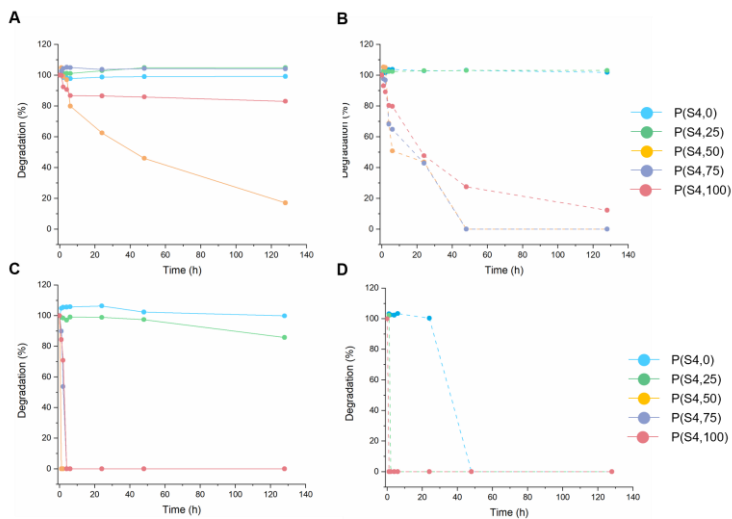


**Figure S4.51.** Hydrolytic degradation of materials ranging from **P(S4,0)** to **P(S4,100)** under neutral (a) and acidic conditions at 25°C (b). Hydrolytic degradation of materials ranging from **P(S4,0)** to **P(S4,100)** under neutral (c) and acidic conditions at 100°C (d).

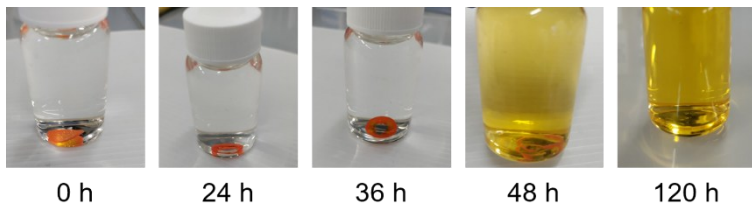


**Figure S4.52.** **P(S4,50)** degradation in 1M MSA (a water-soluble dye was added to the material to improve visibility).

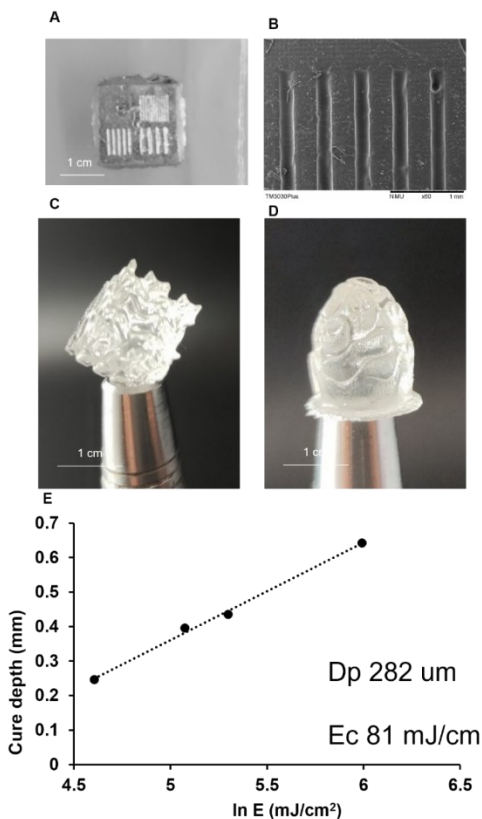


Figure S4.53. a) 3D printed structure for optimisation printed using P(S4,50) b) SEM image showing 100 µm lines c,d) 3D printed gyroid cube and voronoy egg printed using P(S4,50) e) Jacobs working curve of P(S4,50) (BAPO 0.5 wt%, TEA 0.5 WT%).



# 4.5.15. $\omega$ B97-XD/6-311++G(d,p) Optimized Cartesian Coordinates

INT1			H	-1.039009	0.914855
0 1				3.026456	
C	-2.424513	0.710220	H	-0.648354	-0.822220
0.907834				3.172192	
O	-2.753242	1.730800	C	-0.381028	-2.201416
1.454530				0.513643	
O	-2.952304	0.254568	H	0.278657	-2.318034
0.242599				1.368234	
N	-1.483582	-0.207132	H	-0.387030	-2.990378
1.358438				0.231843	
C	-2.340063	-0.997420	H	1.043555	-1.204251
0.630794				0.443461	
C	-3.419598	-2.075391	C	-0.701039	2.967691
0.594875				0.777113	
H	-4.217457	-1.821416	H	-0.762388	3.474487
1.298971				0.193484	
H	-2.993172	-3.042956	H	-0.118484	3.582026
0.876952				1.477052	
H	-3.848237	-2.161641	H	-1.715532	2.852248
0.408009				1.164886	
C	-1.726982	-0.822440	S	2.821142	-0.227437
2.013791				0.286526	
H	-1.236133	-1.750917	O	2.441954	1.175706
2.324568				0.427767	
H	-2.514398	-0.588284	O	1.913371	-0.910504
2.736987				0.837789	
H	-0.995091	-0.010697	O	-0.155904	1.665906
1.997284				0.652848	
C	-1.297006	-1.215785	H	0.738882	1.720222
0.452781				0.282584	
C	-0.640559	0.044515	O	2.833330	-1.056832
2.504331				1.479817	
H	0.387484	0.248606	C	4.384002	-0.316332
2.187864				0.550819	

H 5.115057 0.168368	H 0.053892 1.180179
0.098909	2.178912
H 4.637648 -1.365440 -	H -0.945687 0.154373
0.704700	3.254246
H 4.300462 0.215964 -	H 0.508709 -0.512668
1.498999	2.388348
	C -0.343922 -2.386588
INT2A	0.535836
0 1	H 0.091712 -2.514841
C -2.208165 0.797704	1.526066
0.788235	H -0.914996 -3.269467
O -2.510481 1.768626	0.237455
1.406149	H 0.494964 -2.238903 -
O -2.798320 0.290490 -	0.169329
0.286599	C -0.462219 3.249950 -
N -1.183440 -0.151901	0.563510
1.205227	H -0.221911 3.640556
C -2.188092 -0.959391 -	0.434420
0.670026	H 0.176760 3.747816 -
C -3.283808 -2.022129 -	1.304442
0.688419	H -1.507424 3.482575 -
H -4.061903 -1.706612 -	0.783438
1.387868	O -0.315061 1.846256 -
H -2.881616 -2.979316 -	0.621664
1.030430	H 0.610439 1.614892 -
H -3.735365 -2.152289	0.377097
0.299903	S 2.485706 -0.270370
C -1.486307 -0.792126 -	0.113049
2.017929	O 2.123906 1.159905
H -0.972437 -1.718114 -	0.329339
2.290216	O 1.733163 -0.866652 -
H -2.244166 -0.565091 -	1.022614
2.773126	C 4.208733 -0.266382 -
H -0.757786 0.019635 -	0.361394
1.967943	H 4.312106 0.320085 -
C -1.180287 -1.185642	1.275786
0.428270	H 4.785561 0.181322
C -0.335707 0.175451	0.449510
2.349140	H 4.520754 -1.298522 -
	0.529392

# 4

O 2.389246 -1.079328  
 1.350383  
 INT2B  
 O 1  
 C -2.316019 1.137230 -  
 0.123303  
 O -2.536248 2.201813  
 0.358615  
 O -2.853808 0.602271 -  
 1.213158  
 N -1.462581 0.123582  
 0.480568  
 C -2.352246 -0.730081 -  
 1.433183  
 C -3.544531 -1.685936 -  
 1.423593  
 H -4.240188 -1.381757 -  
 2.209629  
 H -3.217649 -2.708801 -  
 1.628274  
 H -4.069781 -1.661446 -  
 0.464019  
 C -1.565875 -0.765706 -  
 2.742109  
 H -1.120552 -1.754281 -  
 2.885834  
 H -2.254513 -0.563660 -  
 3.567081  
 H -0.780221 -0.007950 -  
 2.732468  
 C -1.451647 -0.947038 -  
 0.244097  
 C -0.709441 0.461005  
 1.685336  
 H -0.189332 -0.421029  
 2.054501  
 H 0.044572 1.204846  
 1.412661

H -1.407665 0.869048  
 2.416900  
 C -0.665257 -2.164377 -  
 0.029986  
 H -0.403701 -2.332462  
 1.014853  
 H -1.165492 -3.032651 -  
 0.463480  
 H 0.292648 -1.982271 -  
 0.555423  
 C 0.342834 3.039066 -  
 1.144964  
 H -0.575772 3.625328 -  
 1.062536  
 H 0.916662 3.121551 -  
 0.215464  
 H 0.945030 3.432617 -  
 1.974029  
 O -0.037982 1.694219 -  
 1.387358  
 H 0.737322 1.117810 -  
 1.255281  
 S 2.414423 -0.311824  
 0.316756  
 O 1.739779 -0.588902 -  
 0.996280  
 O 1.973678 -1.255268  
 1.369089  
 C 4.152821 -0.628492  
 0.044035  
 H 4.273129 -1.671078 -  
 0.254923  
 H 4.506294 0.040590 -  
 0.742184  
 H 4.682560 -0.434823  
 0.978357  
 O 2.293765 1.114516  
 0.688509

INT3

0 1			H 1.581452 0.058640 -
C 2.575334 1.536009			2.607553
0.696517			H 0.798737 -1.429465 -
O 2.885317 2.561445			2.027339
1.250610			H -0.101739 0.098014 -
O 3.221027 0.355523			2.062346
0.882008			C 0.198069 -0.142670
N 1.547637 1.340356 -			1.730819
0.196945			H -0.085321 0.911948
C 2.748502 -0.610591 -			1.766717
0.087151			H -0.597404 -0.736053
C 3.728321 -0.575392 -			2.183447
1.260429			H 1.130650 -0.297537
H 4.731839 -0.789806 -			2.280221
0.882620			H -1.180583 -1.049711 -
H 3.473013 -1.327231 -			0.190340
2.013210			S -2.862366 0.195150 -
H 3.747197 0.410012 -			0.640734
1.735908			O -2.131693 -1.216527 -
C 2.727365 -1.989123			0.464726
0.549498			O -2.463140 0.799714 -
H 2.316911 -2.716285 -			1.903585
0.158414			C -4.533912 -0.392802 -
H 3.748320 -2.290207			0.768173
0.801580			H -4.602930 -1.062925 -
H 2.123585 -2.019742			1.625715
1.456689			H -4.796861 -0.904649
C 1.339974 -0.051028 -			0.157859
0.461431			H -5.164301 0.485889 -
C 0.591086 2.379408 -			0.916366
0.527347			O -2.698838 0.974091
H -0.406701 2.136439 -			0.579188
0.147567			O 0.300689 -0.604266
H 0.938007 3.305135 -			0.381420
0.065556			
H 0.530954 2.514365 -			TS1
1.610964			
C 0.879135 -0.348352 -			0 1
1.878204			C -2.392347 0.818178
			0.559446

# 4

O	-2.801290	1.876017	H	0.808134	-1.569056
0.937053			0.099225		
O	-2.849462	0.115491	C	-0.478401	3.115500
0.478046			1.153010		
N	-1.370329	0.052279	H	-0.045218	3.774397
1.186838			0.389033		
C	-2.117611	-1.120026	H	-0.100000	3.415288
0.627877			2.139538		
C	-3.109708	-2.272978	H	-1.564240	3.234268
0.499586			1.137348		
H	-3.864169	-2.183854	O	-0.199074	1.755280
1.284930			0.883208		
H	-2.593611	-3.230214	H	0.769849	1.628168
0.616317			0.850331		
H	-3.611496	-2.257426	S	2.733111	-0.104940
0.473089			0.010167		
C	-1.390008	-1.099629	O	2.534038	1.192361
1.968602			0.660889		
H	-0.782021	-2.001059	O	1.877234	-1.189667
2.081387			0.648900		
H	-2.132382	-1.066082	C	4.398970	-0.622916
2.771165			0.349755		
H	-0.745758	-0.219380	H	4.511586	-0.682611
2.029690			1.432896		
C	-1.154570	-1.075844	H	5.078630	0.122746
0.534834			0.066880		
C	-0.617292	0.559753	H	4.563863	-1.597010
2.324877			0.113118		
H	-0.950596	1.581757	O	2.546804	-0.110170
2.503836			1.468068		
H	-0.823456	-0.056913			
3.205171			TS2		
H	0.451080	0.543169	O 1		
2.094584			C	2.336999	1.503276
C	-0.140134	-2.009986	0.030176		
0.793861			O	2.374829	2.693227
H	0.296132	-2.000656	0.006117		
1.792445			O	3.265653	0.669384
H	-0.301291	-3.001960	0.421771		
0.370802					

N 1.275877 0.725609 -	H 0.540720 1.551301
0.568487	0.907268
C 2.938561 -0.698589	H -0.835092 0.947774
0.068801	1.854686
C 3.778725 -1.079191 -	H 0.808702 0.995051
1.157512	2.577014
H 4.831681 -0.963922 -	O 0.531646 -0.872531
0.899887	1.107291
H 3.595919 -2.120067 -	H -0.519196 -0.971624
1.427781	0.352981
H 3.553066 -0.441804 -	S -3.379477 -0.020162
2.015025	0.037952
C 3.245916 -1.595717	O -2.315283 -1.027304 -
1.249302	0.271165
H 2.840817 -2.593834	O -3.293437 1.153537 -
1.074395	0.849316
H 4.327862 -1.675982	C -4.924937 -0.835401 -
1.361940	0.333779
H 2.820807 -1.196861	H -4.923511 -1.112484 -
2.167685	1.386918
C 1.490591 -0.568451 -	H -5.008807 -1.719013
0.378605	0.297178
C 0.122298 1.330162 -	H -5.734159 -0.137373 -
1.227983	0.123864
H -0.797536 0.876908 -	O -3.408443 0.315670
0.859933	1.474086
H 0.129451 2.393690 -	
1.000751	
H 0.200512 1.182623 -	PRODUCT
2.305406	0 1
C 0.780239 -1.613502 -	C -0.798114 -1.154111 -
1.158945	0.416820
H 1.185035 -1.591113 -	O -1.682695 -1.920064 -
2.177337	0.709163
H 0.960266 -2.600281 -	O 0.458199 -1.225016 -
0.735503	0.927916
H -0.292415 -1.419007 -	N -0.861365 -0.087968
1.204531	0.450588
C 0.269123 0.623884	C 1.323096 -0.311446 -
1.599744	0.211442

# 4

C	2.018518	-1.125266	
	0.880315		
H	2.553006	-1.954835	
	0.409257		
H	2.740926	-0.514994	
	1.430611		
H	1.296386	-1.543883	
	1.587938		
C	2.342723	0.271400	-
	1.174114		
H	2.964239	1.006553	-
	0.652917		
H	2.990742	-0.527239	-
	1.546664		
H	1.875933	0.764485	-
	2.027018		
C	0.311237	0.728514	
	0.364463		
C	-2.097635	0.333468	
	1.081327		
H	-2.855871	-0.417408	
	0.853690		
H	-1.970023	0.403920	
	2.165200		
H	-2.425938	1.306783	
	0.702153		
C	0.716827	1.367953	
	1.681519		
H	-0.055577	2.062348	
	2.022772		
H	0.858553	0.609357	
	2.453056		
H	1.649940	1.925691	
	1.555992		
C	-0.661549	1.642908	-
	1.717892		
H	-0.252445	0.839040	-
	2.335908		
H	-1.704387	1.429692	-
	1.471076		
H	-0.615269	2.585801	-
	2.264320		
O	0.117870	1.845484	-
	0.536361		
H	-0.015165	3.405907	-
	0.020264		
O	-0.226109	4.349703	
	0.249061		
S	-1.720937	4.392112	
	0.815875		
C	-1.923579	6.155876	
	0.879287		
H	-2.922395	6.341965	
	1.278276		
H	-1.162948	6.570230	
	1.541811		
H	-1.830919	6.555757	-
	0.130755		
O	-1.748100	3.851625	
	2.167529		
O	-2.624476	3.821122	-
	0.173605		

## 4.6. References

1. World Economic Forum Ellen MacArthur Foundation and McKinsey & Company. The New Plastics Economy: Rethinking the future of plastics. *Ellen MacArthur Foundation* 120 (2016).
2. Hahladakis, J. N., Velis, C. A., Weber, R., Iacovidou, E. & Purnell, P. An overview of chemical additives present in plastics: Migration, release, fate and environmental impact during their use, disposal and recycling. *J Hazard Mater* **344**, 179–199 (2018).
3. Geyer, R., Jambeck, J. R. & Law, K. L. Production, use, and fate of all plastics ever made. *Sci Adv* **3**, (2017).
4. Fernández-Dacosta, C. *et al.* Prospective techno-economic and environmental assessment of carbon capture at a refinery and CO<sub>2</sub> utilisation in polyol synthesis. *Journal of CO<sub>2</sub> Utilization* **21**, 405–422 (2017).
5. Spierling, S. *et al.* Bio-based plastics - A review of environmental, social and economic impact assessments. *J Clean Prod* **185**, 476–491 (2018).
6. Jiang, J. *et al.* From plastic waste to wealth using chemical recycling: A review. *J Environ Chem Eng* **10**, 106867 (2022).
7. Nicholls, B. T. & Fors, B. P. Closing the loop on thermoset plastic recycling. *Science* (1979) **384**, 156–157 (2024).
8. Jehanno, C. *et al.* Critical advances and future opportunities in upcycling commodity polymers. *Nature* **603**, 803–814 (2022).
9. Polylactic Acid Market Size, Share & Growth Report, 2030. <https://www.grandviewresearch.com/industry-analysis/polylactic-acid-pla-market>.
10. Grignard, B., Gennen, S., Jérôme, C., Kleij, A. W. & Detrembleur, C. Advances in the use of CO<sub>2</sub> as a renewable feedstock for the synthesis of polymers. *Chem Soc Rev* **48**, 4466–4514 (2019).
11. Vidal, F. *et al.* Designing a circular carbon and plastics economy for a sustainable future. *Nature* **626**, 45–57 (2024).
12. Song, B., Qin, A. & Tang, B. Z. Syntheses, properties, and applications of CO<sub>2</sub>-based functional polymers. *Cell Rep Phys Sci* **3**, 100719 (2022).
13. Narupai, B. & Nelson, A. 100th Anniversary of Macromolecular Science Viewpoint: Macromolecular Materials for Additive Manufacturing. *ACS Macro Lett* **9**, 627–638 (2020).
14. Vidal, F. *et al.* Designing a circular carbon and plastics economy for a sustainable future. *Nature* **626**, 45–57 (2024).
15. Cao, H., Liu, S. & Wang, X. Environmentally benign metal catalyst for the ring-opening copolymerization of epoxide and CO<sub>2</sub>: state-of-the-art, opportunities, and challenges. *Green Chemical Engineering* **3**, 111–124 (2022).
16. Karulf, L., Singh, B., Singh, R. & Repo, T. Carbon dioxide utilization: CO<sub>2</sub>-based polyurethane foam. *Journal of CO<sub>2</sub> Utilization* **91**, 103000 (2025).



17. Hepburn, C. *et al.* The technological and economic prospects for CO<sub>2</sub> utilization and removal. *Nature* vol. 575 87–97 Preprint at <https://doi.org/10.1038/s41586-019-1681-6> (2019).
18. Williams, C. K. & Hillmyer, M. A. Polymers from renewable resources: A perspective for a special issue of polymer reviews. *Polymer Reviews* **48**, 1–10 (2008).
19. Jehanno, C. *et al.* Critical advances and future opportunities in upcycling commodity polymers. *Nature* **603**, 803–814 (2022).
20. Yan, T., Balzer, A. H., Herbert, K. M., Epps, T. H. & Korley, L. S. T. J. Circularity in polymers: addressing performance and sustainability challenges using dynamic covalent chemistries. *Chem Sci* **14**, 5243–5265 (2023).
21. Gerdroodbar, A. E., Karimkhani, V., Dashtimoghadam, E. & Salami-Kalajahi, M. Vitrimization as a bridge of chemical and mechanical recycling. *J Environ Chem Eng* **12**, 112897 (2024).
22. Zheng, J. *et al.* Vitrimers: Current research trends and their emerging applications. *Materials Today* **51**, 586–625 (2021).
23. Lucherelli, M. A., Duval, A. & Avérous, L. Biobased vitrimers: Towards sustainable and adaptable performing polymer materials. *Prog Polym Sci* **127**, 101515 (2022).
24. Röttger, M. *et al.* High-performance vitrimers from commodity thermoplastics through dioxaborolane metathesis. *Science* (1979) **356**, 62–65 (2017).
25. Habets, T. *et al.* Covalent Adaptable Networks through Dynamic N,S-acetal Chemistry: Toward Recyclable CO<sub>2</sub>-Based Thermosets. *J Am Chem Soc* **145**, 25450–25462 (2023).
26. Maes, S. *et al.* Unprecedented associative exchange in CO<sub>2</sub>-sourced cyclic S,O-acetals based covalent adaptable networks. *Polym Chem* **8**, 5255–5446 (2024).
27. Bizet, B., Grau, E., Asua, J. M. & Cramail, H. Hybrid Nonisocyanate Polyurethanes (H-NIPUs): A Pathway towards a Broad Range of Novel Materials. *Macromol Chem Phys* **223**, (2022).
28. Kathalewar, M. S., Joshi, P. B., Sabnis, A. S. & Malshe, V. C. Non-isocyanate polyurethanes: From chemistry to applications. *RSC Adv* **3**, 4110–4129 (2013).
29. Monie, F., Vidil, T., Grignard, B., Cramail, H. & Detrembleur, C. Self-foaming polymers: Opportunities for the next generation of personal protective equipment. *Materials Science and Engineering R: Reports* **145**, 100628 (2021).
30. Monie, F. *et al.* Chemo- and Regioselective Additions of Nucleophiles to Cyclic Carbonates for the Preparation of Self-Blowing Non-Isocyanate Polyurethane Foams. *Angewandte Chemie - International Edition* **59**, 17033–17041 (2020).
31. Monie, F., Grignard, B. & Detrembleur, C. Divergent Aminolysis Approach for Constructing Recyclable Self-Blown Nonisocyanate Polyurethane Foams. *ACS Macro Lett* **11**, 236–242 (2022).
32. Sun, H., Liang, Y., Thompson, M. P. & Gianneschi, N. C. Degradable polymers via olefin metathesis polymerization. *Prog Polym Sci* **120**, 101427 (2021).
33. Parkatzidis, K., Wang, H. S., Truong, N. P. & Anastasaki, A. Recent Developments and Future Challenges in Controlled Radical Polymerization: A 2020 Update. *Chem* vol. 6 1575–1588 Preprint at <https://doi.org/10.1016/j.chempr.2020.06.014> (2020).

34. Rosenboom, J. G., Langer, R. & Traverso, G. Bioplastics for a circular economy. *Nat Rev Mater* **7**, 117–137 (2022).
35. Burghardt, T. E. Developments in the deprotection of thioacetals. *Journal of Sulfur Chemistry* **26**, 411–427 (2005).
36. Laviéville, S. *et al.* Trifluoromethylated *N,S*-acetal as a Chemical Platform for Covalent Adaptable Networks: Fast Thiol Exchange and Strong Hydrostability for a Highly Transparent Material. *Macromolecules* **57**, 10311–10323 (2024).
37. Akar, E., Tunca, U. & Durmaz, H. Polythioacetals: From old chemistry to new perspectives. *Eur Polym J* 113532 (2024) doi:10.1016/j.eurpolymj.2024.113532.
38. Michael, S. & Herbert, W. Protecting Group Strategies in Organic Synthesis. *Angewandte Chemie - International Edition* **35**, 2056–2083 (1996).
39. Kongkatigumjorn, N. & Crespy, D. Strategies to prepare polymers with cleavable linkages releasing active agents in acidic media. *Polym Chem* **15**, 4491–4518 (2024).
40. Zheng, J., Png, Z. M., Quek, X. C. N., Loh, X. J. & Li, Z. Stimuli-cleavable moiety enabled vinyl polymer degradation and emerging applications. *Green Chemistry* **25**, 8903–8934 (2023).
41. Dreiling, R. J., Huynh, K. & Fors, B. P. Degradable thermosets via orthogonal polymerizations of a single monomer. *Nature* **2025** 1–6 (2025) doi:10.1038/s41586-024-08386-w.
42. Lefay, C. & Guillaneuf, Y. Recyclable/degradable materials via the insertion of labile/cleavable bonds using a comonomer approach. *Prog Polym Sci* **147**, (2023).
43. Rahimi, M., Gałęzewska, M., Jerczyński, K., Wróbel, S. & Pietrasik, J. Non-linear functional polymers containing selective/cleavable bonds: Synthesis and their biomedical applications. *Polym Adv Technol* **35**, (2024).
44. Siragusa, F. *et al.* Continuous Flow Synthesis of Functional Isocyanate-Free Poly(oxazolidone)s by Step-Growth Polymerization. *ACS Macro Lett* 644–650 (2024) doi:10.1021/ACSMACROLETT.4C00203.
45. Razavi-Esfali, M. *et al.* Design of functional isocyanate-free poly(oxazolidone)s under mild conditions. *Polym Chem* **15**, 1962–1974 (2024).
46. Habets, T., Siragusa, F., Grignard, B. & Detrembleur, C. Advancing the synthesis of isocyanate-free poly(oxazolidone)s: Scope and limitations. *Macromolecules* **53**, 6396–6408 (2020).
47. Lee, S. Y. *et al.* *A Comprehensive Metabolic Map for Production of Bio-Based Chemicals*. *Nature Catalysis* vol. 2 (2019).
48. Pathania, S., Petrova-Szczasiuk, K., Pentikäinen, O. & Singh, P. K. Oxazolidinones: Are they only good for the discovery of antibiotics? A worm's eye view. *J Mol Struct* **1286**, (2023).
49. Barbachyn, M. R. & Ford, C. W. Oxazolidinone structure-activity relationships leading to linezolid. *Angewandte Chemie - International Edition* **42**, 2010–2023 (2003).
50. Pandit, N., Singla, R. K. & Shrivastava, B. Current Updates on Oxazolidinone and Its Significance. *Int J Med Chem* **2012**, 1–24 (2012).

51. Sun, F., Van der Eycken, E. V. & Feng, H. Recent Advances in the Synthesis and Ring-Opening Transformations of 2-Oxazolidinones. *Adv Synth Catal* **363**, 5168–5195 (2021).
52. Chao, A. & Zhang, D. Investigation of Secondary Amine-Derived Amino Bond Exchange toward the Development of Covalent Adaptable Networks. *Macromolecules* **52**, 495–503 (2019).
53. Li, Q. *et al.* Green and Facile Preparation of Readily Dual-Recyclable Thermosetting Polymers with Superior Stability Based on Asymmetric Acetal. *Macromolecules* **53**, 1474–1485 (2020).
54. Lai, H., Peng, X., Li, L., Zhu, D. & Xiao, P. Novel monomers for photopolymer networks. *Prog Polym Sci* **128**, 101529 (2022).
55. Caliri, M. *et al.* Fully Recyclable Pluripotent Networks for 3D Printing Enabled by Dissociative Dynamic Bonds. *Advanced Materials* 2417355 (2025) doi:10.1002/ADMA.202417355.
56. Ciechacka, A. Analysis and Characterisation of an Acylphosphine Oxide Photoinitiator. 199 (2011).
57. Roper, T. M., Guymon, C. A., Jönsson, E. S. & Hoyle, C. E. Influence of the alkene structure on the mechanism and kinetics of thiol-alkene photopolymerizations with real-time infrared spectroscopy. *J Polym Sci A Polym Chem* **42**, 6283–6298 (2004).
58. Sutherland, B. P., Kabra, M. & Kloxin, C. J. Expanding the thiol-X toolbox: Photoinitiation and materials application of the acid-catalyzed thiol-ene (ACT) reaction. *Polym Chem* **12**, 1562–1570 (2021).
59. Zhou, J. *et al.* Influence of thiol and ene functionalities on thiol-ene networks: Photopolymerization, physical, mechanical, and optical properties. *Polym Test* **32**, 608–616 (2013).
60. Kolibaba, T. J. *et al.* Results of an interlaboratory study on the working curve in vat photopolymerization. *Addit Manuf* **84**, 104082 (2024).
61. Zhang, J. & Xiao, P. 3D printing of photopolymers. *Polym Chem* **9**, 1530–1540 (2018).
62. Jiang, H., Zhao, J. & Wang, A. An efficient and eco-friendly process for the conversion of carbon dioxide into oxazolones and oxazolidinones under supercritical conditions. *Synthesis (Stuttg)* **5**, 763–769 (2008).
63. Chai, J. Da & Head-Gordon, M. Long-range corrected hybrid density functionals with damped atom-atom dispersion corrections. *Physical Chemistry Chemical Physics* **10**, 6615–6620 (2008).
64. You, A., Be, M. & In, I. Self-consistent molecular orbital methods. XX. A basis set for correlated wave functions **2**. (2008).
65. Hehre, W. J., Ditchfield, K. & Pople, J. A. Self-consistent molecular orbital methods. XII. Further extensions of gaussian-type basis sets for use in molecular orbital studies of organic molecules. *J Chem Phys* **56**, 2257–2261 (1972).



# 5

Developing  
the Oxime-ene dynamic chemistry  
towards degradable and recyclable  
NIPUs



## 5.1. Abstract

Polyoxazolidones are a class of non-isocyanate polyurethanes that benefit from easy and accessible synthesis. Research in this kind of class of materials gave rise to a wide variety of functionalities, and polyoxazolidone-based networks are now emerging for delivering high-performance, recyclable materials. Most studies, however, introduce bonds in the network that are difficult to degrade easily and on-demand, severely limiting the end-of-life option for this class of polymers. In this study, we report oximes as powerful nucleophiles for the preparation of polyoxazolidone dynamic networks by reacting bis-oxime derivatives with a tetrafunctional crosslinker bearing alkylidene oxazolidone moieties. We first studied the dynamic oxime-ene reaction in-depth, from its thermodynamics to its exchange kinetics, and we modelled the mechanism by DFT, finding an intermediate behaviour between previously reported *N,S*-acetals and *N,O*-acetal containing polyoxazolidone networks. We then recycled the novel thermosets exploiting the dissociative behaviour of the oxime-ene reaction, both by mechanical and chemical means, reporting encouraging results. We found that the hydrolytic degradation of the materials containing the oxime- $\alpha$ -oxazolidone bond is little to none in water at room temperature while it is greatly accelerated when heated above 60 °C. This opens up the door to applications that require materials that can be recycled both mechanically and chemically, but that eventually degrade at the end of their life, such as single-use plastics or cargo.

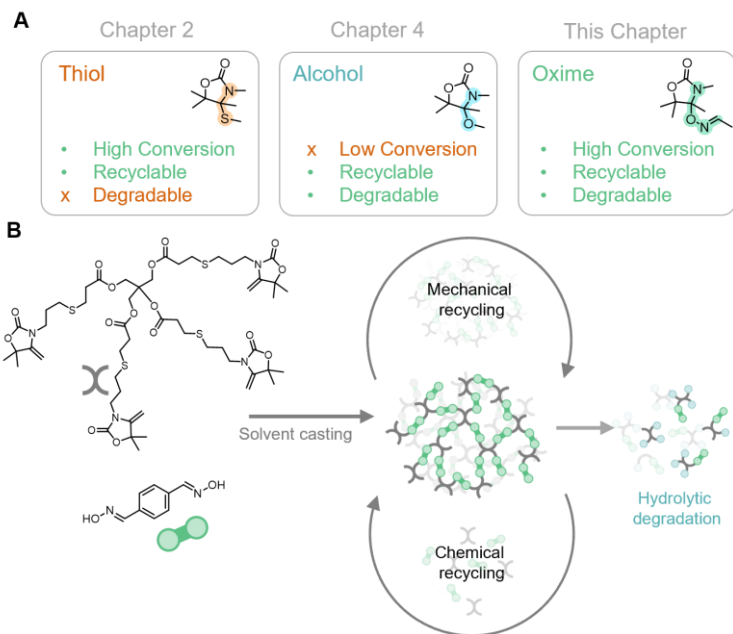


**Figure 5.1.** General scheme describing the work carried out in this article. Differences between *N,S*-acetal, *N,O*-acetal and the oxime- $\alpha$ -oxazolidone dynamic bond (b). Strategy for the preparation of mechanically and chemically recyclable materials that can undergo hydrolytic degradation (c).



## 5.2. Introduction

Non-isocyanate polyurethanes (NIPUs) are receiving increasing attention after REACH's 2023 restriction on the presence (<0.1%) of the precursors for polyurethanes (isocyanates) in commercial applications.<sup>1</sup> These regulations reflect the safety concerns over isocyanates, being the culprit of the Bhopal disaster over 40 years ago, one of the worst accident in chemical history.<sup>2</sup> The most common route for the preparation of NIPUs, the aminolysis of five-membered cyclic carbonates, has returned promising results with their polymeric products finding applications in foams, adhesives and coatings.<sup>3-5</sup> The precursors for this class of polymers are easily derived from CO<sub>2</sub>, further motivating their introduction in today's materials portfolio.<sup>6,7</sup> However, the preparation of these polymers generally entails high temperatures to overcome the low reactivity of the cyclic carbonate species.<sup>8</sup> Hybridization strategies are often proposed to overcome this issue, however, they often return mixed networks that are difficult to recycle back to the monomer.<sup>9-11</sup> Another commonly used strategy, molecular design of the cyclic monomer, offers ways to modulate the reactivity of these species;<sup>12</sup> however, they often stray away from the simple 1-step synthesis of five-membered carbonates,<sup>7</sup> often using phosgene, its derivatives or requiring multistep syntheses.<sup>13-17</sup>

On the other hand, exovinylene cyclic carbonates can be prepared in 1-step synthesis involving the addition of CO<sub>2</sub> to propargyl alcohols.<sup>18</sup> This simple protocol was recently adapted to flow chemistry, opening access to large(r) scale manufacturing.<sup>19</sup> The uncatalyzed aminolysis of exovinylene cyclic carbonates with primary (bis)amines affords poly(hydroxy-oxazolidone)s (PHOX) at ambient temperature, offering a platform to develop this class of highly chemical and thermal resistant polymers in a convenient and safe manner.<sup>20,21</sup> Simple dehydration of the pendant hydroxy-group results in vinylene-containing

poly(oxazolidones); offering a new chemical handle on the polymer backbone to use in, for instance, the cationic thiol-ene chemistry.<sup>22</sup> A following work exploited the reversible addition/elimination of thiols at the exovinylene moiety of the oxazolidone ring to prepare mechanically and chemically recyclable materials with properties ranging from silicone-like to polystyrene-like polymers by changing the rigidity of the (poly)amine linker.<sup>23</sup> Further innovation demonstrated that similar properties can be attained in photocurable poly(oxazolidone) networks (POXa, **Chapter 2** and **3**). As an important discovery, these networks were found to spontaneously phase separate, which in combination with the dynamic *N,S*-acetal chemistry, resulted in pluripotent properties of the 3D printed materials.<sup>24</sup> While highly recyclable, these polymer networks could not be degraded, an essential piece in the sustainable cycle of a plastic material (Figure 5.1-a).<sup>25</sup> Hence, in **Chapter 4**, hydrolysable *N,O*-acetals were introduced in the polymer backbone by a highly reversible reaction with alcohols instead of thiols (Figure 5.1-a). By inserting a varying amount of the cleavable bonds, we demonstrated that the degradation rate of a series of materials could be regulated while maintaining their mechanical reprocessability. However, the cationic addition of alcohols to exovinylene oxazolidones was found to give only low to moderate yields at equilibrium, significantly limiting the accessibility and recyclability of these materials.

In this work, we sought to continue with our efforts to provide degradable NIPU networks, without compromising on material performance and recyclability (Figure 5.1-b). To do so, we propose a new type of dynamic, cleavable bond based on the reaction of oximes (HO-N=C-) with the exovinylene C=C of an oxazolidone, as oximes are known for their high nucleophilicity<sup>26–30</sup> and their ability to degrade in acidic environment.<sup>31–36</sup> We study the reaction in detail, screening the influence of substrate, temperature and solvent. We find that the

reaction shows high conversion (>75%) for most structures and its activation energy lies between the one of *N,O*-acetals and *N,S*-acetals. We model the reaction with density functional theory (DFT) to explain this behaviour. Finally, we introduce this bond in mechanically and chemically recyclable materials that do not degrade at room temperature when exposed to water but completely degrade at 60 °C, overcoming the limitations of previously reported *N,O*-acetals. This work showcases how molecular design tools can be used to inspire a new generation of circular materials.

## 5.3. Results and Discussion

### 5.3.1. Small molecule studies

To initially assess the reactivity of oxazolidones with oximes, we screened the reaction of a model monomer, 3-allyl-5,5-dimethyl-4-methyleneoxazolidin-2-one (**AlloX**) with benzaldehyde oxime (1:1 molar ratio) in bulk and at room temperature. No appreciable reaction was detected in the resulting <sup>1</sup>H NMR spectrum of a reaction aliquot when the two components were mixed in the absence of any acid catalyst. However, upon addition of methanesulfonic acid (MSA) in catalytic amount (1 mol%), we observed an exothermic reaction, with the formation of a white solid after 2 h. As shown in Figure S5.1, the reaction at this point was quantitative and selective as determined by the complete disappearance of the exovinylene C=C double bond signal ( $\delta$  = 4.24 ppm) and the appearance of new singlets originating from the three methyl groups of the oxime-**AlloX** adduct ( $\delta$  = 1.49, 1.36, and 1.35 ppm). Formation of the white solid as the product of the reaction enabled a facile recovery of the product.

Encouraged by this promising reactivity, we screened a variety of monomers with different substituents varying in both steric and electronic properties. We could easily isolate the derivatives of acetaldehyde- (**1**), benzaldehyde- (**2**) and acetoxime (**5**) quantitatively after removal of the acidic catalyst by carrying out the reaction in bulk and employing a simple liquid/liquid extraction purification protocol. The adducts deriving from benzophenone- (**3**), acetophenone- (**4**), and cyclohexanone-oxime (**6**) were obtained by column chromatography in good to high yields (45 to 84%), proving the efficacy of oximes as nucleophiles for the reaction with alkylidene oxazolidones (Figure 5.2-a, S5.2- S5.7). We screened the kinetics of the reaction between the oxime partners and **Allox** using ACN as solvent (0.5 M, 1 mol% MSA). The least sterically hindered oxime, acetaldehyde oxime, performed the best, reaching well over 90% conversion in a 15-minute period (Figure 5.2-b, Figure S5.8). Benzaldehyde oxime performed comparably, with conversions reaching 85% in a similar timeframe (Figure S5.9). Curiously, both acetophenone- and benzophenone oxime showed high conversions, notwithstanding their higher steric hindrance (Figure S5.10, S5.11). This was attributed to the particular electronic properties of the two, with the aryl group's ability to delocalise charge and remove it from the -OH.<sup>37</sup> Further increase in steric hindrance significantly slowed down the reaction with acetoxime and cyclohexane oxime reaching 40 and 15 % conversion in the same timeframe (Figure S5.12, S5.13).

The oxime-ene reaction was strongly influenced by the acidity of the catalyst, while MSA provided with reaction that reached the thermodynamic equilibrium (85% conversion) in a 15-minute period, TFA (1 mol%) required 24 h to reach 75% conversion (Figure S5.14- S5.16) when using benzaldehyde oxime as reactant. Further reduction in acidity (acetic acid) provided with no conversion at all. As previously reported, this type of reaction is greatly influenced by the solvent

employed.<sup>23</sup> Apolar solvents such as toluene were found to be the ideal solvents for the reaction. Increasing polarity lowered the conversion from 92% for toluene to 85 and 64% for ACN and acetone, respectively. Solvents with a higher Lewis base character (DMSO)<sup>38</sup> hindered the reaction greatly, with conversion of just 15% after 30 minutes of reaction (Figure S5.17-S20). Heightening the temperature negatively influenced the reaction's conversion (Figure S5.21-S5.24). A Van't Hoff plot of the equilibrium constant at different temperatures returned a  $\Delta H = -19.5 \text{ kJ}\cdot\text{mol}^{-1}$  and  $\Delta S = -28.7 \text{ J}\cdot(\text{K}\cdot\text{mol})^{-1}$  showing a greater dependence of the equilibrium constant to temperature when compared to previously reported *N,O*-acetals ( $\Delta H = -10.7 \text{ kJ}\cdot\text{mol}^{-1}$  and  $\Delta S = -8.9 \text{ J}\cdot(\text{K}\cdot\text{mol})^{-1}$ ).

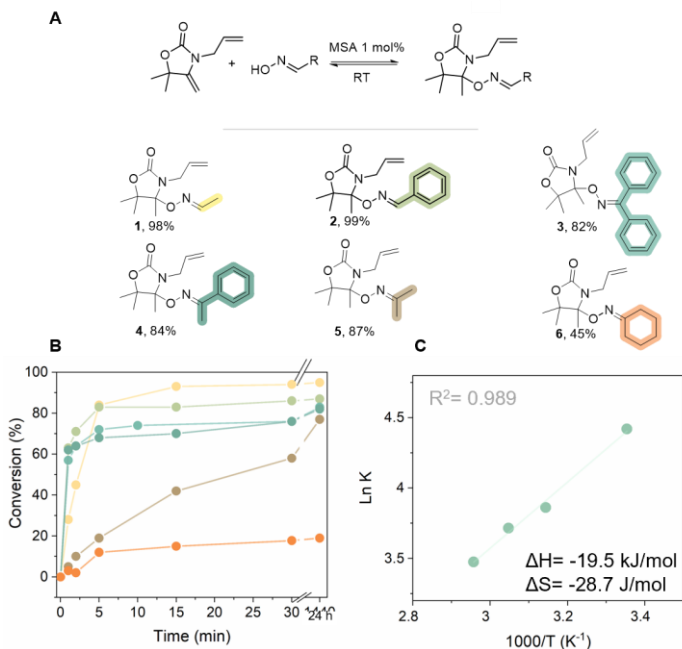


**Figure 5.2.** a) Scope of oxime-ene derivatives and respective isolated yields; b) Kinetics of reaction between a model alkylidene oxazolidone (AlloX) and a series of oxime substrates as monitored by  $^1\text{H}$  NMR (0.5 M ACN, 1 mol%, 25  $^{\circ}\text{C}$ ); c) Van't Hoff plot extracted from the  $^1\text{H}$  NMR temperature screening.

The ability to dissociate covalent bonds is fundamental when designing recyclable CANs, hence, we probed the oxazolidone- $\alpha$ -oxime bond thermal reversibility by  $^1\text{H}$  NMR in bulk. The adduct (**2**) was found to only dissociate if an acidic catalyst was present (MSA 1mol %) as expected from previous experiments in which the formation of the bond could

only be achieved under acidic catalysis. Without catalyst, no dissociation was observed at RT while 2% dissociated adduct was observed in presence of 1 mol% MSA. Increasing the temperature to 100 °C increased the dissociation, reaching 83% with acidic catalyst, respectively (Figure 5.3-a, Figure S5.25,S5.26). Next, we studied the exchange between the benzaldehyde oxime adduct (**2**) and a ten-fold excess of acetaldehyde oxime at different temperatures (25 to 50 °C) by means of  $^1\text{H}$  NMR. The exchange reaction proceeded quickly, reaching equilibrium in around 60 minutes for all temperatures (Figure 5.2-c,d,e,f, Figure S5.27-S5.31). The resulting Arrhenius plot<sup>39</sup> returned an activation energy of  $42.6 \pm 2.5$  kJ/mol, intermediate between the *N,O*-acetal and *N,S*-acetal bonds (38.9 and 64.9 kJ/mol, respectively).<sup>23</sup>

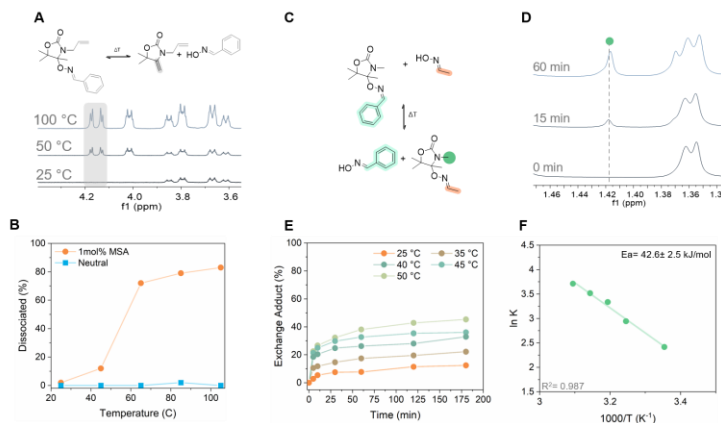


**Figure 5.3.** a)  $^1\text{H}$  NMR spectra of the dissociation of **2** from 25 to 100 °C; b) Dissociation percentage of **2** in neutral and in acidic media as measured by  $^1\text{H}$  NMR; c) scheme of the exchange reaction between **2** and acetaldehyde oxime; d)  $^1\text{H}$  NMR of exchange of **2** and acetaldehyde oxime with conversion graph (e) and the extracted Arrhenius plot (f).

### 5.3.2. Modelling of the Oxime-ene Reaction

The reversibility, together with the intermediate activation energy of the oxazolidone- $\alpha$ -oxime bond were corroborated using density functional theory (DFT, theory level WB97XD/6-31+G(d)). We modelled the reaction of **AlLOx** and acetaldehyde oxime using MSA as catalyst using a conductor-like polarizable medium ( $\epsilon=4.7113$ , chloroform, Figure 5.4). As expected, the first step of the reaction, the formation of the carbocation, was minimally influenced by the type of nucleophile, with similar stabilisation between thiols, alcohols and oximes (Figure S5.32, and Figure S5.33 for the structures of the intermediates and transition states). In fact, the INT1 is stabilised by hydrogen bonding and the interaction between the catalyst and the electron-rich alkylidene double bond (-45.8 kJ/mol). After the protonation of the double bond by MSA (TS1, -21.6 kJ/mol), the charge is delocalised through the oxazolidone ring as exemplified by the change in bond lengths participating in the delocalisation (-51.9 kJ/mol, Table S5.1). After a rearrangement (INT2b, -54.6 kJ/mol), the nucleophilic attack of the oxime on the oxazolidone ring occurs (RDS). This is the main difference from previously reported mechanisms in which the RDS was the protonation of the double bond.<sup>23</sup> With a  $\Delta G$  of 48.9 kJ/mol, the linking of the oxime with the carbon in  $\alpha$  to the carbamate occurs, giving rise to INT3 (-79.3 kJ/mol). Then, the catalyst is regenerated by hydrogen transfer with the hydroxyl of the oxime, and the product is finally formed (-70.3 kJ/mol). All structures are reported in SI in Figure S5.33. Again, the stabilisation of the product is intermediate between the thiol- and alcohol- adduct, explaining the high conversion of the reaction (Figure S5.32).



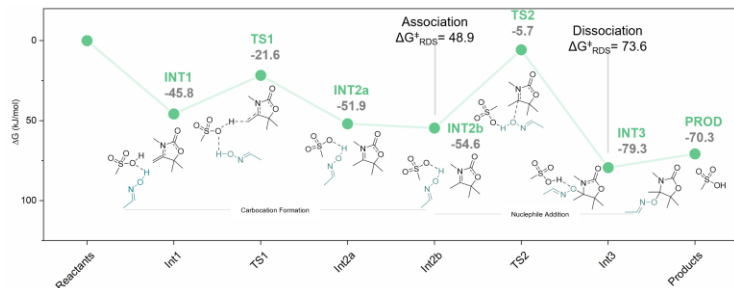


**Figure 5.4.** Gibbs-free energy profile of the reaction pathway for the formation of the oxime-ene moiety between a model oxazolidone and a model oxime (acetaldehyde oxime) catalysed by MSA. Vertical lines show the energy barriers for rate-determining steps.

### 5.3.3. Preparation of Materials Based on the Oxime-ene Reaction

With a full picture of the reaction behaviour, we set off to prepare a material containing the oxazolidone-oxime linkage. First, we prepared a crosslinker bearing four alkylidene oxazolidone moieties. We do so by a simple radical thiol ene reaction between **AlLOx** and pentaerythritol tetrakis(3-mercaptopropionate) (**S4**). Thanks to the different electron richness of the two double bonds, only the allyl bond reacted under the selected experimental conditions.<sup>40</sup> Hence, we were able to form the crosslinker (**7**) in bulk after 30 min of irradiation (BAPO 0.5 wt%, 390 nm, 20 mW/cm<sup>2</sup>) of a 4:1 mixture of **AlLOx** and **S4** as exemplified by <sup>1</sup>H NMR. In fact, we observe the disappearance of the allyl bonds signal (5.15, 5.75 ppm, m) while the exovinylene double bond signals were retained (4.24 ppm) (further characterisations in Figure S5.34-S5.35). A major disadvantage of preparing materials using oximes is their low solubility.

Hence, to prepare the thermoset materials, we required the use of solvents (acetone 50 wt%) to obtain a homogenous mixture between **7**, terephthalaldehyde dioxime and MSA (1 mol%). After 30 min of stirring at 60 °C, a dark yellow mixture was obtained, which was immediately cast onto a silicone mould. As soon as the mixture cooled to RT, it solidified into a self-standing material (Figure 5.5-a). After removal of acetone by vacuum drying (40 °C, 24h), a brittle film was obtained with a high gel content of 92±3% (acetone, swelling index 152±12%). Gratifyingly, its FTIR spectrum showed complete consumption of the exovinylene double bond (1682 cm<sup>-1</sup>) (Figure 5.5-b) together with a low intensity of the -OH stretching resonance after curing (3340 cm<sup>-1</sup>). The DSC trace of the material clearly showed one T<sub>g</sub> at 32 °C together with an endothermic peak at 164 °C, conducive to the network dissociation (Figure 5.5-c). This was further confirmed by the DMA trace of the material. In fact, we could observe both a T<sub>α</sub> (62 °C) and a stark reduction in storage modulus for temperatures above 100 °C, connected to the network dissociation of the material thanks to the reversible oxime-ene reaction (Figure S5.36).<sup>24</sup> The material was very brittle, with a Young's Modulus of 1530±80 MPa and a stress at break of 6.6±0.9 MPa (Figure 5.5-d). The material was found to be very dynamic, with a relaxation time of 119 seconds at 65 °C (Figure 5.5-e). Fitting of the relaxation curves by a single element Maxwell Model<sup>41</sup> (Table S5.2) returned an E<sub>flow</sub> of 120±4 kJ/mol with an excellent linear dependency to temperature (Figure 5.5-f), with a energy of flow that was slightly higher than the previously-reported *N,O*-acetal moiety.

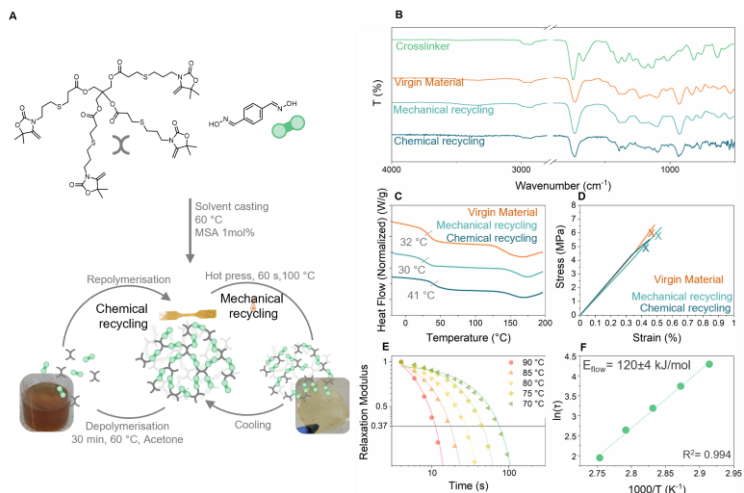


**Figure 5.5.** a) Scheme of the preparation of thermoset materials containing the oxime-ene dynamic bond and their mechanical and chemical degradation; b) FTIR spectra of the crosslinker, virgin, mechanically- and chemically recycled thermoset materials; c) DSC trace of the crosslinker, virgin, mechanically- and chemically recycled thermosets; d) Stress-Strain curves virgin, mechanically- and chemically recycled thermosets; e) Stress relaxation of the virgin material; f) Arrhenius fitting of the stress relaxation data.

We exploited the dynamic behaviour of the material to recycle the material by means of hot pressing (1 MPa, 60 s, 100 °C) to obtain clear, self-standing films (Figure 5.5-a). These had similar characteristics to the virgin material. Its FTIR spectra showed low intensity of the resonance of both the exovinylene double bond and the -OH stretching resonance of the oxime together with similar T<sub>g</sub> (30 °C) (Figure 5.5-b,c). The mechanical properties also varied minimally, showing a Young's

Modulus of  $1480 \pm 152$  MPa and a strain at break of  $6.5 \pm 0.4$  MPa (Figure 5.5-d). While mechanical recycling could be demonstrated, we explored also the possibility to recycle the material chemically. We could depolymerise the material by soaking it into acetone at  $60^\circ\text{C}$  for 30 min under stirring, returning a viscous liquid. The reaction was then quenched using a base (TEA, 5 mol%), diluted with EtOAc and washed with water to remove the catalyst. After removal of the organic solvent, a fully soluble viscous liquid was obtained. 2D NMR (HSQC) analyses of the viscous liquid (Figure 5.5-a) highlighted the presence of free exovinylene double bond (Figure S5.37), demonstrating that the material partially depolymerised by scission of the oxime-ene bond, returning a mixture of oligomers. Quantification of the amount of free exovinylene double bond returned a degree of depolymerisation of 76% (See Section 5.5 for further information). Upon addition of an acidic catalyst (MSA) and mixing at  $60^\circ\text{C}$  in acetone to homogenise the mixture, the resin polymerised again to give a self-standing film. While the FTIR spectrum was similar to the virgin and mechanically recycled materials (Figure 5.5-b), the DSC trace showed a heightened  $T_g$  ( $41^\circ\text{C}$ , Figure 5.5-c). Notwithstanding this, the mechanical properties of the material were slightly lower than the virgin material (Young Modulus=  $1530 \pm 120$  MPa, Stress at Break=  $5.5 \pm 0.7$  MPa, Figure 5.5-d).

#### 5.3.4. Hydrolytic Degradation

We wanted to exploit the presence of the cleavable bonds to enable hydrolytic degradation of the thermosets (Figure 5.6-a). Oximes are well known for being more hydrolytically resistant when compared to acetals, hence, we investigated the stability of the oxime- $\alpha$ -oxazolidone bond.<sup>36,42</sup> This was reflected by model compound  $^1\text{H}$  NMR studies. Model compound **1** was placed in water at RT in both neutral and acidic environment (1 mol% MSA). We could observe that in a two hours

period, the adduct minimally degraded in water (9% degradation) while 64% degradation was noted in acidic environment in the same timeframe (Figure 5.6-b, Figures S5.38,S5.39). The two degraded towards the hydrated oxazolidone product, giving a possibility to recover this monomer for further use after dehydration.<sup>22,23</sup> Satisfyingly, the oxime-ene bond shows a slower hydrolytic degradation when compared to the previously reported *N,O*-acetals, which would degrade considerably in neutral environment, giving a palette of dynamic bonds for the modulation of the degradability of oxazolidone networks.

Encouraged by these results, we explored the degradation behaviour of the thermoset by gravimetry. While at RT in water no degradation was observed in two-weeks timeframe, in acidic environment the material degraded slowly, returning a soft material after 2 days. Consistent mass loss was observed in course of 14 days, with a  $38\pm6\%$  average mass loss. The behaviour changed starkly upon raising the temperature to 60 °C. About 73% of the material was degraded in a neutral environment in one day and was fully decomposed after 3 days, returning a cloudy suspension. Additionally, it required only 24 h to reach full degradation in a 1M solution of MSA in water at the same temperature. The high reversibility, compounded with the degradability potential of the oxime-ene chemistry, showcase the potential of this chemistry to advance POXa material as a future-proof material.

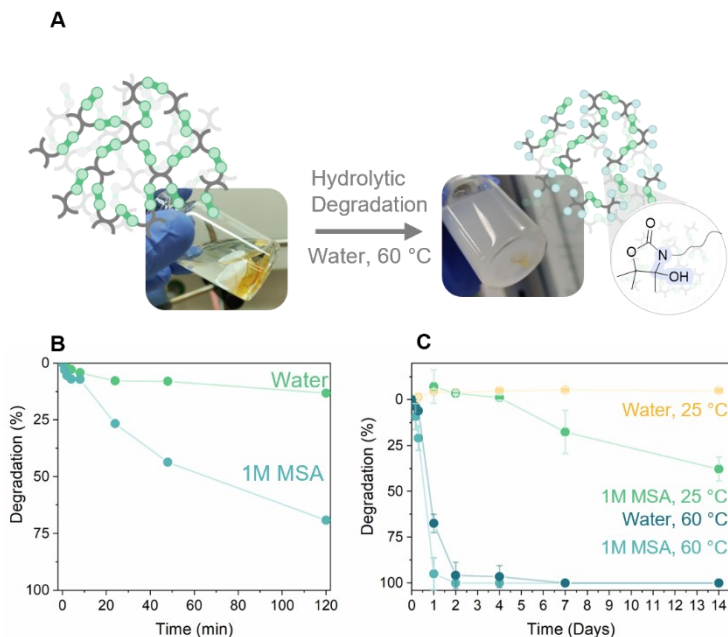


**Figure 5.6.** a) Scheme of the hydrolytic degradation of a network crosslinked with oxime-ene bonds; b) hydrolytic degradation of model compound **1** in water and 1M MSA at RT; d) Hydrolytic degradation of crosslinked material in water and 1M MSA at RT and at 60 °C.

## 5.4. Conclusions

In this work, we presented a new chemistry to prepare mechanically and chemically recyclable NIPUs that are hydrolytically stable at RT while can be quickly degraded at higher temperatures. We found that

oximes reacted quickly and efficiently with alkylidene oxazolidones to form oxime-ene adducts in good to excellent yields (45 to 99%). The reaction was greatly influenced by both the acidity of the catalyst and the polarity of the solvent. Its reversibility was demonstrated by exchange experiments, finding an activation energy of  $42.6 \pm 2.5$  kJ/mol, which is intermediate between the previously reported *N,S*- and *N,O*-acetals. DFT modelling further supported the reaction behaviour, with an intermediate stabilisation of the final product (70.3 kJ/mol). New covalent adaptable networks (CAN) featured by this dynamic oxime-ene bond were then easily prepared by crosslinking a tetrafunctional crosslinker bearing alkylidene oxazolidones and a difunctional oxime (terephthaldehyde oxime). The crosslinking reaction was found to be very quick, with the formation of a solid material in seconds after solvent casting. The dynamic behaviour of the oxime-ene reaction enabled both chemical and mechanical recycling of the material, and the properties of the network were recovered after the mechanical recycling. Furthermore, the oxime-ene adduct was found to have a slow degradation in neutral environment (9% in 2 hrs), while it was degraded quickly in acidic environment (64%). This was reflected in the crosslinked network, with the materials showing no degradation in a week timeframe in water while degrading for  $47 \pm 6\%$  in an acidic environment in the same timeframe. Increasing the temperature gave complete degradation of the material in 24 h in acidic environment while 3 days were needed to degrade in a neutral environment. The quick and efficient dynamics of the oxime-ene chemistry, coupled with its resistance to hydrolytic degradation at RT, highlight its potential for expanding the applicability of polyoxazolidones, opening up the door to application in degradable polymers, cargo delivery and coatings.

## 5.5. Materials and Methods

### 5.5.1. Materials

Acetaldehyde Oxime (TCI 99%), Acetoxime (TCI 99%), Benzaldehyde Oxime (Sigma, 97%), Cyclohexanone Oxime (TCI, >98%), Acetophenone Oxime (Sigma, 95%), Benzophenone Oxime (Sigma, 95%), Methyl 3-mercaptopropionate (Sigma, 98%), Methanesulfonic acid (Sigma, >99%), Pentaerythritol tetrakis(3-mercaptopropionate) (S4, Sigma, ≥95), Triethylamine (TEA, Sigma, 99.5%), and all solvents were used without further purification. Terephthalaldehyde dioxime and **AlLOx** were prepared as previously reported.<sup>24,37</sup>

### 5.5.2. Methods

**Nuclear magnetic resonance (NMR) spectroscopy.** <sup>1</sup>H- and <sup>13</sup>C-NMR analyses were performed on a Bruker Avance 300 MHz spectrometer at 25 °C in the Fourier transform mode using CDCl<sub>3</sub> or DMSO-*d*<sub>6</sub> as solvents.

**HRMS (ESI)** data were acquired in SCAN mode, using a mass range 50–1000 u in resolution mode (FWHM ≈ 20,000) and a scan time of 0.1 s. The source temperature was set to 120 °C and the desolvation temperature to 350 °C. The capillary voltage was 0.7 kV and the cone voltage 15 V. Nitrogen was used as the desolvation and cone gas at flow rates of 600 L/h and 10 L/h, respectively. Before analysis, the mass spectrometer was calibrated with a sodium formate solution. A leucine-enkephalin solution was used for the lock mass correction, monitoring the ions at mass-to-charge ratio (*m/z*) 556.2771 and 278.1141. All of the acquired spectra were automatically corrected



during acquisition based on the lock mass. The samples were dissolved in the corresponding solvent at a concentration of 1 mg/ml and diluted to 20 µg/mL for the analysis.

**Gel content (GC).** Films prepared as described in the experimental section were cut in rectangular shapes and weighted ( $m_1$ ) before immersing 48 h in acetone. After weighing, the swelled films ( $m_2$ ) were dried in a vacuum oven at 60 °C for 24 h. The films were weighed once again ( $m_3$ ). Swelling (SI) and Gel content (GC) were calculated with equation 1 and 2, respectively:

$$SI = 100 * m_2 / m_1 \quad (1)$$

$$GC = 100 * m_3 / m_1 \quad (2)$$

**Tensile tests** were carried out on dogbone samples (ASTM D638 TYPE V) in an Instron 5569 tensile tester (Instron, Norwood, MA, USA). Young's modulus, Tensile strength ( $\sigma_t$ ), Yield strength ( $\sigma_y$ ), and strain at break ( $\epsilon_b$ ) were determined using Bluehill software from the load-displacement curves at a crosshead speed of 10 mm/min. A minimum of three tensile specimens were tested for each reported value.

**Fourier Transform Infrared Spectroscopy (FT-IR) spectra** were recorded on a Nicolet iS20 Spectrometer using Attenuated Total Reflection (ATR) at a resolution of 4 cm<sup>-1</sup> and a total of 32 interferograms.

**Differential Scanning Calorimetry (DSC)** was performed on a TA Instruments DSC 250 calibrated with indium, and the curves were analysed using the Trios software. A heat-cool-heat method was

employed in a range from -20 to 200 °C with ramp of 10 °C/min. Reported values are calculated on the inflexion point of the  $T_g$  signal and refer to the second heating.

**Dynamic Mechanical Analysis (DMA)** was performed on a DMA Q800. A 10 mm x 2 mm x 0.7 mm (l x w x t) was placed in a tension film clamp. An oscillation amplitude of 15  $\mu$ m and a static force of 0.01 N were employed. A ramp of 3 °C/min was used from 35 to 125 with a frequency of 1 Hz.  $T_a$  was measured as the peak in the Tan delta curve.

**Isothermal stress relaxation** was conducted on a DMAQ800 in tension mode. Rectangular samples of 15×6×0.5 mm were used. The sample was held at the desired temperature for 10 min before a 0.5% strain was applied. The strain was kept constant for 20 min. Stress-relaxation of the dynamic cross-linked network was defined using a first order Maxwell model (Equation 3). The Flow Activation Energy ( $E_{flow}$ ) was then extracted by plotting an Arrhenius relationship (Equation 4) with  $\tau^*$  as a function of  $1/T$ .

$$\frac{G(t)}{G_0} = e^{-t/\tau^*} \quad (3)$$

$$\tau^* = \tau_0 e^{E_a/RT} \quad (4)$$

**Material Preparation 7** and terephthaldehyde oxime were mixed in equimolar amount in acetone (50% weight of the monomers). MSA (1mol%) was added and the mixture was mixed at 60 °C for 3 min until an homogenous dark yellow mixture resulted. The mixture was then poured in a Teflon or silicone mold. The resulting dark yellow material

was let to cool before drying overnight under vacuum at 40 °C giving a transparent brittle film.

**Reprocessing of Films,** The material was grinded and then hot-pressed in a Collin P200E hydraulic press for 60 s at 100 °C with an applied pressure of 1 MPa. The resulting film was cooled down for 10 min before cutting dogbone samples (ASTM D638 TYPE V) with a die cutter.

### 5.5.3. Reaction Screening

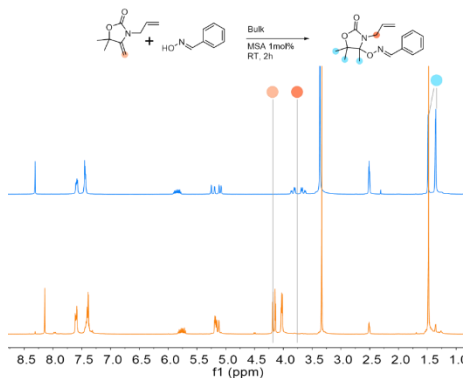
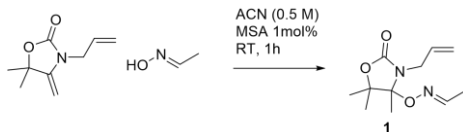


**Figure S5.1.**  $^1\text{H}$  NMR of the reaction between **AlIOx** and benzaldehyde oxime before and after the addition of MSA (1 mol%, bulk, RT, 2h).

## 5.5.4. Synthesis of Model Compounds

### 5.5.4.1. Synthesis of **1**



Scheme S5.1. Synthesis of **1**.

**Allox** (0.5 g, 3 mmol, 1 eq), acetaldehyde oxime (0.182 g, 3.1 mmol, 1.05 eq) and MSA (3 mg, 1 mol%) were dissolved in ACN (0.5 M). The mixture was stirred for 2 h before being quenched with TEA (50  $\mu$ L). The resulting mixture was diluted with Ethyl acetate (25 mL) and washed thrice with water (3x25 mL), once with brine (25 mL). The organic phase was separated and dried over  $\text{MgSO}_4$  before being evaporated *via* rotary evaporation. The product was obtained as a transparent crystalline solid (0.685 g, 98% yield)

**$^1\text{H}$  NMR** (300 MHz,  $\text{DMSO-d}_6$ )  $\delta$  6.98 (q,  $J$  = 5.4 Hz, 1H), 5.94 – 5.68 (m, 1H), 5.30 – 4.97 (m, 2H), 3.86 – 3.49 (m, 2H), 1.78 (d,  $J$  = 5.5 Hz, 3H), 1.42 (s, 3H), 1.32 (s, 3H), 1.29 (s, 3H).  **$^{13}\text{C}$ -NMR** (75 MHz,  $\text{DMSO-d}_6$ )  $\delta$  148.71, 134.62, 115.77, 96.02, 84.16, 42.19, 40.34, 40.06, 39.78, 39.50, 39.23, 38.95, 38.67, 25.90, 19.60, 17.60, 12.01. **HRMS**  $m/z$ :  $[\text{M-H}]^+$ , 227.1396; found, 289.1390

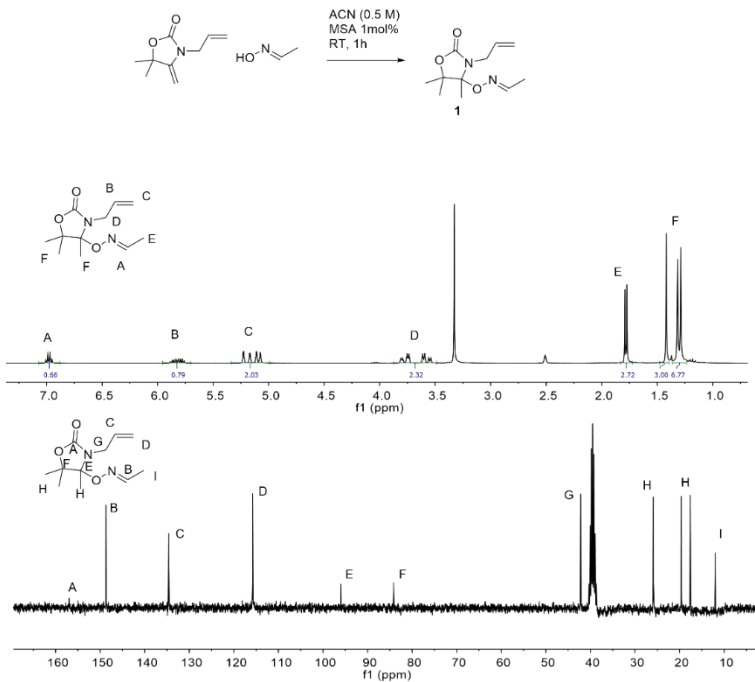
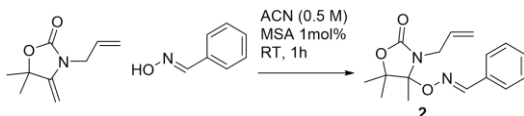


Figure S5.2. <sup>1</sup>H and <sup>13</sup>C NMR of **1**.

## 4.1.

5.5.4.2. Synthesis of **2**Scheme S5.2. Synthesis of **2**.

**Allox** (0.5 g, 3 mmol, 1 eq), benzaldehyde oxime (0.37 g, 3.1 mmol, 1.05 eq) and MSA (3 mg, 1 mol%) were dissolved in ACN (0.5 M). The mixture was stirred for 2 h before being quenched with TEA (50  $\mu\text{L}$ ). The resulting mixture was diluted with Ethyl acetate (25 mL) and washed thrice with water (3x25 mL), once with brine (25 mL). The organic phase was separated and dried over  $\text{MgSO}_4$  before being evaporated *via* rotary evaporation. The product was obtained as a white powder (0.855 g, 99% yield)

$^1\text{H}$  NMR (300 MHz,  $\text{DMSO}-d_6$ )  $\delta$  8.31 (s, 1H), 7.76 – 7.52 (m, 2H), 7.52 – 7.30 (m, 3H), 5.84 (m, 1H), 5.43 – 4.92 (m, 2H), 4.04 – 3.55 (m, 2H), 1.49 (s, 3H), 1.36 (s, 3H), 1.35 (s, 3H).  $^{13}\text{C}$ -NMR (75 MHz,  $\text{DMSO}-d_6$ )  $\delta$  157.18, 149.58, 134.54, 131.83, 130.34, 128.84, 126.95, 115.89, 97.12, 84.30, 42.32, 40.34, 40.06, 39.78, 39.50, 39.23, 38.95, 38.67, 25.90, 19.89, 17.37. **HRMS**  $m/z$ :  $[\text{M}-\text{H}]^+$ , 289.1548; found, 289.1547

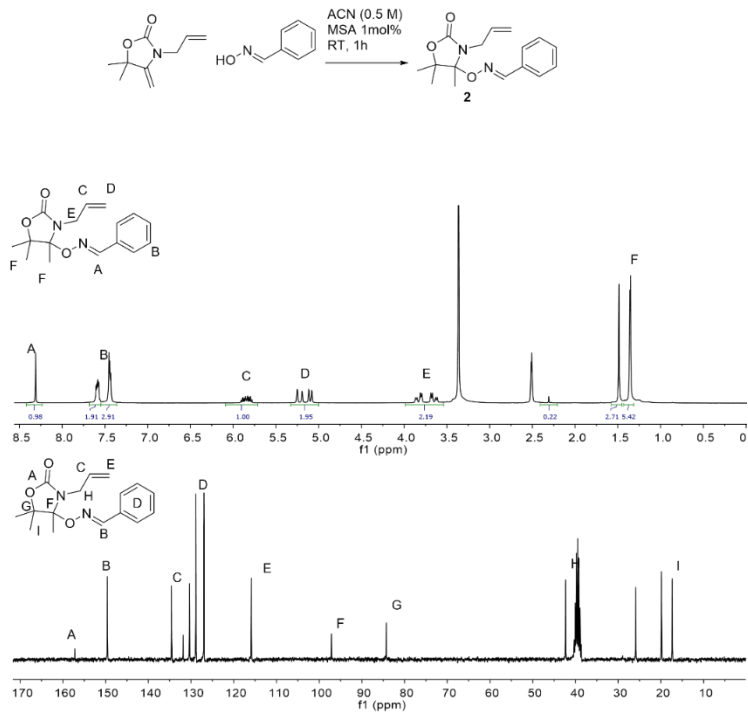
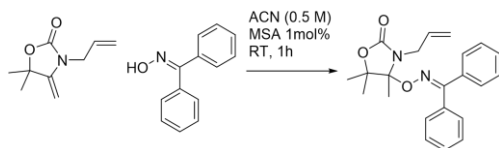


Figure S5.3. <sup>1</sup>H and <sup>13</sup>C NMR of **2**.

5.5.4.3. Synthesis of **3**Scheme S5.3. Synthesis of **3**.

**Allox** (0.05 g, 0.3 mmol, 1 eq), benzophenone oxime (0.059 g, 0.31 mmol, 1.05 eq) and MSA (0.3 mg, 1 mol%) were dissolved in ACN (0.5 M). The mixture was stirred for 2 h before being quenched with TEA (50  $\mu$ L). The resulting mixture was diluted with Ethyl acetate (25 mL) and washed thrice with water (3x25 mL), once with brine (25 mL). The organic phase was separated and dried over  $\text{MgSO}_4$  before being evaporated *via* rotary evaporation. The product was obtained by column chromatography in Hex/EtOAc (7.5/1.5 ratio,  $\text{I}_2$  and Vanillin stain) as a yellow powder (0.09 g, 82% yield)

$^1\text{H}$  NMR (300 MHz,  $\text{DMSO}-d_6$ )  $\delta$  7.55 – 7.11 (m, 10H), 5.92 – 5.75 (m, 1H), 5.28 – 5.00 (m, 2H), 3.91 – 3.59 (m, 2H), 1.36 (s, 3H), 1.33 (s, 6H).  $^{13}\text{C}$ -NMR (75 MHz,  $\text{DMSO}-d_6$ )  $\delta$  157.16, 156.37, 135.63, 134.45, 132.37, 129.75, 128.84, 128.32, 128.25, 128.09, 127.39, 126.92, 115.91, 97.33, 84.19, 42.44, 25.77, 19.97, 17.24. **HRMS**  $m/z$ :  $[\text{M}-\text{H}]^+$ , 365.1868; found, 365.1860



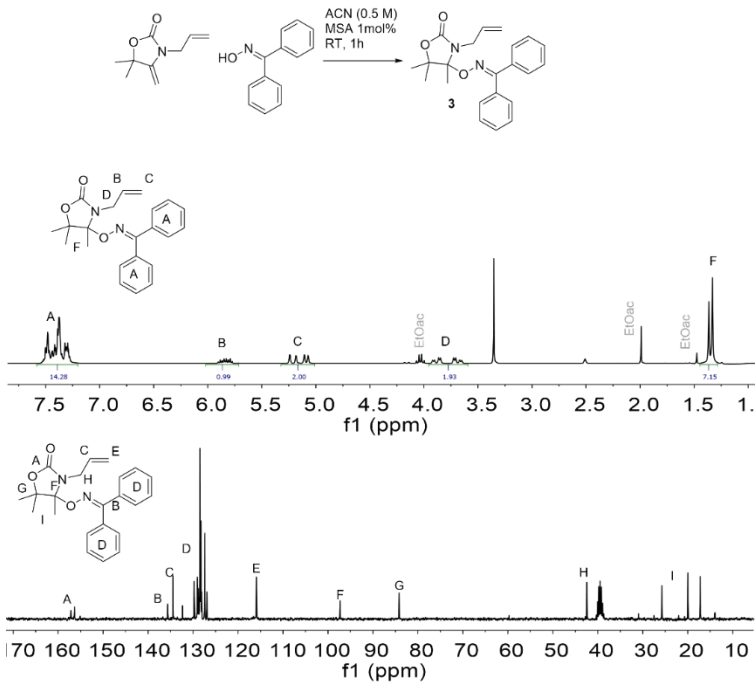
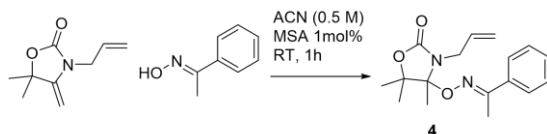


Figure S5.4. <sup>1</sup>H and <sup>13</sup>C NMR of **3**.

5.5.4.4. Synthesis of **4**Scheme S5.4. Synthesis of **4**.

**Allox** (0.05 g, .3 mmol, 1 eq), acetophenone oxime (0.042 g, 0.31 mmol, 1.05 eq) and MSA (0.3 mg, 1 mol%) were dissolved in ACN (0.5 M). The mixture was stirred for 2 h before being quenched with TEA (50  $\mu$ L). The resulting mixture was diluted with Ethyl acetate (25 mL) and washed thrice with water (3x25 mL), once with brine (25 mL). The product was obtained by column chromatography in Hex/EtOAc (7.5/1.5 ratio,  $I_2$  and Vanillin stain) as a yellow powder (0.07 g, 84% yield).

$^1\text{H}$  NMR (300 MHz, DMSO- $d_6$ )  $\delta$  7.88 – 7.59 (m, 2H), 7.56 – 7.31 (m, 3H), 6.01 – 5.72 (m, 1H), 5.52 – 4.89 (m, 2H), 3.73 (m, 2H), 2.22 (s, 3H), 1.50 (s, 3H), 1.36 (s, 3H), 1.32 (s, 3H).  $^{13}\text{C}$ -NMR (75 MHz, DMSO- $d_6$ )  $\delta$  13C NMR (75 MHz, DMSO)  $\delta$  157.23, 154.93, 135.66, 134.54, 129.48, 128.43, 125.90, 115.76, 96.89, 84.07, 42.32, 40.34, 40.05, 39.78, 39.50, 39.22, 38.94, 25.84, 19.73, 17.48, 12.34. **HRMS**  $m/z$ :  $[\text{M}-\text{H}]^+$ , 303.1709; found, 303.1703

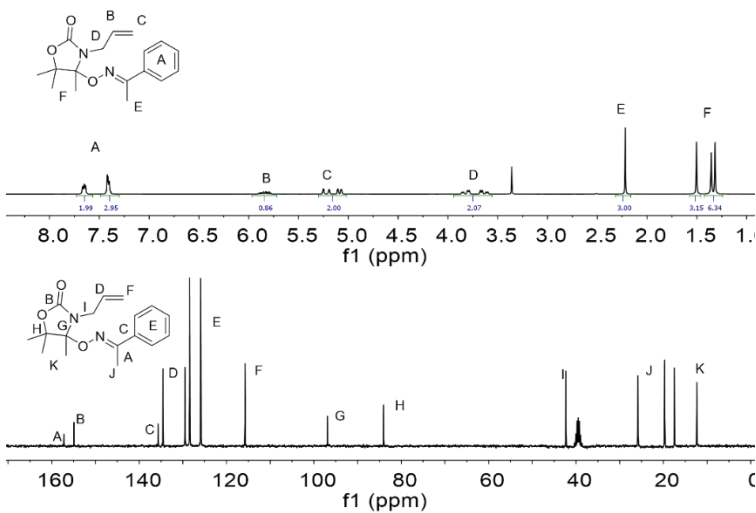
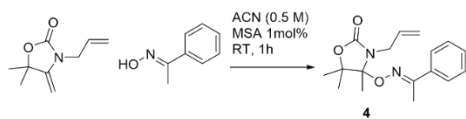
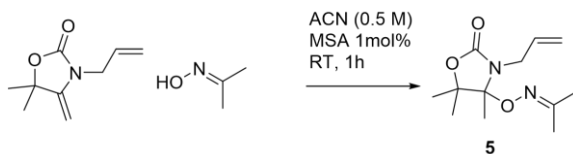


Figure S5.5. <sup>1</sup>H and <sup>13</sup>C NMR of **4**.

5.5.4.5. Synthesis of **5**Scheme S5.5. Synthesis of **5**.

**Allox** (0.5 g, 3 mmol, 1 eq), acetoxime (0.225 g, 3.1 mmol, 1.05 eq) and MSA (3 mg, 1 mol%) were dissolved in ACN (0.5 M). The mixture was stirred for 2 h before being quenched with TEA (50  $\mu$ L). The resulting mixture was diluted with Ethyl acetate (25 mL) and washed thrice with water (3x25 mL), once with brine (25 mL). The organic phase was separated and dried over  $\text{MgSO}_4$  before being evaporated *via* rotary evaporation. The product was obtained as a transparent crystalline solid (0.63 g, 99% yield)

$^1\text{H}$  NMR (300 MHz,  $\text{DMSO}-d_6$ )  $\delta$  5.82 (m, 1H), 5.29 – 4.95 (m, 2H), 3.95 – 3.47 (m, 2H), 1.81 (s, 6H), 1.39 (s, 3H), 1.30 (s, 3H), 1.29 (s, 3H).  $^{13}\text{C}$ -NMR (75 MHz,  $\text{DMSO}-d_6$ )  $\delta$  156.98, 155.87, 134.73, 115.59, 95.56, 84.02, 42.28, 40.33, 40.06, 39.78, 39.50, 39.22, 38.94, 38.66, 25.83, 21.72, 19.72, 17.67, 15.52. **HRMS**  $m/z$ :  $[\text{M}-\text{H}]^+$ , 241.1555; found, 241.1547

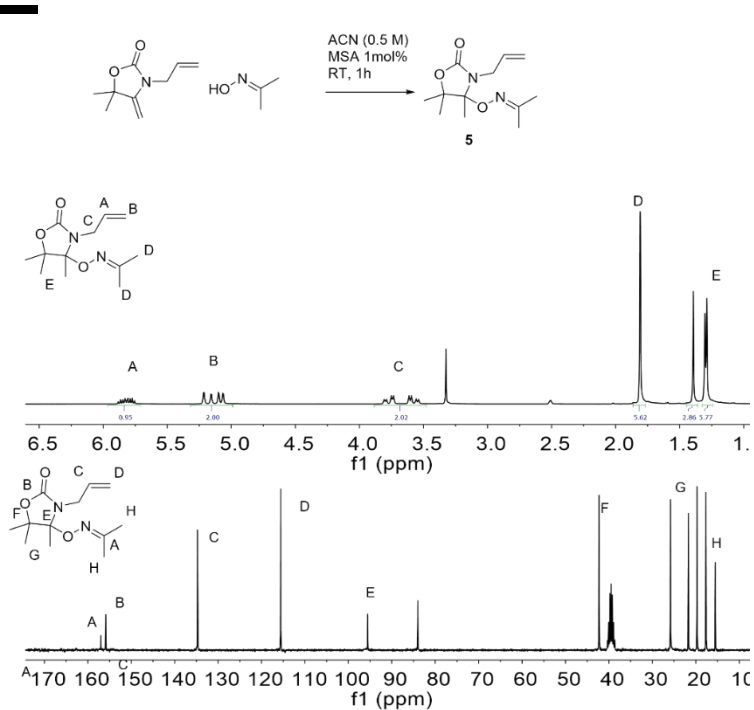
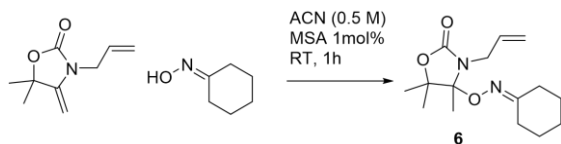
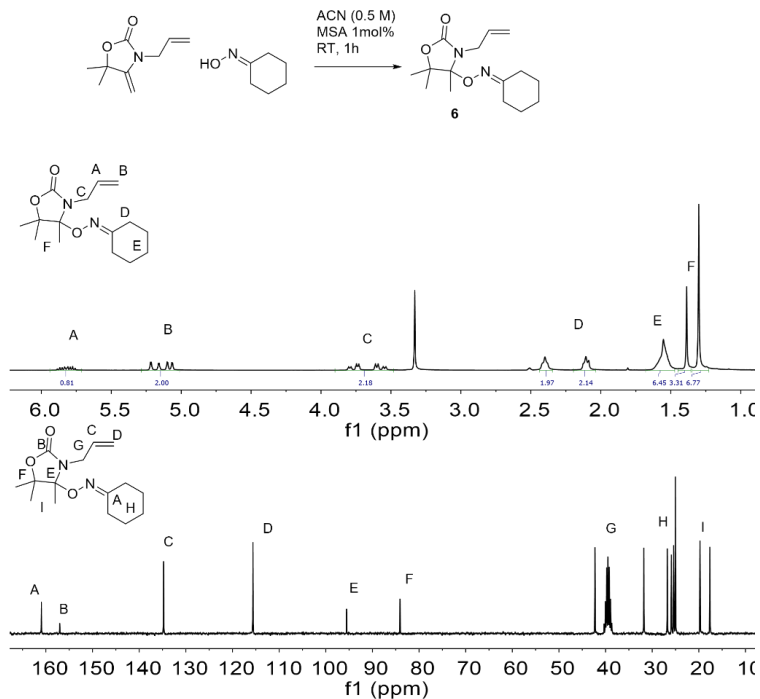


Figure S5.6. <sup>1</sup>H and <sup>13</sup>C NMR of **5**.

5.5.4.6. Synthesis of **6**Scheme S5.6. Synthesis of **6**.

**Allox** (0.5 g, 3 mmol, 1 eq), cyclohexanone oxime (0.35 g, 3.1 mmol, 1.05 eq) and MSA (3 mg, 1 mol%) were dissolved in ACN (0.5 M). The mixture was stirred for 2 h before being quenched with TEA (50  $\mu$ L). The resulting mixture was diluted with Ethyl acetate (25 mL) and washed thrice with water (3x25 mL), once with brine (25 mL). The organic phase was separated and dried over  $\text{MgSO}_4$  before being evaporated *via* rotary evaporation. The product was obtained by column chromatography in Hex/EtOAc (7.5/1.5 ratio,  $\text{I}_2$  and Vanillin stain) as a white powder (0.7 g, 82% yield).

$^1\text{H}$  NMR (300 MHz,  $\text{DMSO}-d_6$ )  $\delta$  5.98 – 5.69 (m, 1H), 5.31 – 4.94 (m, 2H), 4.01 – 3.48 (m, 2H), 2.43 – 2.04 (m, 4H), 1.55 (s, 6H), 1.39 (s, 3H), 1.30 (s, 6H).  $^{13}\text{C}$ -NMR (75 MHz,  $\text{DMSO}-d_6$ )  $\delta$  160.97, 157.04, 134.77, 115.61, 95.54, 84.08, 42.28, 40.33, 40.06, 39.78, 39.50, 39.22, 38.94, 38.66, 31.80, 26.77, 25.90, 25.41, 25.04, 19.76, 17.65. **HRMS**  $m/z$ :  $[\text{M}-\text{H}]^+$ , 281.1858; found, 281.1860



Scheme S5.7. <sup>1</sup>H and <sup>13</sup>C NMR of **6**.

### 5.5.5. Monomer Kinetics

Model reactions between **AlLOx** and a set of oximes were carried out. The two components dissolved in ACN (0.5M) in equal oxime to exovinylene double bond ratio with the catalyst (MSA 1mol%). Aliquots of the reaction mixture were sampled over time and quenched with TEA. The reactions were monitored by <sup>1</sup>H-NMR in DMSO-*d*<sub>6</sub> spectroscopy to determine the conversion in the product using equation 1

$$Conversion (\%) = \frac{I_t}{I_0} * 100 \quad (1)$$

The conversion was calculated with Equation 1 (where  $I_t$  is the integral at time  $t$  and  $I_0$  the integral at time 0) by taking into consideration the signal of the CH<sub>2</sub> of the exovinylene double bond of **AlLOx** (4.15 ppm). The signals were normalized using the signal of the allyl bond (multiplet, 5.16 ppm).

*Acetaldehyde oxime kinetics:* **AlLOx** (1.0 eq), acetaldehyde oxime (1.0 eq) were dissolved in ACN (0.5M) in a glass vial. The catalyst was then added (MSA, 1mol%). The mixture was sampled at 0, 1, 2, 5, 10 min and immediately quenched with 10  $\mu$ L of TEA before being dissolved in deuterated DMSO.



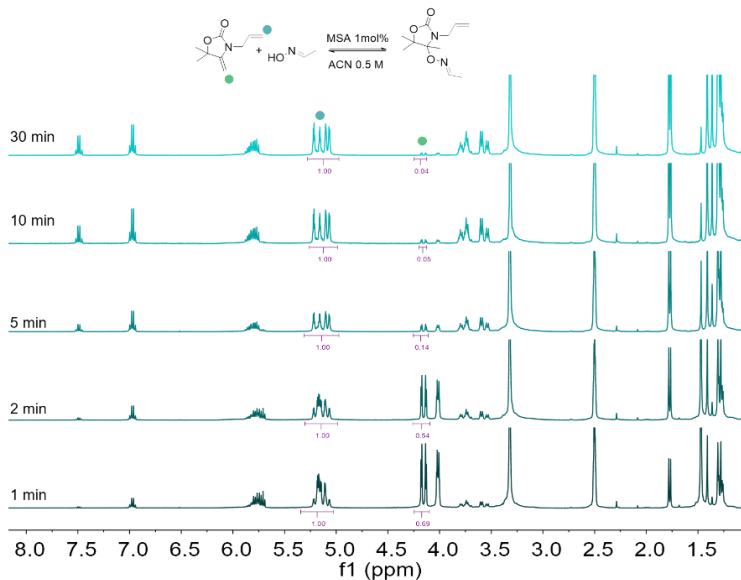


**Figure S5.7.** <sup>1</sup>H NMR of the reaction between **Allox** and acetaldehyde oxime.

**Benzaldehyde oxime kinetics:** **Allox** (1.0 eq), Benzaldehyde oxime (1.0 eq) were dissolved in ACN (0.5M) in a glass vial. The catalyst was then added (MSA, 1mol%). The mixture was sampled at 0, 1, 2, 5, 10 min and immediately quenched with 10  $\mu$ L of TEA before being dissolved in deuterated DMSO.

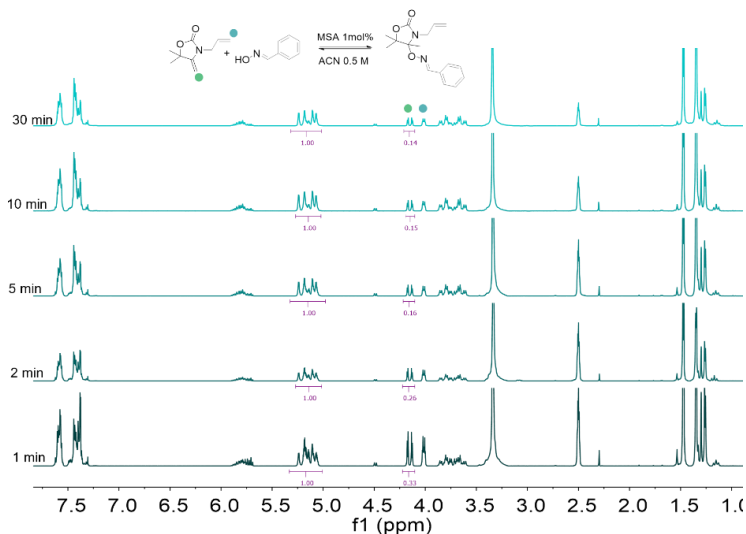


**Figure S5.8.**  $^1\text{H}$  NMR of the reaction between **Allox** and Benzaldehyde oxime.

**Benzophenone oxime kinetics:** **Allox** (1.0 eq) and benzophenone oxime (1.0 eq) were dissolved in ACN (0.5M) in a glass vial. The catalyst was then added (MSA, 1mol%). The mixture was sampled at 0, 1, 2, 5, 10 min and immediately quenched with 10  $\mu\text{L}$  of TEA before being dissolved in deuterated DMSO.

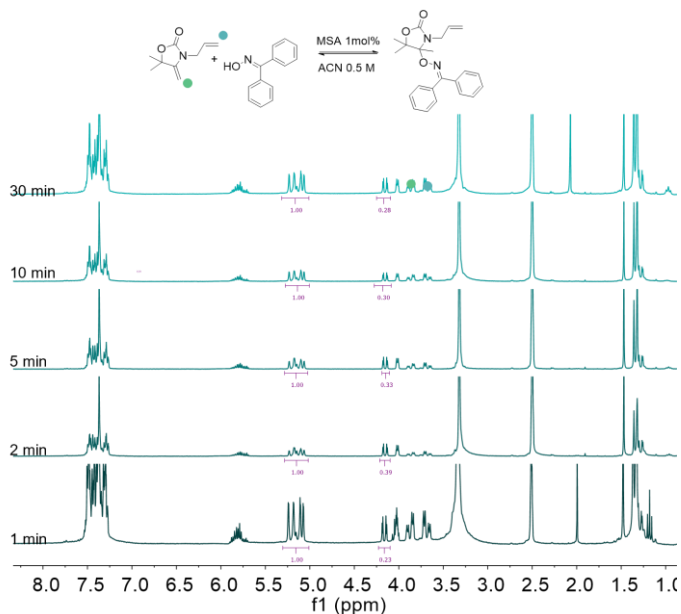


**Figure S5.9.**  $^1\text{H}$  NMR of the reaction between **Allox** and Benzophenone oxime.

**Acetophenone oxime kinetics:** **Allox** (1.0 eq) and acetophenone oxime (1.0 eq) were dissolved in ACN (0.5M) in a glass vial. The catalyst was then added (MSA, 1mol%). The mixture was sampled at 0, 1, 2, 5, 10 min and immediately quenched with 10  $\mu\text{L}$  of TEA before being dissolved in deuterated DMSO.

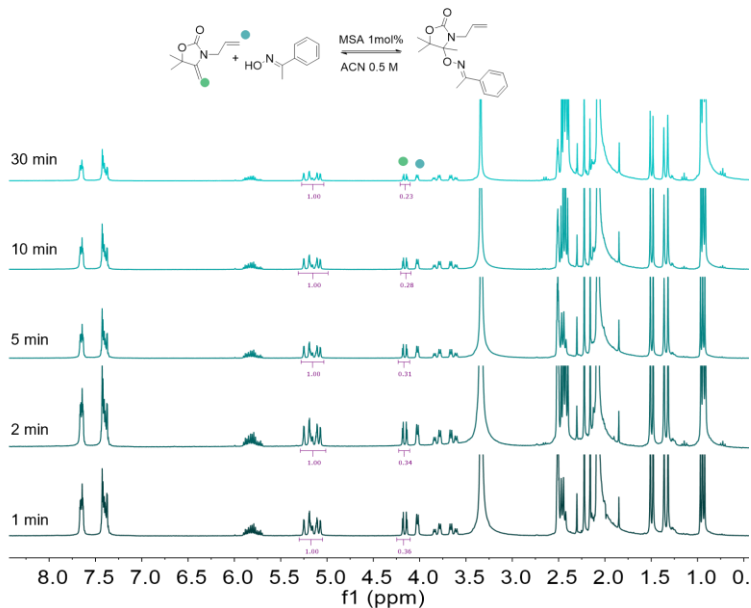


**Figure S5.10.** <sup>1</sup>H NMR of the reaction between **Allox** and Acetophenone oxime.

**Acetoxime kinetics:** **Allox** (1.0 eq) and acetoxime (1.0 eq) were dissolved in ACN (0.5M) in a glass vial. The catalyst was then added (MSA, 1mol%). The mixture was sampled at 0, 1, 2, 5, 10 min and immediately quenched with 10  $\mu$ L of TEA before being dissolved in deuterated DMSO.

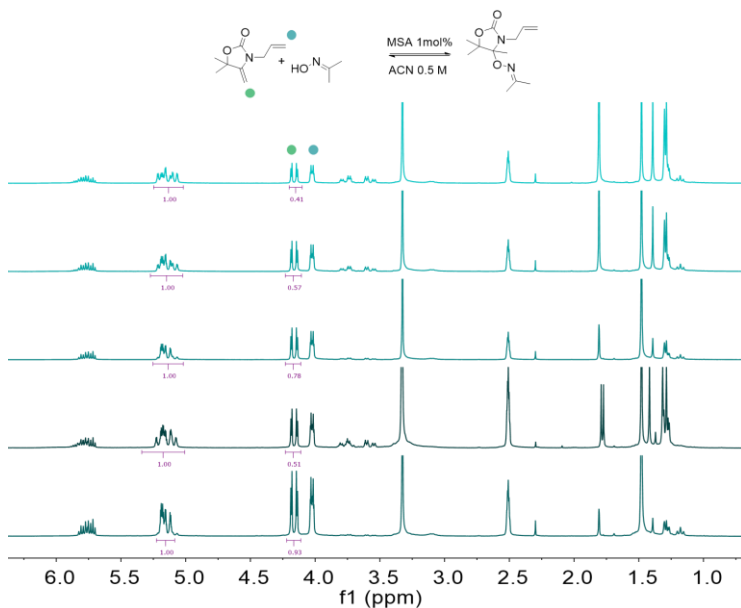
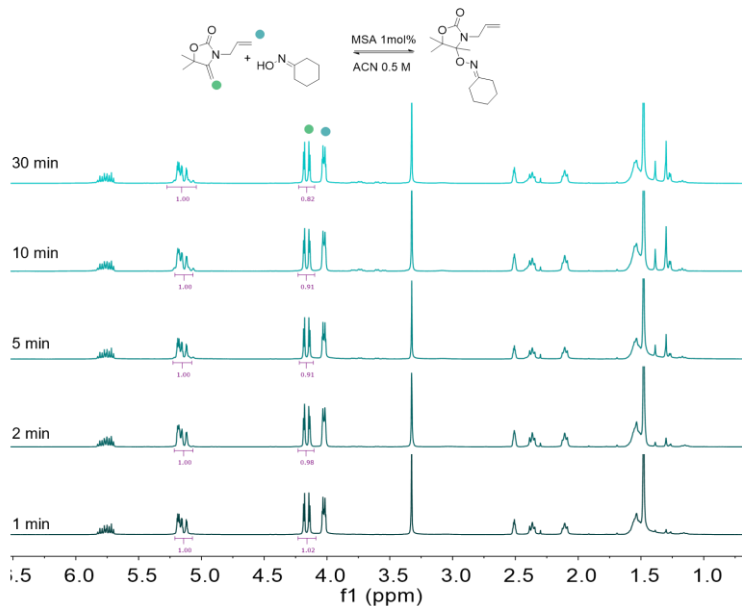


Figure S5.11.  $^1\text{H}$  NMR of the reaction between **ALLOx** and Acetoxime.

**Cyclohexanone oxime kinetics:** **ALLOx** (1.0 eq) and cyclohexanone oxime (1.0 eq) were dissolved in ACN (0.5M) in a glass vial. The catalyst was then added (MSA, 1mol%). The mixture was sampled at 0, 1, 2, 5, 10 min and immediately quenched with 10  $\mu\text{L}$  of TEA before being dissolved in deuterated DMSO.



**Figure S5.12.** <sup>1</sup>H NMR of the reaction between **Allox** and Cyclohexanone oxime.

### 5.5.6. Catalyst Screening

Model reactions between **Allox** and a benzaldehyde oxime were carried out. The two components dissolved in ACN (0.5M) in equal oxime to double bond ratio with the catalyst (MSA, TFA or AcOH 1mol%). Aliquots of the reaction mixture were sampled over time and quenched with TEA. The reactions were monitored by <sup>1</sup>H-NMR in DMSO-*d*<sub>6</sub> spectroscopy to determine the conversion in the product.

The conversion was calculated with Equation 1 by taking into consideration the signal of the CH<sub>2</sub> of the exovinylene double bond of **Allox** (4.15 ppm). The signals were normalized using the signal of the allyl bond (multiplet, 5.16 ppm).

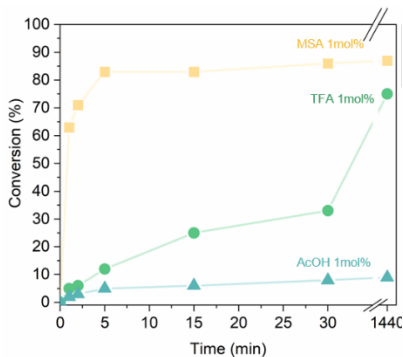


*Figure S5.13.* Conversion over time of the reaction between benzaldehyde oxime and **Allox** (0.5M ACN, RT).

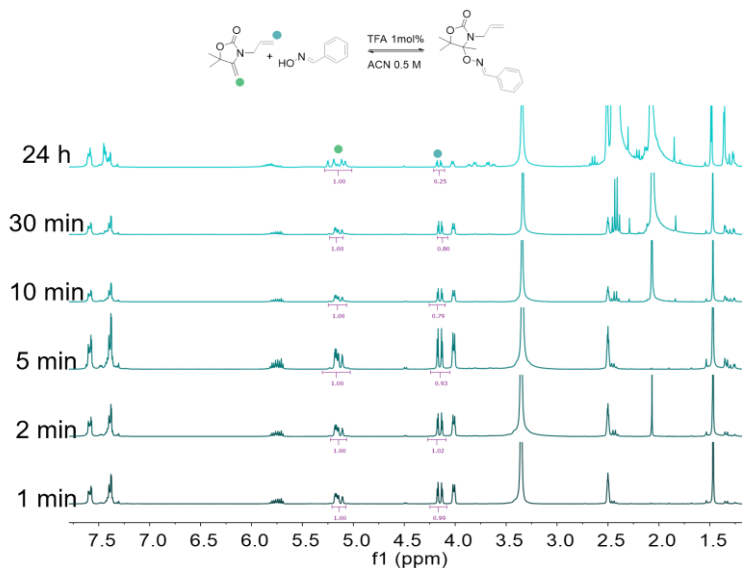


**Figure S5.14.** Kinetics of the reaction between benzaldehyde oxime and **AlLOx** (0.5M ACN, RT) catalysed by TFA (1 mol%).



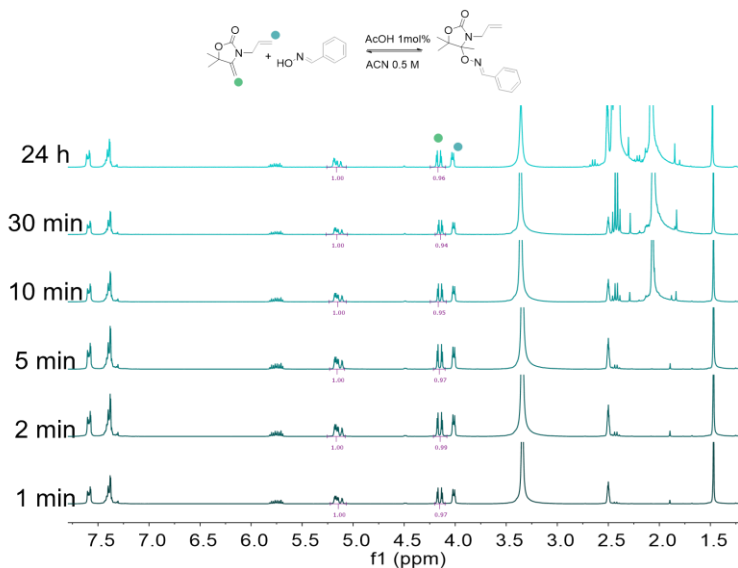


**Figure S5.15.** Kinetics of the reaction between benzaldehyde oxime and AllOx (0.5M ACN, RT) catalysed by AcOH (1mol%).

### 5.5.7. Solvent Screening

Model reactions between **Allox** and benzaldehyde oxime were carried out. The two components dissolved in the corresponding solvent (0.5M) in equal oxime to exovinylene double bond ratio with the catalyst (MSA, 1mol%). Aliquots of the reaction mixture were sampled over time and quenched with TEA. The reactions were monitored by  $^1\text{H-NMR}$  in  $\text{DMSO-}d_6$  spectroscopy to determine the conversion of the product.

The conversion was calculated with Equation 1 by taking into consideration the signal of the  $\text{CH}_2$  of the exovinylene double bond of **Allox** (4.15 ppm). The signals were normalized using the signal of the allyl bond (multiplet, 5.16 ppm).

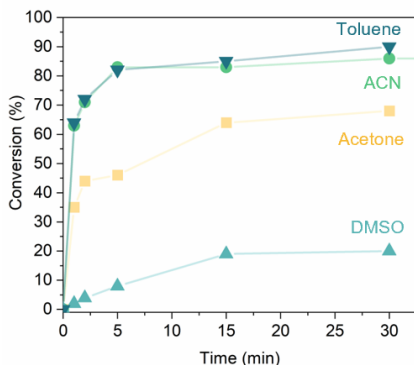


*Figure S5.16.* Conversion over time of the reaction between benzaldehyde oxime and **Allox** (0.5M, 1mol% MSA, RT) in a variety of solvents.

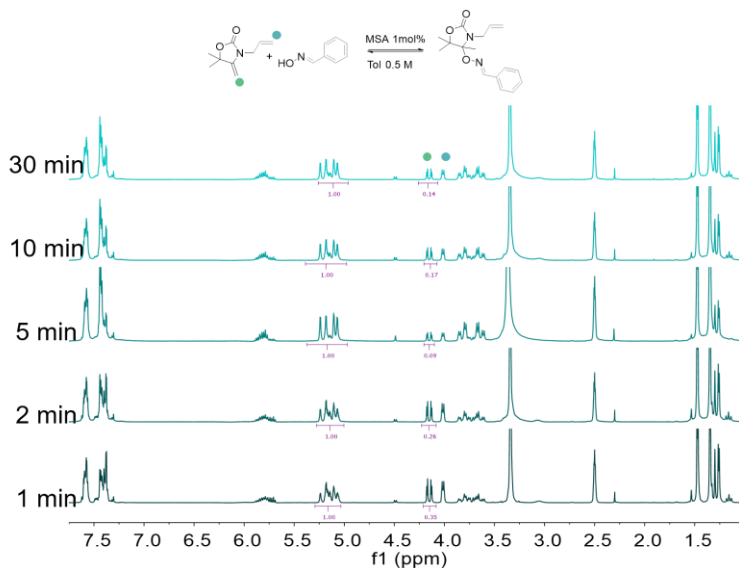


**Figure S5.17.** Kinetics of the reaction between benzaldehyde oxime and Allox (0.5M, 1mol% MSA RT) in toluene.

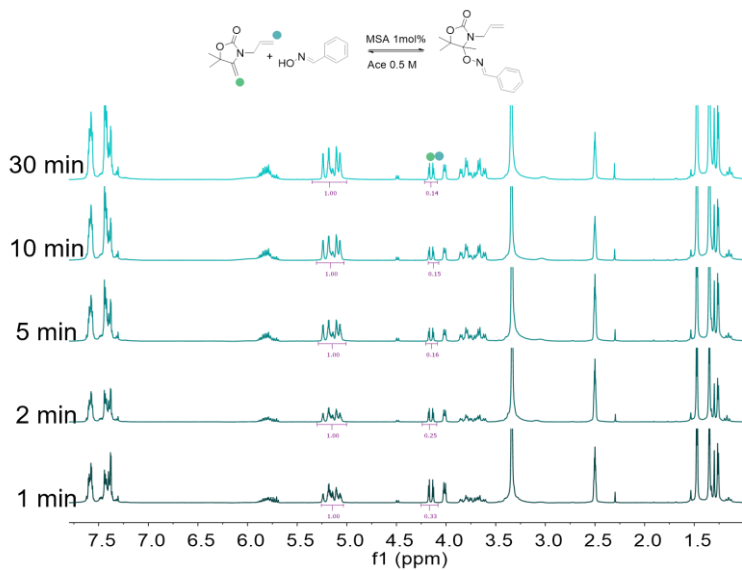


**Figure S5.18.** Kinetics of the reaction between benzaldehyde oxime and Allox (0.5M, 1mol% MSA RT) in acetone.

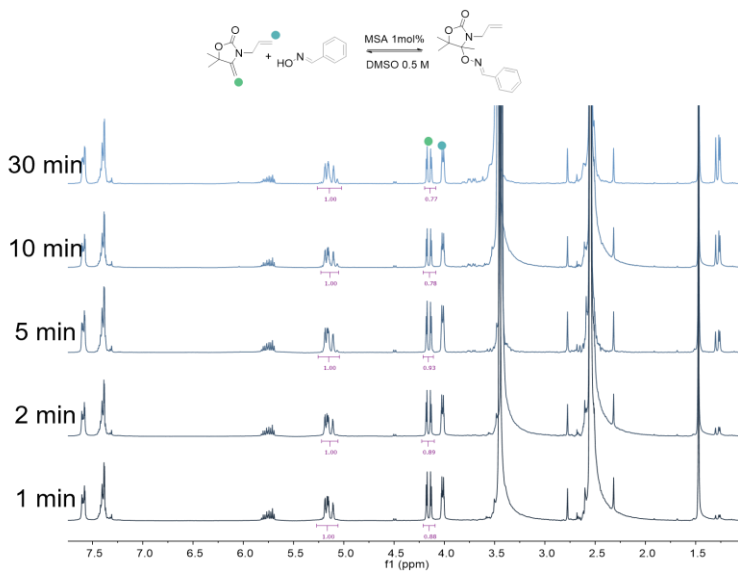


**Figure S5.19.** Kinetics of the reaction between benzaldehyde oxime and Allox (0.5M, 1mol% MSA RT) in DMSO.

### 5.5.8. Temperature Screening

Model reactions between **AlLOx** and benzaldehyde oxime were carried out. The two components dissolved in ACN (0.5M) in equal oxime to exovinylene double bond ratio with the catalyst (MSA 1mol%) at different temperatures. Aliquots of the reaction mixture were sampled over time and quenched with TEA. The reactions were monitored by  $^1\text{H}$ -NMR in  $\text{DMSO-}d_6$  spectroscopy to determine the conversion in the product.

The conversion was calculated with Equation 1 by taking into consideration the signal of the  $\text{CH}_2$  of the exovinylene double bond of **AlLOx** (4.15 ppm). The signals were normalized using the signal of the allyl bond (multiplet, 5.16 ppm).

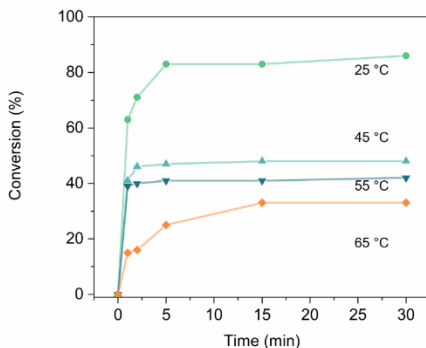


**Figure S5.20.** Conversion over time of the reaction between benzaldehyde oxime and **AlLOx** (0.5M, 1mol% MSA) in a range of temperatures.

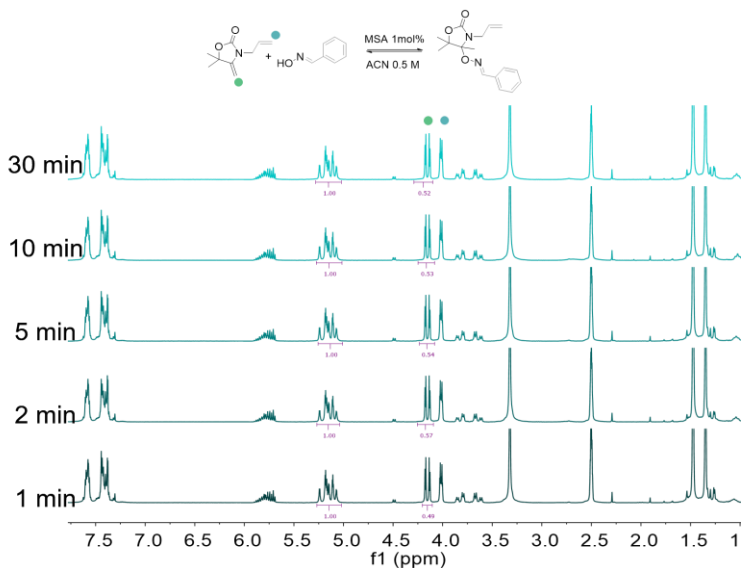


**Figure S5.21.** Kinetics of the reaction between benzaldehyde oxime and Allox (0.5M ACN, 1mol% MSA) at 45 °C.

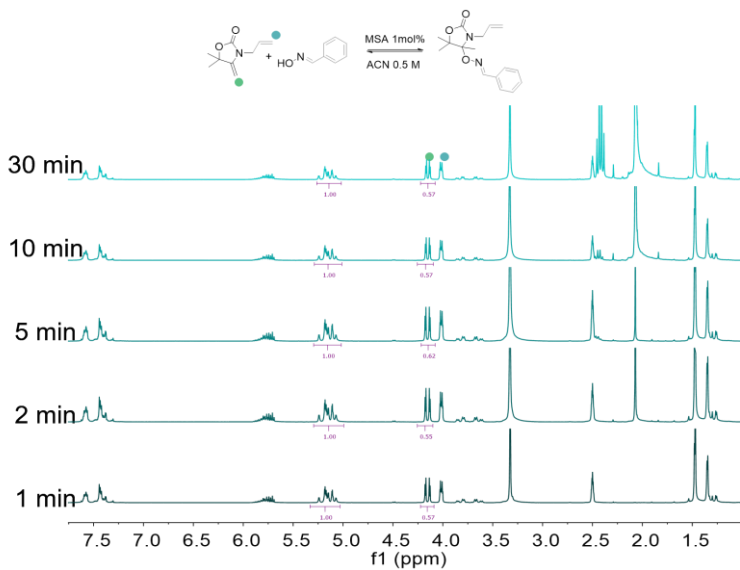
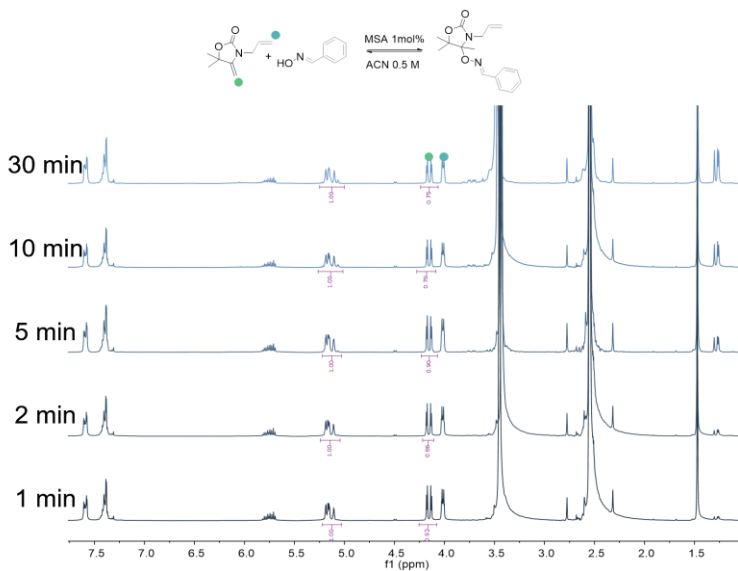


Figure S5.22. Kinetics of the reaction between benzaldehyde oxime and Alloxan (0.5M ACN, 1mol% MSA) at 55 °C.





**Figure S5.23.** Kinetics of the reaction between benzaldehyde oxime and Allox (0.5M ACN, 1mol% MSA) at 65 °C.

### 5.5.9. Temperature Dissociation

**1** was heated at different temperatures in bulk with or without MSA (1mol%) for 15 min before being dissolved in DMSO-*d*<sub>6</sub> and quenched with TEA. The solution <sup>1</sup>H NMR was then registered. The reduction in the CH<sub>2</sub> of **1** (3.75 ppm) was monitored against the allyl bond signal (5.18 ppm, used as internal standard)

The conversion was calculated with Equation 1 by taking into consideration the signal of the CH<sub>2</sub> of the allyl double bond of **1** (3.77 ppm). The signals were normalized using the signal of the allyl bond (multiplet, 5.16 ppm).

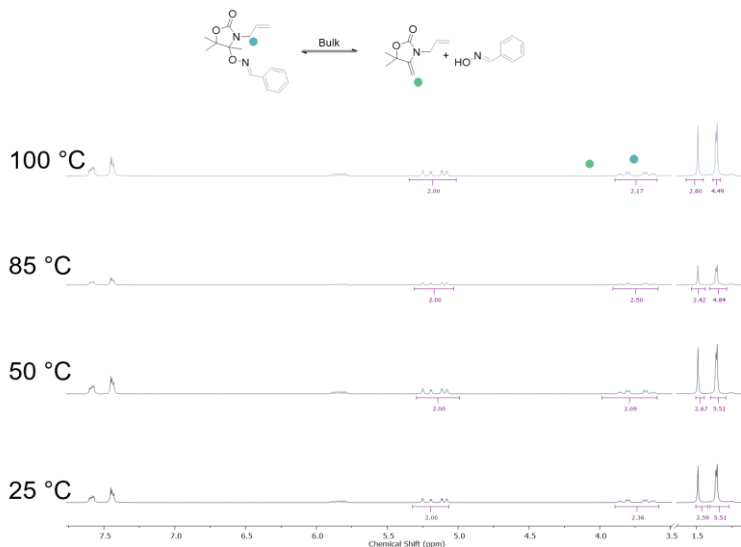


Figure S5.25. <sup>1</sup>H NMR spectra of dissociation of **1** from 25 to 100 °C.

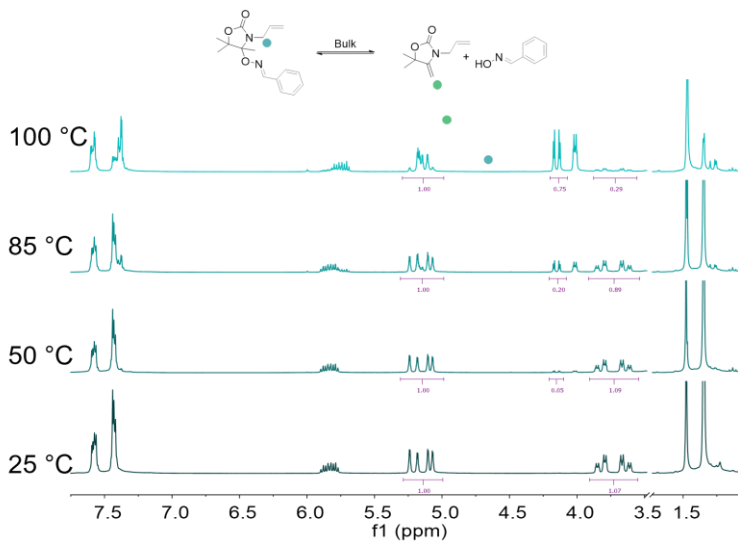
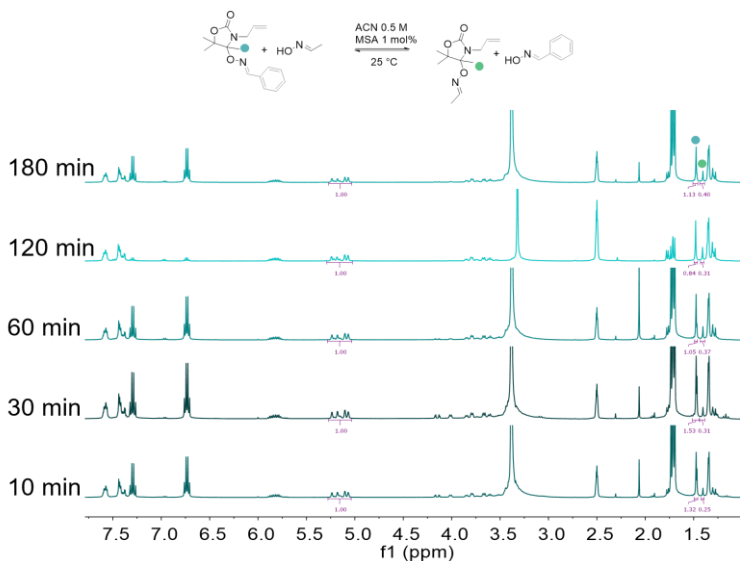


Figure S5.26.  $^1\text{H}$  NMR spectra of dissociation of **1** from 25 to 100 °C with MSA 1mol%.

## 5.5.10. Exchange

Exchange reactions between **2** and acetaldehyde oxime were carried out. The two components dissolved in ACN (0.5M) in 1:10 ratio with the catalyst (MSA 1mol%). Aliquots of the reaction mixture were sampled over time and quenched with TEA. The reactions were monitored by  $^1\text{H}$ -NMR in  $\text{DMSO-}d_6$  by integrating the  $-\text{CH}_3$  signal of the exchanged adduct (1.40 ppm) compared to the methyl of **2** (1.47 ppm) to determine the conversion in the product using equation 1.



**Figure S5.27.**  $^1\text{H}$  NMR spectra of exchange between **1** and acetaldehyde oxime at 25 °C (0.5 M ACN, MSA 1mol%).

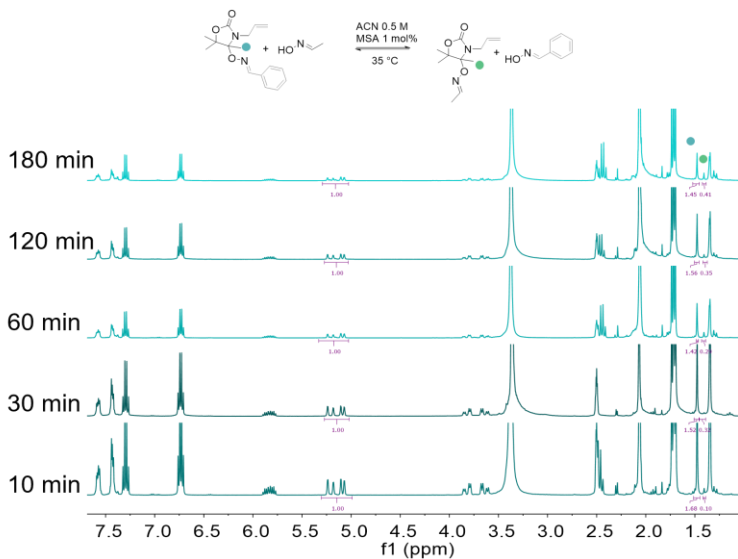


**Figure S5.28.**  $^1\text{H}$  NMR spectra of exchange between **1** and acetaldehyde oxime at 35 °C (0.5 M ACN, MSA 1 mol%).

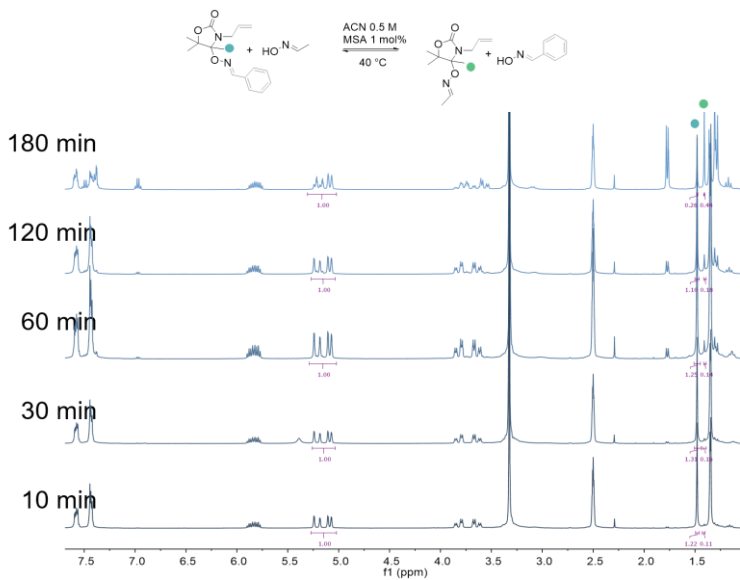


**Figure S5.29.** <sup>1</sup>H NMR spectra of exchange between **1** and acetaldehyde oxime at 40 °C (0.5 M ACN, MSA 1 mol%).

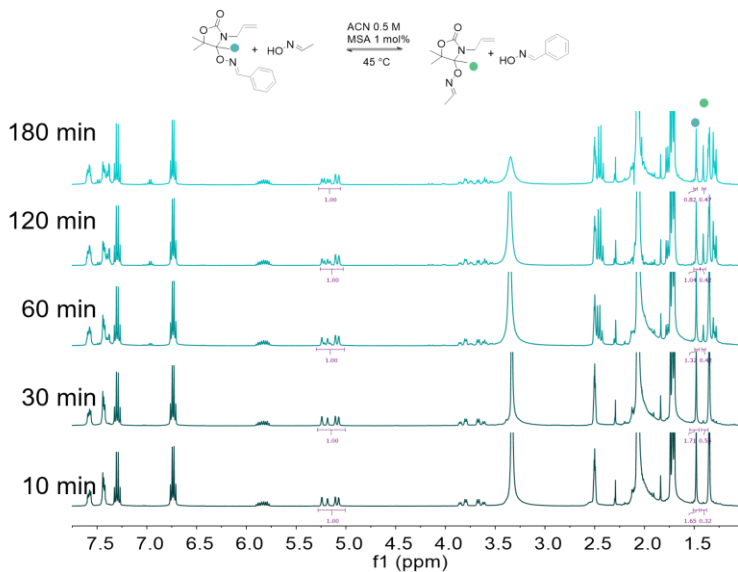


**Figure S5.30.**  $^1\text{H}$  NMR spectra of exchange between **1** and acetaldehyde oxime at 45 °C (0.5 M ACN, MSA 1 mol%).

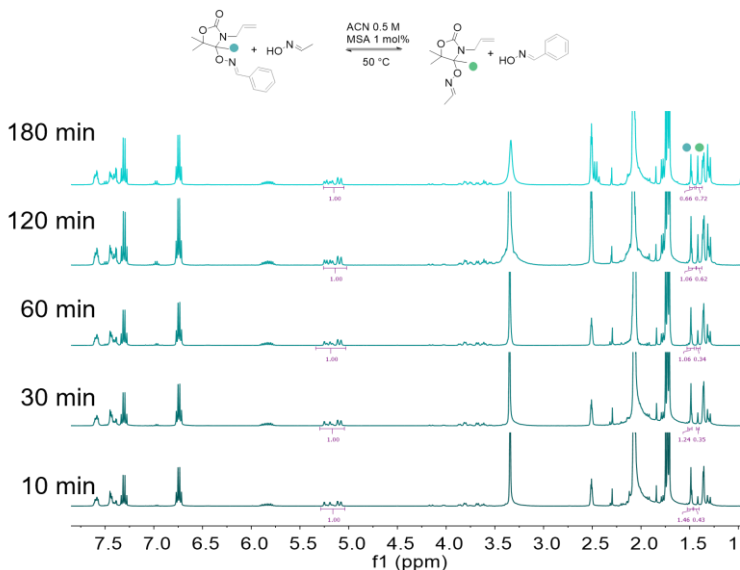


**Figure S5.31.** <sup>1</sup>H NMR spectra of exchange between **1** and acetaldehyde oxime at 50 °C (0.5 M ACN, MSA 1 mol%).

### 5.5.11. DFT

DFT calculations of geometries, energies and vibrational frequencies reported in this paper were carried out with the ωB97X-D functional<sup>43</sup> using the 6-311++G(d,p) basis set with the CPCM solvation model (chloroform) in the Gaussian 16 package. All frequencies of each structure have also been calculated to verify the presence of a single imaginary frequency for transition states and the absence of imaginary frequency for ground states.



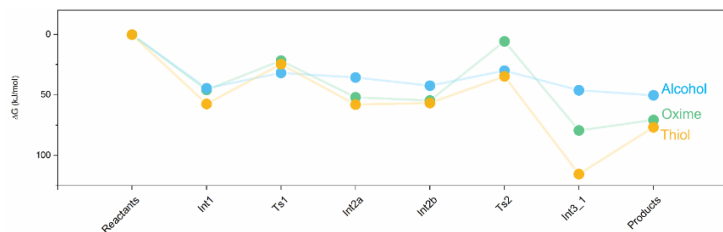
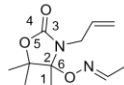


**Figure S5.32.** DFT Modelling of the reaction between alkylidene oxazolidone and different nucleophiles (Thiol, alcohol and oxime).<sup>23</sup>

**Table S5.1.** Bond lengths for intermediates and transition states along the reaction path (expressed in Å).



	SR	INT1	TS1	INT2A	INT2B	TS2	INT3
C-C (1)	1.331	1.338	1.387	1.467	1.463	1.494	1.516
C-N (2)	1.386	1.378	1.330	1.290	1.292	1.361	1.432
N-C (3)	1.372	1.381	1.414	1.448	1.450	1.392	1.367
C-O (4)	1.211	1.202	1.923	1.186	1.185	1.197	1.206
C-O (5)	1.343	1.339	1.329	1.319	1.321	1.336	1.348
C-O (6)	-	-	-	-	-	-	1.455
H-C			1.341				
O-H			1.274				
C-O						1.872	
-O-H-						1.464	
-H-O-						1.039	

The starting point consists of the reactants and the catalyst separated enough where it is considered that no interaction is taking place between them (SR), that starting geometry is optimized to **int1**, where all of them are interacting. These interactions result in a stabilization energy of -10.9 kcal/mol. The main interactions are hydrogen bonds between the negatively charged carbon atom of the alkene and the acidic proton of MSA and between the acidic proton of the thiol and a free oxygen atom of MSA.

The first interaction is already responsible for a slight bond (1) length increase of the alkene. Upon transfer of the acidic proton of MSA to the alkene through TS1, the so-formed carbocation in **int2** is stabilized by the nitrogen atom which can share electrons to build a stable  $\pi$  bond. All bond lengths in the ring are strongly impacted by this step as indicated in Table S1.

The previous C=C alkene bond becomes a sigma C-C bond (1) with increased bond length (+0.129 Å). On the other side, the C-N bond (2) decreases with the creation of the stable  $\pi$  bond. The nitrogen atom thus shares less electrons with the electron-poor carbon of the carbonyl group, resulting in a N-C(O) bond (3) length increase (+0.076 Å).

Additional hydrogen bonds stabilize **int2**, rendering this intermediate as energetically stable as the reactants complex. The second step begins with **int2** where hydrogen bonds with the proton of the thiol and the proton of the methyl group of the oxazolidone ring are located on the same oxygen donor group of the MSA, whose negative charge is stabilized by these interactions.

The addition of the oxime to the electrophilic carbon takes place as the proton from the oxime is transferred to the MSA. The C=N (2)  $\pi$  bond is suppressed, and the bond length readily increases (+0.140 Å). The nitrogen is then able to share back more electrons with the carbonyl atom resulting in a bond (3) length decrease (-0.083 Å).

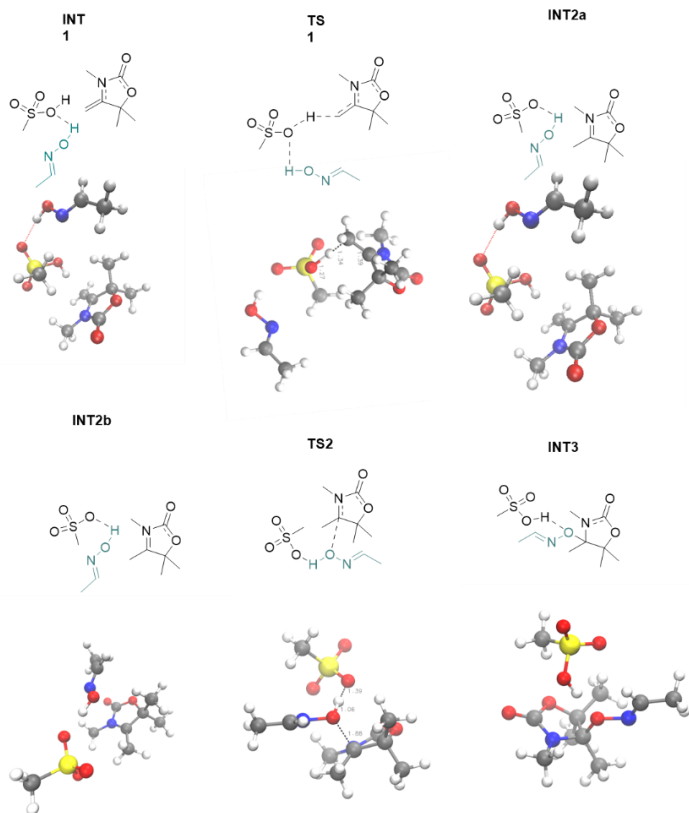


*Figure S5.33.* 2D and 3D structures of optimised intermediate and transition states of the modelled reaction path.

### 5.5.12. Synthesis of **7**

Pentaerythritol tetrakis(3-mercaptopropionate) (1 g, 2 mmol, 1 eq) and **AlIOx** (1.4 g, 8 mmol, 4 eq), BAPO (0.5 wt%) were mixed in a glass vial. The mixture irradiated with a light source centered around 390 nm (20 mW/cm<sup>2</sup>, low pressure mercury lamp) for 30 min while stirring. The resulting yellow mixture was recovered quantitatively and used without further purification.

**<sup>1</sup>H NMR** (300 MHz, DMSO-*d*<sub>6</sub>) δ 4.21 (dd, *J* = 19.1, 2.7 Hz, 8H), 4.01 (s, 6H), 3.47 (t, *J* = 7.0 Hz, 8H), 2.76 – 2.46 (m, 27H), 1.76 (t, *J* = 7.2 Hz, 8H), 1.46 (s, 24H).

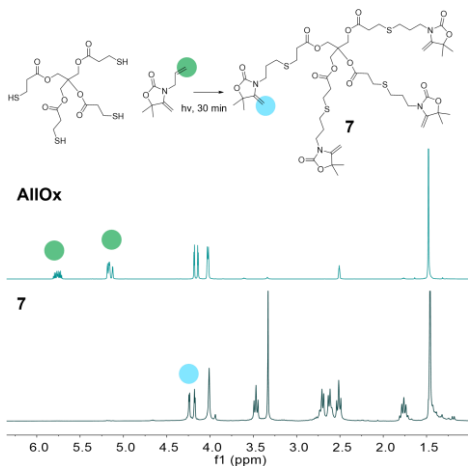


**Figure S5.34.** Synthetic scheme and <sup>1</sup>H NMR spectra pre and post irradiation of a mixture of **AlIOx** and Pentaerythritol tetrakis(3-mercaptopropionate).

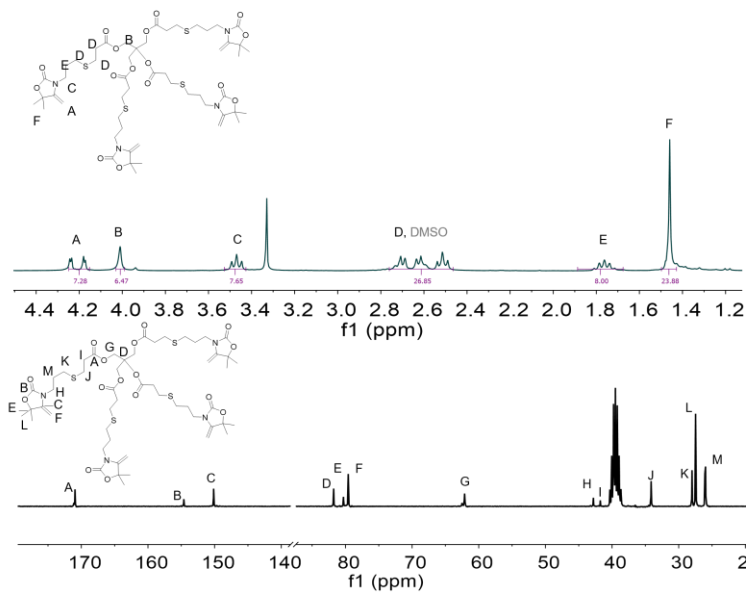
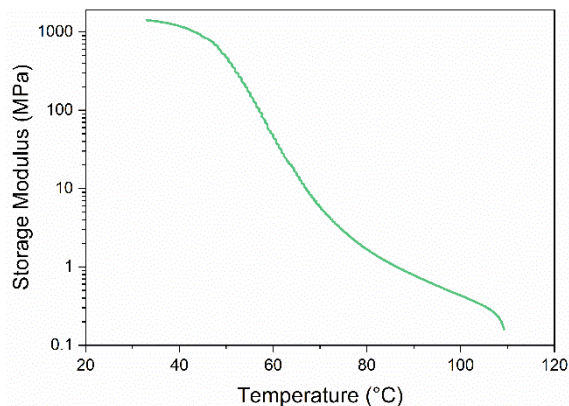


Figure S5.35.  $^1\text{H}$  NMR and  $^{13}\text{C}$  NMR of 7.

### 5.5.13. Material Characterisation



*Figure S5.36.* DMA trace of the material produced by crosslinking **7** and terephthaldehyde oxime.

*Table S5.2.* Fitting parameters of stress relaxation curves.

Temperature °C	R <sup>2</sup>
70	0.956
75	0.998
80	0.997
85	0.998
90	0.998

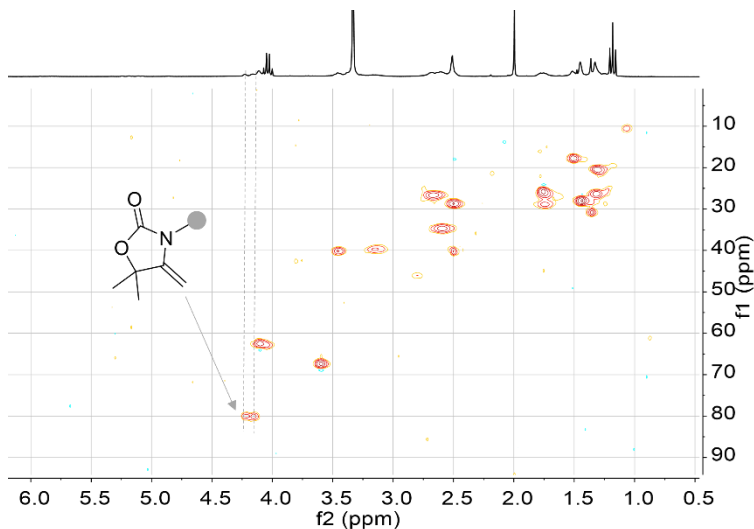


*Figure S5.37.* HSQC analysis of the liquid resulting from the depolymerisation of the network prepared by crosslinking of terephthalaldehyde oxime and **7**.

The depolymerisation was quantified by using the signal at 1.75 ppm (m,  $-\text{CH}_2-\text{CH}_2-\text{N}$ ) as internal standard and comparing it with the integral of the signal of the exovinylene double bond (4.22 ppm, br).

### 5.5.14. Hydrolytic Degradation

Model Compound **1** was placed in water or a 1M solution of MSA (0.1 M) and stirred at 200 RPM. The mixture was sampled over time and its  $^1\text{H}$  NMR spectrum immediately registered. The hydrolysis degree was calculated from the reduction of the signal of the  $-\text{CH}_3$  of **1** (1.41 s) using equation 1. This data was compared to the appearance of the signal of the  $-\text{CH}_3$  of the hydrolysis product (1.22, s) to validate the full conversion to hydrated product. The signal of the  $-\text{CH}_2$  of the allyl bond was employed as an internal standard.

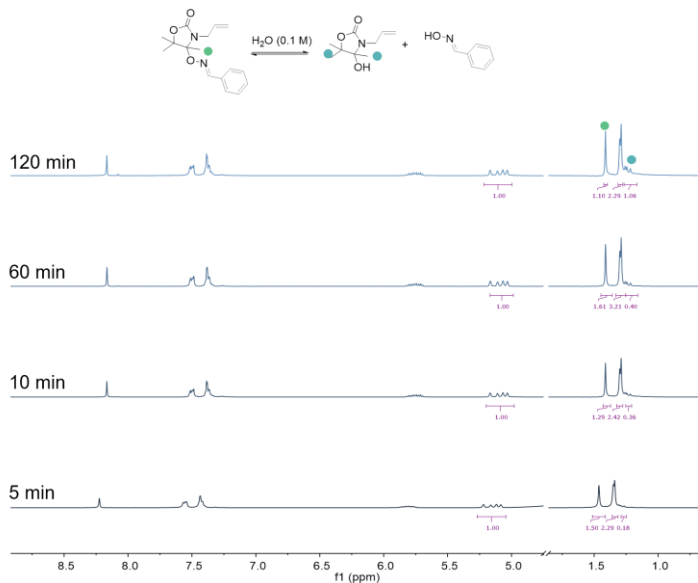


**Figure S5.38.**  $^1\text{H}$  NMR of hydrolytic degradation of **1** at different times in water.



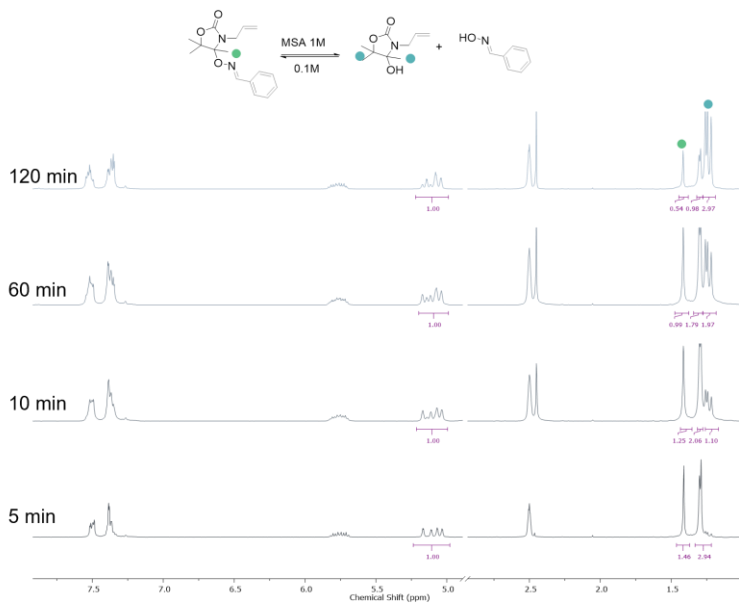


Figure S5.39. <sup>1</sup>H NMR of hydrolytic degradation of **1** at different times in 1M MSA.

## 5.5.15. $\omega$ B97-XD/6-311++G(d,p) Optimized Cartesian Coordinates

SR				C	0.928287	-0.223170	-0.184953
C	6.687544	0.156848	-0.022133	H	0.159241	-0.691134	0.432634
O	7.402294	-1.108271	0.062485	H	0.966387	-0.735767	-1.147981
C	6.547735	-2.144714	0.061774	H	1.892275	-0.331214	0.315890
C	5.233990	-0.281676	-0.076040	C	-0.728299	1.446302	-1.124499
C	7.128971	0.859352	-1.296971	H	-0.703237	0.917645	-2.079092
H	6.592200	1.804585	-1.400905	H	-1.545803	1.041035	-0.524484
H	8.200435	1.066454	-1.257412	H	-0.928719	2.503158	-1.309106
H	6.916392	0.240192	-2.170502	O	3.256375	3.381800	-0.958506
C	7.005885	0.957929	1.231094	N	1.756404	2.894054	0.731524
H	8.076922	1.165242	1.279508	C	2.260716	3.792754	1.749690
H	6.465434	1.906503	1.209289	H	2.594257	3.222902	2.619685
H	6.707508	0.407224	2.125136	H	3.101099	4.341234	1.329119
O	6.897021	-3.302047	0.125045	H	1.483005	4.497244	2.055842
N	5.263866	-1.666352	-0.020908	C	-0.087992	1.930523	1.980641
C	4.093395	-2.511562	-0.043296	H	0.104703	2.507565	2.876702
H	3.531638	-2.352705	-0.967154	H	-0.878424	1.191373	2.007471
H	4.419611	-3.548335	0.009359	O	-4.070648	4.901576	-1.926108
H	3.450289	-2.287771	0.811510	H	-3.770848	5.416347	-1.161525
C	4.152921	0.490732	-0.158498	N	-2.891294	4.428680	-2.480716
H	3.154382	0.074169	-0.190526	C	-3.092491	3.666745	-3.474859
H	4.257318	1.567069	-0.195427	H	-4.111751	3.447209	-3.798544
O	-1.989077	7.592662	0.412246	C	-1.941866	3.069071	-4.211062
H	-1.259995	7.934948	-0.109951	H	-1.961842	3.379075	-5.259683
N	-3.121176	8.008606	-0.289432	H	-0.993094	3.374731	-3.767992
C	-4.189159	7.632717	0.282130	H	-2.007615	1.977404	-4.195529
H	-4.140895	7.056684	1.208373	S	-1.567784	5.481588	0.687789
C	-5.517496	7.972813	-0.302085	O	-0.932810	5.814698	1.946121
H	-5.402485	8.533202	-1.230395	O	-2.788577	6.166900	0.301718
H	-6.086034	7.060241	-0.501415	C	-0.394064	5.614453	-0.632913
H	-6.099101	8.568916	0.406726	H	0.489892	5.032658	-0.378232
S	-6.767233	-3.891812	0.108224	H	-0.886492	5.246021	-1.533585
O	-6.009225	-5.010497	-0.411853	H	-0.139808	6.670269	-0.720025
O	-7.291914	-3.927512	1.450938	O	-1.968615	3.935877	0.689943
C	-5.852220	-2.389920	-0.128996	H	-1.301646	3.366704	1.137338
H	-4.974847	-2.453479	0.513352				
H	-6.485909	-1.554992	0.163124	TS1			
H	-5.559699	-2.322802	-1.175048	C	-0.975520	0.375720	-0.566006
O	-8.052236	-3.670513	-0.844529	O	0.247831	0.725212	-1.265531
H	-7.890571	-4.037829	-1.723378	C	0.693935	1.915137	-0.876311
				C	-1.209376	1.587409	0.304676
				C	-0.708677	-0.869273	0.269589
				H	-1.611460	-1.149337	0.814474
				H	-0.429719	-1.690223	-0.392323
				H	0.097747	-0.696718	0.984483
				C	-2.081013	0.181382	-1.594082
Int1							
C	0.592142	1.246230	-0.397574				
O	1.647089	1.834149	-1.209223				
C	2.321339	2.765007	-0.521944				
C	0.691511	2.035103	0.897628				

H -1.812848 -0.646323 -2.251999  
 H -3.017846 -0.059025 -1.089155  
 H -2.230301 1.083253 -2.188857  
 O 1.680890 2.457225 -1.269767  
 N -0.204363 2.430470 0.085859  
 C -0.020695 3.728512 0.722471  
 H 0.122865 3.589315 1.794597  
 H 0.866020 4.185505 0.289608  
 H -0.897846 4.349487 0.533196  
 C -2.331595 1.828476 1.083831  
 H -2.261151 2.606720 1.837886  
 H -2.919790 0.957561 1.356186  
 O -6.723931 3.672186 -3.195591  
 H -6.216684 4.150135 -2.514071  
 N -5.747043 3.020181 -3.926421  
 C -6.227420 2.306428 -4.859107  
 H -7.307788 2.257346 -5.010262  
 C -5.322848 1.529883 -5.755497  
 H -5.460770 1.838459 -6.795789  
 H -4.279142 1.679675 -5.475381  
 H -5.557496 0.462922 -5.700678  
 S -3.762604 4.363091 -1.088858  
 O -2.958046 5.075626 -0.095265  
 O -5.090173 4.930909 -1.354441  
 C -2.874803 4.353570 -2.629714  
 H -1.903132 3.889210 -2.467649  
 H -3.477063 3.794860 -3.346763  
 H -2.754738 5.389325 -2.945126  
 O -3.901549 2.887228 -0.716267  
 H -3.096360 2.402477 0.144050

## Int2a

C -1.718586 0.728505 0.347621  
 O -0.902764 1.489737 1.275667  
 C -0.165703 2.380199 0.641392  
 C -1.338697 1.334913 -0.969376  
 C -3.185466 0.935627 0.697107  
 H -3.819160 0.440051 -0.039948  
 H -3.368542 0.498971 1.679918  
 H -3.422793 1.998628 0.710667  
 C -1.286846 -0.735231 0.405419  
 H -1.473690 -1.111501 1.411611  
 H -1.875722 -1.322153 -0.300959  
 H -0.227018 -0.848846 0.171483  
 O 0.599967 3.158110 1.104374  
 N -0.429134 2.229089 -0.774265  
 C 0.204991 3.080713 -1.774567  
 H -0.578249 3.645112 -2.284032  
 H 0.883179 3.749176 -1.250565  
 H 0.759439 2.455824 -2.474055  
 C -1.882845 0.977831 -2.283931  
 H -2.266603 1.894533 -2.750840

H -2.680935 0.244569 -2.202829  
 O -5.167981 1.079115 -1.946909  
 H -5.030746 2.033671 -1.743798  
 N -5.107527 0.853765 -3.309265  
 C -4.945598 1.876930 -4.047514  
 H -4.856720 2.877037 -3.618347  
 C -4.858705 1.721454 -5.528972  
 H -3.903626 2.110359 -5.894001  
 H -4.951628 0.673068 -5.815323  
 H -5.649852 2.297227 -6.017719  
 S -3.407936 4.371386 -1.282889  
 O -2.546690 4.051225 -0.125044  
 O -4.725535 3.685404 -1.219908  
 C -3.762073 6.116520 -1.193932  
 H -2.817068 6.656059 -1.237514  
 H -4.395541 6.381148 -2.039123  
 H -4.273290 6.313249 -0.252870  
 O -2.724934 4.137556 -2.577086  
 H -1.077974 0.594268 -2.918981

## Int2b

C -6.567975 -2.626519 1.441823  
 O -7.728208 -2.435540 2.288737  
 C -7.819006 -1.179806 2.687646  
 C -6.018211 -1.231060 1.334057  
 C -7.012002 -3.167787 0.089451  
 H -6.135128 -3.368432 -0.528099  
 H -7.548951 -4.103502 0.248334  
 H -7.649207 -2.453074 -0.430274  
 C -5.599823 -3.554637 2.171456  
 H -6.095564 -4.512755 2.330203  
 H -4.708622 -3.720945 1.565663  
 H -5.305035 -3.141228 3.137244  
 O -8.603742 -0.709283 3.440359  
 N -6.739493 -0.442863 2.060089  
 C -6.641364 0.999848 2.266443  
 H -7.489070 1.458586 1.758769  
 H -6.685888 1.188546 3.337360  
 H -5.718388 1.374614 1.830401  
 C -4.861160 -0.868337 0.513889  
 H -4.372649 0.044560 0.850257  
 H -5.222358 -0.673811 -0.506222  
 O -8.156615 -0.185802 -0.910100  
 H -7.628761 0.646489 -0.860694  
 N -9.054346 -0.092794 0.140781  
 C -9.990376 -0.948356 0.055681  
 H -10.032430 -1.625836 -0.800017  
 C -11.038347 -1.035439 1.111248  
 H -11.030112 -2.028325 1.570816  
 H -10.874608 -0.285533 1.885006  
 H -12.028500 -0.891115 0.669994  
 S -5.337436 2.252554 -1.076384

O	-4.524095	2.371121	0.152603
O	-6.786899	2.078984	-0.764143
C	-5.216675	3.819036	-1.922483
H	-4.169042	3.992783	-2.164217
H	-5.815491	3.764425	-2.830347
H	-5.591735	4.597441	-1.259863
O	-4.847080	1.218178	-2.006728
H	-4.156407	-1.697783	0.463459

## TS2

C	-7.500857	-1.881858	2.515237
O	-7.126084	-0.817079	3.419190
C	-6.050299	-0.174377	2.965111
C	-6.653678	-1.569400	1.275149
C	-9.008318	-1.860187	2.342429
H	-9.307592	-2.560717	1.561471
H	-9.469537	-2.166971	3.282429
H	-9.363909	-0.865296	2.082867
C	-7.025038	-3.198573	3.132131
H	-7.492515	-3.306250	4.111202
H	-7.324616	-4.042494	2.508701
H	-5.940581	-3.213457	3.258534
O	-5.438148	0.661798	3.554902
N	-5.725997	-0.694440	1.696291
C	-4.615873	-0.144953	0.927179
H	-3.828784	0.129802	1.626661
H	-4.242021	-0.901711	0.240977
H	-4.953288	0.742690	0.390032
C	-6.330438	-2.636815	0.287050
H	-5.874787	-2.227945	-0.612111
H	-7.230788	-3.187017	0.015812
O	-7.865461	-0.587047	0.219155
H	-7.901882	0.342549	0.723505
N	-7.346605	-0.242524	-1.056637
C	-7.976759	-0.859848	-1.970935
H	-8.790892	-1.538712	-1.713848
C	-7.608877	-0.654055	-3.395957
H	-8.480090	-0.296469	-3.950997
H	-6.793910	0.062730	-3.492515
H	-7.312340	-1.608202	-3.840236
S	-7.445139	2.851738	0.981742
O	-7.702497	3.889217	1.980339
O	-7.962674	1.511693	1.465728
C	-8.444609	3.220804	-0.452090
H	-8.122051	4.182970	-0.847548
H	-8.286954	2.431820	-1.186784
H	-9.487864	3.263550	-0.142978
O	-6.055426	2.752247	0.516947
H	-5.620524	-3.323811	0.752965

## Int3

C	-7.583910	-1.247194	2.112483
O	-7.685024	-0.574216	3.400224
C	-6.556820	0.120895	3.648132
C	-6.473489	-0.418076	1.395532
C	-8.949865	-1.196166	1.458377
H	-8.908097	-1.655667	0.469525
H	-9.657999	-1.756263	2.072441
H	-9.306277	-0.172033	1.350486
C	-7.147081	-2.680297	2.391705
H	-7.886554	-3.153058	3.039930
H	-7.085578	-3.252076	1.464172
H	-6.176648	-2.713390	2.891631
O	-6.323915	0.638389	4.712049
N	-5.780401	0.125355	2.525085
C	-4.551294	0.886982	2.421669
H	-4.660319	1.697825	1.698121
H	-4.336744	1.310062	3.401248
H	-3.724417	0.240556	2.122291
C	-5.577268	-1.181250	0.439830
H	-4.908458	-0.485404	-0.069153
H	-6.168197	-1.699491	-0.312989
O	-7.029479	0.751893	0.732329
H	-7.510568	2.075437	1.689811
N	-7.511696	0.479917	-0.558453
C	-7.977154	1.524605	-1.105789
H	-7.974227	2.483093	-0.587330
C	-8.552649	1.448715	-2.476525
H	-8.022824	2.135096	-3.142334
H	-8.487832	0.435625	-2.873609
H	-9.599773	1.762369	-2.452706
S	-9.305213	2.995707	2.471654
O	-9.553859	4.404064	2.678367
O	-7.727146	2.847469	2.268153
C	-9.592674	2.116321	3.983377
H	-10.653843	2.213454	4.209499
H	-9.315655	1.074005	3.832599
H	-8.984695	2.573412	4.761712
O	-9.969442	2.306429	1.377829
H	-4.979417	-1.905290	0.992627

## wB97X-D

## 5.6. References

1. Regulation - 2020/1149 - EN - EUR-Lex. <https://eur-lex.europa.eu/legal-content/EN/ALL/?uri=CELEX%3A32020R1149>.
2. Broughton, E. The Bhopal disaster and its aftermath: A review. *Environ Health* **4**, 1–6 (2005).
3. Monie, F., Grignard, B. & Detrembleur, C. Divergent Aminolysis Approach for Constructing Recyclable Self-Blown Nonisocyanate Polyurethane Foams. *ACS Macro Lett* **11**, 236–242 (2022).
4. Rokicki, G., Parzuchowski, P. G. & Mazurek, M. Non-isocyanate polyurethanes: Synthesis, properties, and applications. *Polym Adv Technol* **26**, 707–761 (2015).
5. Kathalewar, M. S., Joshi, P. B., Sabnis, A. S. & Malshe, V. C. Non-isocyanate polyurethanes: From chemistry to applications. *RSC Adv* **3**, 4110–4129 (2013).
6. Vidal, F. *et al.* Designing a circular carbon and plastics economy for a sustainable future. *Nature* **626**, 45–57 (2024).
7. Mundo, F., Caillol, S., Ladmira, V. & Meier, M. A. R. On Sustainability Aspects of the Synthesis of Five-Membered Cyclic Carbonates. *ACS Sustain Chem Eng* **12**, 6452–6466 (2024).
8. Cornille, A., Auvergne, R., Figovsky, O., Boutevin, B. & Caillol, S. A perspective approach to sustainable routes for non-isocyanate polyurethanes. *Eur Polym J* **87**, 535–552 (2017).
9. Decostanzi, M., Bonneaud, C. & Caillol, S. From hydroxyurethane methacrylates to hybrid nonisocyanate polyurethanes. *J Polym Sci A Polym Chem* **57**, 1224–1232 (2019).
10. Ecochard, Y. & Caillol, S. Hybrid polyhydroxyurethanes: How to overcome limitations and reach cutting edge properties? *Eur Polym J* **137**, 109915 (2020).
11. Bizet, B., Grau, E., Asua, J. M. & Cramail, H. Hybrid Nonisocyanate Polyurethanes (H-NIPUs): A Pathway towards a Broad Range of Novel Materials. *Macromolecular Chemistry and Physics* vol. 223 2100437 Preprint at <https://doi.org/10.1002/macp.202100437> (2022).
12. Gomez-Lopez, A., Elizalde, F., Calvo, I. & Sardon, H. Trends in non-isocyanate polyurethane (NIPU) development. *Chemical Communications* **57**, 12254–12265 (2021).
13. Sahu, D. P. A convenient and safe synthesis of 4,5-disubstituted-2-oxo-1,3-dioxolenes<sup>†</sup>. *IJC-B Vol.41B(08) [August 2002]* **41**, 1722–1723 (2002).
14. Qiao, C. *et al.* An Organocatalytic Route to endo-Vinylene Carbonates from Carbon Dioxide-Based exo-Vinylene Carbonates. *Adv Synth Catal* **366**, 291–298 (2024).
15. Fischler, H. M., Heine, H. G. & Hartmann, W. Darstellung einiger dialkylsubstituierter vinylencarbonate und ihre photosensibilisierte cycloaddition an äthylen. *Tetrahedron Lett* **13**, 1701–1704 (1972).

16. Yuen, A. *et al.* Room temperature synthesis of non-isocyanate polyurethanes (NIPUs) using highly reactive N-substituted 8-membered cyclic carbonates. *Polym Chem* **7**, 2105–2111 (2016).
17. Tomita, H., Sanda, F. & Endo, T. Polyaddition of bis(seven-membered cyclic carbonate) with diamines: A novel and efficient synthetic method for polyhydroxyurethanes. *J Polym Sci A Polym Chem* **39**, 4091–4100 (2001).
18. Ngassam Tounzoua, C., Grignard, B. & Detrembleur, C. Exovinylene Cyclic Carbonates: Multifaceted CO<sub>2</sub>-Based Building Blocks for Modern Chemistry and Polymer Science. *Angewandte Chemie - International Edition* vol. 61 Preprint at <https://doi.org/10.1002/anie.202116066> (2022).
19. Stiernet, P. *et al.* Rapid CO<sub>2</sub> coupling to propargylic alcohols: unlocking the production of  $\alpha$ -alkylidene cyclic carbonates via continuous flow. *Green Chemistry* (2024) doi:10.1039/D4GC05716C.
20. Gennen, S., Grignard, B., Tassaing, T., Jérôme, C. & Detrembleur, C. CO<sub>2</sub>-Sourced  $\alpha$ -Alkylidene Cyclic Carbonates: A Step Forward in the Quest for Functional Regioregular Poly(urethane)s and Poly(carbonate)s. *Angewandte Chemie - International Edition* **56**, 10394–10398 (2017).
21. Grignard, B., Gennen, S., Jérôme, C., Kleij, A. W. & Detrembleur, C. Advances in the use of CO<sub>2</sub> as a renewable feedstock for the synthesis of polymers. *Chem Soc Rev* **48**, 4466–4514 (2019).
22. Habets, T., Siragusa, F., Grignard, B. & Detrembleur, C. Advancing the synthesis of isocyanate-free poly(oxazolidones)s: Scope and limitations. *Macromolecules* **53**, 6396–6408 (2020).
23. Habets, T. *et al.* Covalent Adaptable Networks through Dynamic N,S-Acetal Chemistry: Toward Recyclable CO<sub>2</sub>-Based Thermosets. *J Am Chem Soc* **145**, 25450–25462 (2023).
24. Caliri, M. *et al.* Fully Recyclable Pluripotent Networks for 3D Printing Enabled by Dissociative Dynamic Bonds. *Advanced Materials* 2417355 (2025) doi:10.1002/ADMA.202417355.
25. Yan, T., Balzer, A. H., Herbert, K. M., Epps, T. H. & Korley, L. S. T. J. Circularity in polymers: addressing performance and sustainability challenges using dynamic covalent chemistries. *Chem Sci* **14**, 5243–5265 (2023).
26. Zhang, L. & You, Z. Dynamic Oxime-Urethane Bonds, a Versatile Unit of High Performance Self-healing Polymers for Diverse Applications. *Chinese Journal of Polymer Science (English Edition)* **39**, 1281–1291 (2021).
27. Ābele, E. & Lukevics, E. Recent advances in the chemistry of oximes. *Org Prep Proced Int* **32**, 235–264 (2000).
28. Mukherjee, S., Bapat, A. P., Hill, M. R. & Sumerlin, B. S. Oximes as reversible links in polymer chemistry: dynamic macromolecular stars. *Polym Chem* **5**, 6923–6931 (2014).
29. Collins, J., Xiao, Z., Espinosa-Gomez, A., Fors, B. P. & Connal, L. A. Extremely rapid and versatile synthesis of high molecular weight step growth polymers via oxime click chemistry. *Polym Chem* **7**, 2581–2588 (2016).

30. Collins, J., Xiao, Z., Müllner, M. & Connal, L. A. The emergence of oxime click chemistry and its utility in polymer science. *Polym Chem* **7**, 3812–3826 (2016).
31. Kalia, J. & Raines, R. T. Hydrolytic stability of hydrazones and oximes. *Angewandte Chemie - International Edition* **47**, 7523–7526 (2008).
32. Grover, G. N., Braden, R. L. & Christman, K. L. Oxime cross-linked injectable hydrogels for catheter delivery. *Advanced Materials* **25**, 2937–2942 (2013).
33. Novoa-Carballal, R. & Müller, A. H. E. Synthesis of polysaccharide-b-PEG block copolymers by oxime click. *Chemical Communications* **48**, 3781–3783 (2012).
34. Ghosh, S., Cabral, J. D., Hanton, L. R. & Moratti, S. C. Strong poly(ethylene oxide) based gel adhesives via oxime cross-linking. *Acta Biomater* **29**, 206–214 (2016).
35. Collins, J., Xiao, Z. & Connal, L. A. Tunable degradation of polyethylene glycol-like polymers based on imine and oxime bonds. *J Polym Sci A Polym Chem* **55**, 3826–3831 (2017).
36. Kongkatigumjorn, N. & Crespy, D. Strategies to prepare polymers with cleavable linkages releasing active agents in acidic media. *Polym Chem* **15**, 4491–4518 (2024).
37. Pettazzoni, L. et al. Oxime metathesis: tuneable and versatile chemistry for dynamic networks. *Chem Sci* **15**, 2359–2364 (2024).
38. Laurence, C. & Gal, J. F. Lewis Basicity and Affinity Scales: Data and Measurement. *Lewis Basicity and Affinity Scales: Data and Measurement* 1–460 (2009) doi:10.1002/9780470681909.
39. Chao, A. & Zhang, D. Investigation of Secondary Amine-Derived Aminal Bond Exchange toward the Development of Covalent Adaptable Networks. *Macromolecules* **52**, 495–503 (2019).
40. Sutherland, B. P., Kabra, M. & Kloxin, C. J. Expanding the thiol-X toolbox: Photoinitiation and materials application of the acid-catalyzed thiol-ene (ACT) reaction. *Polym Chem* **12**, 1562–1570 (2021).
41. Zhang, V., Kang, B., Accardo, J. V. & Kalow, J. A. Structure-Reactivity-Property Relationships in Covalent Adaptable Networks. *J Am Chem Soc* **144**, 22358–22377 (2022).
42. Jin, Y. et al. Oxime linkage: A robust tool for the design of pH-sensitive polymeric drug carriers. *Biomacromolecules* **12**, 3460–3468 (2011).
43. Chai, J. Da & Head-Gordon, M. Long-range corrected hybrid density functionals with damped atom–atom dispersion corrections. *Physical Chemistry Chemical Physics* **10**, 6615–6620 (2008).







# 7

## General Conclusions



## 7.1. Conclusions

Interwoven in the chapters of this thesis is the clear potential of polyoxazolidones (POXas) to drive innovation in the field of NIPUs. These polymers can be prepared under mild conditions, and, in this work, were demonstrated to be prepared by photocuring in seconds. Their properties can vary wildly by adjusting the underlying chemistry used for crosslinking, as highlighted in **Chapters 2,4** and **5**. Combining this together with the inherent sustainability of additive manufacturing highlights a path forward for innovating the field.

One of the main developments of **Chapter 2** was the introduction of a new monomer. Previous efforts in the field were limited by the relative inaccessibility of adequate substrates, low solubility or the use of dangerous reagents. In this study, we established a route to access a highly reactive, liquid monomer in large scale, with minimal purification required. We developed its chemistry via two thiol ene reactions, cationic and radical. By combining the two, we obtained materials that presented a phase-separated morphology driven by a dynamic reaction-induced phase separation. By heat treating these materials, we could regulate the size and distribution of the phase-separated morphology, deeply changing their mechanical properties (Young's Modulus from 2 to 3000 MPa) from a single material. Thanks to the ability of the *N,S*-acetal dynamic bond to dissociate at high temperatures, together with the viscoelastic characteristics of these materials, we realised the FDM printing of isotropic objects. Furthermore, thanks to the ability to obtain different mechanical properties from the same material, we realized a functional gripper with rigid arms and a flexible connecting band. We demonstrated that the material could be recycled up to ten times without major loss of mechanical properties, a major step forward in the introduction of pluripotent materials in real-world applications.

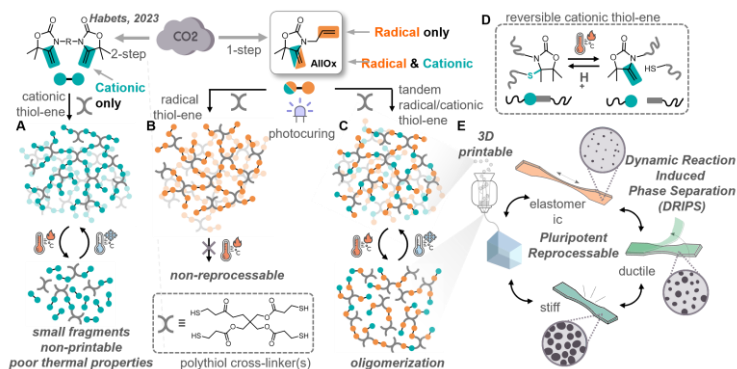
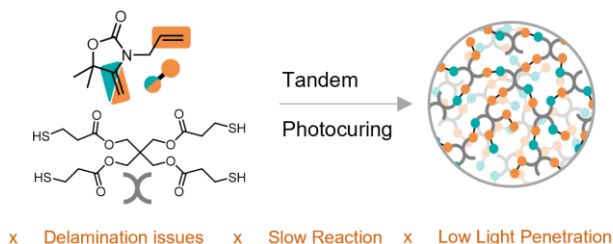


**Figure 7.1.** General scheme describing the work carried out in **Chapter 2**. Previous work carried out in the field of *N,S*-acetals (a). Radical-only strategy (b) compared to tandem strategy giving FDM-compatible tandem materials (c). Scheme of the reversible *N,S*-acetal Reaction (d) and scheme of pluripotent materials (e).

Further developments of pluripotent materials were described in **Chapter 3**. Encouraged by the rapid photocuring of the tandem materials of **Chapter 2**, we further developed the photochemistry to enable the DLP printing of pluripotent materials. First, seeing that previously utilised photoinitiators suffered from excessive absorption, we changed the photosensitiser from ITX to ANT. While this gave a two-fold increase in printing times, problems of delamination still plagued the system, mainly given by the asymmetrical reactivity of AIOx. Hence, a 2-step curing procedure was developed, in which first the cationic thiol-ene reaction was carried out to give prepolymer, followed

## A Previous Chapter



## B Chapter 3

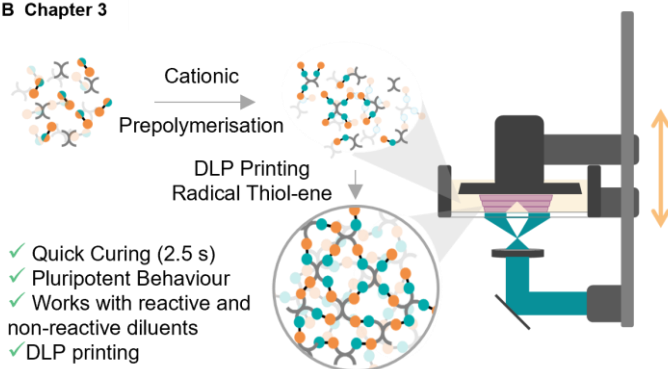


**Figure 7.2.** General scheme describing the work carried out in **Chapter 3**. The strategy followed for **Chapter 2** and its limitations (a) and 2-step curing for DLP printing of pluripotent materials (b).

by faster radical thiol ene. This gave material that could cure in few seconds compared to minutes of earlier formulations. Several reactive and non-reactive diluents were screened to assess their impact on the pluripotent behaviour of the materials. It was found that as long as the connectivity between dynamic bonds was maintained, the pluripotent

behaviour of the final material was still present. However, amongst all tested reactive diluents, only TVC gave materials with a  $T_g$  higher than RT, enabling the formulation of pluripotent materials. Their 3D printing was realised with an increase in printing times of 40 times when compared to the initial formulation. In fact, a 100  $\mu\text{m}$  layer could be cured in 2s exposure. With this resin, we could produce a high-resolution gyroid cube as a demonstration of the potential of the resin for DLP printing.

While the material developed in the previous two chapters had interesting and rare properties, they were based on *N,S*-acetal bonds. These species, while endowing the materials with great recyclability, hinder their degradation, a key piece in the design of truly sustainable materials. Hence in **Chapter 4**, inspired by other hydro-degradable bonds such as *O,O*-acetals or amins, we developed a new type of dynamic bond, *N,O*-acetals. We explore the thermodynamics of this bond, finding that the low stabilisation of the product compared to the reagents (calculated by DFT) severely limited the conversion. This negatively affected the yield in derivatives, giving maximum yields of 60% and requiring column chromatography for the purification and usage of a glovebox to avoid side reactions with water. Notwithstanding this, a diallyl monomer containing the *N,O*-acetal moiety could be prepared in reasonable yields and was installed in a range of photocurable materials. The curing kinetics were seconds, enabling high-resolution DLP printing of complex structures. Furthermore, by mixing this cleavable monomer together with **AlLOx**, we could regulate the water degradability of the materials.

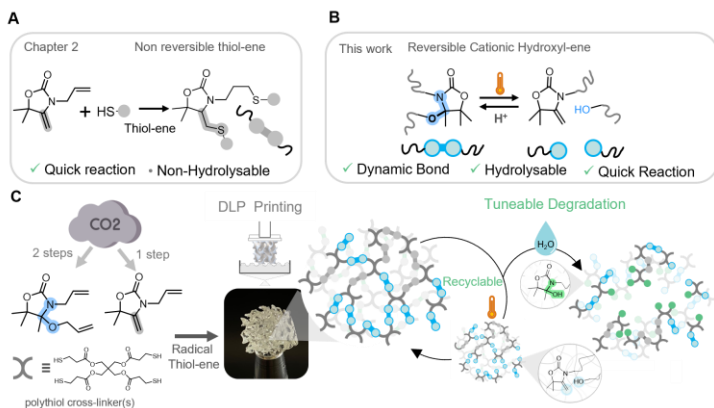


**Figure 7.3.** General scheme describing the work carried out in **Chapter 4**. Radical thiol-ene to form non hydrolysable bonds. Dynamic N,O acetal reaction (b). Strategy for the preparation of 3D printable materials with tuneable degradability (c).

**Chapter 5** dedicates itself to monomer design with the ultimate goal of finding a dynamic bond that had high conversions in its preparation and was degradable. We found the perfect combination in oximes, thanks to their higher nucleophilicity, the reaction between **AlLOx** and oximes proceeded rapidly and offered conversions above 80% for most substrates. This behaviour was further supported by DFT, in which we found oximes having an intermediate behaviour as the one of alcohols and the one of thiols. We installed this functionality in materials and demonstrated that the oxime- $\alpha$ -oxazolidone bond was more resistant to hydrolysis at room temperature, but completely degrades in water above 60 °C, solving a major limitation of unwanted room temperature degradation seen in *N,O*-acetals.



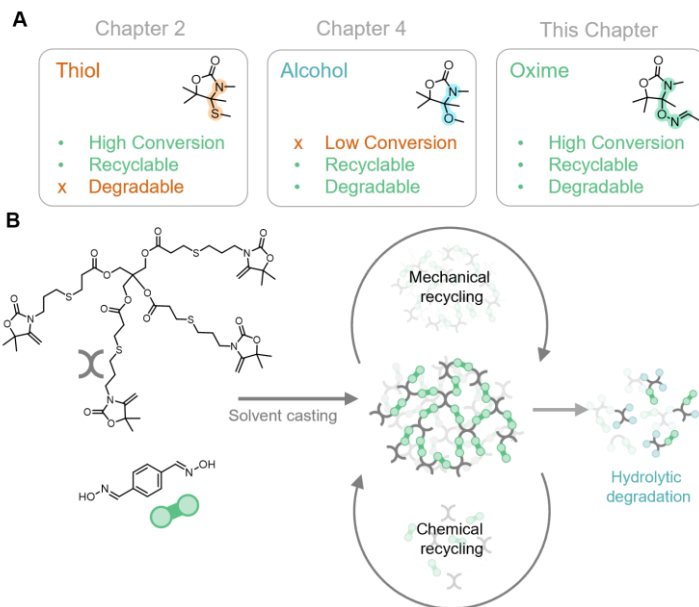


**Figure 7.4.** General scheme describing the work carried out in **Chapter 5**. Differences between *N,S*-acetal, *N,O* acetal and the oxime- $\alpha$ -oxazolidone dynamic bond (b). Strategy for the preparation of mechanically and chemically recyclable materials that can undergo hydrolytic degradation (c).

Finally, **Chapter 6** reports the preparation of dynamic networks for biomedical applications. We employ the *N,S*-acetal chemistry to produce a slippery coating that has similar properties to coatings prepared with linear species but is more resistant to water while providing similar performances. The coatings are recyclable and self-healable thanks to the presence of the *N, S*-acetal dynamic bond.

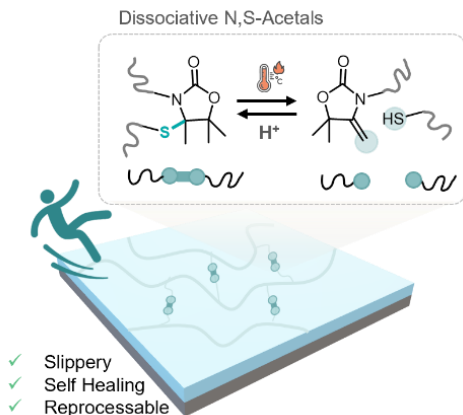


**Figure 7.5.** General scheme describing the work carried out in Chapter 6. The *N,S*-acetal dynamic bond was employed to produce dynamically crosslinked coatings that enhance the slipperiness of surfaces.

## 7.2. Perspective

This document reports major efforts towards the reduction of bottlenecks in the field of NIPU, reporting a new toolbox for photocuring and degradation of POXas and their 3D printing. Being the nature of this work exploratory, many questions have been left unanswered.

While the materials reported in **Chapter 2** have a very interesting behaviour, the underlying mechanism behind the dynamic reaction-induced phase separation remains, to this day, unclear. While we report the first studies attempting to pinpoint the phase composition, further studies using advanced NMR spectroscopy techniques (Spin-lattice relaxation time measurements), flash DSC and AFM are required to reveal the differences between the phases. The group is currently working towards these goals, combining them with computational approaches.

Encouraging results came from **Chapter 3**, in which we unveil that pluripotent material is not so uncommon and can exist also in presence of other species in the materials. This can greatly vary the possible composition of the resins and gives access to high resolution DLP printing of pluripotent materials. Further efforts should be focused on optimising the printing conditions for these materials to enable their advanced manufacturing. Furthermore, developing methods to better localise the heat, for example employing the photothermal effect, would major benefit this technology, enabling a better control of the mechanical properties of the materials at precise location.

The major bottleneck to further application of the dynamic bond reported in **Chapter 4** remains their low accessibility. Hence, **Chapter 5** works towards this with the introduction of a reaction with a higher conversion. With this, we report the first POXa network that is both recyclable and degradable, pointing toward the potential of these kinds

of materials in a variety of applications. While interesting, the materials reported are extremely brittle, and further formulations should be developed. The oxime-ene reaction therein reported is well-behaved and could be applied to a variety of POXas, further expanding the toolbox accessible to today's polymer chemist.

**Chapter 6** recollects a small example of bringing a lab-scale technology to the industrial scale. While the developed materials were not dynamic enough to undergo co-extrusion, further network engineering could bring this property, as previously demonstrated by both **Chapter 2** and the literature.

Lastly, as reported in **Section 1.1** we would like to again highlight that this thesis was developed in a framework of exploration of new polymer species. Today's world sees most planetary boundaries being exceeded, and the most important for the synthetic chemist, new entities, being one of the worst performing. Hence, further developments of all types of polymeric materials developed herein should be made by considering the frailness of the system earth in a framework of material stewardship. That means taking care of the material from its synthesis to its repurpose and developing materials with a well-informed approach. For example, while attempts at creating degradable materials were made, their biodegradation and toxicity was not evaluated and should be clarified before any larger-scale application is envisioned. Furthermore, Life cycle assessment, techno-economical, socio-economical and "absolute" environmental sustainability assessments should be carried out to truly quantify the potential of the materials herein developed for the sustainable benefits of society.

## 7.3. List of Publications

Part of this thesis has been published or will be published in the future. Below a list of the published works:

**1.** M. Caliori, F. Vidal, D. Mantione, G. Seychal, M. Campoy-Quiles, L. Irusta, M. Fernandez, X. L. de Pariza, T. Habets, N. Aramburu, J.-M. Raquez, B. Grignard, A. J. Müller, C. Detrembleur, H. Sardon, Fully Recyclable Pluripotent Networks for 3D Printing Enabled by Dissociative Dynamic Bonds. *Adv. Mater.* 2025, 2417355. <https://doi.org/10.1002/adma.202417355>

Furthermore, these works are submitted or programmed to be submitted in the near future.

**1.** M. Caliori, I. Teotonico, M. I. Irigoyen Irtatsun, A. Mugika, T. Isolabella, D. Mantione, L. Irusta, B. Grignard, F. Vidal, C. Detrembleur, H. Sardon. A Platform for Tuneable Degradation of 3D printable polymers containing dissociative CO<sub>2</sub>-derived *N,O*-acetals (provisional title)

**2.** M. Caliori, M. I. Irigoyen Irtatsun, F. Vidal, C. Detrembleur, H. Sardon. Developing the Oxime-ene dynamic chemistry towards degradable and recyclable NIPUs (Provisional Title)

**3.** DLP printing of Pluripotent materials based on the *N,S*-acetal chemistry. M. Caliori, C. Detrembleur, H. Sardon (Provisional Title)

The author also participated in several collaborations as listed below:

**1.** A. Lamas, L. Polo Fonseca, C. Moussard, D. de M. Zanata, G. Perli, M. Ximenis, X. Lopez de Pariza, G. Seychal, M. Caliori, M. Itxaso, R. Aguirresarobe, I. Calvo, H. Sardon, Exploiting the Base-Triggered Thiol/Vinyl Ether Addition to Prepare Well-Defined Microphase Separated Thermo-Switchable Adhesives. *Adv. Funct. Mater.* 2025, 35, 2412584. <https://doi.org/10.1002/adfm.202412584>

2. Thomas Habets, Guillem Seychal, Marco Caliri, Jean-Marie Raquez, Haritz Sardon, Bruno Grignard, and Christophe Detrembleur, Covalent Adaptable Networks through Dynamic *N,S*-acetal Chemistry: Toward Recyclable CO<sub>2</sub>-Based Thermosets, *Journal of the American Chemical Society* 2023 145 (46), 25450-25462, DOI: 10.1021/jacs.3c10080

